JUL 21 2004

# REPORT DOCUMENTATION PAGE

*Form Approved*
*OMB No. 0704-0188*



| 1. AGENCY USE ONLY *(Leave blank)* | 2. REPORT DATE | 3. REPORT TYPE AND DATES COVERED |
|---|---|---|
| | 15.Jul.04 | DISSERTATION |

**4. TITLE AND SUBTITLE**
INTERACTION OF LARGE SCALE ZONAL FLOW ANOMALIES AND TOPOGRAPHY

**5. FUNDING NUMBERS**

**6. AUTHOR(S)**
MAJ BYERLE LEE A

**7. PERFORMING ORGANIZATION NAME(S) AND ADDRESS(ES)**
UNIVERSITY OF UTAH

**8. PERFORMING ORGANIZATION REPORT NUMBER**
CI04-451

**9. SPONSORING/MONITORING AGENCY NAME(S) AND ADDRESS(ES)**
THE DEPARTMENT OF THE AIR FORCE
AFIT/CIA, BLDG 125
2950 P STREET
WPAFB OH 45433

**10. SPONSORING/MONITORING AGENCY REPORT NUMBER**

**11. SUPPLEMENTARY NOTES**

**12a. DISTRIBUTION AVAILABILITY STATEMENT**
Unlimited distribution
In Accordance With AFI 35-205/AFIT Sup 1

**12b. DISTRIBUTION CODE**

**13. ABSTRACT** *(Maximum 200 words)*

DISTRIBUTION STATEMENT A
Approved for Public Release
Distribution Unlimited

20040730 043

**14. SUBJECT TERMS**

**15. NUMBER OF PAGES**
199

**16. PRICE CODE**

| 17. SECURITY CLASSIFICATION OF REPORT | 18. SECURITY CLASSIFICATION OF THIS PAGE | 19. SECURITY CLASSIFICATION OF ABSTRACT | 20. LIMITATION OF ABSTRACT |
|---|---|---|---|
| | | | |

# INTERACTION OF LARGE SCALE ZONAL FLOW ANOMALIES AND TOPOGRAPHY

by

Lee A. Byerle

A dissertation submitted to the faculty of
The University of Utah
in partial fulfillment of the requirements for the degree of

Doctor of Philosophy

Department of Meteorology

The University of Utah

August 2004

## ABSTRACT

Relatively long-term fluctuations are evident in the low level circulations surrounding the Andes and the Rocky Mountains. Some of these fluctuations are commonly explained by local, thermal influences that characterize monsoons as well as by regional responses to remote, tropical forcings. This study first explores the seasonal cycle of low level circulations in the vicinity of the Andes and compares it to other mountainous regions such as the Rockies and the Tibetan plateau. Pronounced mechanical flow modifications appear to be associated with orographic deflection over both the Andes and the Rockies. Reanalysis diagnostics, and medium range and month-long integrations of the Utah Global Model (UGM) are presented. Analyses of orographically forced, stationary Rossby waves suggest that climatological, annual and interannual variations observed around the largest mountain ranges may be explained in terms of mechanical, orographic flow deflection. Over South America, this effect tends to produce an orographically bound cyclone in all seasons, with a poleward low-level jet (LLJ) east of the Andes.

The relative importance of initial state detail over subtropical South America during summer is also examined. Experiments with the rotated, variable resolution UGM assess the impact of initial state changes upon regional predictability. Preliminary results show that forecasts of lower troposphere winds can be strongly influenced by the initial state specification over South America through the first 5 days.

Medium range forecasts over North America during anomalous summer floods (1993) and droughts (1988) are investigated. Results suggest that orographic processes modulate

the summer, Great Plains LLJ and related hydrology of the Mississippi River basin. If anomalously strong and broad, upper level zonal flow exists over the orography, then the associated large inertia will promote predictability in all components, including the LLJ and summer precipitation, for a relatively long period. An additional hypothesis is that predictability enhancement occurs in winter cases of highly anomalous zonal flows over western North America. Results of 15 day simulations using a variety of operational and research global model configurations are presented to diagnose the predictability of precipitation and large scale features. Model forecasts of precipitation accumulation delineate qualitatively between wet and dry events at both 5 and 10 days. Improved performance may be related to the large inertia of the flow in wet events, and to increased predictability of initial, large scale anomalies in both wet and dry events.

ACKNOWLEDGMENTS

I would like to express my heartfelt appreciation to my advisor, Professor Jan Paegle. I would not have completed this project without his patient guidance, encouragement and vision. I am equally grateful to Professor Julia Nogués-Paegle for her inspiration and guidance throughout graduate school. I thank my additional committee members, Professors John Horel, Kingtse Mo and Ed Zipser, for their counsel and insight which have improved this research. Thank you to Professor Celeste Saulo for assistance with the data sensitivity model experiments over South America. I want to thank all of the faculty, staff and students who have influenced me academically and personally, and for their friendship and lasting memories. I am particularly indebted to Bryan White for his treasured computer and network assistance, and to Leslie Allaire and Kathy Roberts for wonderful administrative support. I would like mention Jennifer Roman for her help and our collaboration; Ryan Swanson for assistance with data processing; and Sally Benson and Don Shannon for help with the manuscript format. I thank my parents and family for their love and support throughout my life. Most of all, I thank my wife and son, [redacted] and [redacted] for their patience and inspiration and for the joy we share together.

This research was supported by NSF grants ATM0106776 and ATM0109241, and NOAA/PACS grants NA06GP0451 and NA030AR4310094 to the University of Utah. I would like to thank the Air Force Institute of Technology for sponsorship. The views expressed in this research are those of the author and do not reflect the official policy or position of the United States Air Force, Department of Defense, or the U.S. Government.

TABLE OF CONTENTS

# CHAPTER 1

## INTRODUCTION

The goals of the present research are to study and contrast low-level atmospheric circulations over North and South America, with emphasis upon orographically modulated components such as low-level jets (LLJs). The LLJs are particularly conspicuous east of the Rockies and Andes Mountain ranges. Many prior studies have identified the role played by North American LLJs for regional hydrology on the scale of large river basins.

Although the presence of similar jets was suspected east of the Andes in South America, observational support for this was sparse before an intensive field program (SALLJEX, the "South American Low-Level Jet Experiment") that took place during southern summer 2002-2003. The present thesis research commenced about 18 months before the field program, and the goal was to identify LLJ signatures obtained in gridded observations and in model simulations, and to draw preliminary inferences about the causes of the jets and their potential predictability.

An important step in the study is to contrast the jet structures analyzed around South America with those analyzed over North America, and to provide and test hypotheses that explain similarities and differences found in the North and South American jets. Because the emphasis is on low-level wind systems and atmospheric moisture transports, the research focusses upon the lower troposphere at 700 mb. This is selected as a level that is

sufficiently low to reflect lower troposphere circulations, and also sufficiently elevated to be above the earth's surface in regions flanking higher orography.

Diagnostics of interannual, seasonal and intraseasonal variability at 700 mb appear to be at least partly explained in terms of one of the simplest classical theories for orographically modified flow, and much of the thesis is structured in terms of this perspective, as outlined below. In addition to promoting theoretical understanding of episodic LLJ variability, the research has a practical component relating to medium range predictability enhancement of LLJs and related precipitation distribution associated with orographic modulation of large scale anomalies. The remainder of the introduction provides an overview of the diagnostic and prognostic studies carried out in subsequent sections. More complete literature surveys are included as appropriate within each of the following chapters.

## 1.1 Overview of Diagnostic Phase

A relatively old dynamical theory (e.g., Charney, 1979) states that sufficiently strong westerly winds tend to produce anticyclonic responses over orography, while relatively weaker winds tend to produce cyclones over orography. These conclusions also depend upon the horizontal extent and latitudinal position of the most prominent orography. The simple theory appears to explain climatological, annual and interannual variations observed around the largest mountain ranges, including the Andes and the Rocky Mountains, and the associated LLJs east of the orography, as well as elements of regional atmospheric hydrology. This research investigates the mechanical influences of orography and large scale ambient flows on surrounding low-level circulations. Experiments using a

global model will examine the mechanical effects of orography on medium range to intraseasonal time scales.

A climatology of 850-mb eddy winds over North and South America is shown in Fig. 1.1. The data are averaged over 50 years (1951-2000) using the National Centers for Environmental Prediction/National Center for Atmospheric Research (NCEP/NCAR) Reanalysis monthly archives. Northern winter is defined as the December to February (DJF) average, while northern summer is represented as the mean for June to August (JJA). The wave portion, or eddies of the winds, are defined by subtracting the zonal average. During summer (Fig. 1.1a), a cyclonic circulation appears around the Rocky Mountain region. A bold arrow over Texas indicates the region of the Great Plains LLJ. By contrast, an anticyclonic circulation appears around the Rockies during winter (Fig. 1.1b). The seasonal reversal is often attributed to the seasonal changes of heating and cooling over the Western cordillera (e.g., Gutzler and Preston, 1997). Forecasters over the western U.S. commonly use the terminology "thermal low" to characterize summer conditions, contrasting it to stagnant, stable conditions and a "cold core anticyclone" during winter. Ringler and Cook (1999) conclude that the summer surface low is mainly driven by heating, and they note the pronounced surface heat flux (~100 W/(m*m)) and heating (~3 K/day) from Goddard Earth Observing System 4 dimensional assimilated data. The climatology of the seasonal cycle over North America has also been presented by Stone (2004), with emphasis on monthly transitions and atmospheric kinematics. This study additionally examines predictability and precipitation processes.

One of the first things noticed in the reanalyses (Fig. 1.1) was that a seasonal reversal in the low-level circulation does not occur around the subtropical Andes region. An eddy cyclonic circulation surrounds the Andes region during summer (Fig. 1.1c), and it also

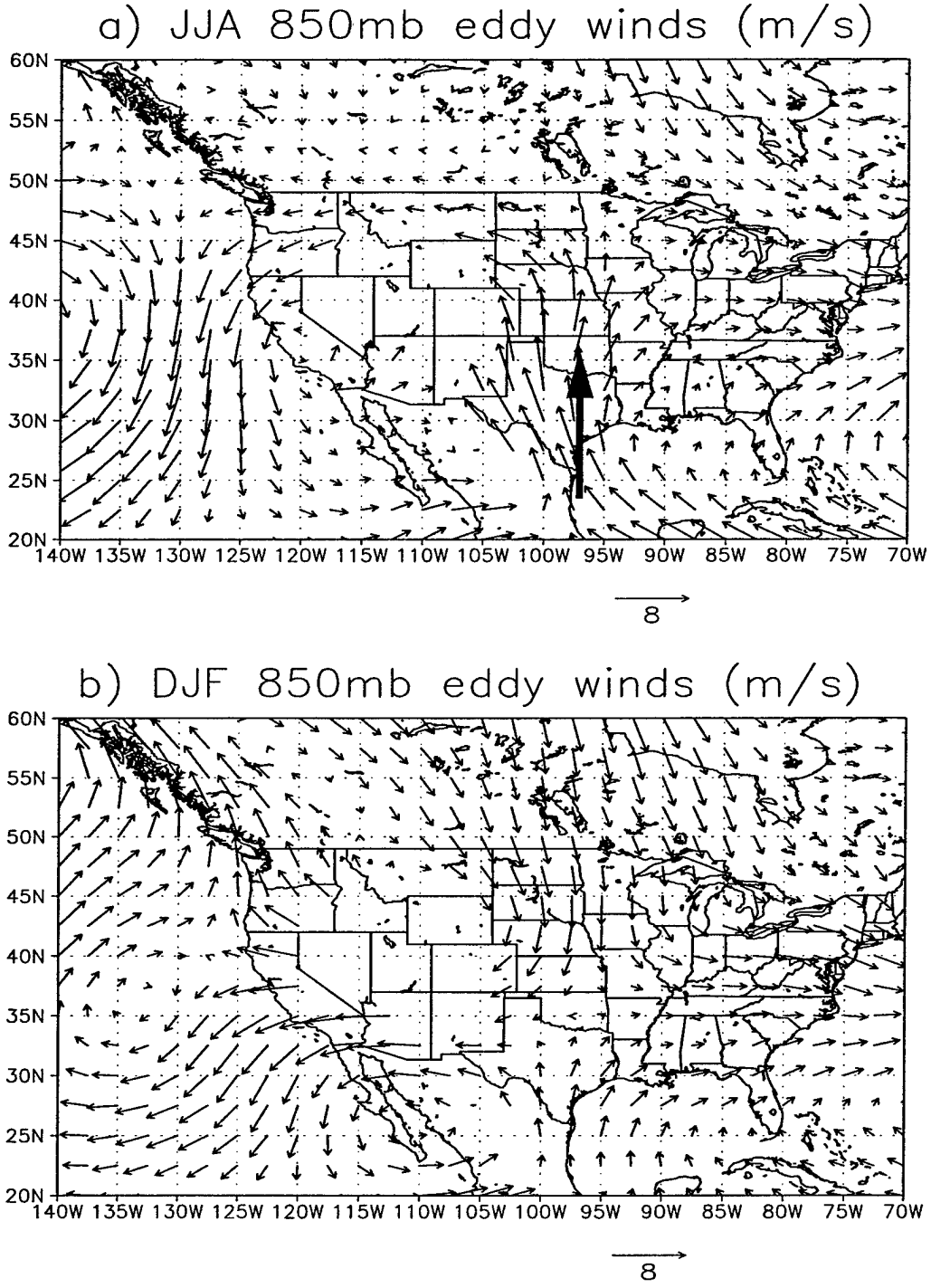


FIG. 1.1. 850-mb eddy winds (m/s) for a 50-year average (1951-2000) from the NCEP/ NCAR Reanalysis during (a) summer (JJA) over North America, (b) winter (DJF) over North America, (c) summer (DJF) over South America, and (d) winter (JJA) over South America. Elevations above 1500 m in the Reanalysis are masked.

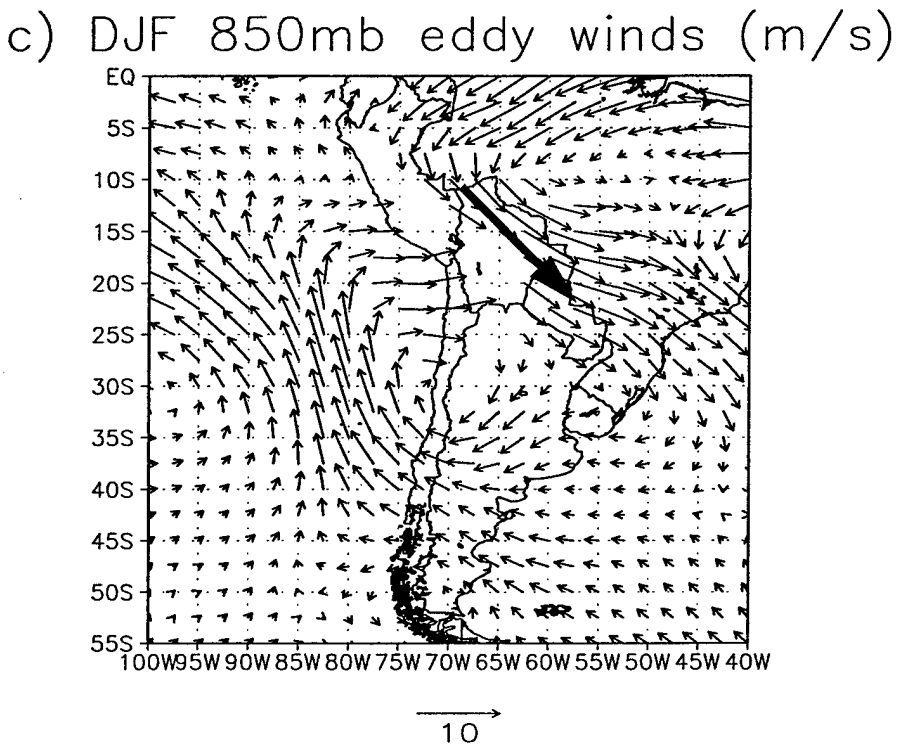


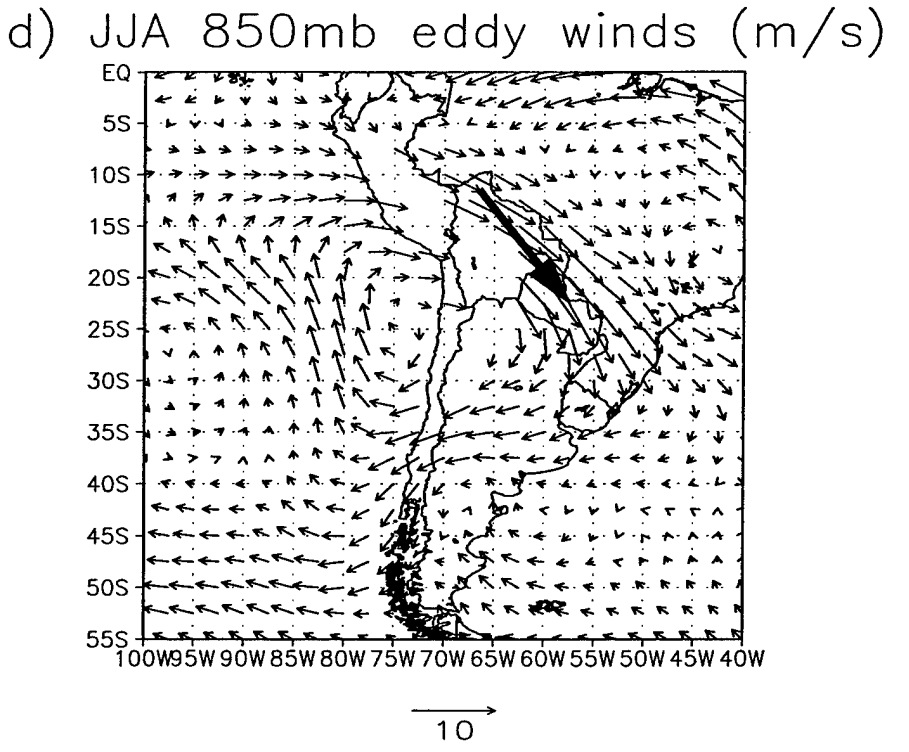


Fig. 1.1, continued.

persists during winter (Fig. 1.1d) when the effects of surface sensible and latent heating over the Bolivian Altiplano become minimized. Bold arrows indicate the region of the east Andes LLJ, present in both summer and winter, in contrast to the Great Plains LLJ, a distinctively summer time feature. Therefore, while a thermally based explanation may be sufficient to explain the climatological signal from season-to-season around one region of high orography (the Rocky Mountains), it does not suffice for another (the Andes Mountains). In a nutshell, much of this research aims to identify dynamical processes which may explain all of the situations depicted in Fig. 1.1, and to explore whether the processes may promote predictability.

Fig. 1.2 shows the correlation over the 1951-2000 period using monthly data from the NCEP/NCAR Reanalysis between the area averaged, 200-mb zonal flow in the outlined box over the Andes Mountains (35°S-20°S) and precipitation at all locations over land during austral summer (DJF). The figure shows that an increase in the area averaged, upper troposphere zonal flow over orography ("forcing") corresponds to heavier precipitation over the La Plata River basin, shown by the correlation coefficients. Dashed arrows indicate that a climatological cyclonic circulation surrounding the orography is enhanced in the presence of stronger zonal flow. The LLJ east of the Andes is a component of this cyclonic circulation. The LLJ transports moisture southward from the Amazon basin and contributes to increased precipitation ("response") over the La Plata region, during episodes of enhanced upper tropospheric westerlies.

A time correlation of 200-mb zonal flow with precipitation over land is depicted in Fig. 1.3 for North America at midlatitudes during summer (JJA). Statistically significant correlation coefficients (shaded) are over portions of the Great basin and the Mississippi River basin (MRB). Negative correlations are over the desert Southwest. Increased upper

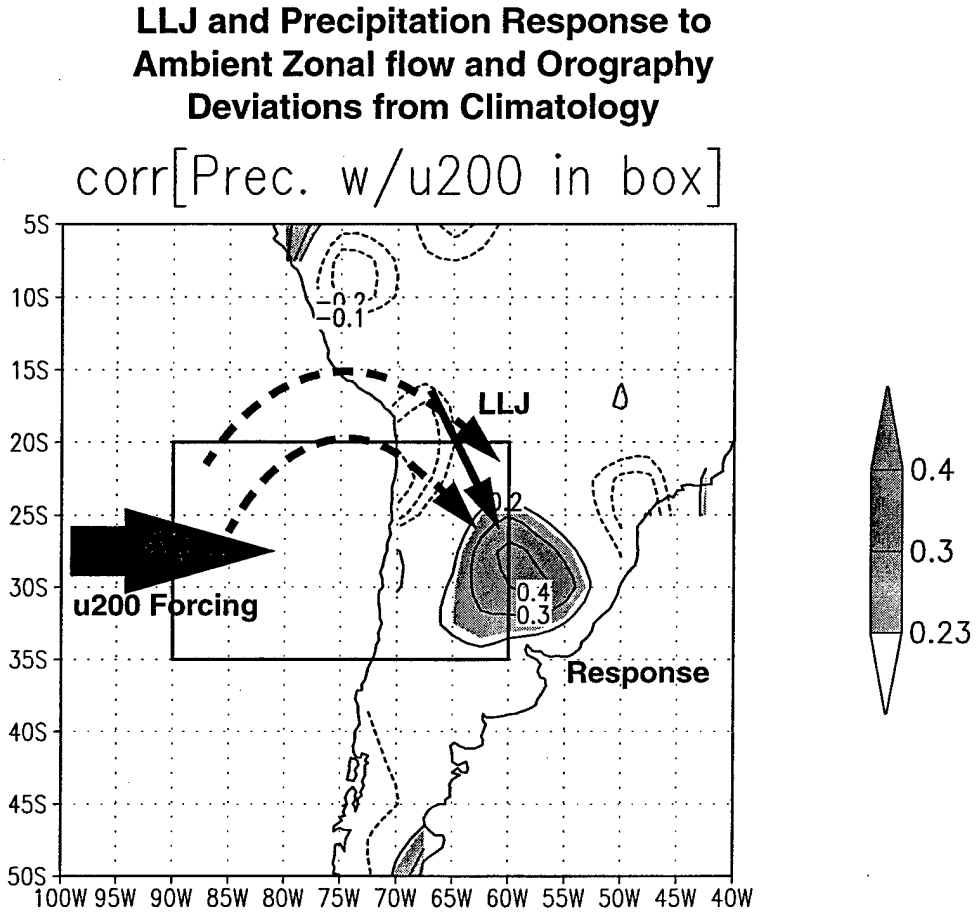


FIG. 1.2. Temporal correlation of the area averaged, 200-mb zonal wind in the box with precipitaton at all locations over land (PREC/L of Chen et al., 2002) during summer (DJF) over South America from 1951-2000. Only coefficients meeting the 95% statistical significance criteria are shaded. The area averaged, 200-mb zonal flow over subtropical Andes orography provides mechanical forcing which enhances the eddy cyclonic circulation (depicted by dashed arrows). The solid arrow over land represents the east Andes low-level jet (LLJ), which contributes to the precipitation response over the La Plata River basin.

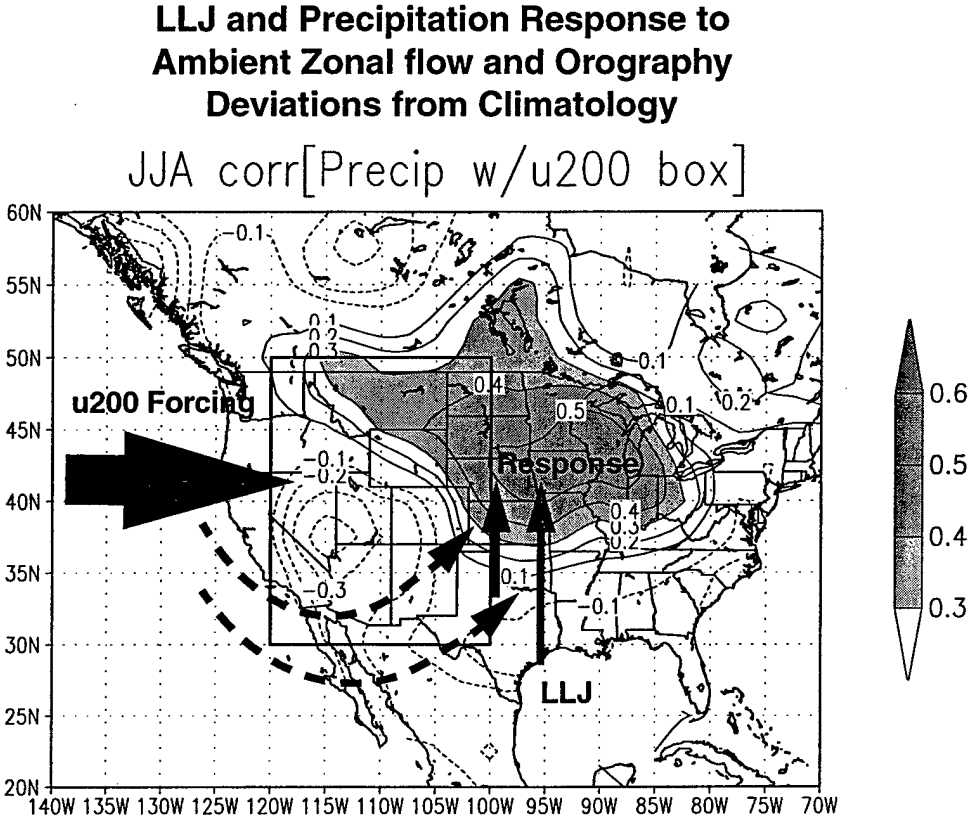


FIG. 1.3. Temporal correlation of the area averaged, 200-mb zonal wind in the box with precipitaton at all locations over land (PREC/L of Chen et al., 2002) during summer (JJA) over North America from 1951-2000. Only coefficients meeting the 99% statistical significance criteria are shaded. The area averaged, 200-mb zonal flow over the Rocky Mountains provides mechanical forcing which enhances the eddy cyclonic circulation (depicted by dashed arrows). The solid arrows over land represent the Great Plains low-level jet (LLJ), which contributes to the precipitation response over the Mississippi River basin.

troposphere, zonal flow over the Rocky Mountains enhances the summer cyclonic circulation located over the western U.S. The Great Plains LLJ is a component of this orographically bound circulation, similar to the east Andes LLJ during summer. Correlation of meridional wind in the region of the Great Plains LLJ with precipitation is displayed in Fig. 1.4. Comparison of Fig. 1.4 with Fig. 1.3 suggests that increased moisture flux into the MRB, and therefore heavier precipitation, may occur when upper tropospheric westerlies increase across the Rocky Mountains.

Interaction of orography with the large scale flow is evident over the Andes and the Rockies during summer. The seasonal and longer term changes of the ambient flow occurring on large scales may be related to fluctuations in both the Great Plains and east Andes LLJs, whose response occurs in summer on the smaller scales of cloud generation and precipitation. A hypothesis of this research is that if anomalously strong and broad, upper-level zonal flow exists over the orography, then the associated large inertia will promote predictability in all components, including the Great Plains LLJ for a relatively long period.

## 1.2 Overview of Predictability Phase

The importance of second week predictability of extreme events for both societal and economic benefit has been recognized by scientists involved in THORPEX, an international research program (Shapiro et al., 2003 and references therein). Goals of THORPEX include improving "high-impact" weather forecasts in the 1-14 day range. Shapiro et al. (2003) and others (e.g., Simmons and Hollingsworth, 2002) have noted that the limit of predictability is generally 7 days for synoptic scale weather systems and the associated high-impact weather occurring on smaller scales. These limits were attributed to initial state and data assimilation uncertainties, model uncertainties, and so-called "intrinsic

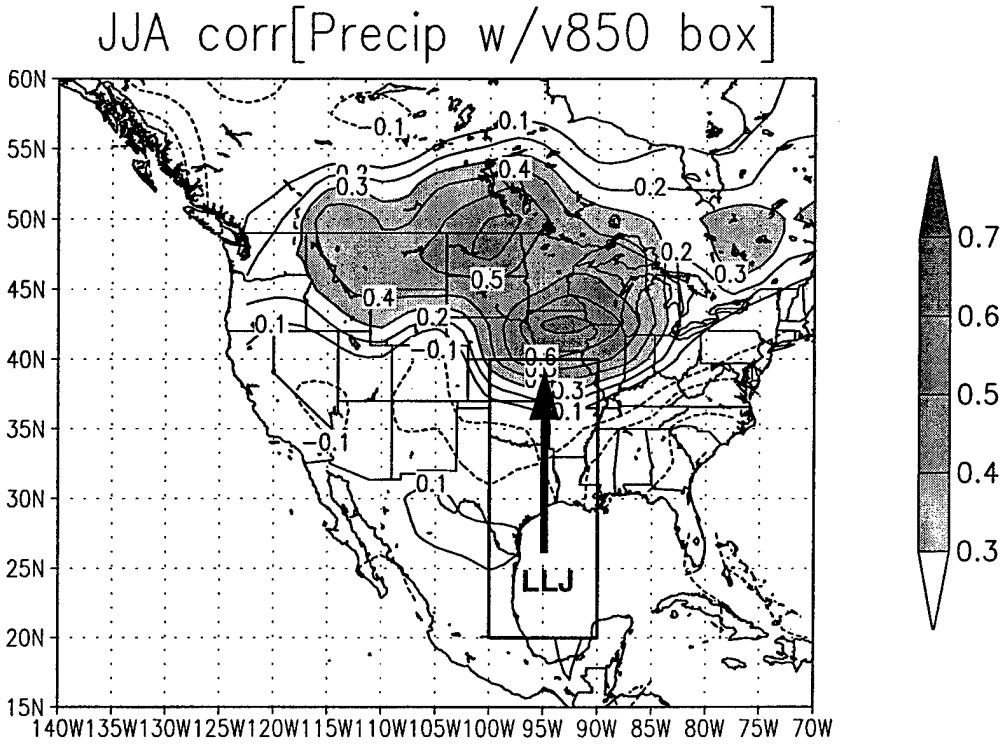


FIG. 1.4. The temporal correlation coefficients of the area averaged, 850-mb, meridional wind in the outlined box (20°N-40°N, 100°W-90°W) with gauge precipitation over land (PREC/L of Chen et al., 2002) for summer (JJA), 1951 to 2000. The box is over a region in which the Great Plains LLJ is active during northern summer. The contour interval is 0.1 and the zero line is omitted. Coefficients meeting the 99% statistical significance criteria (0.3) are shaded.

uncertainties" that are unresolved in models

This study investigates predictability of anomalous summer floods and droughts over the midwestern U.S., which were characterized by anomalous zonal flows upstream over the Rocky Mountains. Some basin scale representation of observed precipitation features is evident into the second week of prediction, implying longer predictability of extreme summer events than in some prior studies (e.g., Simmons and Hollingsworth, 2002).

Medium range predictability in winter cases of anomalous, upper troposphere zonal flows over the western U.S. is also examined. Fig. 1.5 shows deviations from the winter climatology over North America. Monthly averaged precipitation at all locations is correlated with area averaged, 200-mb zonal flow over a region encompassing the Rockies. The highest correlation coefficient during winter is over the West (0.6). When the zonal wind is stronger than climatology, an increased precipitation response would effect winter hydrology and snow pack generation over the high terrain of western North America.

Forecast sensitivity to initial state data changes over South America is also explored. The observing system over Central and South America has recently been improved by addition of several pibal soundings by the Pan American Climate Studies Sounding Network (PACS-SONET; http://www.nssl.noaa.gov/projects/pacs). In addition, an international experiment was recently mounted to observe low-level circulations situated east of the Andes. The South American Low-Level Jet Experiment (SALLJEX) extended from 15 November 2002 to 15 February 2003 (http://www.clivar.org/organization/vamos/index.htm). This cooperative effort involved atmospheric scientists in six South American countries and others from North America, and focused on a region of South America extending from central Argentina through Bolivia, Paraguay and southern Brazil, where the density and frequency of atmospheric observations were enhanced with extra pibal and

**Winter Precipitation Response to Ambient Zonal flow and Orography Deviations from Climatology**

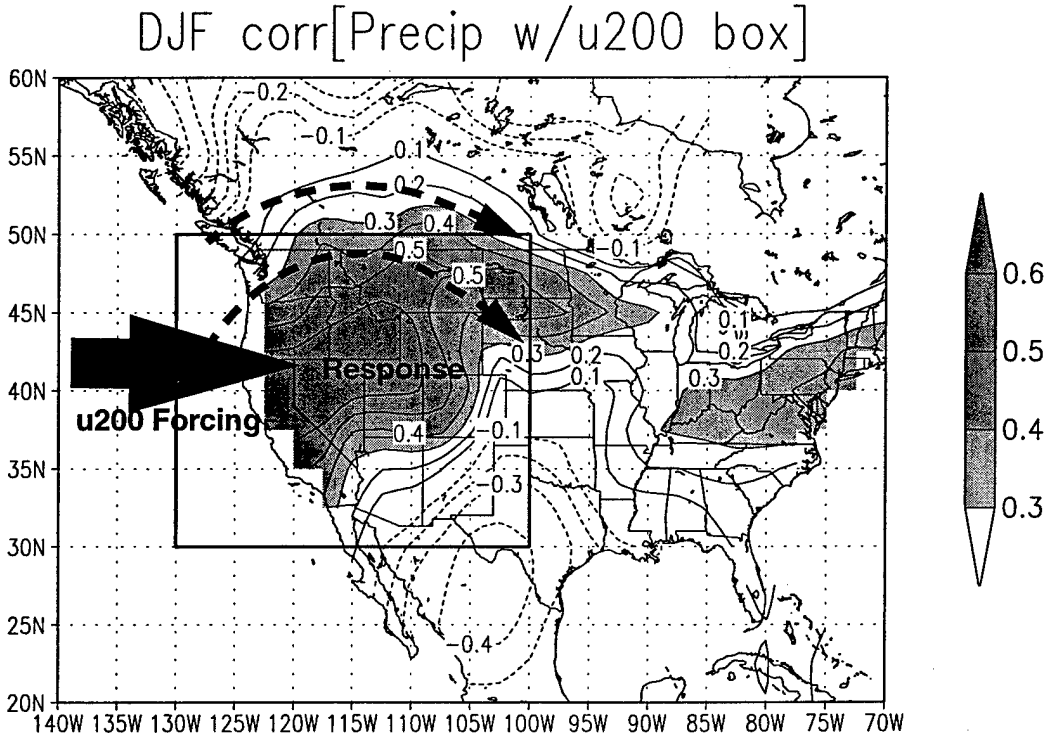


FIG. 1.5. Temporal correlation of the area averaged, 200-mb, zonal wind in the box with precipitaton at all locations over land (PREC/L of Chen et al., 2002) during winter (DJF), over North America, from 1951-2000. Only coefficients meeting the 99% statistical significance criteria are shaded. Enhancement of the area averaged, 200-mb, zonal flow over the Rocky Mountains provides mechanical forcing which weakens the eddy anticyclonic circulation (depicted by dashed arrows).

radiosonde observations.

The observations produced by this experiment are currently undergoing quality control, and their adequate inclusion within initial states of forecast models will require an extensive assimilation effort. The goal here is to present preliminary results with the Utah Global Model (UGM; Paegle, 1989) that are designed to anticipate the sensitivity of weather prediction in the South American region to atmospheric detail that is included or excluded in the specification of the initial state over and around South America. Rotated, variable resolution UGM configurations that allow interaction between the atmosphere of the inner higher resolution region (centered over tropical South America) with the outer, global domain (e.g., Wang et al., 1999) are used.

A brief outline of the Chapter topics follows. Chapter 2 discusses the seasonal cycle of low-level flows flanking the Andes and their interannual variability. Interaction of the large scale zonal wind field with the mechanical effects of Andes orography is presented. The connection of these elements was first proposed by Charney and Eliassen (1949) for the Northern Hemisphere, but they appear to explain a variety of observed features in the long term, averaged flows over both South and North America, including, for the former, the relation of El Niño Southern Oscillation (ENSO) to the LLJ and to wet episodes over the La Plata basin during periods of increased, upper troposphere, westerly flow over the region.

Sensitivity to initial state data changes over South America during summer is presented in Chapter 3. The rotated, variable resolution version of the UGM is applied. The approach is to initialize the UGM first with coarse resolution (2.5°) NCEP/NCAR Reanalyses globally in a control integration. Simulations are then performed in which the reanalyses are replaced with higher resolution (1°) Global Data Assimilation System (GDAS)

analyses from NCEP. GDAS analyses are intended to represent surrogates for analyses which include higher resolution observations. The switch from Reanalysis to GDAS initial states is performed in selected regions to study the potential predictability impact of initial state changes in different portions of the globe, including some that correspond to the South American sector within which analyses may be influenced by the SALLJEX and PACS-SONET observations. Tests of numerical sensitivity to the rotated approach are also presented.

Chapter 4 explores the modulation of the Great Plains LLJ and moisture transports by orography and large scale circulations. Mechanical flow deflection by the Rocky Mountains is diagnosed in 50 years of monthly averaged NCEP/NCAR Reanalysis fields and in a series of integrations using a primitive equation version of the UGM. Ensembles of medium range forecasts are made for the 1993 U.S. floods and for the 1988 U.S. drought. The forecasts distinguish some of the observed precipitation differences between these years, but the magnitude of the differences is underestimated. It is likely that the predictability of anomalies is enhanced by orography, and that this could also occur in winter.

Chapter 5 presents diagnostics and 15-day simulations over North America during winter. Forecasts are selected based upon anomalously weak and strong zonal flows during January. Results from 15-day simulations using a variety of global model simulations are presented to diagnose the predictability of precipitation and large scale features. Model forecasts delineate qualitatively between wet and dry events at both 5 and 10 days. Anomaly correlations of the geopotential height field reveal useful predictability for some ensembles extending to 9.5 days. Uniform resolution forecasts are compared to model configurations which employ rotated variable resolution. Diagnostics and model simulations of a small number of extreme events suggest that mechanical flow modifications

associated with ambient flows exist over the orography during the winter season, and that a predictable regional response may be present to about 10 days. Chapter 6 provides a discussion and conclusions.

# CHAPTER 2

# MODULATION AROUND THE ANDES

## 2.1 Introduction

Many previous studies of low-level jets (LLJs) have emphasized the important role of heating. Paegle (1998) provides a comparative overview of South American LLJs contrasted with similar circulations observed in other regions and concludes, in agreement with other studies, that sensible and latent heating are important for the observed evolution of the diurnal cycle. Latent and sensible heating are also important on longer time scales for the ambient South American circulations within which the LLJ is embedded. Zhou and Lau (1998) clearly demonstrate the monsoon character of several components of the South American summer time circulation, and refer to the composite picture as the "South American Monsoon System." They conclude that intense, turbulent, sensible heat flux induced by increasing surface temperature in summer drives the Chaco low over the Bolivian altiplano. Latent heat release from deep cumulus convection then becomes dominant during summer.

The purpose of Chapter 2 is to diagnose the longer term characteristics of the low-level circulation surrounding the Andes. The east Andes LLJ is viewed as a component of this circulation, and emphasis is on fluctuations of seasonal and monthly averages as revealed by the National Center for Environmental Prediction/National Center for Atmospheric Research (NCEP/NCAR) Reanalyses (Kalnay et al., 1996; Kistler et al., 2001). These figures suggest strong orographic modulation of lower troposphere winds by the Andes.

Orographically bound circulations have received much attention in theoretical and observational studies. Charney and Eliassen (1949) presented a pioneering theoretical investigation of the role of orography in barotropic models. That study concludes, "The establishment of the continents as the primary perturbing influence enables us...to determine the position of individual troughs. These...are determined by a world wide adjustment to the shape of the continents." It finally states, "If it should prove possible to forecast the variation of the zonal index, it would also be possible to at least make an elementary forecast of the change in world weather." These inferences are entirely based on an equivalent barotropic model in which mechanical effects of orography operate and thermal effects are excluded. In this context, it may be possible to connect the east Andes LLJ to the orographically bound cyclone that typifies central South America and the modulation of both features by ambient zonal winds and their anomalies.

A series of prior investigations have explored the role of mechanical flow blocking by the Andes. The global linear analysis by Nigam et al. (1988) suggests the mechanical effect has a first order influence over much of the world, but it is less important than heating and transient effects, particularly at 300 mb around the Andes. Their results emphasize the 300-mb response, and they are limited to linear treatments. Kleeman (1989) uses a linear, two-level model to emphasize the influence of the Andes on summer time, low-level circulations. Representing orography with a meridional wall in the lower boundary layer, he explains east Andes LLJs as back reflection of short Rossby wave modes associated with topography. Gandu and Geisler (1991) provide further analyses of the role of the Andes in idealized, limited area simulations. Their integrations invoke latent heating and depict a summer, steady-state, lower troposphere cyclonic circulation near the Andes, including a northwesterly LLJ east of the Andes.

Fig. 13 of Nogués-Paegle et al. (1998) illustrates the solutions of nonlinear global models executed with realistic orography and forced by observed, ambient zonal flows in winter and summer. Those integrations show circulation patterns in the lower troposphere around the Rockies and Andes whose orientation does not depend on heating. They suggest sensible heating accentuates mechanically forced circulations over both North and South America in winter and summer.

The present study attempts to add to this information base with an emphasis upon the enhancement of predictability possibly residing in the interaction of the large scale zonal wind field with the mechanical effects of orography. The connection, first proposed by Charney and Eliassen (1949), appears to explain a variety of observed features in the long term averaged flows over and east of the Andes, including the relation of El Niño Southern Oscillation (ENSO) to the LLJ and to wet episodes over the La Plata basin during periods of increased, upper tropospheric, westerly flow over the region.

Links of ENSO with streamflow and precipitation anomalies over subtropical South America have been well documented (e.g., Ropelewski and Halpert, 1987; Mechoso and Iribarren, 1992; Genta et al., 1998; and Grimm et al., 1998). Mechoso and Iribarren (1992) and Genta et al. (1998), for example, show enhanced streamflows associated with higher precipitation rates occur in major rivers of the La Plata basin during the spring and summer of warm ENSO years. The former study also documents below average streamflows from early winter to midsummer of La Niña years. Grimm et al. (1998) find precipitation over southeastern South America is most pronounced during austral spring of warm events, around the same time mesoscale convective complexes are most active in the region. They associate the intensification with stronger subtropical westerlies over the region, and an enhanced baroclinic environment (see their Fig. 12).

Section 2.2 presents climatological averages that suggest roles for both mechanical and heating effects for the east Andes circulation. The heating is most important in summer, but the similarity of the lower tropospheric winter and summer flows suggests a prominent role for mechanical effects in both seasons. Section 2.3 presents comparisons of South American circulations with those found over North America and Asia, showing much of the North American response is in midlatitudes, while Asian and South American responses are centered in the subtropics. Section 2.4 describes the correlation of the South American orographic cyclone, east Andes LLJs and South American rainfall with ambient, large-scale zonal flow anomalies. Sections 2.5 and 2.6 present a dynamical interpretation emphasizing simple barotropic idealizations and primitive equation model simulations with the Utah Global Model (UGM). Similar diagnostics and UGM simulations will be introduced in Chapter 4, applied over North America.

## 2.2 Climatology of the Seasonal Cycle

The data presented in this section (unless noted otherwise) are based on a 50-year record (1951-2000) of monthly averaged circulations from the NCEP/NCAR Reanalysis. Summer and winter averages are first presented, focussing on the eddy fields to facilitate a subsequent theoretical interpretation in section 2.5. The annual march of vorticity over the subtropical Andes is also discussed. Eddy fields are obtained by subtracting the zonal average from the full fields.

Diagnostics in regions of orography such as the Andes must take into account the limitations of the reanalysis system. The NCEP/NCAR Reanalysis on a 2.5° X 2.5° grid represents the Andes with 3750 to 3800 m peaks, well below the actual 6000 m to 6900 m peaks. The width and longitudinal extent of the Andes are represented somewhat realistically in the Reanalysis. For example, the 1000 m contour at 20°S spans about 7° in longi-

tude (from about 70°W-64°W), similar to the actual east-west width.

Climatological features over subtropical South America are now presented, with emphasis on the 700-mb and 200-mb levels. The upper and lower troposphere circulation is presented in Fig. 2.1. Fig. 2.1a and 2.1b display December to February (DJF) and June to August (JJA), 700-mb eddy geopotential heights and winds for the 50-year average (1951-2000). Fig. 2.1c and 2.1d illustrate 200-mb, eddy geopotential heights for summer and winter, respectively. The full fields, including the zonal average, are depicted in Fig. 2.1e to 2.1h. The summer pattern contains an anticyclone at 200 mb over subtropical South America from approximately 15°S to 35°S. This distinct feature, sometimes referred to as the "Bolivian High," is centered slightly south and east of Bolivia in the eddy pattern (compare Fig. 2.1c and 2.1g).

In contrast to the summer pattern, the upper troposphere winter wave pattern of Fig. 2.1d contains a cyclonic circulation over subtropical South America from approximately 15°S-30°S. This circulation is not present in the full winter field (Fig. 2.1h). The average, 700-mb field in summer (Fig. 2.1e) has cyclonic curvature near 30°S, 75°W, in a region where the background flow is predominantly anticyclonic, and well north of the middle and upper troposphere westerly jet maxima. This region of cyclonic curvature extends farther north in winter (Fig. 2.1f). A northeast-to-southwest oriented pressure gradient force is pronounced over land (15°S-25°S) in winter, accentuating northwesterly flow to the east of the Andes (compare to summer, Fig. 2.1e).

While the winter-summer transitions are pronounced at 200 mb in the eddy field, the eddy circulation at 700 mb does not change significantly from summer to winter (compare Fig. 2.1a and 2.1b). This is evident in the 700-mb eddy vorticity fields shown in Fig. 2.2. Negative (cyclonic) vorticity flanks the Andes in both seasons and the centers of vorticity

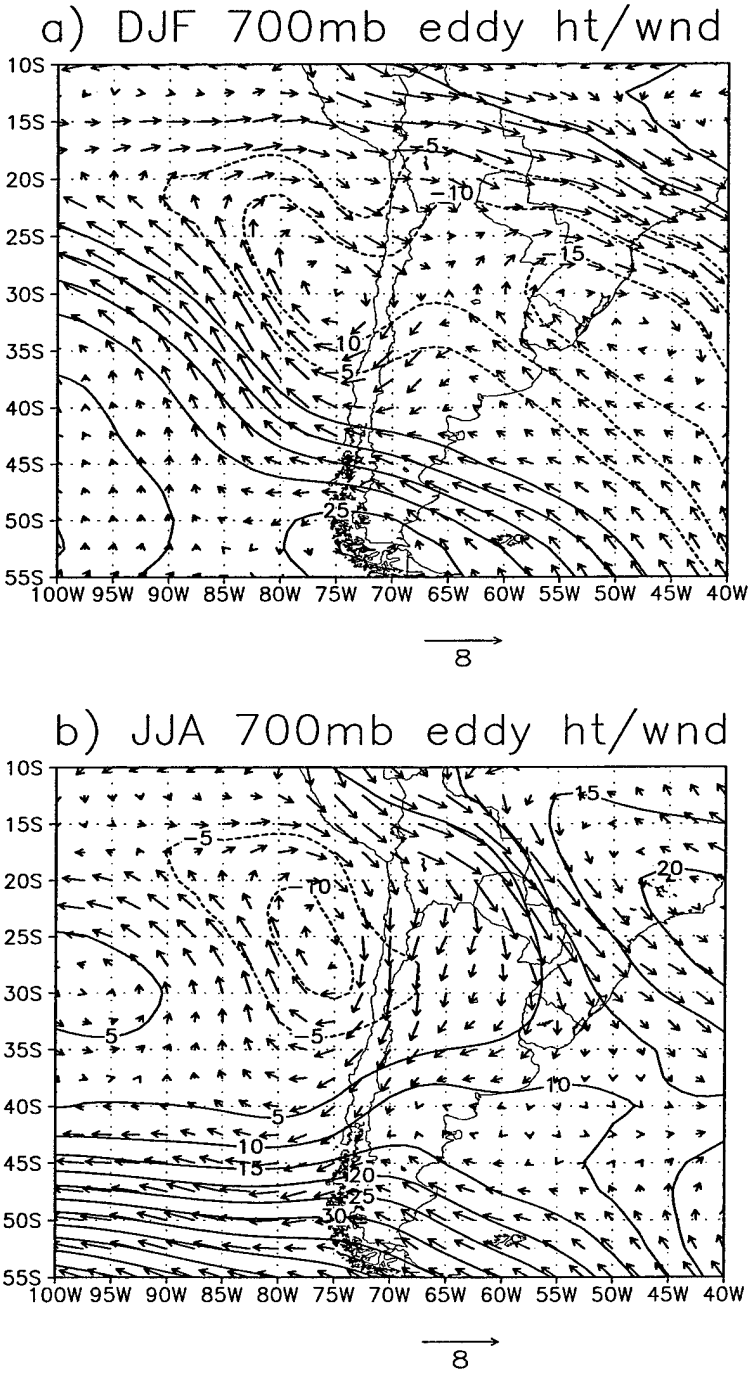


FIG. 2.1. Heights (m) and wind vectors (m/s) over South America. (a) shows the summer (DJF), 700-mb eddy field; (b) winter (JJA), 700-mb eddy field; (c) summer, 200-mb eddy field; (d) winter, 200-mb eddy field; (e) summer, 700-mb full field; (f) winter, 700-mb full field; (g) summer, 200-mb full field; and (h) winter, 200-mb full field. Thick arrows in (e) and (f) depict the area of northwesterlies associated with a typical low-level jet (LLJ) region north of about 25°S. Dashed lines in (a)-(d) depict negative eddy heights.

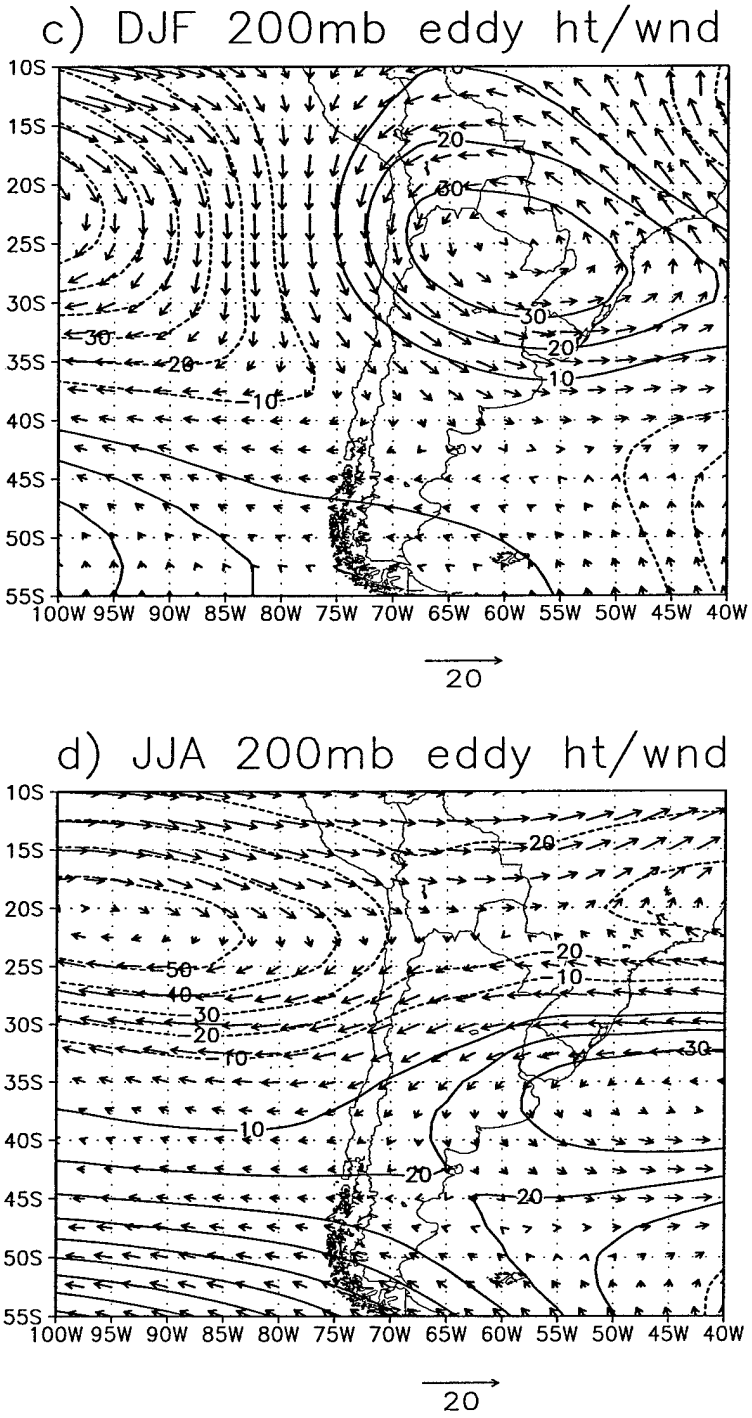


Fig. 2.1, continued.

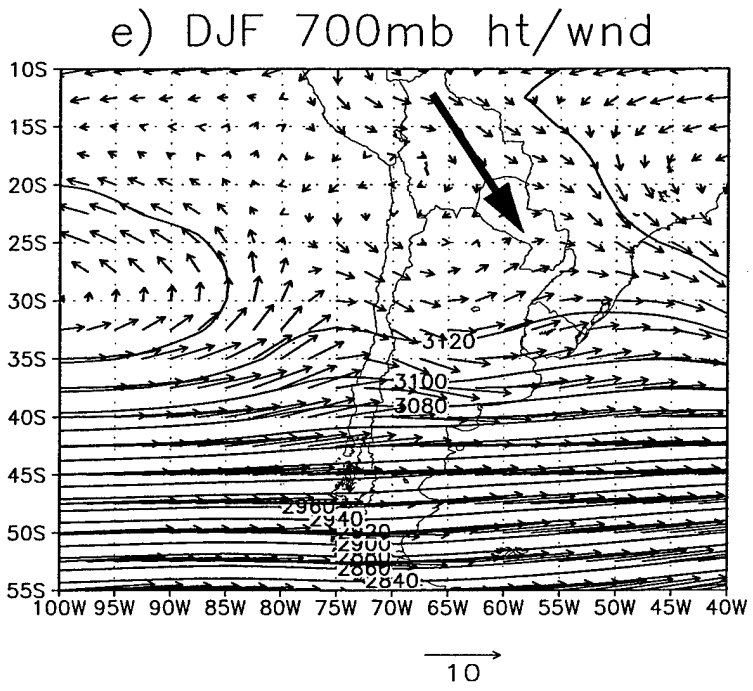


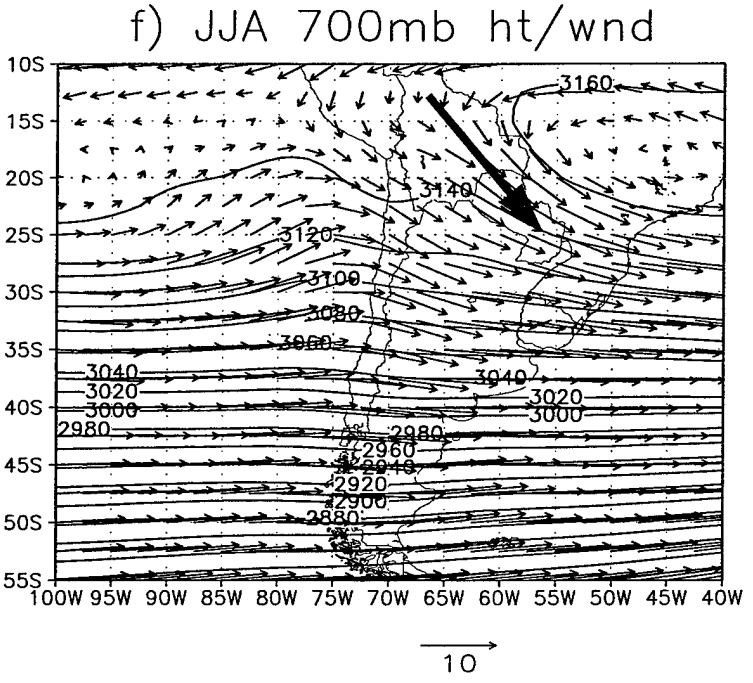


Fig. 2.1, continued.

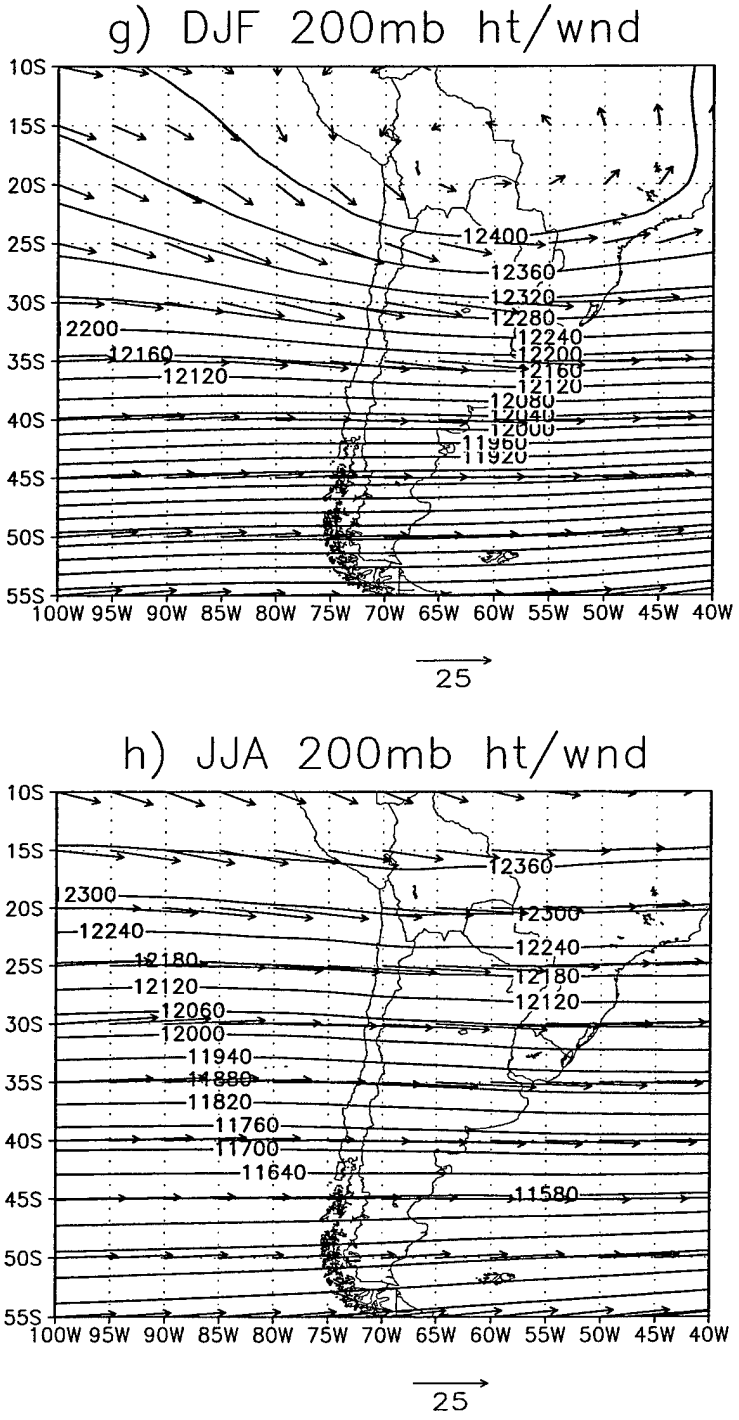


Fig. 2.1, continued.

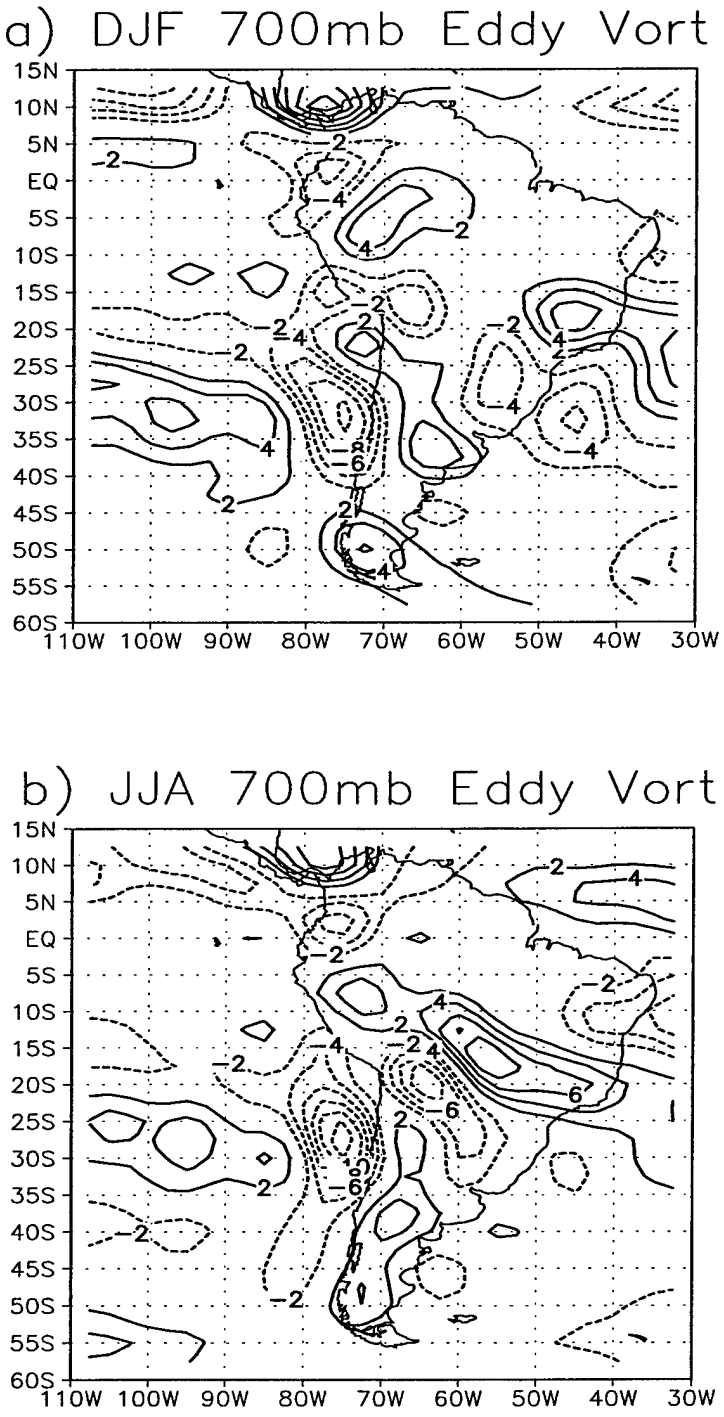


FIG. 2.2. 700-mb eddy vorticity over South America. (a) shows summer (DJF), and (b) winter (JJA) eddy vorticity. Dashed contours indicate cyclonic, and solid contours indicate anticyclonic vorticity. The contour interval is 2 and the units are (1E-06/s).

are slightly stronger in winter (compare Fig. 2.2a and Fig. 2.2b).

Fig. 2.3 illustrates the 850-mb temperature patterns accompanying the summer to winter transitions. A thermal ridge is evident in the vicinity of the Andes in summer (Fig. 2.3a), but it is substantially weaker in winter (Fig. 2.3b). Zhou and Lau (1998) suggest the summer surface cyclone results mainly from increased solar insolation of the Bolivian plateau. Although the summer lower troposphere cyclone may have some relation to the strongly heated Andes slopes in that season, alternative mechanisms are sought for cyclonic vorticity maxima in winter, which do not have a pronounced warm core. This question is addressed in more detail in section 2.5.

Fig. 2.4 shows the seasonal cycle of vorticity at 700 mb, area averaged from 40°S-20°S, and 80°W-60°W, in the vicinity of the Andes and the eddy cyclonic circulation described in Fig. 2.1. Fig. 2.4a shows the complete relative vorticity, while Fig. 2.4b depicts the monthly evolution of the longitudinally varying wave (eddy) portion of the vorticity pattern, in which zonal mean values have been subtracted. Positive (anticyclonic) relative vorticity is evident in the full field in all months except September (Fig. 2.4a), when it becomes zero. The eddy field, however, indicates negative (cyclonic) vorticity in all months, with a maximum in cyclonic vorticity in September.

Some aspects of the winter-to-summer circulation changes over South America are consistent with monsoon dynamics. These include vertically reversing cyclonic/anticyclonic circulations in the vicinity of the highest Andes during summer. These features are next compared to changes found over other mountainous regions that are sometimes connected to monsoon effects.

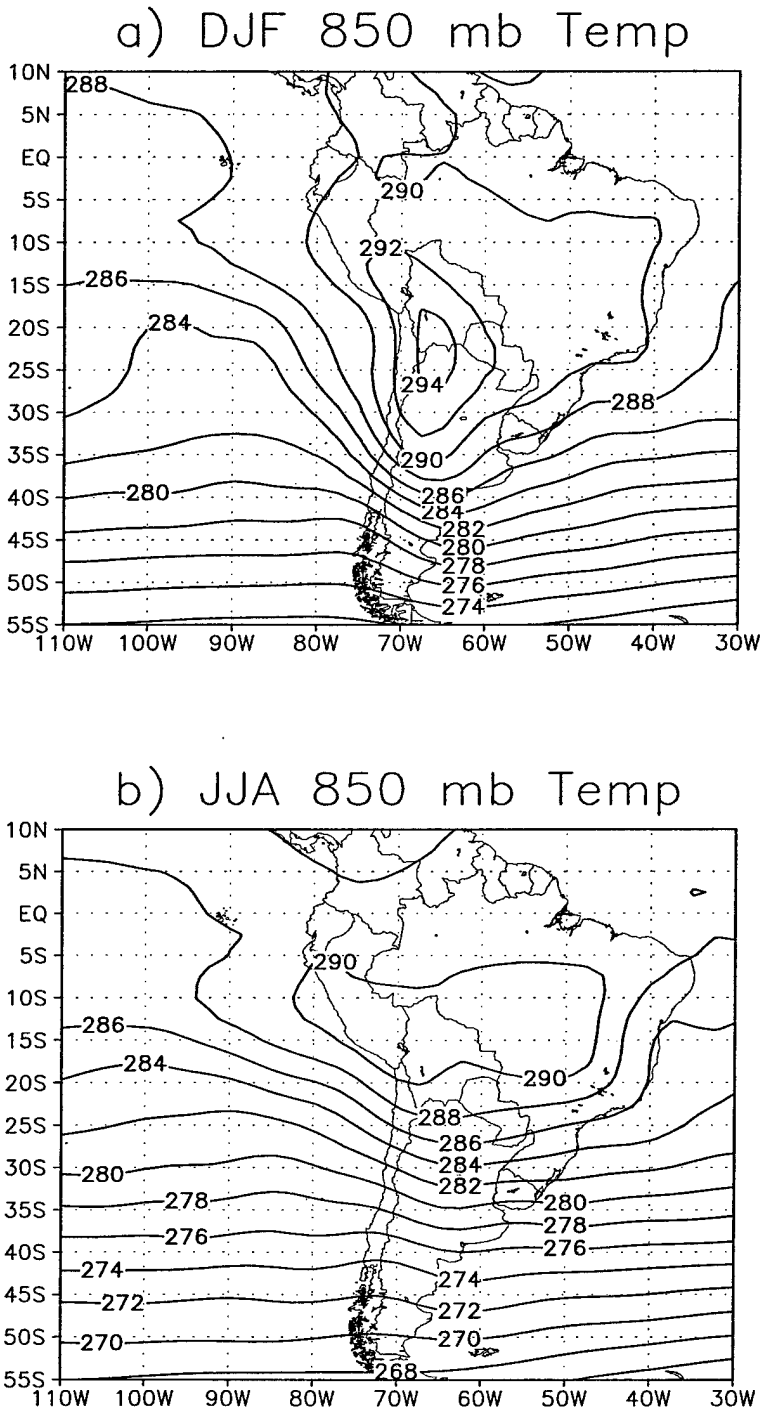


FIG. 2.3. Average 850-mb temperatures during (a) summer (DJF) and (b) winter (JJA), contoured every 2K (1951-2000).

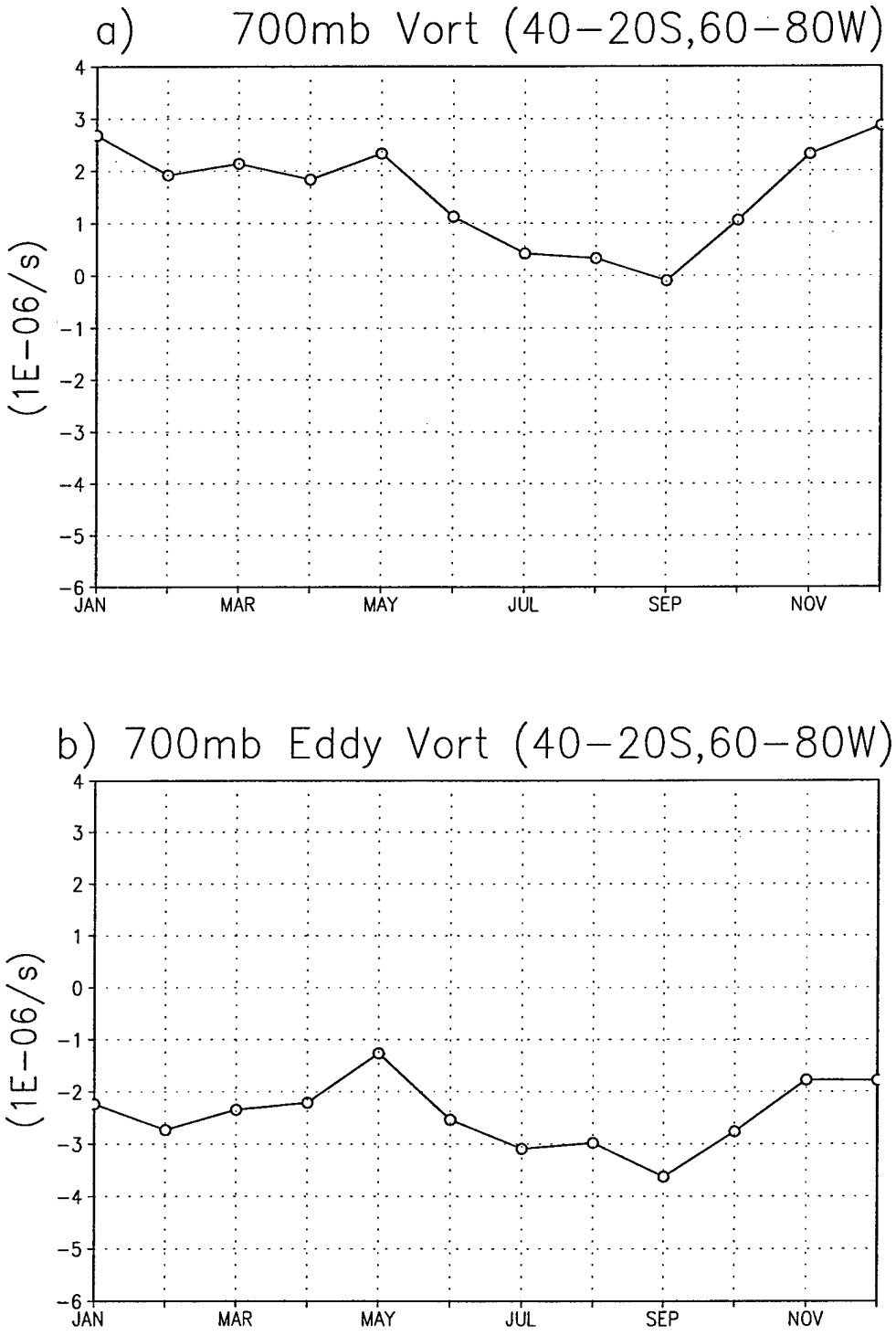


FIG. 2.4. Area averaged vorticity (units 1E-06/s) over the Andes region from 40°S-20°S, 80°W-60°W. (a) shows the relative vorticity, and (b) shows the eddy component of vorticity. Positive (Negative) values indicate anticyclonic (cyclonic) vorticity.

## 2.3 Comparison to Other Regions

Fig. 2.5 displays summer and winter eddy heights and circulations over Asia at 700 mb (Fig. 2.5a,b) and 200 mb (Fig. 2.5c,d). At 700 mb, the summer (Fig. 2.5a) and, to some extent, the winter pattern (Fig. 2.5b) both exhibit cyclonic circulations from 15°N to 35°N, centered on the highest orography (located near 90°E). The cyclonic tendency in winter (Fig. 2.5b) over the Tibetan plateau is more apparent from the monthly evolution of area averaged 700-mb vorticity over the region (20°N-40°N, 70°E-105°E), shown in Fig. 2.6. The dimensions of the box in Fig. 2.6 were selected to minimize the intersection of the 700-mb atmospheric level with orography at the perimeter. The march of relative vorticity (Fig. 2.6a) shows positive values for most of the year, becoming zero in October and weakly negative in November. The eddy field (Fig. 2.6b) shows positive (cyclonic) vorticity throughout the year, with maxima from May to July.

By contrast to 700 mb in summer (Fig. 2.5a), the upper troposphere eddy circulation of Fig. 2.5c contains an eddy anticyclone in summer. The upper tropospheric, eddy circulation over South Asia in winter (Fig. 2.5d) is characterized by anticyclonic rotation and cyclonic shear in the vicinity of the highest orography (30°N-35°N).

Fig. 2.7 shows summer to winter transitions in the eddy heights and winds over North America. Midlatitudes show a pronounced, lower troposphere winter, anticyclone (Fig. 2.7b) that is replaced by cyclonic flow along the west coast in summer (Fig. 2.7a). The upper troposphere, west coast cyclone of summer (Fig. 2.7c) is replaced by an anticyclone in winter (Fig. 2.7d). Fig. 2.8 depicts the seasonal cycle of relative and eddy vorticity over the Rocky Mountains, in the vicinity of the circulation reversals shown in Fig. 2.7 (30°N-50°N, 130°W-110°W). The relative vorticity distinctly shows a winter anticyclone and a cyclone beginning in early spring (Fig. 2.8a). The strongest cyclonic (positive) vorticity

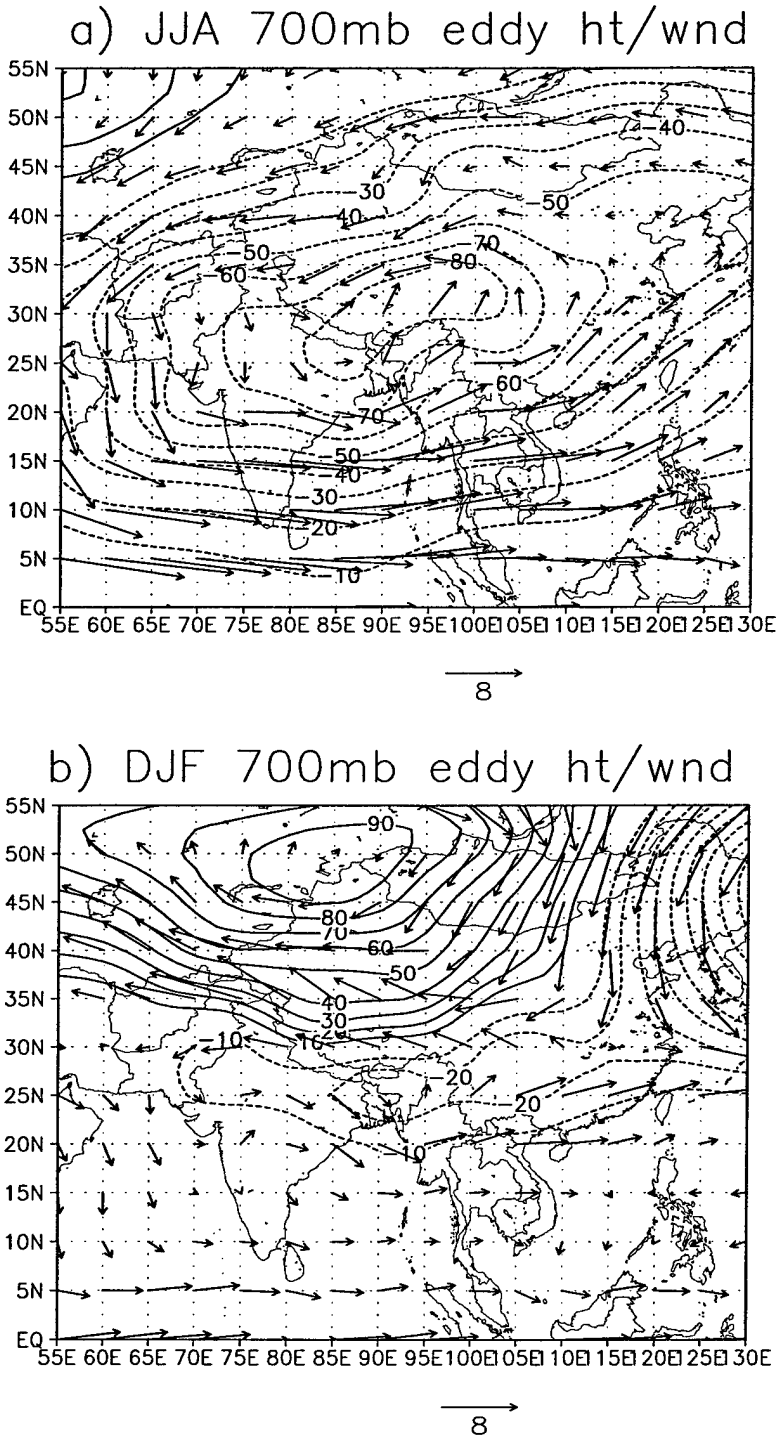


FIG. 2.5. Eddy heights (m) and wind vectors (m/s) over South Asia for (a) summer (JJA), 700 mb; (b) winter (DJF), 700 mb; (c) summer, 200 mb and (d) winter, 200 mb. Wind vectors are plotted at every other grid point for clarity. Dashed lines depict negative eddy heights.

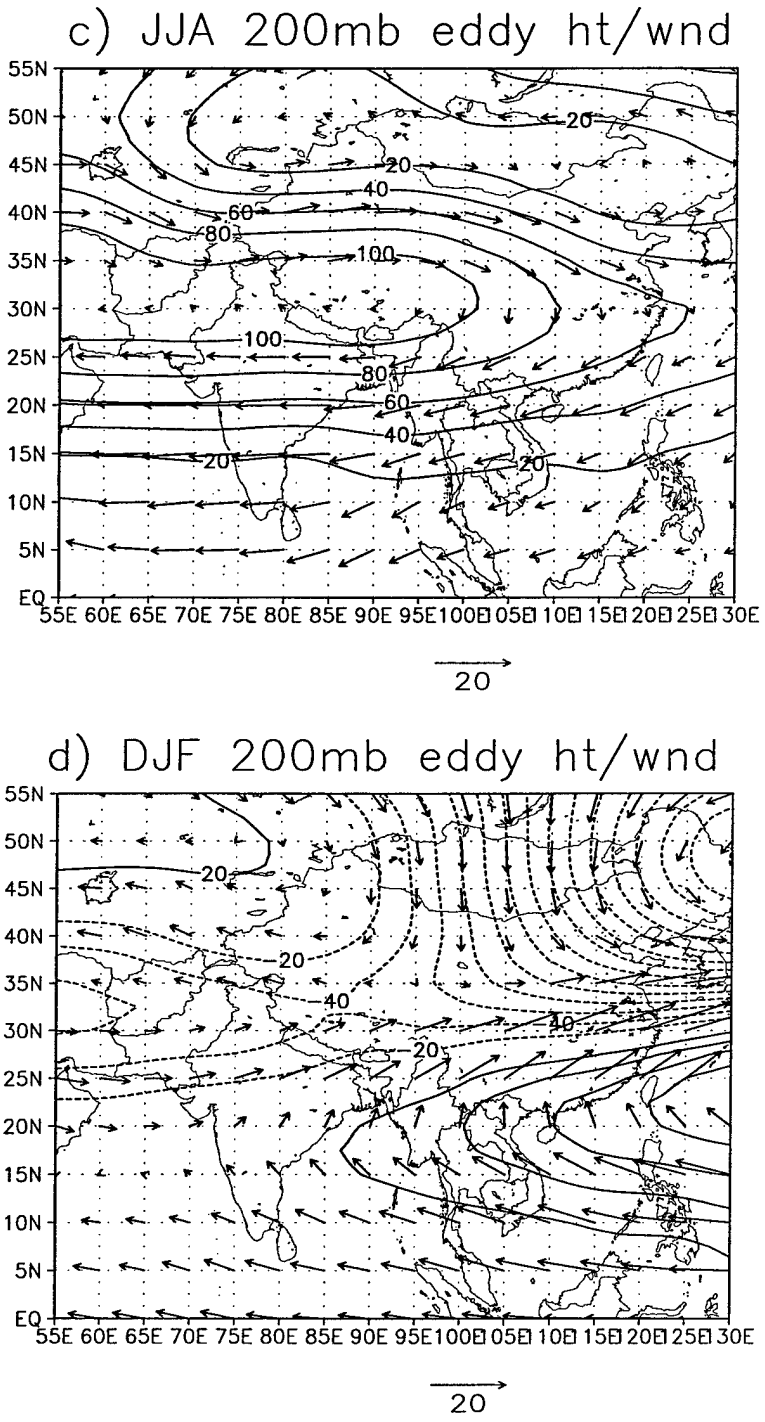


Fig. 2.5, continued.

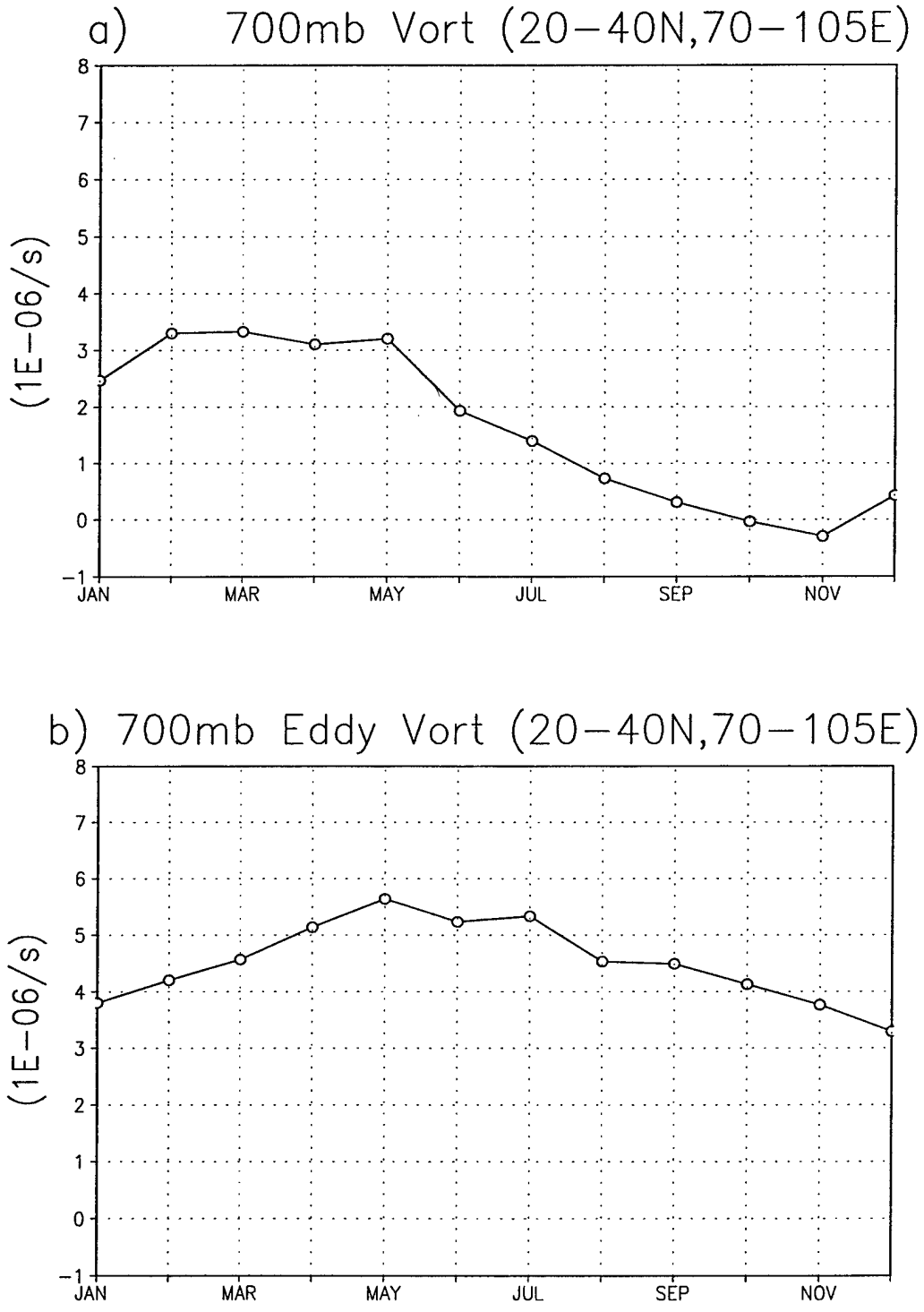


FIG. 2.6. Area averaged vorticity (units 1E-06/s) over the South Asian region from 20°N-40°N, 70°E-105°E. (a) shows the relative vorticity, and (b) shows the eddy component of vorticity. Positive (Negative) values indicate cyclonic (anticyclonic) vorticity.

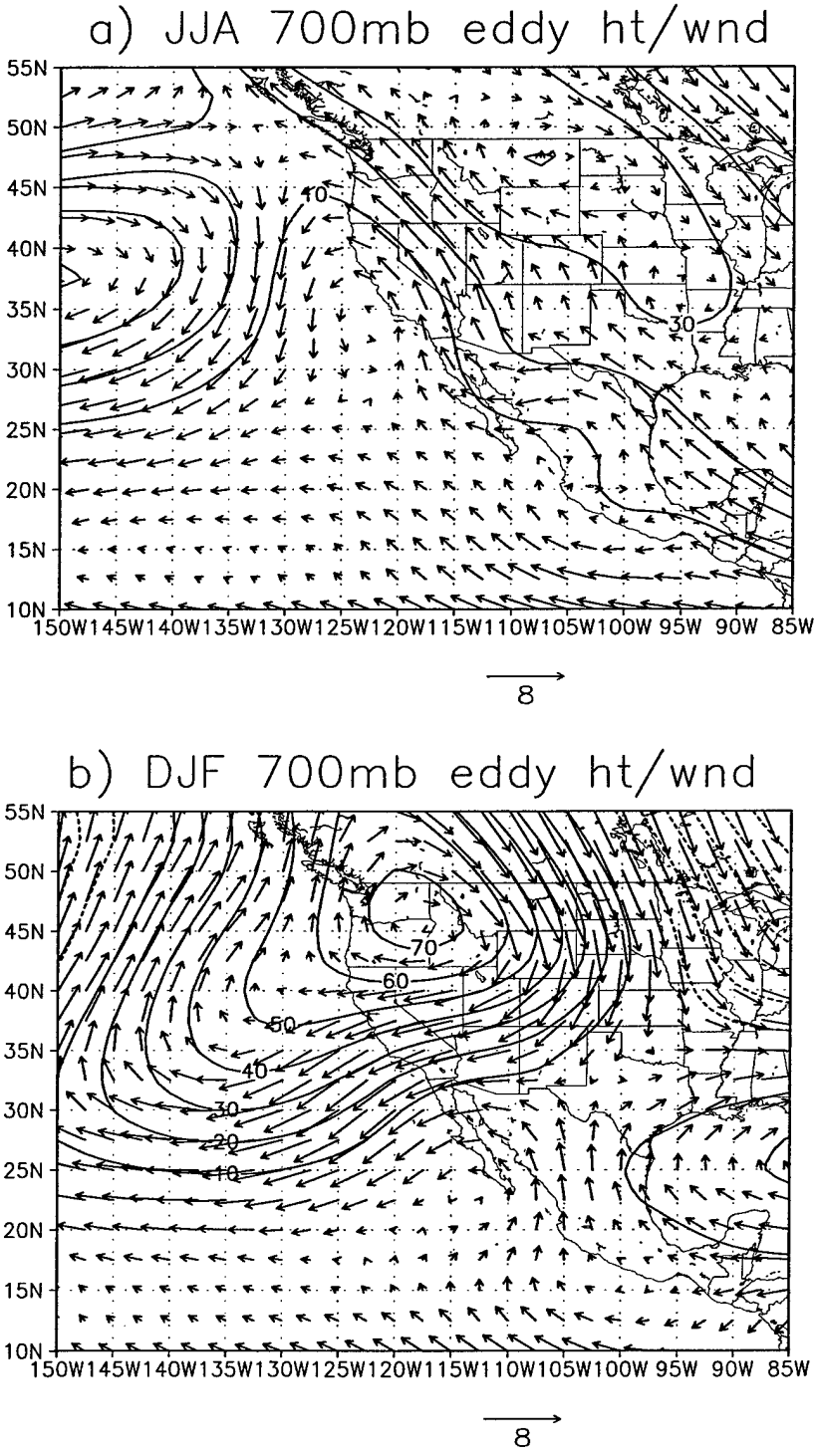


FIG. 2.7. Eddy heights (m) and wind vectors (m/s) over North America for (a) summer (JJA), 700 mb; (b) winter (DJF), 700 mb; (c) summer, 200 mb and (d) winter, 200 mb. Dashed lines depict negative eddy heights.

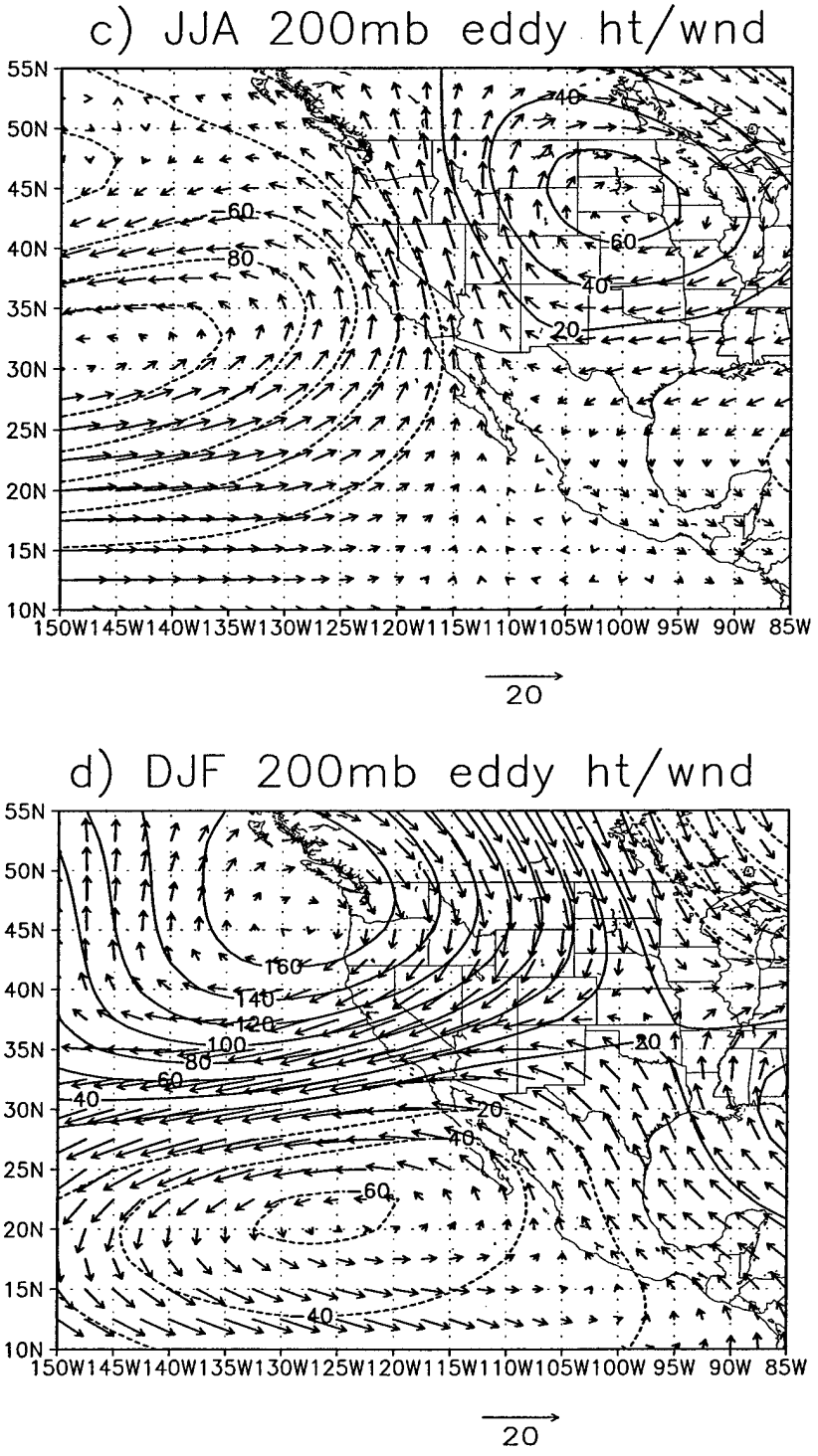


Fig. 2.7, continued.

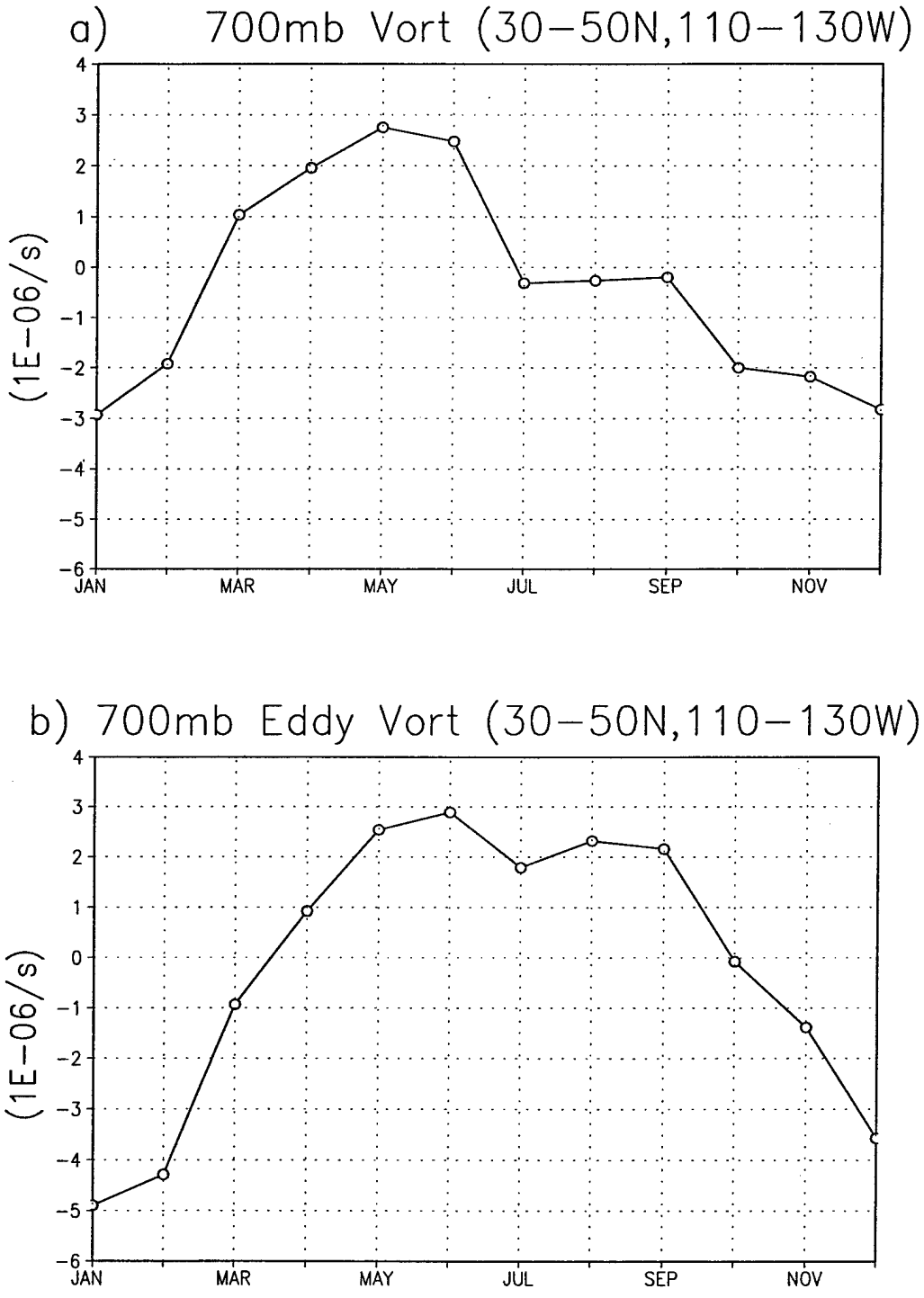


FIG. 2.8. Area averaged vorticity (units 1E-06/s) over the Rocky Mountain region from 30°N-50°N, 130°W-110°W. (a) shows the relative vorticity, and (b) shows the eddy component of vorticity. Positive (Negative) values indicate cyclonic (anticyclonic) vorticity.

occurs in May. The monthly evolution of the eddy field (Fig. 2.8b) clearly shows the winter to summer reversals. Eddy vorticity is at a maximum (most cyclonic) in June, with slightly weaker values in July and August.

The seasonal and vertical reversals found over western North America are quite distinct from those located over South America and Asia. The main differences are the presence of winter anticyclonic flow over the central Rockies, while the highest and broadest sections of the Andes and Tibetan plateau are characterized by cyclonic winter circulations. Another difference is the appearance of a summer, upper-level cyclonic circulation around the southwestern Rockies (Fig. 2.7c), while anticyclonic upper tropospheric circulations are found above both the Andes and Tibetan plateau, associated with warm-core, monsoonal reversals in summer (Fig. 2.1c and Fig. 2.5c, respectively).

Warm core reversals in summer and winter circulations, shown above, are common features of South Asia and South America. Monsoon characteristics, however, are unique (e.g., Zhou and Lau, 1998), due largely to the contrasting orography of the two regions. The longitudinal width of South Asian orography at 30° latitude, for example, is about three times that of the Andes at the same latitude, and the Andes have a much greater latitudinal extent. However, the monsoon reversals of the Andes and South Asian region appear more similar, qualitatively, compared to the reversals over the Rocky Mountains. Possible explanations for these distinctions are proposed in section 2.5.

## 2.4 Interannual Variability

The climatological average is significantly perturbed in individual years. The present focus is on year-to-year variability with an emphasis on atmospheric features that contribute importantly to the water budget and precipitation of South America. A northwesterly LLJ is commonly situated east of the Andes Mountains, and it transports atmospheric

moisture from the humid Amazon rain forest toward the fertile plains of subtropical South America (e.g., Nogués-Paegle and Mo, 1997). Northwesterlies east of the Andes are evident in both summer and winter in the 700 mb fields of Fig. 2.1; and they are particularly pronounced over Bolivia, extending southeastward across Paraguay and southeast Brazil, including portions of the La Plata River basin. The wind system is thus a prominent component of the cyclonic circulation in both summer and winter.

Fig. 2.9 presents winter and summer time correlations of the local, 700-mb wind with the 200-mb zonal flow. The 200-mb zonal flow is averaged over the indicated box centered above the Andes and extends from 20°S-40°S. The eastward/northward component of the vectors denotes the magnitude of the correlation coefficient between the area averaged upper tropospheric wind within the box against the local zonal/meridional flow component at 700 mb. Stronger, upper tropospheric, subtropical westerlies correlate with increased lower tropospheric, cyclonic rotation within the boxed region; and with an eastward and southward flow emanating from the Amazon basin toward the La Plata River basin of southeast Brazil, Paraguay, Uruguay and northern Argentina (Fig. 2.9a,b). The cyclonic tendency in the vicinity of the Andes is present in both seasons, though more definitive during summer (Fig. 2.9a).

The result suggests a potential for enhanced, inter-basin moisture transport from the Amazon to the La Plata basin in the presence of relatively strong subtropical, upper troposphere westerlies over the Andes (e.g., during warm ENSO events). Fig. 2.9c and 2.9d shows results similar to those presented in Fig. 2.9a and 2.9b using correlations of area averaged, upper troposphere zonal flow against local, vertically integrated moisture flux. The correlations were calculated using a 29-year subinterval of the 50-year record. This subinterval extends from 1968-96, and uses an NCEP/NCAR Reanalysis dataset that

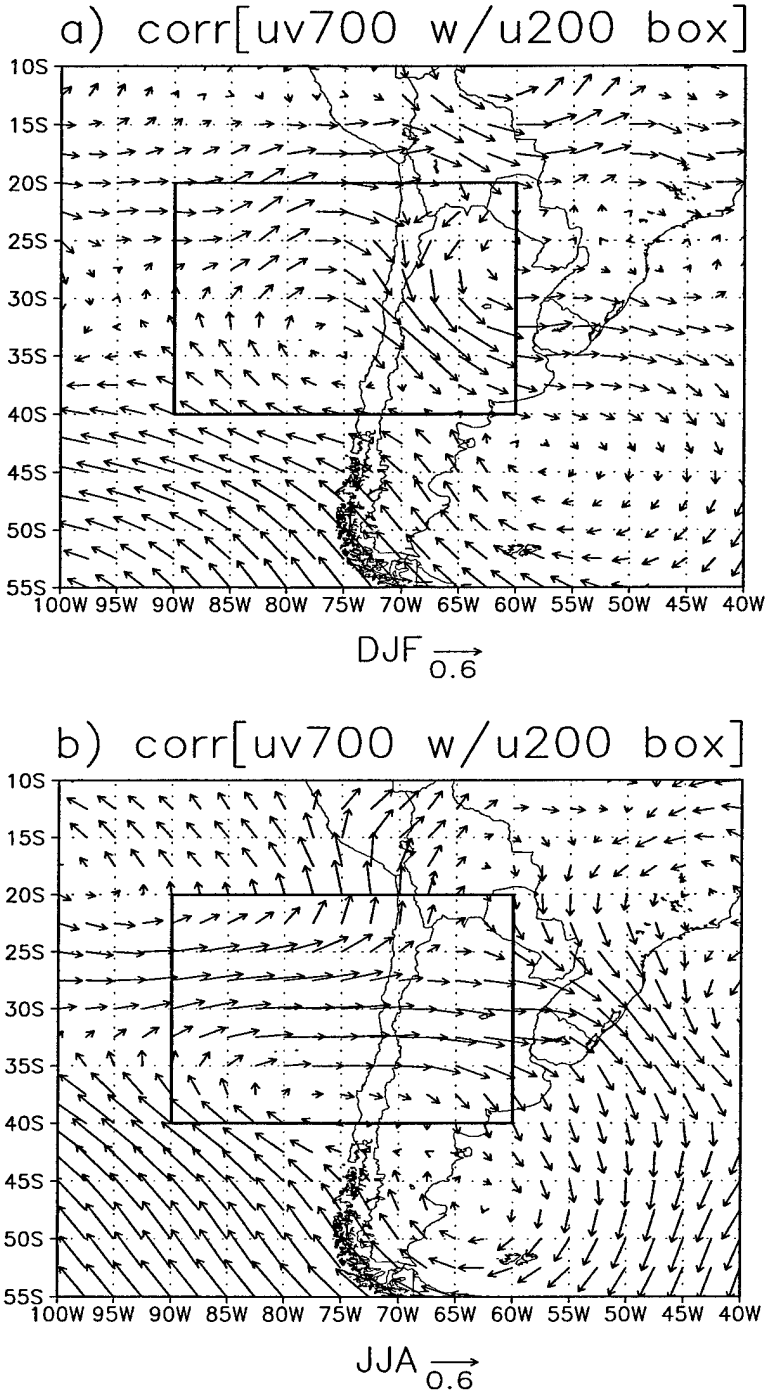


FIG. 2.9. Time correlation vectors (arrows indicate magnitude). (a) shows the summer (DJF) correlation of area averaged, 200-mb, zonal wind in the box with 700-mb wind at all locations. (b) is similar to (a) but for winter (JJA). (c) shows the summer correlation of area averaged, 200-mb zonal wind in the box with vertically integrated moisture flux. (d) is similar to (c) but for winter. (c) and (d) are plotted using a higher resolution subset of the Reanalysis from 1968-1996.

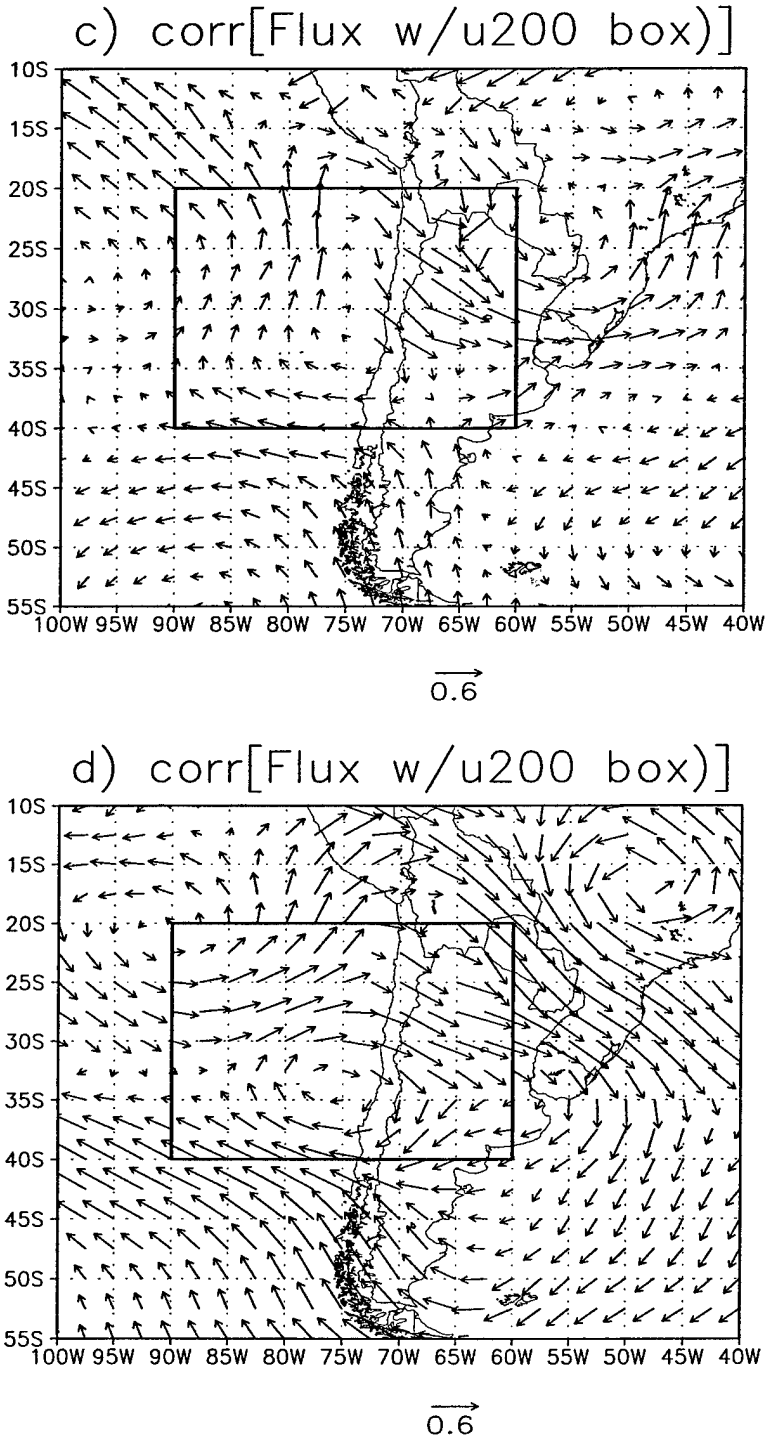


Fig. 2.9, continued.

includes 28 vertical levels and 7 levels below 850 mb (see Mo et al., 1997). The fluxes are available at 6 hourly intervals and were computed from daily, rather than monthly averages, reflecting the influence of transients. Stronger southward moisture flux tends to emanate from the Amazon basin when the westerly flow increases across the Andes.

The enhanced atmospheric moisture flux from the Amazon basin contributes to heavier precipitation over the La Plata basin. This connection is evident in the precipitation anomalies displayed for two summer seasons over South America in Fig. 2.10. Fig. 2.10a shows anomalies for summer 1997-98, and Fig. 2.10b displays anomalies for summer 1998-99. Anomalies are computed by subtracting the seasonal, long-term (50-year) mean from the individual, seasonal averages. The analysis uses the land portion of the global Precipitation Reconstruction (PREC/L) analyses of Chen et al. (2002). The precipitation analyses are defined by interpolation of gauge observations over land from the Global Historical Climatology Network (GHCN, Version 2) and the Climate Anomaly Monitoring System (CAMS). Summer 1997-98 was a warm, El Niño event in the eastern Pacific Ocean, while the following summer represented cold, La Niña conditions in the east Pacific. Warm, eastern tropical Pacific surface temperatures commonly accelerate the regional subtropical jet, thereby increasing the zonal upper tropospheric subtropical flow over the East Pacific (e.g., Paegle et al., 1987). A substantially stronger westerly wind is present in the upper troposphere during the warm event that is absent in the cold event. The area averaged, 200-mb zonal wind over the boxed region outlined in Fig. 2.9 (20°S-40°S, 90°W-60°W) was 26 m/s for DJF 1997-98, but only 18 m/s during DJF 1998-99. A 50-year, temporal correlation of 200-mb, cross-Andes zonal flow with regional precipitation has been presented in Chapter 1 (Fig. 1.2). The largest correlation coefficient (0.3) is centered on the La Plata basin and is statistically significant at the 99% level.

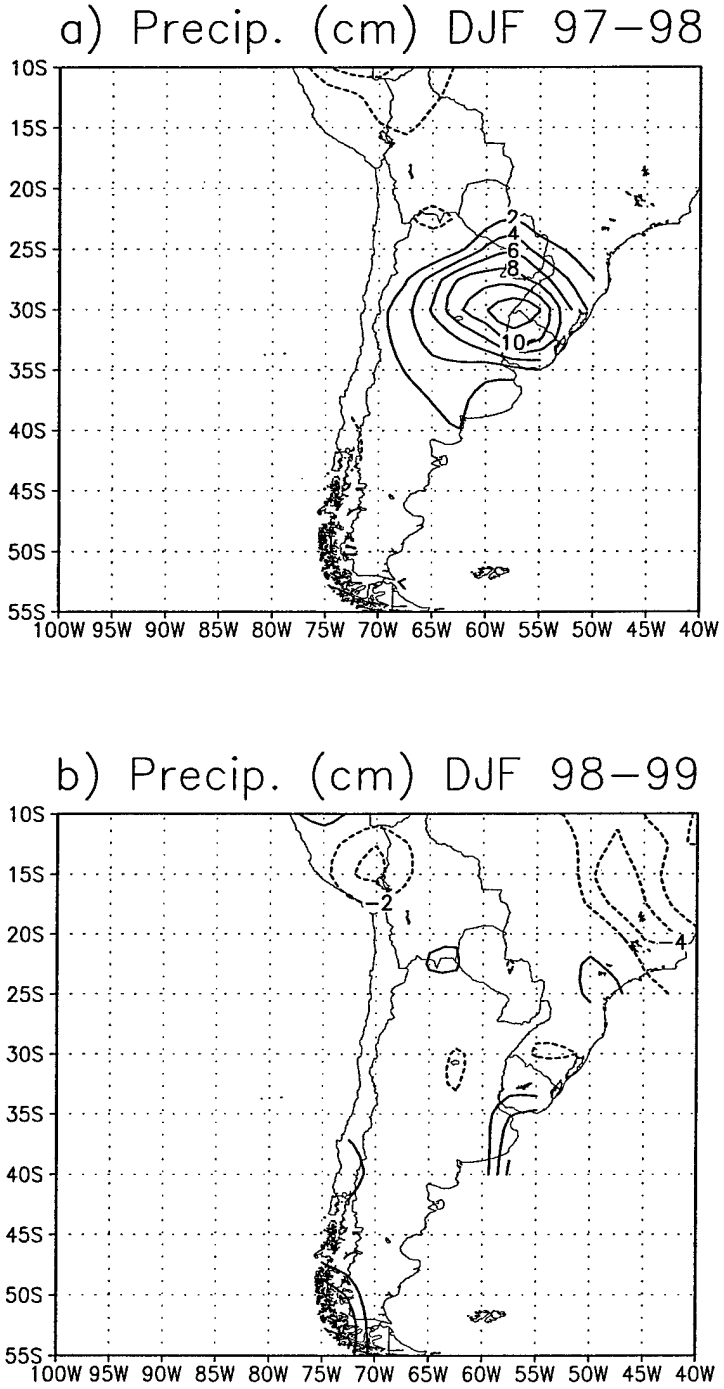


FIG. 2.10. Precipitation anomalies (cm) from the gauge data set (PREC/L) of Chen et al. (2002) for (a) summer (DJF), 1997-98; and (b) summer, 1998-99. Solid contours are positive, and dashed contours are negative anomalies.

The next subsection presents preliminary theoretical analyses that may explain the cyclonic lower troposphere circulation that is centered on the subtropical Andes in both summer and winter, as well as the enhancement of this circulation and attendant meridional moisture flux east of the Andes by stronger ambient westerlies.

## 2.5 Dynamical Interpretation

Three processes that may influence monsoonal circulations in the vicinity of high orography are enumerated below:

i) Thermal effect of surface heating on an elevated surface;

ii) Thermal effect of latent heating above elevated slopes;

iii) Mechanical effect of orography.

Surface heating (mechanism i) of an elevated plateau generates upslope, buoyancy driven circulations. The convergence of such slope-driven flow toward the highest mountains produces low-level cyclonic rotation in the vicinity of the orography (e.g., Broccoli and Manabe, 1992; Gutzler and Preston, 1997; and Zhou and Lau, 1998). The lower tropospheric cyclonic flows found in the vicinity of the Andes in Fig. 2.1a and 2.1b are qualitatively consistent with this mechanism, but the seasonal transitions are not. If this were the dominant mechanism, the cyclonic circulation should decrease from summer to winter as surface heating diminishes. Although the warmed plateau effect reduces from summer to winter (compare Fig. 2.3a with 2.3b), the cyclonic vorticity does not decrease from summer to winter (compare Fig. 2.2a with Fig. 2.2b), and instead shows some increase in the colder season.

Thermal effects of atmospheric latent heating associated with precipitation on elevated slopes (mechanism ii) would also produce cyclonic rotation of the lower troposphere in the vicinity of rainy slopes. Because latent heating is commonly distributed through a deep

tropospheric layer, upward motion associated with latent heat of condensation usually extends vertically through much of the troposphere and produces divergence in the upper troposphere. The divergence generates anticyclonic rotation in the upper troposphere. Rao and Ergodan (1989) suggest latent heat release from organized convection is the largest contributor to the Altiplano heat source in the vicinity of Bolivia.

The summer eddy pattern of Fig. 2.1a displays cyclonic rotation in the lower troposphere, while Fig. 2.1c displays anticyclonic rotation in the summer upper troposphere. This vertical monsoonal circulation reversal also characterizes summer conditions of South Asia (see Fig. 2.5a and 2.5c), and provides strong observational support for mechanism (ii) for the summer season.

This mechanism, however, does not explain the cyclonic circulations situated in the vicinity of the Andes during winter (Fig. 2.1b and 2.1d), and also does not directly explain the correlation of upper troposphere zonal wind with lower troposphere cyclonic vorticity in both winter and summer. The zonal flow correlations with precipitation (Fig. 1.2) show regions of both increased and decreased precipitation over the Andes during episodes of stronger westerly flow, and there is no evidence of systematically increased latent heating over the highest Andes with stronger westerly flow over this region in summer.

The mechanical effect of orography (mechanism iii) is a third possible explanation for the observed circulation in the vicinity of the Andes. Campetella and Vera (2002) describe mechanical effects of orographic blocking in baroclinic treatments on synoptic time scales. Here, the focus is on the simpler barotropic vorticity equation, applied with a beta plane approximation to a one layer atmosphere above idealized orography. Stationary Rossby waves forced by orography produce an orographic anticyclone in the presence of strong zonal flow, and they produce a cyclone in the presence of weaker westerly flow.

The next section addresses flow oscillations predicted by barotropic theory in the presence of ambient zonal flow changes, and the possible relevance of the theory to observations in the vicinity of high terrain.

## 2.6 Barotropic Analysis of Mechanical Flow Blocking

### 2.6.1 Single Layer Model

The phase speed, C, of Rossby waves in a nondivergent, single-layer barotropic model is:

$$C = \left( \bar{u} - \frac{\beta}{k^2} \right) \tag{2.1}$$

Here, $\bar{u}$ is the background flow, which is assumed to be uniform and only in the zonal direction; k is horizontal wave number; and $\beta$ is the meridional gradient of the Coriolis parameter (Beta parameter), assumed to be constant in the present Beta plane approximation. For the case of quasi-stationary, seasonal response to orography, C=0, and "supercritical" conditions exist when

$$\left( \bar{u} - \frac{\beta}{k^2} \right) > 0 \tag{2.2}$$

while "subcritical" conditions exist when

$$\left( \bar{u} - \frac{\beta}{k^2} \right) < 0; \tag{2.3}$$

and resonance occurs when

$$\left(\bar{u} - \frac{\beta}{k^2}\right) = 0 . \tag{2.4}$$

It is easy to demonstrate (see Appendix) that the steady solution produces an anticyclone over mountains and a cyclone over valleys for supercritical conditions; and the opposite distribution, with a cyclone over mountains, for subcritical conditions. This situation is discussed by Charney and DeVore (1979) and by Nogués-Paegle (1979), who study the idealized case forced by only one spectral component in the surface orography. Those investigations focus upon the solution bifurcation and destabilization that occur as the flow fluctuates about the resonant values separating sub- and supercritical conditions. A simplified analysis that suffices for the present interpretation is given in the Appendix.

Subcritical conditions are more likely to be satisfied for mountains situated in the subtropics than for those located in midlatitudes for two reasons. First, the Beta ($\beta$) parameter is larger in the subtropics, and second, the midtroposphere flow is generally weaker in the subtropics than in midlatitudes. The Andes and Tibetan plateau are large mountain ranges with highest elevations near the subtropics, which could favor cyclonic rotation in all seasons, as reanalyzed at 700 mb in both locations (Fig. 2.1a and 2.1b, and Fig. 2.5a and 2.5b) during winter and summer. By contrast, the highest portion of the Rocky Mountain chain is centered in midlatitudes, characterized by lower values of the $\beta$ parameter and stronger zonal winds, particularly during the winter. Consequently, the 700-mb anticyclone situated over central portions of North America in winter (Fig. 2.7b) may be explained by supercritical flows in that season for those latitudes. The transition to a cyclonic circulation in summer (Fig. 2.7a) suggests the weakening zonal flow may have become subcritical in

that season. Of course, the surface thermal forcing and other remote influences may also explain the summer-to-winter transitions.

The barotropic analysis helps explain why the orographically bound, Andes cyclonic circulation increases with stronger westerlies (Fig. 2.9a and 2.9b). The assumption that the actual ambient flow remains subcritical for most of the effective orographic spectrum of the Andes corresponds to the conclusion that the denominator of the amplitude coefficient, $B_{kl}$, of equation (A.18) in the Appendix is negative for most of the response. Increasing/decreasing zonal flow would increase/decrease the magnitude, $|B_{kl}|$, of the response, leading to enhanced cyclones for stronger flows. Preliminary comparison of DJF 1997-98 to DJF 1998-99 may offer one example. Both summers have a mean 700-mb eddy cyclonic circulation near 30°S, 75°W (not shown), similar to the long-term average (Fig. 2.1a). However, the eddy heights in the former year are about 30 m lower than in the latter year, accompanied by stronger northwesterly flow east of the Andes. As noted in section 2.4, the reanalyzed, area averaged, 200-mb zonal flow over the subtropical Andes region was about 8 m/s stronger in DJF 1997-98 than in the following summer.

One possible discrepancy with the single level barotropic theory is that the Reanalysis depicts eddy circulation centers displaced somewhat west of the highest orography, rather than over the orography, as predicted by theory (e.g., Fig. 2.1 and 2.7). This discrepancy may reflect the limitations of the theory. It is also possible that the effective mountain profile should account for not only the surface topography, but also the blocking effect of the stagnated airmass commonly found upwind of large orographic barriers.

This possibility would increase the effective barrier width and tend to shift its effective center westward. Paegle (2000) suggests this possibility is included in primitive equation simulations over North America but not explicitly in a 1-layer barotropic analysis. The

possible role for upstream stagnation has not been examined in detail.

The simple model described above neglects friction. For the barotropic response to mountains, Dickinson (1978) and Holton (1992, and references therein), demonstrate that inclusion of Ekman pumping (boundary layer drag) yields a response located 1/4 of a wavelength east of the orography to remove the resonant singularity. Holton (1992) (pp. 221-222) assumes a spin down time of 5 days and topography at 45°N. The next section describes simulations in a more complete global model, which includes frictional effects and a more realistic spectrum of orography.

### 2.6.2 Primitive Equation Model Simulations

In order to more clearly support or refute the possibility that observed seasonal reversals are affected by the simple barotropic mechanism in question, it is necessary to demonstrate that the mechanical effects of orography are at least as important as thermal influences in more complete analyses. Such analyses should include a multilevel model that retains a full and realistic spectrum of orography, and also retains heating and realistic shear in the background flow. Nigam et al. (1988) use a linear model to distinguish the mechanical, orographic effect in winter from the thermal effect for synoptic scales (see their Fig. 3), and Nogués-Paegle et al. (1998, see their Fig. 13) show the role of mechanical forcing and surface heating in nonlinear analyses with a five-level model. Campetella and Vera (2002) show that the mechanical effect becomes especially pronounced in transient baroclinic simulations of synoptic cyclones impinging the Andes, and Salio et al. (2002) present more detailed descriptions of Chaco lows and thermal effects.

Higher resolution simulations display an even stronger response to mechanical effects in nonlinear treatments. Simulations are next presented using a 20-level, spectral, primitive equation version of the Utah Global Model (UGM). They suggest a mechanical influ-

ence on the seasonal reversal around the Andes Mountains, and thus on the east Andes LLJ.

The model is described by Paegle (1989). It uses pressure-based sigma coordinates and predicts vorticity, divergence, thermal and moisture fields. The method is similar to approaches used in operational centers except numerical approximations of horizontal derivatives are based on Fourier series in longitude and finite elements in latitude. The present integrations have a 2.22° spacing in latitude and a wave number 42 truncation in longitude. They omit radiative and latent heating and provide a realistic ambient flow, taken from observed seasonal (DJF and JJA) conditions from the NCEP/NCAR Reanalysis, averaged from 1951 to 2000. This allows reasonable vertical shear and more general processes than does a simple barotropic model (section 2.6). Model orography is also from the NCEP/NCAR Reanalysis. The integrations use a 15-minute time step. The zonally averaged portion of the simulated circulation is nudged to the reanalysis value for each season by rapid relaxation of the rotational part of the zonally averaged flow toward the climatology for each season. The mechanical effect is illustrated through the difference in runs with orography over the entire globe and runs without orography over South America. For the latter, initial surface pressure over South America is set to a constant (1013 mb) over the region from 82°W-28°W, and 55°S-13°N.

Fig. 2.11 shows differences in the average wind vectors (mountain minus no-mountain) for simulations with and without orography. A cyclone which appears tied to local orography is evident in the difference field for both summer (Fig. 2.11a) and winter (Fig. 2.11b) over South America. The average is for the final 30 days of a 40-day forecast at sigma level 0.78. The result is similar to Fig. 13 of Nogués-Paegle et al. (1998), but it suggests an even stronger mechanical signal. This may be due to the higher resolution of present integrations. During summer (Fig. 2.11a), the cyclonic circulation in the difference

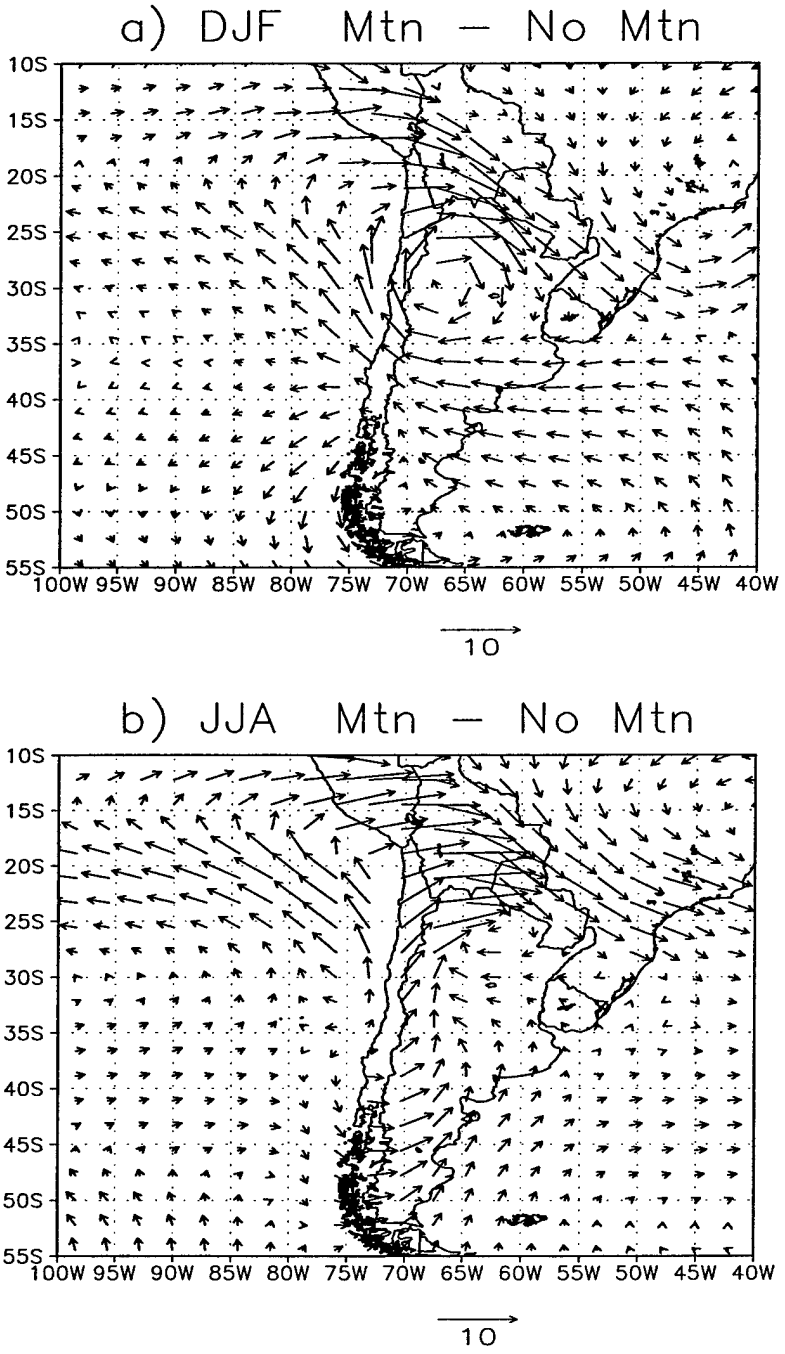


FIG. 2.11. Orographic effect for a 20-level, adiabatic version of the UGM, truncated at wave number 42, for month long integrations of the (a) summer (DJF), and (b) winter (JJA) climatological averages (1951-2000). The panels represent the average difference in wind vectors (m/s) at sigma level 0.78 between simulations with and without orography over South America for the last 30 days of 40-day simulations.

field is closed and centered at about 30°S and 66°W. Northwesterly winds at about 5-10 knots are over Bolivia and Paraguay during both summer and winter (Fig. 2.11a,b). The orographic effect of the UGM only partly agrees with the observed eddy cyclonic circulations in Fig. 2.1a and Fig. 2.1b. In particular, the model circulations are displaced to the east of the reanalyzed circulations, which are centered just west of the Andes. This suggests other mechanisms, in addition to local topography, account for the seasonal circulations in the vicinity of the Andes. Other explanations may also account for the acceleration of the LLJ east of the Andes corresponding to ambient zonal flows in the upper troposphere (section 2.5). Uccellini and Johnson (1979), for example, demonstrate that ageostrophic, low-level flows originating near the exit regions of jet streaks contribute to the maintenance of thermal wind balance and may also contribute to enhanced LLJs independently of orography.

This simplified summary pertains only to the climatological average. Analyses with higher temporal resolution show large synoptic scale, day-to-day variability, which has been discussed by other investigators with emphasis upon the east Andes LLJ (e.g., Virji, 1981; Douglas et al., 1998 and 1999; Campetella and Vera, 2002; and Salio et al., 2002).

In the current perspective, the east Andes LLJ is a component of the topographically-bound, lower troposphere cyclonic circulation surrounding the Andes. Strengthening of the cyclonic flow and LLJ occur in the presence of enhanced westerly flow across the Andes. In the climatological average, this jet blows poleward in both winter and summer because of the persistence of the lower level cyclone in monthly averages. By contrast, monthly averaged flows located east of the central Rockies of the western United States tend to blow poleward in summer, but equatorward in winter as the orographically bound vortex reverses spin from summer to winter (see Fig. 1.1). The orographic cyclone and attendant LLJ exhibit substantial interannual variability of monthly averages, as described

in section 2.4.

The next chapter examines regional forecast sensitivity to local and remote targeting of initial state detail over South America during summer.

# CHAPTER 3

# SENSITIVITY TO INITIAL DATA CHANGES

Prediction of weather and short range climate evolution over South America is characterized by different challenges than those that arise for North America. This chapter focusses upon special challenges posed by observation gaps in the Southern Hemisphere (SH) atmosphere. The operational observing network of land radiosondes is much more sparse here (e.g., see Fig. 1 of Saulo et al., 2001) than over the Northern Hemisphere (NH), while the southern oceans may be observed almost as well by satellites as are the northern oceans. It is consequently unclear whether data sparse regions of the oceans or continents represent the most strongly limiting components of the southern observing system. The relative importance of initial state detail over South America and detail external to South America is examined with a set of experiments using the variable resolution UGM designed to assess impact of initial state changes upon regional predictability.

## 3.1 Background and Motivation

Several studies have focussed upon the impact of supplemental observations within data sparse regions of the western hemisphere upon forecasts over populated regions of North America. Langland et al. (1999) evaluated the role of experimental dropsonde data over the north Pacific upon short range weather prediction over North America. The additional data collected during the North Pacific Experiment (NORPEX) in January and February 1998 were included within the data assimilation system of the Medium Range

Forecast (MRF) model. A phase of the California Land-Falling Jets Experiment (CALJET) also took place during the same winter (Ralph et al., 1999). This latter experiment was designed to obtain observations for improved forecast guidance in the 0-12 hour range. Both CALJET and NORPEX field experiments have been repeated during more recent winters. Other field projects designed to improve understanding and forecasting of winter weather events over the complex geography of western North America include the Intermountain Precipitation Experiment (IPEX, Schultz et al., 2002) and Improvement of Microphysical Parameterization through Observational Verification Experiment (IMPROVE, Stoelinga et al., 2003).

The added observations obtained in experiments such as NORPEX show a positive impact upon short term forecasts over North America. The improvement is particularly evident over western portions of the U.S. in which the forecast skill of a variety of operational and research models has been shown to be remarkably similar by White et al. (1999). White et al. (1999) suggest that the proximity of the data sparse region of the Pacific has negative impact upon both highly resolved and well-developed models, as well as less sophisticated models, and that this may be the main limitation to accurate winter weather prediction at 36 hours over the western U.S.

The NORPEX dropsondes were deployed over the north Pacific instead of North America because the North American region is relatively well analyzed by the high density, operational radiosonde stations. Much of North America is situated in the zone of ambient westerly winds within which weather events propagate rapidly from west to east, particularly during the winter season. Atmospheric changes tend to move eastward quickly from the north Pacific across North America on a time scale of approximately 5

days or less during the northern winter (Langland et al., 1999; and Miguez-Macho and Paegle, 2001).

By contrast, the characteristics of the South American observing system and regional weather evolution are rather different. Much of South America is located in the tropics and subtropics within which eastward propagation of Rossby wave influences is relatively slow, particularly during the important warm seasons that tend to be wet over the continent.

Several field programs have been mounted over South America with the intent to improve atmospheric observations here. Some projects, such as the Atmospheric Boundary Layer Experiment (ABLE 2B, Garstang et al., 1990), have studied surface processes over the Amazon basin, with particular emphasis on evapotranspiration. Nicolini et al. (2002) show that better surface observations and treatment of surface conditions are more important than improved specification of initial state uncertainty for short range, limited area predictions over South America. Limited area model sensitivity to initial condition uncertainty is, however, diminished by use of boundary conditions that constrain error growth (e.g., Anthes, 1983; and Errico and Baumhefner, 1987). Uncertainty of lateral boundary conditions has been found to be more important than initial state uncertainty in some regional model simulations (e.g., Paegle et al., 1997). Nicolini et al. (2002) demonstrate a similarly important role for the specification of the bottom boundary condition.

Global models are required to minimize the overwhelming role of lateral boundary constraints upon error growth of limited area models. Unfortunately, global models often have relatively coarse resolution, and this limits their local utility in regions such as South America, where the Andes mountains impose first order influences upon regional weather

evolution (e.g., Kleeman, 1989; Gandu and Geisler, 1991; and Campetella and Vera, 2002). The Andes present a special challenge to numerical simulation because of their effective ridge heights extending to the midtroposphere and mesoscale east-west dimensions.

The purpose of this chapter is to address the question of initial state uncertainty growth over South America. A variable resolution version of the global model presented in Chapter 2 is used, and except for variable resolution it is very similar to the one used by Miguez-Macho and Paegle (2001, hereafter, MMP01) for NH inital state modifications.

As described in Chapter 1, the observing system over Central and South America has recently been improved by addition of several pibal soundings from PACS-SONET (http://www.nssl.noaa.gov/projects/pacs). In addition, the South American Low-Level Jet Experiment (SALLJEX) was recently conducted to observe low-level circulations east of the Andes (http://www.clivar.org/organization/vamos/index.htm). The goal of this chapter is to present preliminary predictability studies with the UGM that are designed to anticipate the sensitivity of weather prediction in the South American region to atmospheric detail that is included or excluded in the specification of the initial state over and around South America.

The approach is to initialize the UGM first with the coarse resolution NCEP/NCAR Reanalyses globally in a control integration. Experimental integrations are then performed in which the reanalyses are replaced with higher resolution, NCEP Global Data Assimilation System (GDAS) analyses. The GDAS analyses are intended to serve as proxies for analyses including higher resolution observations. The switch from Reanalysis to GDAS initial states is performed globally and over South America to study the potential predict-

ability impact of initial state changes in different portions of the globe.

Section 3.2 describes the global analyses; the rotated, variable resolution UGM; and the methodology for data changes over selected regions. MMP01 examined the sensitivity of initial state data changes on medium range forecasts over North America during winter using a uniform resolution version of the UGM. Section 3.3 repeats similar experiments for northern winter 2003, using the rotated, variable resolution UGM, more suited for South America. The results and conclusions for midlatitudes of northern winter are similar to MMP01 and are included for comparison to the South American data sensitivity tests, presented in Section 3.4. Section 3.4 also presents numerical tests of the suitability of the rotated, variable resolution approach. Section 3.5 provides further discussion.

## 3.2 Data, Model and Experiment Design

### 3.2.1 Datasets

The NCEP/NCAR Reanalysis is a state-of-the-art, retrospective analysis of assimilated observations which uses a frozen data assimilation system (Kalnay et al., 1996). The horizontal resolution is 2.5° with wave number 37 truncation, and there are 26 vertical levels. Additional details on the Reanalysis are provided in section 4.3.1. Operational GDAS analyses are used to initialize NCEP's Global Forecast System (GFS) model at wave number T254. GDAS data have horizontal resolution of 1° on 26 vertical levels and are available via anonymous file transfer protocol (ftp.prd.ncep.noaa.gov).

Fig. 3.1 presents magnitudes of 500-mb wind differences between the Reanalysis and GDAS on 17 January 2003, 00 UTC. Differences are generally on the order of 5 m/s. They tend to be largest over the oceans (maximum 18 m/s), near the poles and over data sparse land regions, where lack of conventional surface based rawinsonde data may produce val-

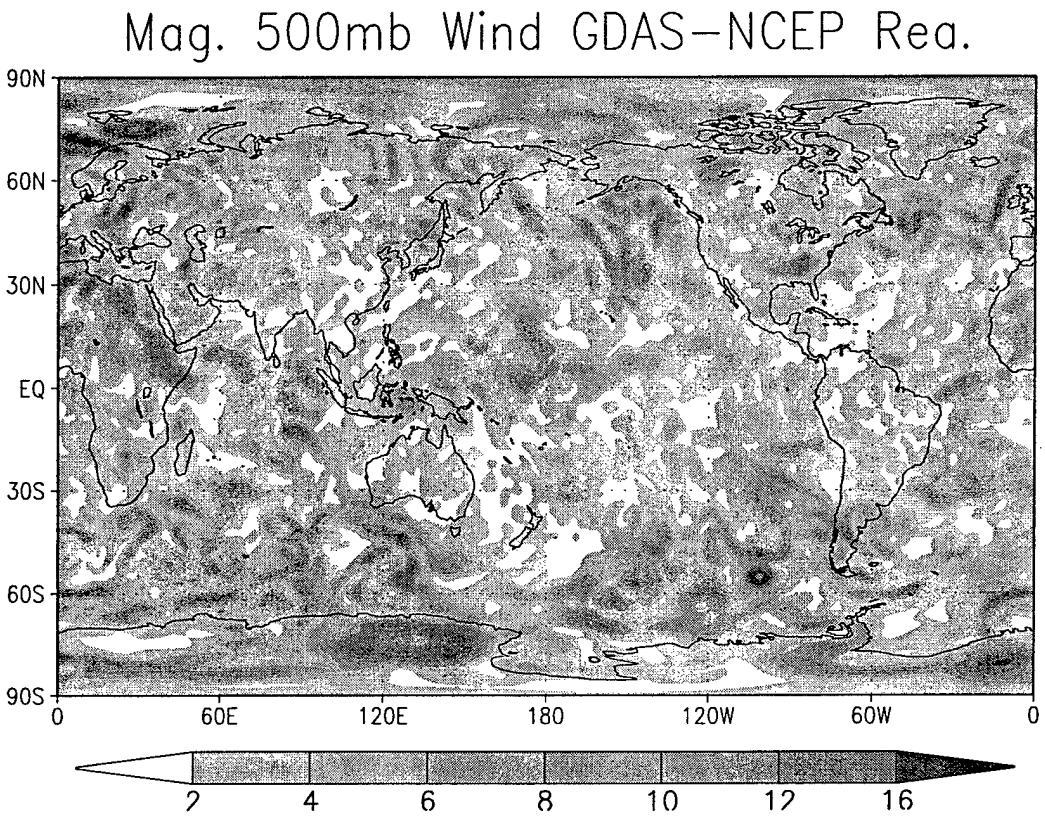


FIG. 3.1. The magnitude of the differences in 500-mb wind (m/s) between the GDAS analysis and NCEP/NCAR Reanalysis (GDAS minus NCEP/NCAR Reanalysis) at 00 UTC on 17 January 2003. The Reanalysis has been interpolated to 1° spacing to match the horizontal resolution of the GDAS analysis.

ues that are strongly influenced by the forecast model used for the first guess. Notable differences are also evident over the southeastern U.S. (about 15 m/s) and off the western coast of Ireland.

The enstrophy spectrum of the two global analyses is examined next. Enstrophy is the square of the vorticity field, and its spectrum emphasizes shorter waves. The streamfunction is first computed globally from the wind field, and then projected onto spherical harmonics. Globally integrated enstrophy may be expressed as:

$$\int_A (\nabla^2 \Psi)^2 DA \doteq \sum_{mn} \left( A_n^{\ m} \right)^2 [n(n+1)]^2 \tag{3.1}$$

where A is the global area, $\Psi$ is streamfunction; and $A_n^{\ m}$ is the amplitude coefficient of the spherical harmonic component of degree $n$ and order $m$. The quantity:

$$\left[ \sum_m \left( A_n^{\ m} \right)^2 \right]^{\frac{1}{2}} \tag{3.2}$$

is plotted against global wave number $n$ in Fig. 3.2, for 30 January 2003 at sigma level 0.2. The highest values are evident in the lowest wave numbers. The GDAS analysis contains higher enstrophy in the larger wave numbers, while the Reanalysis spectrum drops abruptly beyond wave number 30 (Fig. 3.2).

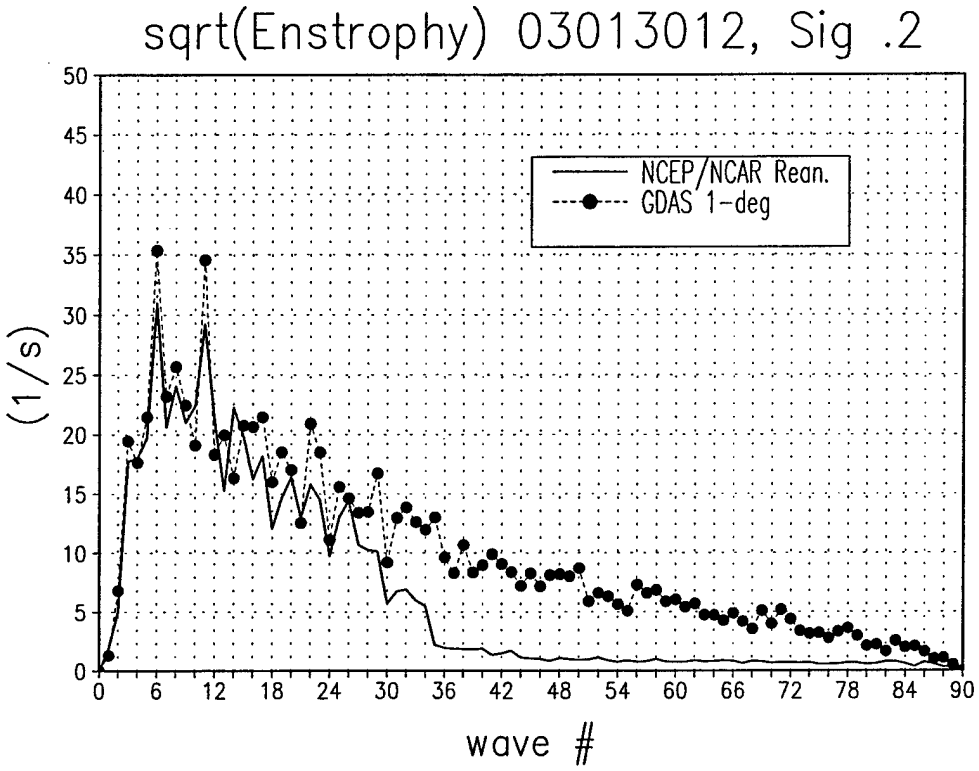


FIG. 3.2. The square root of the globally averaged enstrophy spectrum (1/s) as a function of wave number at 12 UTC on 30 January 2003, for the NCEP/NCAR Reanalysis (line) and GDAS analysis (circles), at sigma level 0.2.

### 3.2.2 Rotated, Variable Resolution Model

The UGM was originally developed by Paegle (1989) with a variable resolution capability designed to address predictability questions of the sort particularly relevant in the present application. A variable resolution version of the model has been used in barotropic predictability experiments by Paegle et al. (1997). The primitive equation version of the rotated, variable resolution version is presented here. More details of the UGM are described in section 4.3.1.

Fig. 3.3 demonstrates the uniform and rotated, variable resolution model grid and topography. The method takes advantage of the convergence of the meridians and therefore closer spacing between grid points near the polar regions (Fig. 3.3a). The mathematical north pole is shifted to 10°S, 60°W, in Fig. 3.3b. Higher resolution near the rotated north pole and surrounding region is obtained by increasing the concentration of latitudinal grid points north of 45°N while decreasing the resolution to the south with respect to the mathematical grid (Fig. 3.3b). The configuration is similar to two-way nested grid techniques available in other models in which resolution changes abruptly. For example, Coté et al. (1998a,b) employ a rotated, variable resolution model for application to a broad range of time scales. Unlike the method applied here, the mathematical poles are rotated away from the high resolution inner domain.

In Fig. 3.3b, equally spaced, 3° latitude increments extend from from the south pole, northward to 44°N. Latitudinal spacing decreases to 1° from 45°N to the mathematical north pole, situated at 10°S, 60°W. There are 91 grid points in latitude, 128 in longitude and 23 levels in the vertical. Experiments with the two-way nested grid targeting South America are initialized at 00 UTC, 17 January 2003 and 12 UTC, 30 January 2003.

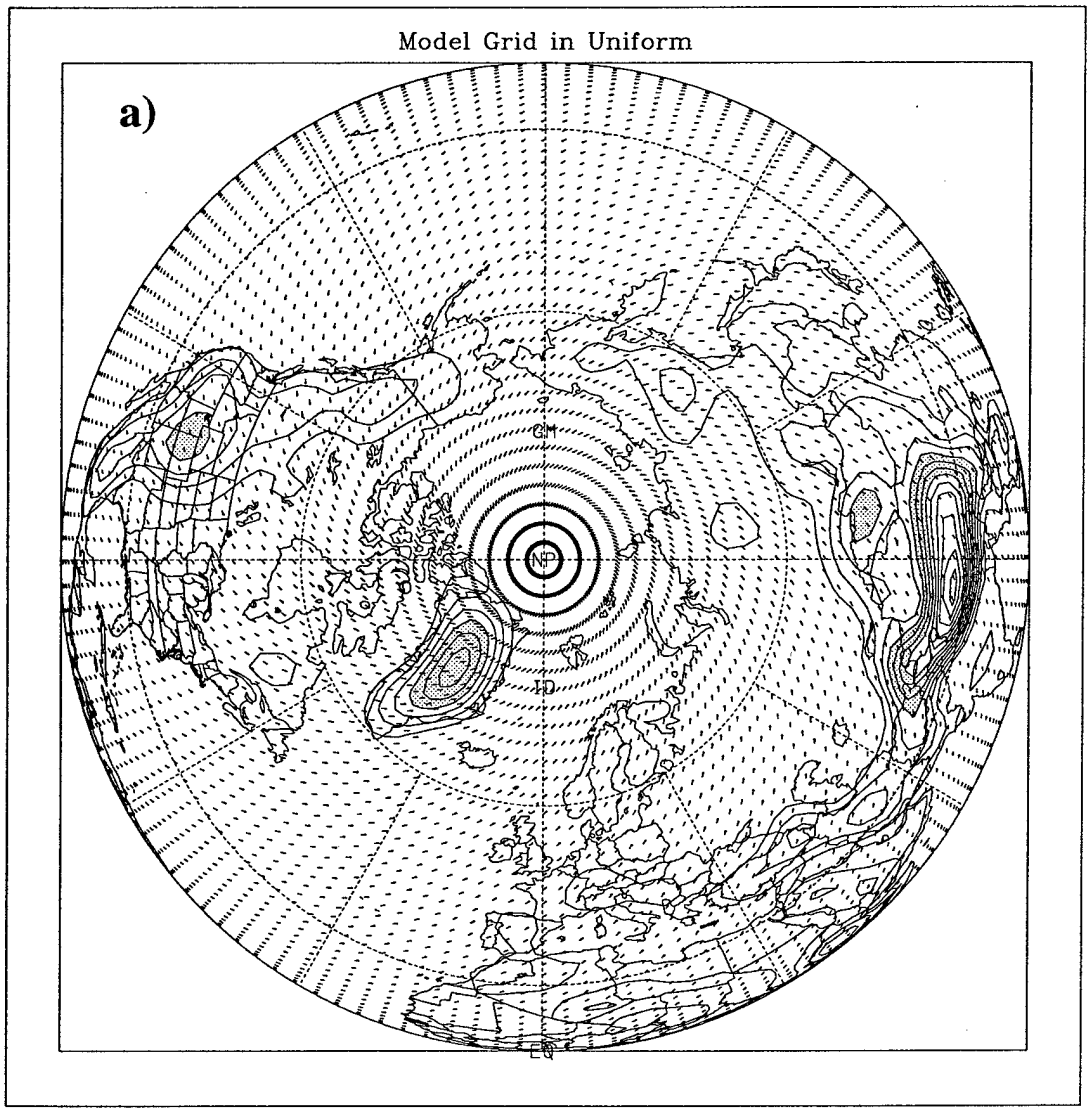


FIG. 3.3. Utah Global Model grid. (a) Contours of topography with uniform resolution, 129 points in longitude, 91 points in latitude. (b) Similar to (a), but the mathematical pole has been rotated to 10°S, 60°W, with the same number of grid points. Latitude spacing is 1°, north of 45°N and 3° resolution south of 45°N with respect to the rotated pole. Contours are every 500 m in (a) and (b). Topography higher than 2000 m is shaded in (a).

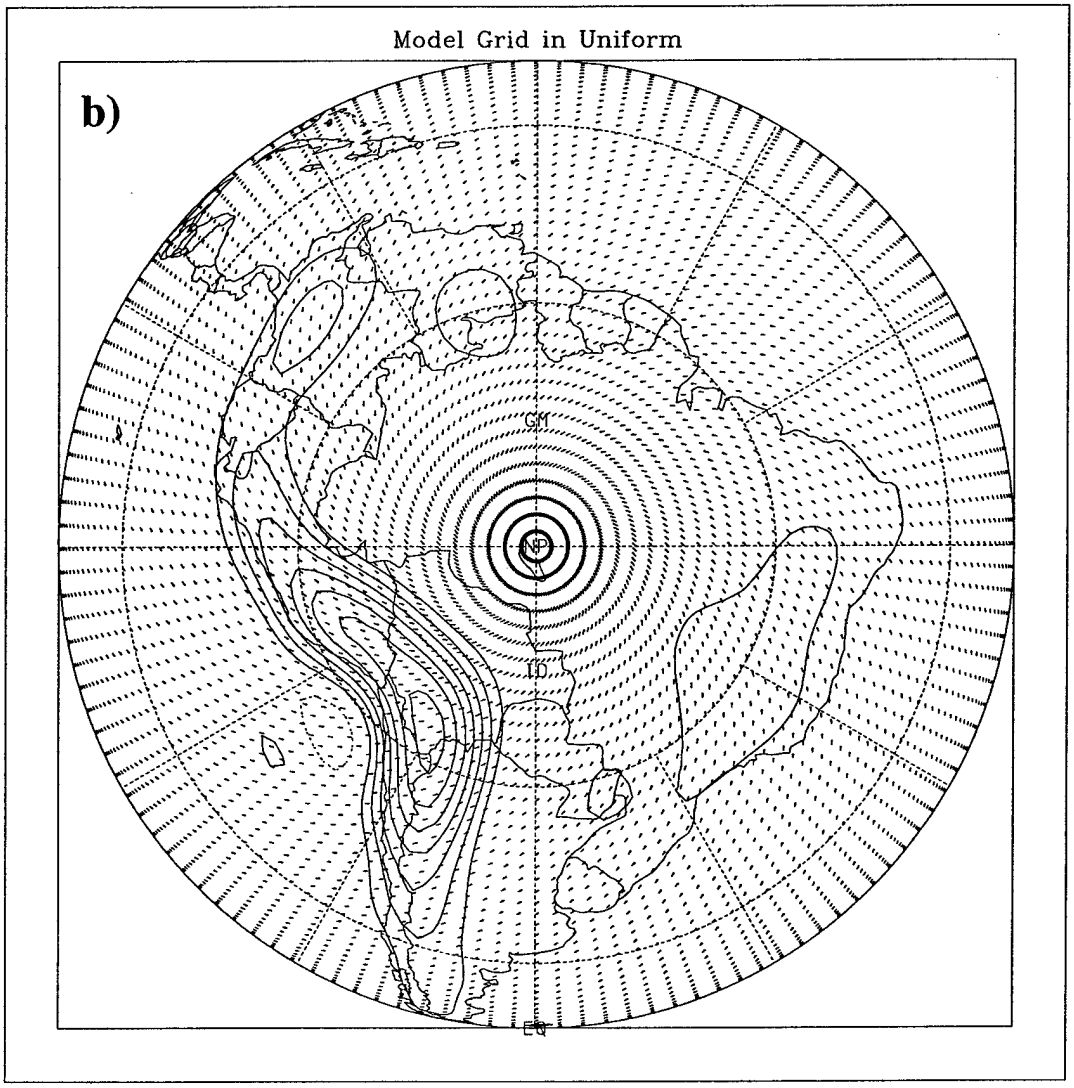


Fig. 3.3, continued.

Results of the former initialization time are described in section 3.4.

For comparison to the experiments which focus upon South America, results which target the NH during winter (section 3.3) are presented first. These contrast with experiments done previously at uniform resolution with the UGM by MMP01. Here, the same version of the UGM is employed, with the mathematical north pole centered over the northeast Pacific Ocean (31°N, 152°W). The simulations are initialized at 12 UTC, 2 February 2003.

The time step is 400 seconds. Surface latent heat flux is specified over the globe using the 49-year, NCEP/NCAR Reanalysis monthly average corresponding to the month the integrations are initialized (January or February). Graphical representation of model output requires interpolation to a uniform, 1° resolution global grid.

### 3.2.3 Experiment Design

The approach is to first initialize the model with coarse resolution analyses in a control integration, and to subsequently replace these coarse analyses with higher resolution analyses. The higher resolution initial state transplants are performed globally, and in separate experiments that target the South American (northeast Pacific) sector as well as all regions outside South America (outside the northeast Pacific). The switch from Reanalysis to GDAS initial states is performed in selected regions to study the potential predictability impact of initial state changes in different portions of the globe, including some that correspond to the South American sector within which analyses may be influenced by the SALLJEX and PACS-SONET observations. Results are compared to similar experiments conducted over the NH during winter (e.g., MMP01). This new work uses the variable resolution approach and higher resolution GDAS initial data, allowing more sensitivity to ini-

tial state refinements than was found by MMP01.

### 3.3 Initial Data Changes Over Northeast Pacific

The initial conditions of the control experiment (from the NCEP Reanalysis) are perturbed by changing them to GDAS analyses over a zone of the northeast Pacific that extends in a 20° latitudinal radius around the mathematical north pole (31°N, 152°W). The change from Reanalysis to GDAS is done smoothly with five grid points of linear transition from 66°N to 71°N of the mathematical grid. The region extends from approximately 10°N to just south of the Aleutian Island chain (51°N); and from near the dateline to the western coast of North America (Fig. 3.4). The initial time is 17 February 2003 at 12 UTC.

A complementary experiment is also performed where the change in initial state analysis is made over the rest of the globe and external to the northeast Pacific Ocean. The validation domain is in the region of the box in Fig. 3.4.

Fig. 3.4 portrays the meridional wind differences at sigma level 0.525 between the experiment initialized with the NCEP Reanalysis globally and the GDAS analysis over the northeast Pacific. At the initial time (Fig. 3.4a), differences between the Reanalysis and GDAS are only apparent over the northeast Pacific and gradually diminish to zero over the transition zone. Differences peak at about 10 m/s. After 96 hours, differences are found mainly outside of the domain and eastward, and peak values have decreased (Fig. 3.4b).

Fig. 3.5 displays the differences in the midtroposphere meridional flow between the experiments initialized with the Reanalysis and GDAS globally. Initial differences (Fig. 3.5a) are highest over the Rocky Mountains (near 15 m/s) and in the Gulf of Alaska (near 12 m/s). Differences after 96 hours have similar magnitudes (Fig. 3.5b).

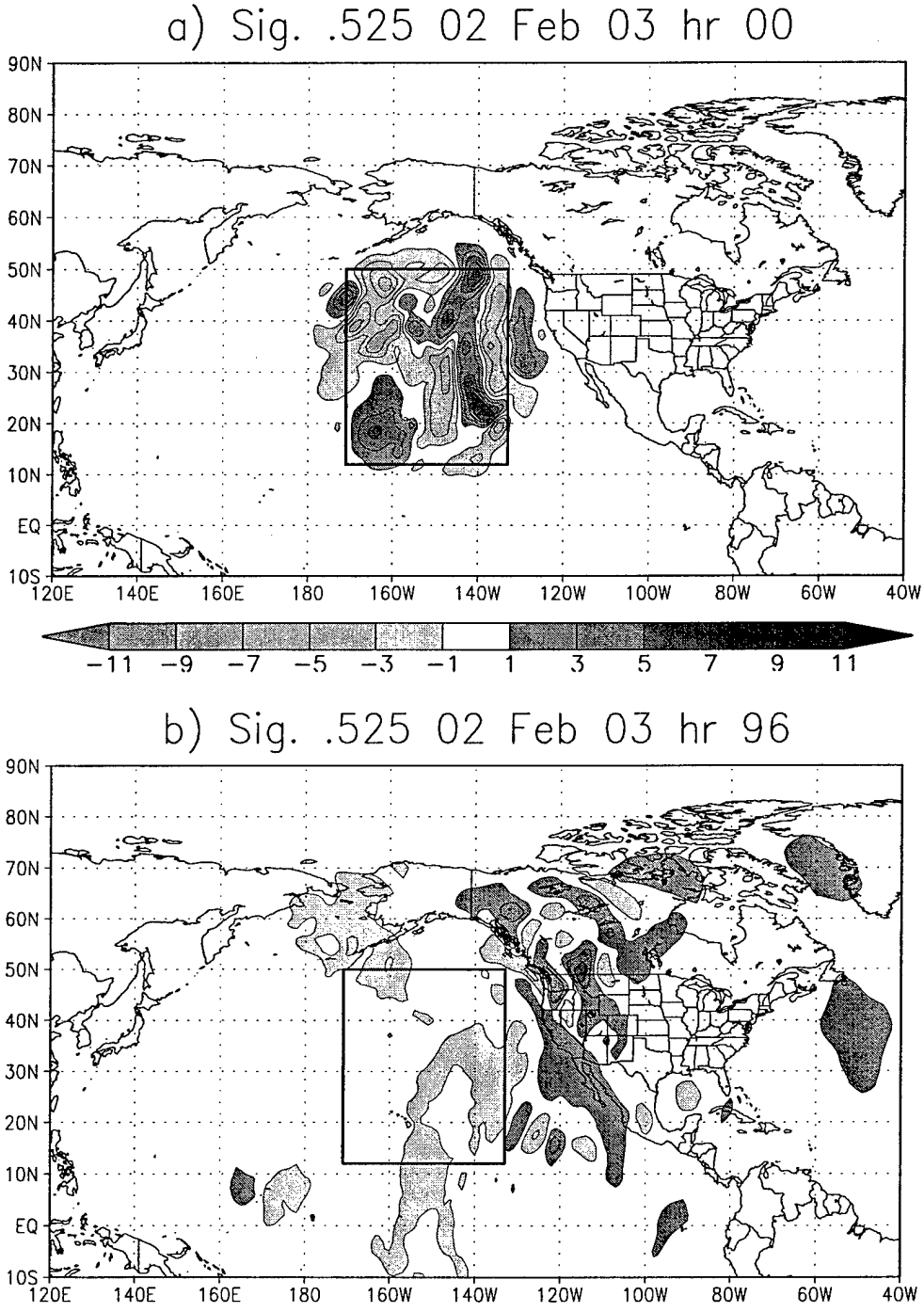


FIG. 3.4. Meridional flow differences at sigma 0.525 between the experiment with initial uncertainty (NCEP Reanalysis minus GDAS) over the northeast Pacific and the control, intialized with the NCEP Reanalysis globally. (a) Initial time, and (b) forecast hour 96. Units are m/s and the contour interval is 2 m/s. The sign of values is indicated with shading. The validation domain is outlined.

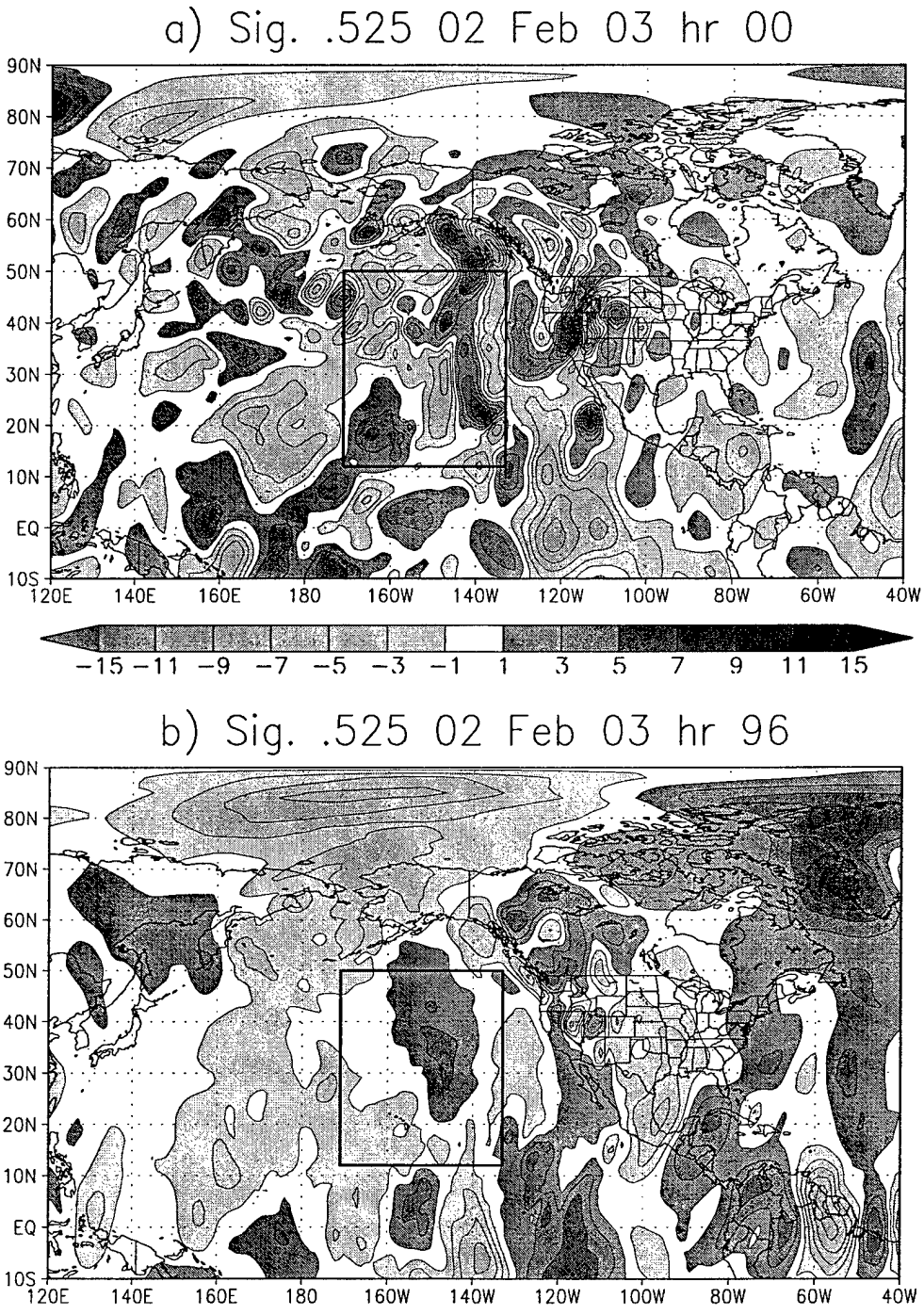


FIG. 3.5. Meridional flow differences at sigma 0.525 between the experiment with initial uncertainty (NCEP Reanalysis minus GDAS) over the whole globe and the control, intialized with the NCEP Reanalysis globally. (a) Initial time, and (b) forecast hour 96. Units are m/s and the contour interval is 2 m/s. The sign of values is indicated with shading. The validation domain is outlined.

The next experiment uses the NCEP Reanalysis within the northeast Pacific region and the GDAS analysis outside this zone for the initial state. Differences in meridional flow at sigma 0.525, relative to the control (NCEP Reanalysis), are presented in Fig. 3.6. At the initial time (Fig. 3.6a) differences are zero over the northeast Pacific. Differences at 96 hours (Fig. 3.6b) look very similar to the pattern of Fig. 3.5b, which shows the differences in the forecast when the initial data change is made globally.

The initial, regional data change over the northeast Pacific (Fig. 3.4a) represents a small contribution to the total, global forecast differences after 96 hours (compare Fig. 3.4b and Fig. 3.5b). The complementary experiment represents a larger contribution to global forecast differences after 96 hours (Fig. 3.6b). Results therefore support the similar conclusion of MMP01: that the initial state modifications made over the northeast Pacific are not as important as initial state differences external to the region at 96 hours, even in the new rotated, variable resolution case using GDAS analyses.

The forecasts of the experiments relative to the control are quantified with variances computed over the northeast Pacific validation domain:

$$\text{variance} = \frac{\int_A (v_s - v_{con})^2 DA}{\int_A DA}, \tag{3.3}$$

where A is the area of the validation (northeast Pacific region; e.g., box in Fig. 3.4a), $v_s$ is the meridional wind component for the considered experiment and $v_{con}$ for the control, which uses initial data globally from the NCEP/NCAR Reanalysis.

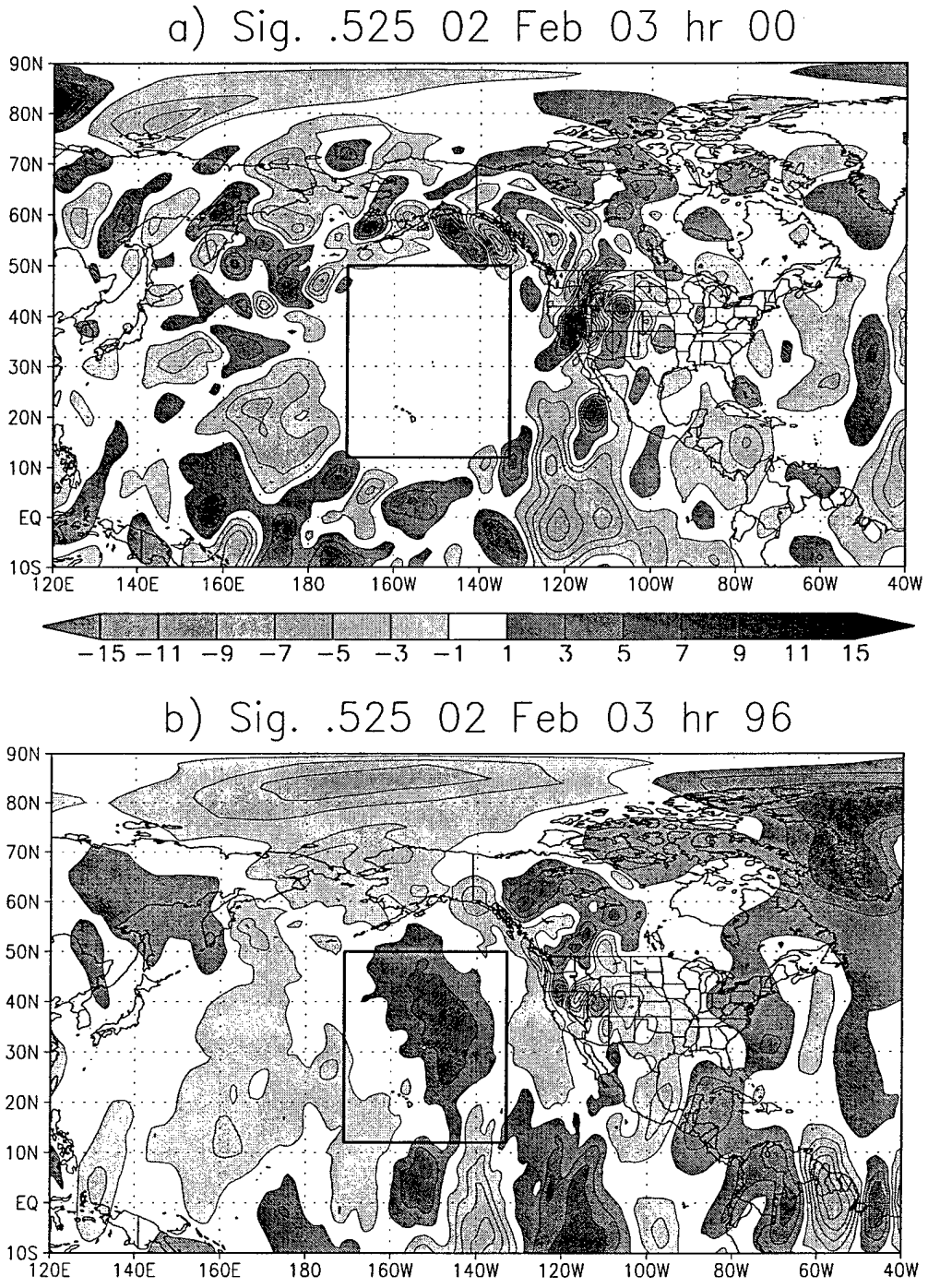


FIG. 3.6. Meridional flow differences at sigma 0.525 between the experiment with initial uncertainty (NCEP Reanalysis minus GDAS) outside the northeast Pacific and the control, intialized with the NCEP Reanalysis globally. (a) Initial time, and (b) forecast hour 96. Units are m/s and the contour interval is 2 m/s. The sign of values is indicated with shading. The validation domain is outlined.

Fig. 3.7 shows variances at sigma 0.525 of the meridional wind. The solid curve is for the experiment with the global initial data change. It exhibits no growth through about the first 3 days of the forecast. The dotted curve with solid circles represents the experiment with the initial data change over the northeast Pacific. The variance is equal to that of the global difference experiment at the initial time, and it subsequently decreases to near 0 after 60 hours.

The variance of the meridional flow for the experiment with initial uncertainty outside the northeast Pacific is given by the dotted curve with open circles (Fig. 3.7). It is 0 at the initial time, and increases to equal the effect of the regional data change experiment after about 24 hours. It gradually increases after 48 hours and evolves similarly to the experiment with initial data changes made globally. Similar diagnostics are now applied for the experiments that target South America.

## 3.4 Initial Data Changes Over South America

Fig. 3.8 shows meridional wind differences for the regional targeting experiment where the data is switched from the Reanalysis to GDAS over South America. The mathematical pole of the UGM has been rotated to southwestern Brazil for these experiments (10°S, 60°W). Differences in the low-level meridional flow (sigma 0.875) are also presented (Fig. 3.8b). Initial differences peak at about 7 m/s at both atmospheric levels around South America, and they become zero outside of the transition zone. After 96 hours, maximum differences are near 9 m/s and are situated mainly within the targeted region of South America (Fig. 3.8c and d). Forecast differences to the southeast of South America continue evolving downstream in the subtropics beyond 4 days (not shown).

Fig. 3.9 displays the differences in the midtroposphere and low-level meridional flow

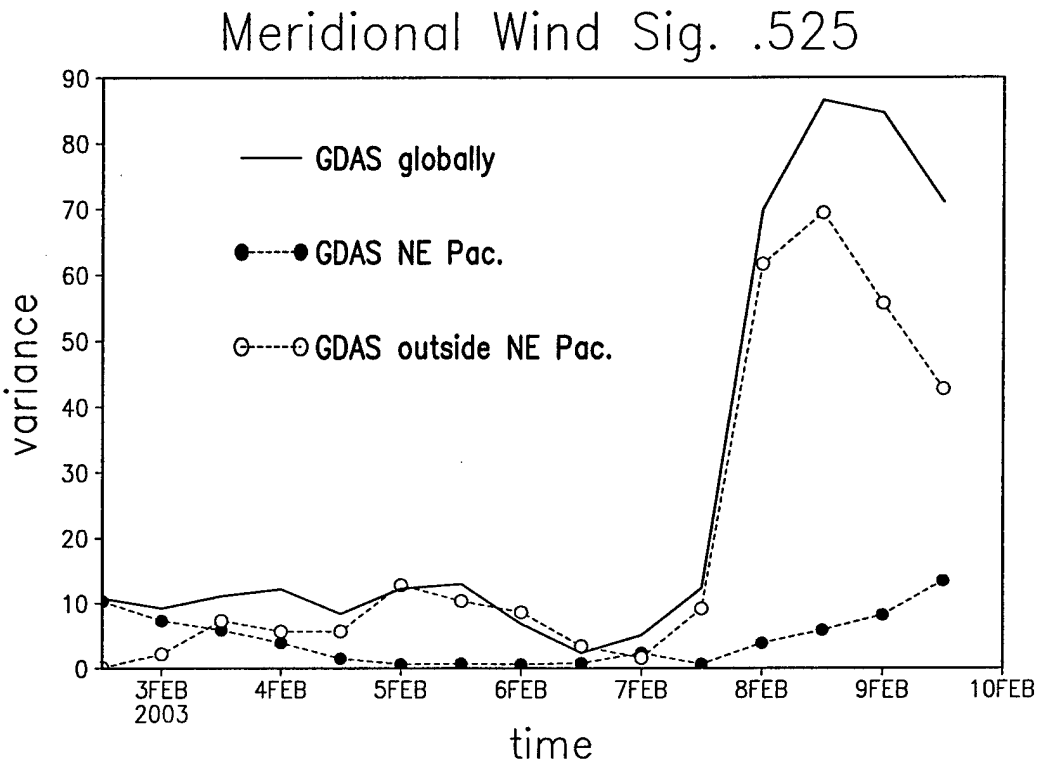


FIG. 3.7. Variance of the meridional wind at sigma 0.525 computed over the northeast Pacific domain. The solid curve shows the variance with respect to the control (initialized with the NCEP/NCAR Reanalysis, globally) for the experiment initialized globally with the GDAS analysis. Dotted curves are for the experiment with initial uncertainty over the northeast Pacific region (closed circles), and the complementary case, perturbing the rest of the globe (open circles). Units are (m*m)/(s*s).

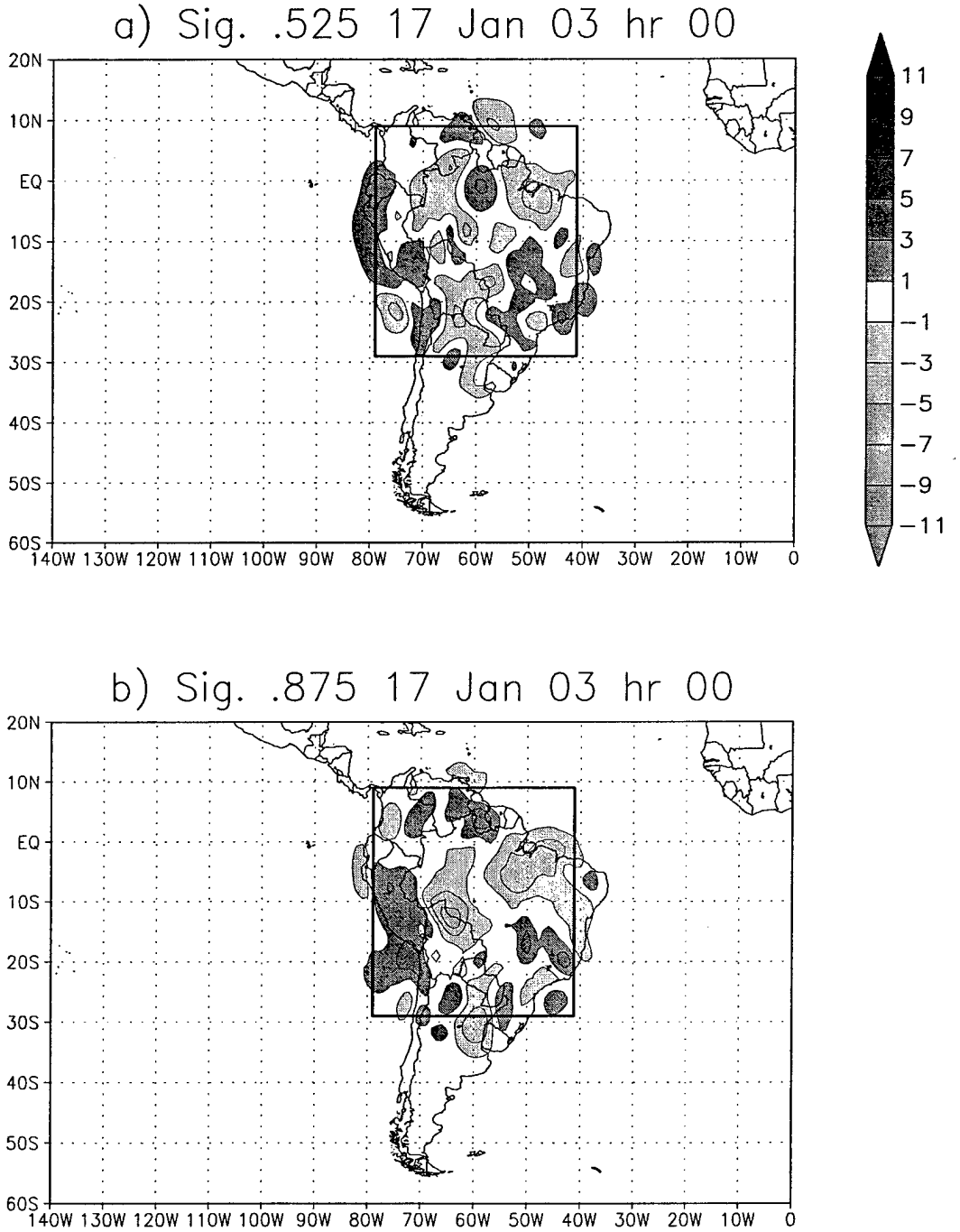


FIG. 3.8. Meridional flow differences between the experiment with initial uncertainty (NCEP Reanalysis minus GDAS) over South America and the control, intialized with the NCEP Reanalysis globally. (a) Initial time, sigma 0.525; (b) initial time, sigma 0.875; (c) forecast hour 96, sigma 0.525 and (d) forecast hour 96, sigma 0.875. Units are m/s and the contour interval is 2 m/s. The sign of values is indicated with shading. The validation domain is outlined.

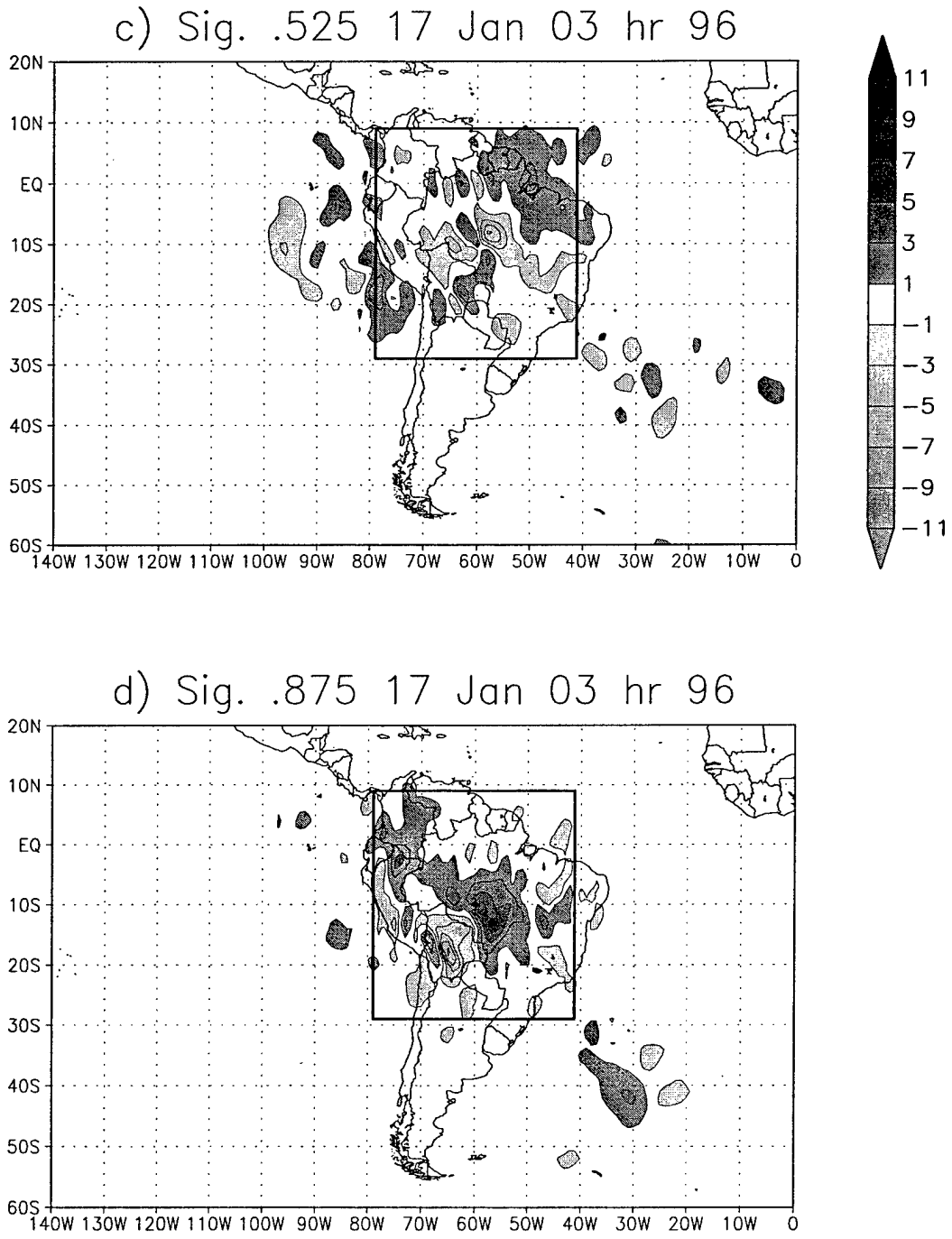


Fig. 3.8, continued.

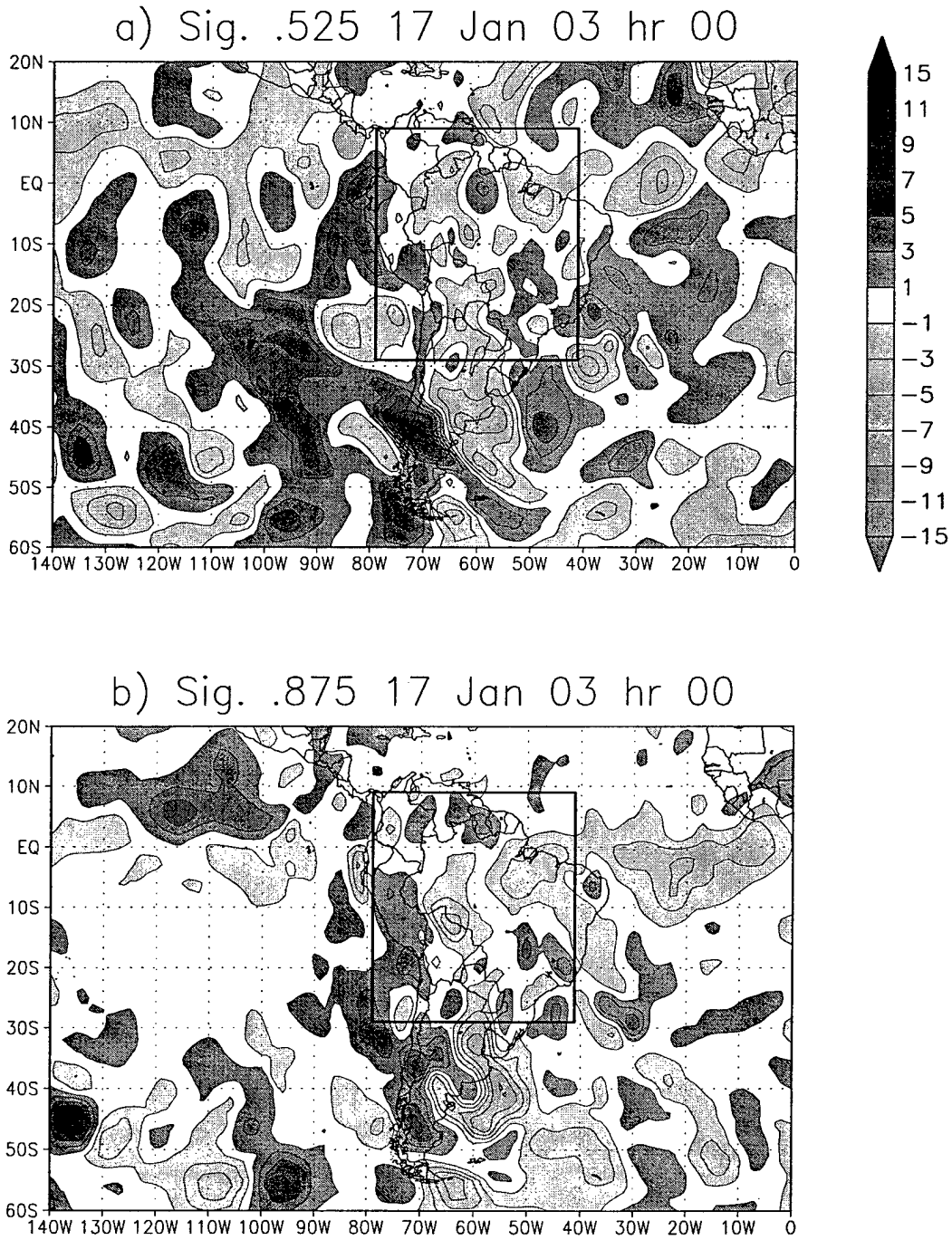


FIG. 3.9. Meridional flow differences between the experiment with initial uncertainty (NCEP Reanalysis minus GDAS) over the whole globe and the control, intialized with the NCEP Reanalysis globally. (a) Initial time, sigma 0.525; (b) initial time, sigma 0.875; (c) forecast hour 96, sigma 0.525 and (d) forecast hour 96, sigma 0.875. Units are m/s and the contour interval is 2 m/s. The sign of values is indicated with shading. The validation domain is outlined.

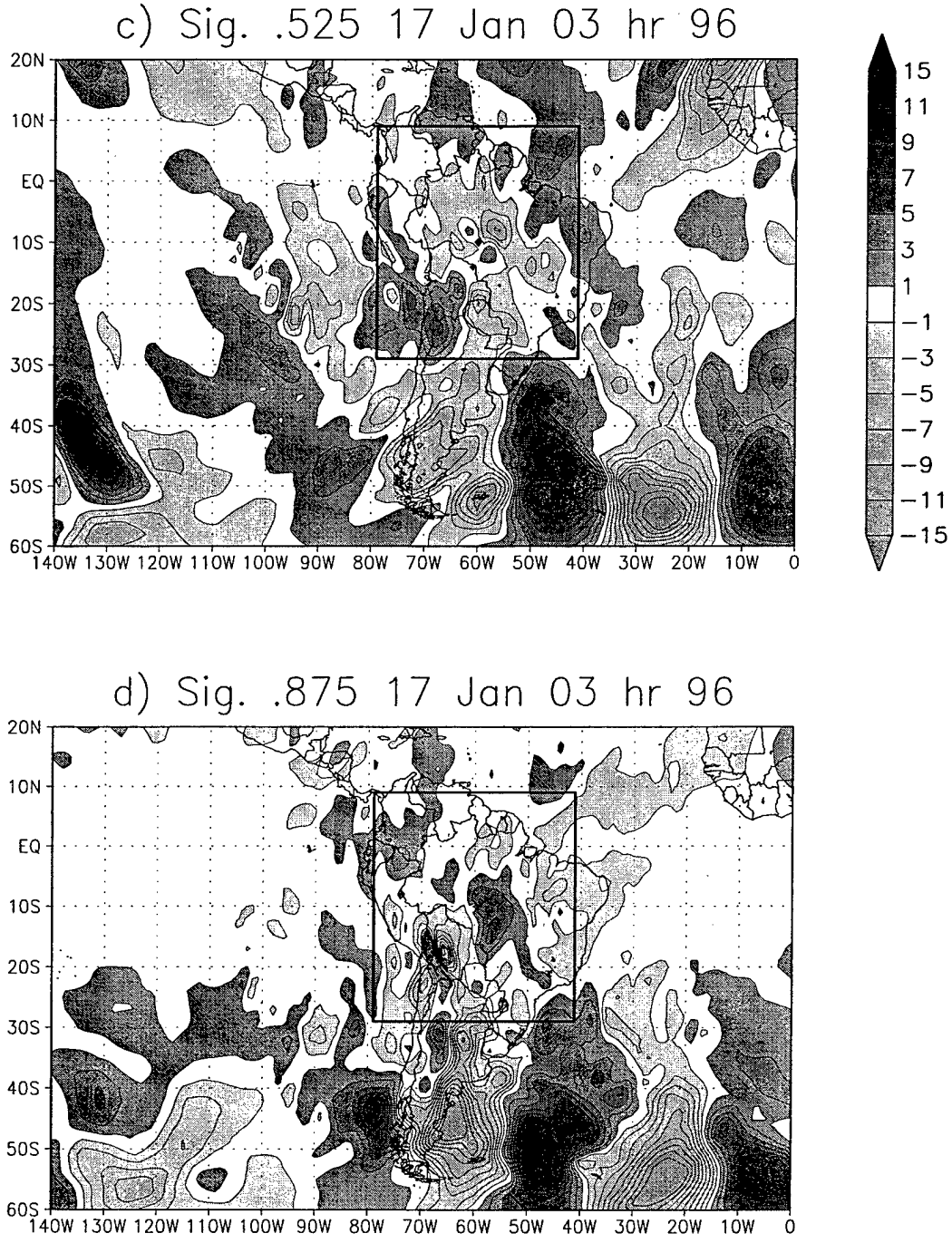


Fig. 3.9, continued.

between the experiments initialized on 17 January with the Reanalysis and GDAS globally (Reanalysis minus GDAS). At forecast hour 96, differences are near 17 m/s in some mid-latitude locations in both the mid and lower troposphere (Fig. 3.9c and d). The magnitudes of the differences over South America are generally comparable to those at the initial time, with the exception of the Andes region in the lower troposphere (Fig. 3.9d).

Complementary experiments to those which target uncertainty over South America are displayed in Fig. 3.10. The initial data change between the Reanalysis and GDAS is made outside of the South American region. The forecast difference with respect to the control is therefore zero over the South American region. Initial differences are largest near 40°S over South America (Fig. 3.10a and b), in the vicinity of troughs analyzed in the mid and lower troposphere by the Reanalysis (not shown). After 96 hours, peak forecast differences are in the midlatitudes (Fig. 3.10c and d). Compared to the winter cases of section 3.3, the experiments with initial uncertainty inside and outside of South America (Fig. 3.8c and Fig. 3.10c, respectively) both produce similar response magnitudes as does the experiment in which initial uncertainty is prescribed globally (Fig. 3.9c). In the lower troposphere of the simulation with uncertainty outside of South America (Fig. 3.10d), the contributions to the global, meridional wind differences (Fig. 3.9d) are somewhat smaller, locally, compared to forecast differences for the experiment with initial uncertainty targeting South America (Fig. 3.8d). Results suggest that initial, local data changes over South America may affect the lower troposphere forecast evolution for a longer time when compared to targeted winter cases of the NH (section 3.3).

Forecast differences are quantified in Fig. 3.11 as in section 3.3 (see equation 3.3) with variances computed over the South American region (e.g., box in Fig. 3.8a). Fig. 3.11a

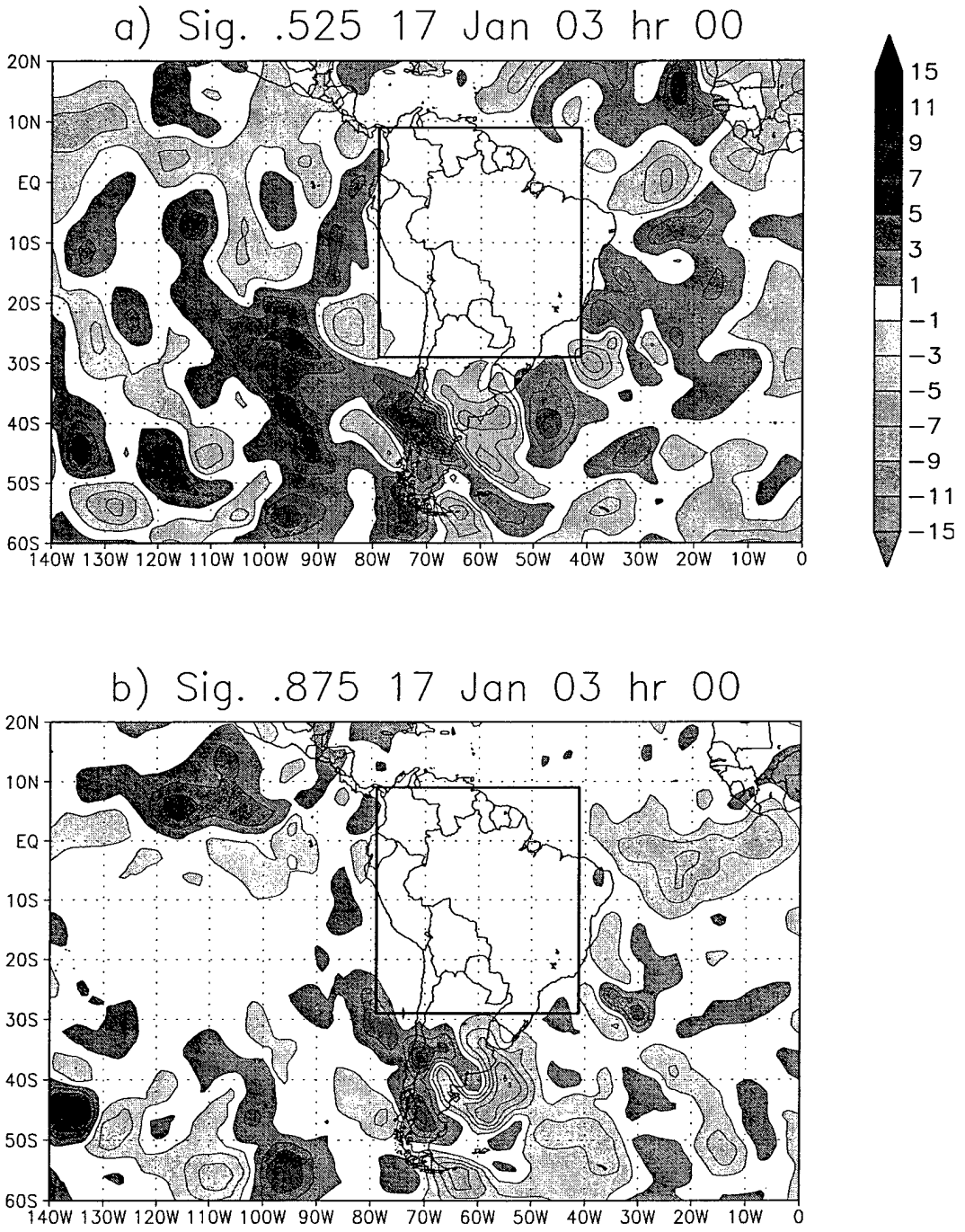


FIG. 3.10. Meridional flow differences between the experiment with initial uncertainty (NCEP Reanalysis minus GDAS) outside of South America and the control, intialized with the NCEP Reanalysis globally. (a) Initial time, sigma 0.525; (b) initial time, sigma 0.875; (c) forecast hour 96, sigma 0.525 and (d) forecast hour 96, sigma 0.875. Units are m/s and the contour interval is 2 m/s. The sign of values is indicated with shading. The validation domain is outlined.

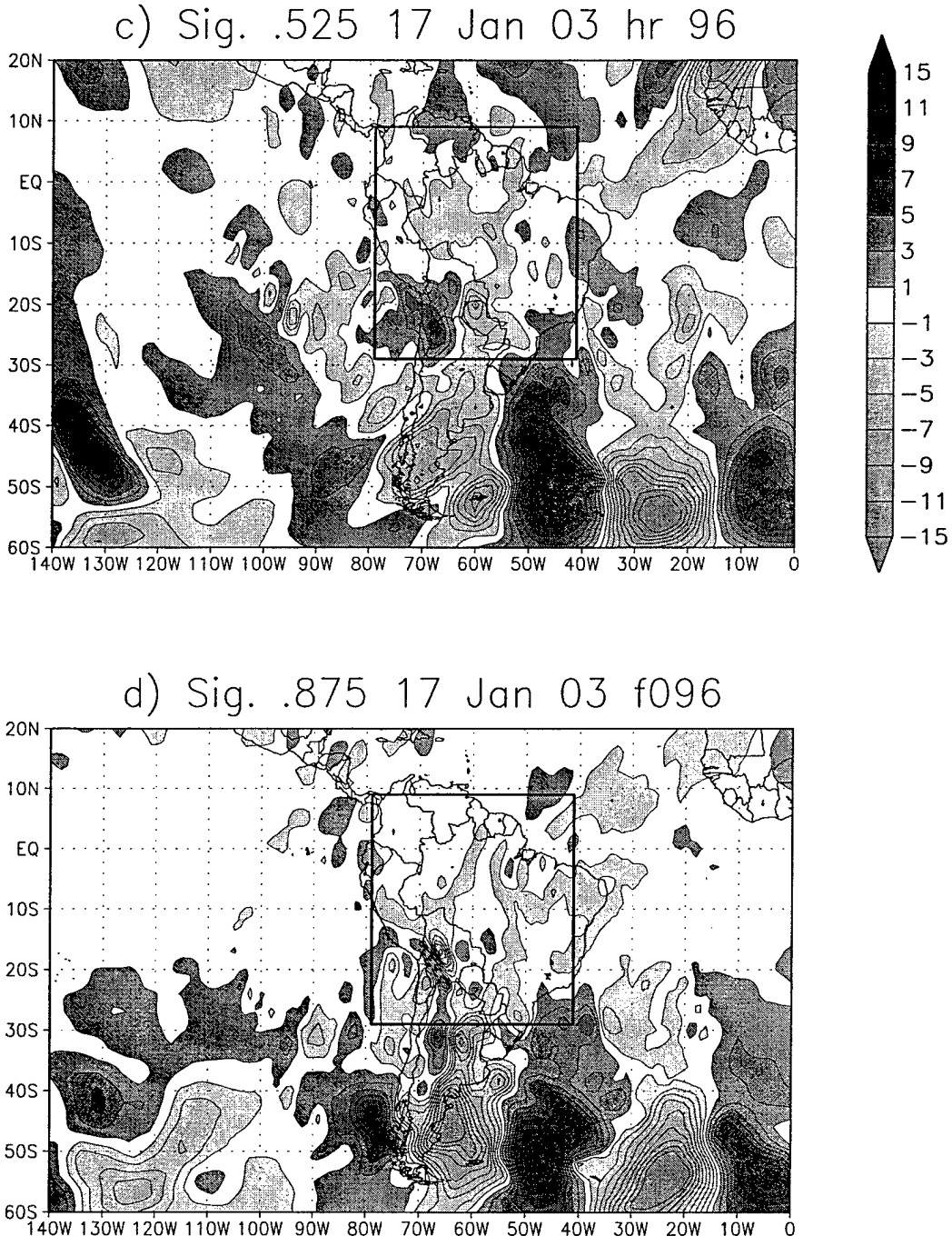


Fig. 3.10, continued.

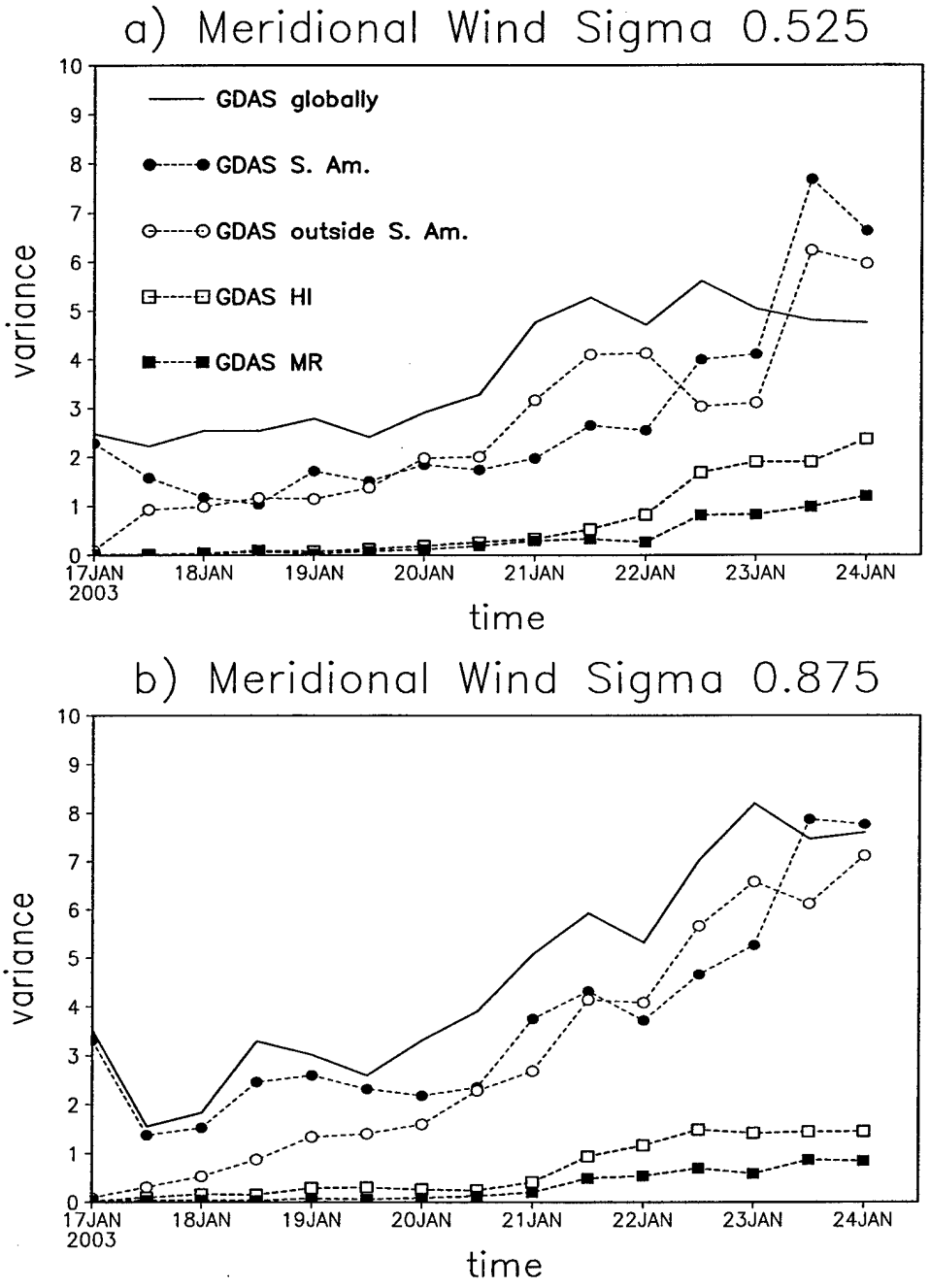


FIG. 3.11. Variance computed over the South American domain. (a) Meridional wind at (a) sigma 0.525, and (b) sigma 0.875, and (c) specific humidity at sigma 0.875. The solid curve shows variance for the experiment initialized globally from the GDAS analysis. Dashed curves with circles are for the experiment with initial uncertainty over the South American region (closed) and the complementary case, perturbing the rest of the globe (open). Curves with boxes are for the experiments which test numerical sensitivity, described in the text. Units are (m*m)/(s*s) in (a) and (b) and (g*g)/(kg*kg) in (c).

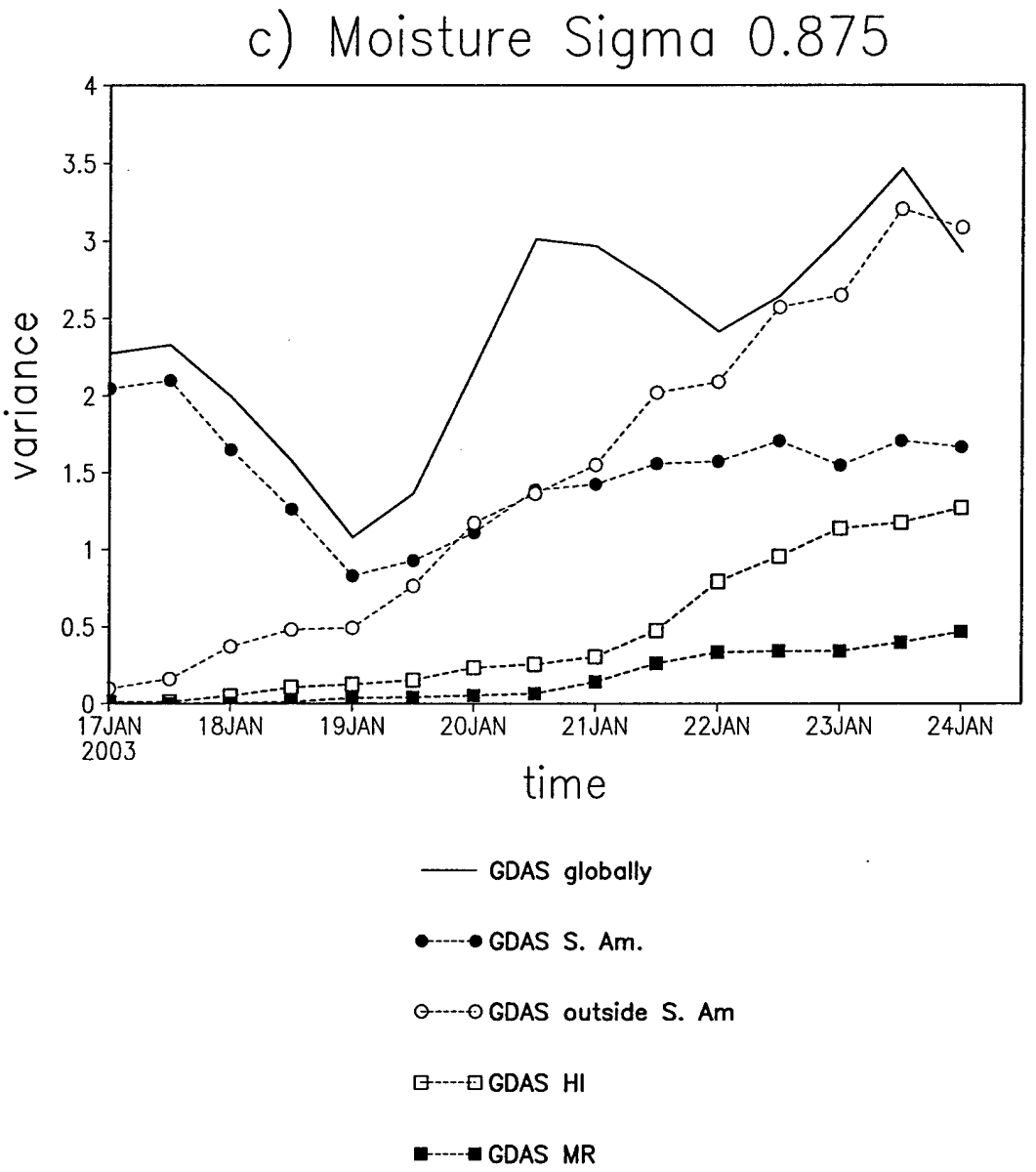


Fig. 3.11, continued.

shows the variance in the meridional wind at sigma 0.525. The solid line represents the difference between experiments initialized globally with the Reanalysis and GDAS. The variance increases steadily through most of the forecast. The experiment in which the switch from Reanalysis to GDAS is done over South America (solid circles) has similar magnitude as the global data change experiment at hour 0 and steadily decreases through the first 36 hours. Variance for the experiment in which that data is changed from Reanalysis to GDAS externally to South America is depicted as open circles. The curves for the two latter experiments (solid circles and open circles) evolve similarly in the midtroposphere from about day 1 to day 3.5 (Fig. 3.11a).

Results for the lower troposphere meridional wind and specific humidity variance are plotted in Figs. 3.11b and c. Initial state changes made locally (solid circles) contribute at least as much as or more to the total variance through the first 4 to 4.5 days of prediction as in the case where initial data changes occur outside of South America (open circles) (Fig. 3.11b). The impact of the local specification on moisture predicted at sigma level 0.875 is also evident through the first 4 days of prediction (Fig. 3.11c).

Curves containing boxes represent the variance evolution for additional experiments which examine the impact of numerical irregularities that may arise in the rotated, variable resolution approach. The "control" run for these experiments is the same configuration as in all previously described experiments except it uses the GDAS analysis globally instead of the NCEP Reanalysis.

The curve labelled "GDAS MR" (solid boxes, Fig. 3.11) is for an experiment initialized with GDAS analyses over the globe, and the north pole is located over southwest Brazil (as in all previous runs); but it has higher resolution in latitude, using 141 points (as

opposed to 91 in the control). Therefore, the higher resolution (1°) inner nest covers a larger region (1 hemisphere), and the perimeter of the two-way nest is more distant from the region of concern. The resolution is 1.8° outside of this hemispheric cup. Forecast differences between this experiment and the control quantify the impact of the abrupt resolution change in latitude which occurs in the control run. The transition in the control is from a 1°, inner nest, to a 3°, outer global region, taking place at 45° of the mathematical pole. As in previous experiments, the output for each simulation is interpolated to a uniform, 1° global grid to examine the differences. Evolution of the "GDAS MR" curve for each of the variables in Fig. 3.11 suggests that the impact of the abrupt transition zone is minimal relative to impacts in the other experiments.

The curve labelled "GDAS HI" (open boxes, Fig. 3.11) is an experiment in which the configuration in latitude is that same as "GDAS MR," but the resolution in longitude is also increased to 257 equally spaced points, corresponding to 1.4° longitude resolution. A measure of the variance in this experiment with respect to the same control as "GDAS MR" (GDAS globally) provides a further measure of the impact of the abrupt transition zone in latitude of the control. As with "GDAS MR," the variance is small relative to that in other experiments. The variance increases in both the mid and lower troposphere beyond day 4 of the forecast (Fig. 3.11a-c), but it remains below the sensitivity of the other experiments through day 7. It is concluded that numerical methods associated with the rotated pole, variable resolution approach do not produce notable distortion, and that results do not change strongly with resolution enhancement.

## 3.5 Discussion

Saulo et al. (2001) show relatively slow growth of forecast errors over South America. In some instances and locations, short term forecast errors of the MRF were found by Saulo et al. (2001) to be smaller than analysis errors. One possible interpretation of this result is that the initial state errors here are so large that they are not substantially exceeded by forecast errors in short term predictions. Another possibility is that other components of the forecast problem such as complex orography, a rainforest with poorly specified land use properties, and tropical convection, are of overwhelming importance. Finally, lateral boundary conditions may have constrained the sensitivity of those experiments. Related uncertainties may strongly constrain predictability even with accurate specification of the atmospheric state. This chapter presents results of preliminary experiments which examine the importance of initial state detail over and around the region during summer in a global model. During the summer wet season, the lower troposphere has particular significance through its role in water vapor transport, such as the moisture corridor the east Andes LLJ provides between the Amazon and La Plata region.

The 17 January experiments suggest that forecasts of lower troposphere winds are strongly influenced by detail of the initial state specification over South America through about the first 4-5 days of prediction. On the other hand, marked sensitivity of uncertainty impact is found for different synoptic situations used for the initialization, such as the case initialized on 30 January (not shown). Experiments for 30 January contain less variance in moisture and low-level wind over South America, and the influence of local targeting relative to external targeting is about the same from about day 2-4 (not shown).

The small case sampling does not suffice to systematically quantify the importance of

initial conditions over the SALLJEX region. They do suggest that initial information over South America may be at least as important as initial state specification outside the region in some events (section 3.4), and this was never the case in MMP01. The latter study constitutes 34 different NH, midlatitude, winter cases. Preliminary results of this chapter imply an important role for in-situ observations for both the description and prediction of the regional and continental-scale hydrologic cycle over South America.

Tests for numerical irregularities associated with the rotated, variable resolution UGM have not been previously documented. Variance evolution of various model configurations has been used to quantify the impacts for the cases targeting South America. Results suggest the feasibility of the present rotated, two-way nest approach for these time scales, and support the utility of the method in present applications. Similar tests examining a rotated, global variable resolution set-up have been documented by Coté et al. (1998b). Their method rotates the mathematical poles away from the inner nest, producing a more isotropic subregion. They find "acceptably small" differences between rotated and uniform simulations over and around the inner domain at the 48-hour point (see their Fig. 7). UGM results also suggest that the chosen modeling technique is not as important as the seasonality or data sparsity over the targeted regions. Repeating the experiments of MMP01 over northern midlatitudes during winter with the rotated approach yields similar results to the earlier, unrotated experiments (section 3.3).

The next chapter shifts focus to North America during the summer season. It will propose that intraseasonal, seasonal, and interannual variations of the Great Plains LLJ may be partly explained by variations of ambient zonal flows over the Rockies. Following the theory described in Chapter 2, it is suggested that the Rockies induce an orographically

bound lower troposphere cyclone in summer, as found around the Andes.

# CHAPTER 4

# MODULATION OF THE GREAT PLAINS LOW-LEVEL JET

## 4.1 Introduction

This chapter is related to past studies by Mo et al. (1995) and Wang et al. (1999) that examined extended range influences on the atmospheric portion of the hydrologic cycle over the Global Energy and Water Cycle Experiment (GEWEX) Continental-Scale International Project (GCIP) domain. Mo et al. (1995) examined the onset and maintenance of the 1993 summer floods using Eliassen-Palm fluxes. They suggested that an anomalously strong westerly flow over the Rocky Mountains was maintained by low-pass filtered eddies over the North Pacific, and that orographic effects accelerated a cyclonic pattern in the vicinity of the Rocky Mountains. These features supported a strong southerly low-level jet (LLJ) east of the mountains and accelerated the influx of water vapor from the Gulf of Mexico toward the upper and central Mississippi River basins.

The first goal is to examine the role of this mechanism in climatological correlations of cross-Rockies zonal flows with the hydrological cycle over North America. Section 4.2 uses monthly averaged NCEP/NCAR Reanalyses to demonstrate that the Great Plains LLJ during summer, related water vapor transports, and Mississippi River basin (MRB) rains tend to increase during extended periods of anomalously strong zonal flow over the western United States.

The correlations suggest that an orographically bound cyclonic acceleration occurs over the western U.S. when the summer, upper troposphere zonal flow is relatively strong

above the Rockies. Similar correlations are found between the midlatitude zonal index averaged over the full latitude circle and orographically bound cyclones in summer. Section 4.3 presents 13-day, ensemble simulations using the Utah Global Model (UGM) for summer 1993 and 1988, which investigate predictability over the MRB for these years of extensive zonal flow anomalies. It is hypothesized that the long term inertia of the global-scale wind anomaly may extend the period of predictability.

Many other predictability studies for the floods of 1993 and droughts of 1988 have emphasized land-surface parameterizations. Within the 1999 GCIP special issue of the *Journal of Geophysical Research*, at least 15 articles and references therein examined the important role of land-surface processes and energy budgets upon precipitation over the continental United States. At least eight of these investigations are modelling studies of the 1993 floods and 1988 drought, and the majority emphasize monthly to seasonal integrations. Beljaars et al. (1996) found better forecast skill for month long simulations resides in the representation of soil moisture and strong feedbacks between the land surface hydrology and precipitation. Viterbo and Betts (1999) used July ensemble forecasts with the European Center for Medium Range Weather Forecasts (ECMWF) system and found large soil water anomalies contributed to the July 1993 flooding. Replacing the July 1993 soil water with soil water from June 1988 in the ensemble forecast reduced the precipitation anomaly by 40%. Other studies have considered the important role of sea surface temperature (SST) anomalies and other remote teleconnections influencing regional and local flow anomalies (e.g., severe drought) over the Great Plains (e.g., Namias, 1983; Trenberth et al., 1988; Namias, 1991; Mo et al., 1991; and Trenberth and Branstator, 1992). Bell and Janowiak (1995) found a strong relationship between anomalous SSTs during the warm 1992-93 ENSO and the extratropical circulations which contributed to

the summer 1993 floods over the Midwest. The present study takes a similar approach to the studies listed above with emphasis on dynamical processes associated with ambient flows over the Rocky Mountains.

Section 4.4 examines some dynamical implications of Mo et al.'s (1995) hypothesis that the 1993 MRB floods in part represent a mechanical, orographic response to the anomalously strong zonal circulation of this period. The single level barotropic analysis used in the Mo et al. (1995) spherical treatment is extended in section 4.4, and results suggest that the summer time flow over North America typically promotes a cyclone in the vicinity of the Rockies. This orographic cyclone may be interpreted as a subresonant response for stationary Rossby waves. A consistent interpretation of the observations and reanalyzed fields (section 4.2) is that increased zonal flow during summer accelerates the orographic vortex as the resonant point in the response is approached.

Section 4.5 presents preliminary evidence that the observed winter to summer reversal of the Great Plains LLJ may also be explained as a reversal from superresonant orographic responses in winter to subresonant responses in summer. This interpretation provides an alternative, mechanical explanation to thermal influences related to surface heating that have often been used to explain observed winter-summer climatological reversals above the Rockies, as well as anomalies from the climatology.

## 4.2 Interannual Variability Over North America

### 4.2.1 The Great Plains Low-Level Jet

All diagnostics, unless noted otherwise, are based on a 50-year record (1951-2000) of monthly averaged circulations from the NCEP/NCAR Reanalysis (Kalnay et al., 1996; Kistler et al., 2001), as in Chapter 2. The assimilation system is based on NCEP's 1995 operational global spectral model with a T62 resolution on 28 vertical sigma levels (~210

km horizontal resolution). Primary fields used here from the Reanalysis are the rotational wind and specific humidity. Kalnay et al. (1996) described the rotational wind as one of the "type A" variables, influenced most strongly by assimilated observations. Specific humidity, used to compute vertically integrated moisture flux, is a "type B" variable, considered somewhat less reliable since both the observational data and the assimilation model affect this quantity. Surface latent heat flux, used for model initialization in section 4.3, is a "type C" variable, derived only from model data.

A 50-year climatology (1951-2000) of 850-mb wind vectors and eddy heights over North America for June to August (JJA) is shown in Fig. 4.1. The eddies are defined by subtracting the zonal average. Most of the Rocky Mountain region lies above the 850-mb level, so Reanalysis data shown there have been artificially interpolated below the surface of the earth and the 850-mb pattern is poorly defined. A significant feature east of the Rockies is the presence of a north-to-south-oriented, southerly LLJ, which extends from the western Gulf of Mexico and Mexico, northward into the Great Plains to about 45°N (Fig. 4.1a). The LLJ is a persistent summer time feature over the Great Plains, and it is absent in the 850-mb winter eddy height and wind fields (Fig. 1.1b). Low-level northerlies off the coast of California turn cyclonically west of Baja California near 25°N.

The first part of the investigation looks at how ambient flows over the Rocky Mountains may relate to the Great Plains LLJ. A 50-year time series of the area averaged, 200-mb zonal flow is calculated over the Rockies during summer (JJA) from 120°W-100°W, 30°N-50°N. The weakest and strongest cases of summer, ambient flow over the Rockies are then selected when the area averaged zonal flow is above or below the 200-mb zonal mean by an amount equaling plus or minus 1.2 times the standard deviation from the mean. These cases explain about 12% of the variance, assuming a Gaussian distribution.

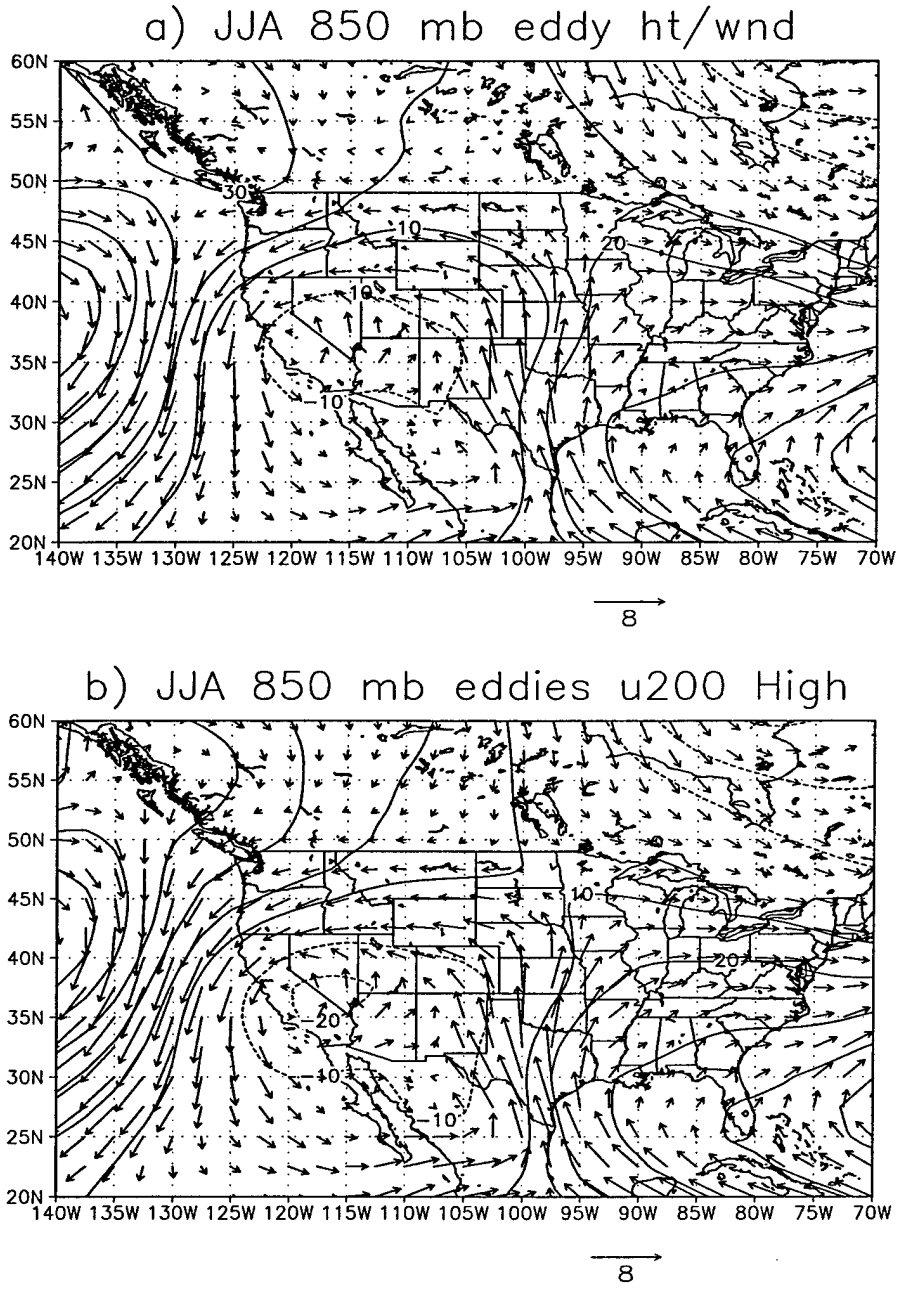


FIG. 4.1. Climatology of the 850-mb eddy heights (m) and wind vectors (m/s) during summer (JJA), from the NCEP/NCAR Reanalysis monthly archive. Eddies are defined by subtracting the zonal average. (a) The 1951-2000 climatology. (b) A composite for the 6 seasons (1951, 58, 78, 80, 92, and 93) in which the area averaged, 200-mb zonal wind over the Rocky Mountains is strongest, as described in the text. (c) A composite for the 6 seasons (1955, 61, 70, 71, 83, and 88) of weakest 200-mb zonal flow over the Rockies. (d) The difference between Figs. 4.1b and 4.1c (4.1b minus 4.1c), which shows the 850-mb circulation differences between the years of highest (Fig. 4.1b) and lowest (Fig. 4.1c) 200-mb zonal flow over the Rocky Mountains.

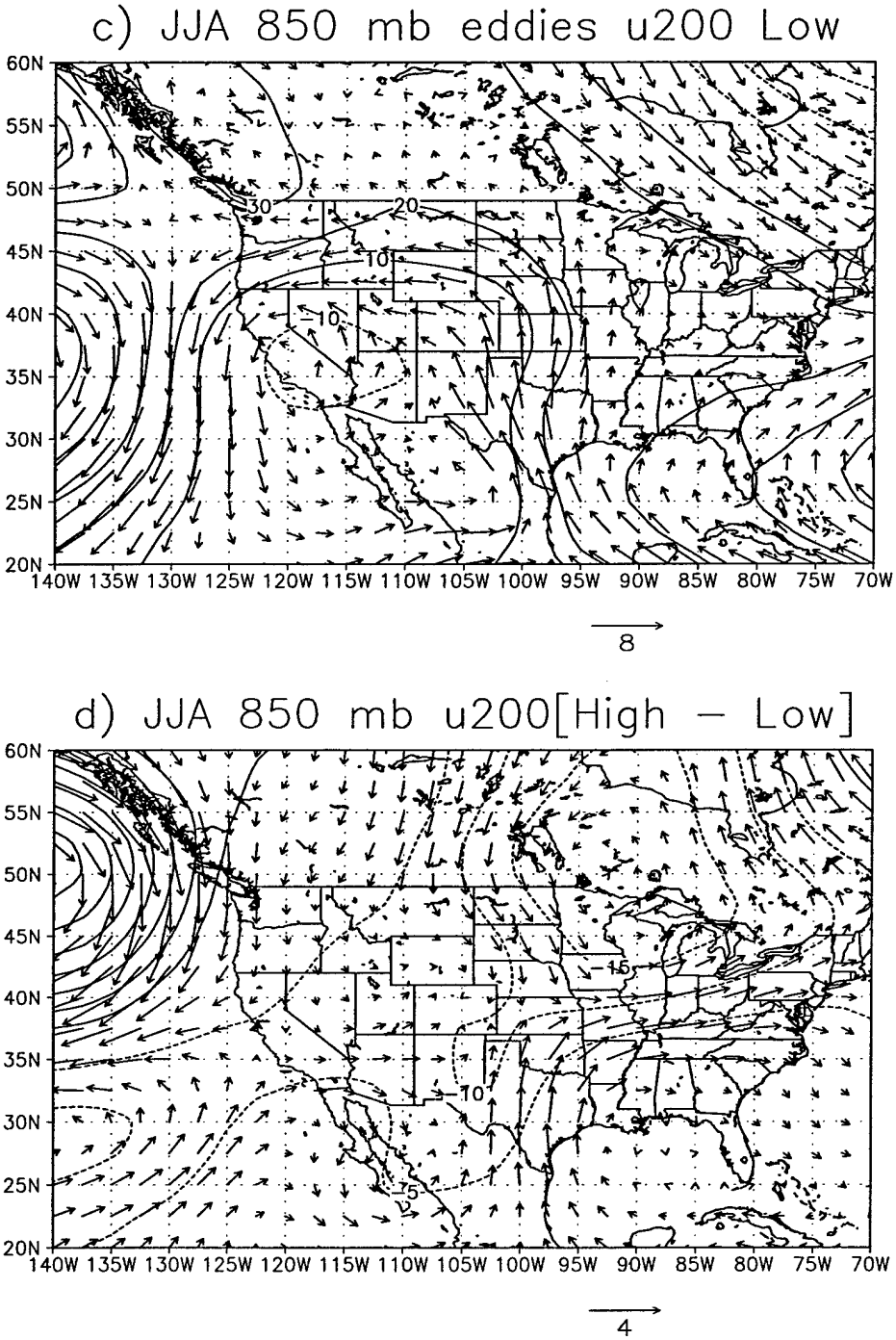


Fig. 4.1, continued.

In the 50-year record, 6 cases meet the criteria for strong events and 6 meet the criteria for weak events.

Fig. 4.1b shows the eddy heights and winds at 850 mb for summers with the strongest 200-mb flow ("u200 high"), and Fig. 4.1c during summers of the weakest 200-mb flow over the region ("u200 low"). U200 high values range from about 18 to 20 m/s, while low cases range from about 11.5 to 13.5 m/s. The selected years are 1951, 1958, 1978, 1980, 1992 and 1993 for u200 high; and 1955, 1961, 1970, 1971, 1983 and 1988 for u200 low. The difference field between u200 high and low cases is presented in Fig. 4.1d. The 850-mb southerlies are almost twice as strong over Texas in the u200 high cases compared to the u200 low cases. The anticylonic circulation near the Gulf of Alaska is more pronounced during u200 high cases, and lower geopotential heights are centered over the northern U.S. and Canada in the difference field (Fig. 4.1d).

Fig. 4.2 shows the vertically integrated, meridional moisture flux for the u200 high and low composites. The highest moisture flux contour is 4 units over Texas for the u200 high cases (Fig. 4.2a), while it is 2.5 units for u200 low cases (Fig. 4.2b). The composite wind difference (Fig. 4.1d) and the moisture flux differences in Fig. 4.2 have similarities to the 850-mb, meridional wind differences between "flood look-alike" (FLA) and "anti-flood look-alike" (AFLA) cases Mo et al. (1995) identified using ECMWF pentad data and synoptic scale features (see their Fig. 13).

Fig. 1.4 shows 50-year (1951-2000) temporal correlations of the local, meridional, 850- mb wind in a box located near the climatological region of the Great Plains LLJ, with gauge precipitation over land. The 850-mb meridional wind is area averaged over the indicated box, extending from 20°N-40°N, and the precipitation is taken from the Global Precipitation Reconstruction Analysis over Land (PREC/L) produced by Chen et al. (2002).

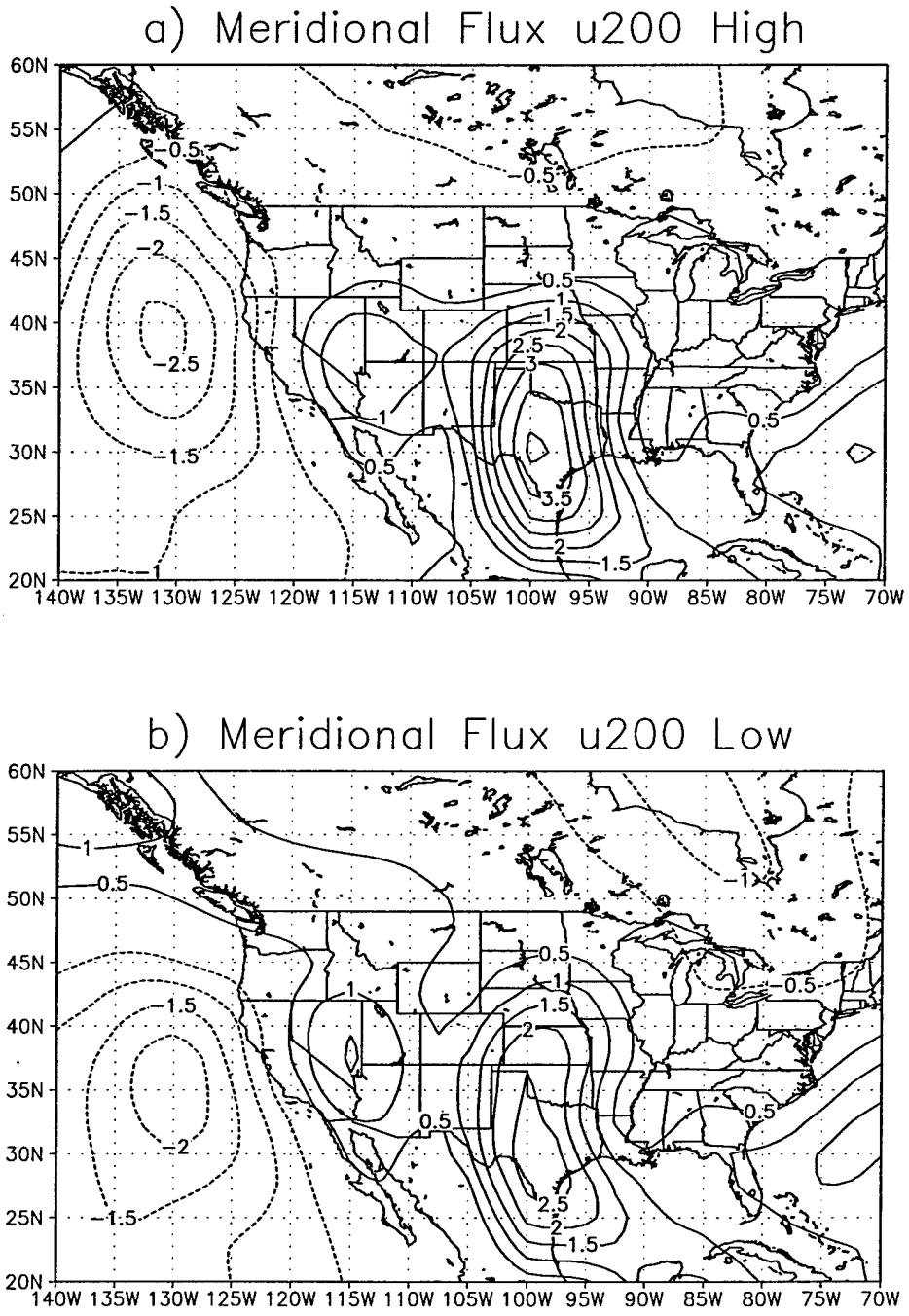


FIG. 4.2. Vertically integrated, meridional moisture flux composites for the selected summers (JJA) of high (a) and low (b) 200-mb zonal flow over the Rockies, as described in Fig. 4.1 and the text. (a) shows the average moisture flux for summer seasons when the area averaged, 200-mb zonal flow over the Rocky Mountains is strongest. (b) As in (a) but for cases of the weakest 200-mb flow over the Rocky Mountains. The contour interval in (a) and (b) is 50 kg*(m/s) and the zero line is omitted.

This uses interpolated gauge observations over land from the Global Historical Climatology Network (GHCN), Version 2. In Fig. 1.4, correlation coefficients of 0.3 and higher are statistically significant at the 99% level for 50° of freedom. Low-level southerlies in the boxed region are strongly correlated with precipitation over the northern U.S. and in the Great Plains and Midwest, with the largest correlation coefficient of 0.7 over Iowa. Highest correlation coefficients are close to the exit region of the climatological LLJ depicted in Fig. 4.1a.

Paegle (1998) briefly summarizes some of the dynamical factors influencing LLJs over the gently sloping topography of the Great Plains, including (1) diurnal, buoyancy-forced oscillations which depend on heating (Holton, 1967); (2) diurnal, frictional effects (Blackadar, 1957); and (3) Wexler's (1961) extension of western boundary dynamics in oceanography as applied to the Great Plains LLJ. Mechanisms (1) and (2) produce nocturnal enhancement of the Great Plains LLJ (e.g., Bonner and Paegle, 1970). Wexler's (1961) theory suggests that the blocking effect of orography influences the strength of the LLJ in association with episodic fluctuations in low-level easterlies within the subtropics that are deflected poleward by the east slope of the North American cordillera.

The present study, by contrast, investigates the strength of the ambient, upper troposphere westerlies impinging upon the Rocky Mountains and their possible association with the strength of the Great Plains LLJ for medium range and longer time scales. Other studies have examined the enhancement of LLJs over the Great Plains and other parts of the U.S. independent of orography and for shorter time scales. Uccellini and Johnson (1979) and Uccellini (1980), for example, found that for synoptic scales, low-level, ageostrophic winds associated with jet streak exit regions may be associated with an enhancement of LLJs, particularly over the Great Plains and eastern North America. The next

subsection examines ambient zonal flows in the upper troposphere and their correlations with wind and moisture fields over the MRB.

### 4.2.2 Correlations with Ambient, Upper Troposphere Flows

Fig 4.3 displays temporal correlations (1951-2000) over North America. The local, 700-mb wind is correlated with the 200-mb zonal flow for the summer average (JJA). The 200-mb zonal flow is area averaged over the indicated box centered over the Rockies and extends from 30°N-50°N. The eastward/northward component of the vectors denotes the magnitude of the correlation coefficient between the area averaged, upper tropospheric wind in the box against the local zonal/meridional flow component at 700 mb. Features at 700 mb over the western U.S. are emphasized, where artificial interpolation below the surface of the earth is not required over most of the region.

An increase in upper tropospheric westerlies in the box during summer (Fig. 4.3a) results in a cyclonic circulation in the correlation vectors at 700 mb over the Rocky Mountain region. The cyclonic tendency over the mountains may therefore be related to an increase in the strength of the westerlies over the mountains. Southwesterly and southerly correlation vectors near the western Gulf of Mexico and Texas apparently converge over the Mississippi River basin (MRB), near northern Missouri. The 700-mb level is generally above the mean height of the Great Plains LLJ. In order to test whether the correlations of ambient zonal flow over the Rockies may relate to the LLJ, similar correlations with vertically integrated moisture flux and with winds at 850 mb are discussed below.

Fig. 4.3b shows time correlations of the local, vertically integrated moisture flux with ambient, 200-mb zonal flow within the boxed region. Only vectors that are statistically significant at the 99% level (0.3) are plotted, and the statistically significant, meridional coefficients are contoured. Over the western U.S., the pattern is similar to the correlations

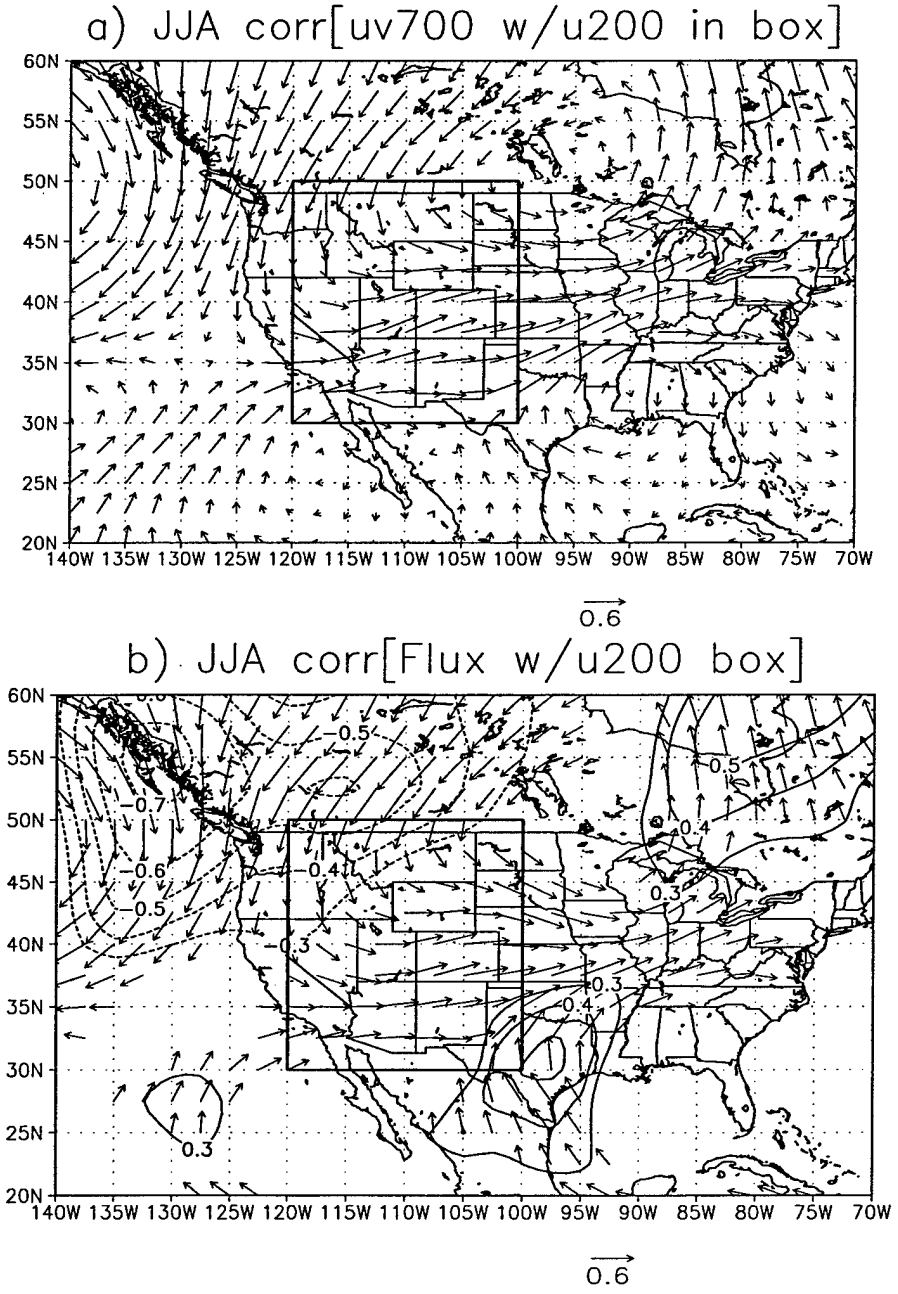


FIG. 4.3. Time correlation over North America (1951-2000) during summer (JJA). (a) Correlation vectors of the area averaged, 200-mb, zonal wind in the outlined box (30°N-50°N, 120°W-100°W) with 700-mb wind at all locations. (b) Similar to (a), but 200-mb, zonal wind in the outlined box correlated with vertically integrated moisture flux. The magnitudes of the correlation vectors are indicated at the bottom of each panel. In (b), the meridional components of the correlation coefficients are contoured, and only vector and meridional coefficients meeting the 99% statistical significance criteria (0.3) are shown.

with 700-mb wind (Fig. 4.3a). The correlation vectors and meridional contours show evidence that moisture travels from the Gulf of Mexico into the central U.S. during periods of increased 200-mb zonal flow over the mountains. Fig. 4.4 is similar to Fig. 4.3b but for a correlation of 200-mb zonal flow over the box with the 850-mb wind at all locations. Correlation vectors with statistical significance are absent over most of the boxed region, where most of the surface of the earth lies below 850 mb. East of the Rocky Mountains, the correlation vectors are at a maximum (0.6) over Texas, with meridional correlation coefficients from 0.5 to 0.3 extending northeastward. The correlation vectors, particularly over the western Gulf of Mexico and Texas, are oriented similarly to the mean LLJ vectors at 850 mb (Fig. 4.1a). Increased 200-mb zonal flow over the Rockies correlates with increased tropical southerlies (Fig. 4.4) and moisture transport (Fig. 4.3b) into the MRB.

The next question is whether global, upper tropospheric, ambient flows within the full latitude belt encompassing the central Rocky Mountains may also influence the low-level circulation over and to the east of the orography. The purpose is to test whether much larger scales and lower wave numbers within the latitude belt of the Rockies may also elicit a similar response as found for zonal flows within the boxed region (e.g., Figs. 4.3 and 4.4). The time correlation is shown in Fig. 4.5. The area averaged, 200-mb zonal flow around the entire globe within the latitude belt from 30°N-50°N is correlated with the local, 700-mb wind in Fig. 4.5a (the latitude belt is outlined). Upper tropospheric westerlies correlate with cyclonic turning in the 700-mb wind over the Great basin. The correlation vectors over the western and central U.S. are reminiscent of Fig. 4.3a, though the magnitudes of the vectors are smaller.

The large inertia associated with the zonally averaged wind and its interaction with orography may contribute to enhanced predictability over the GCIP region during sum-

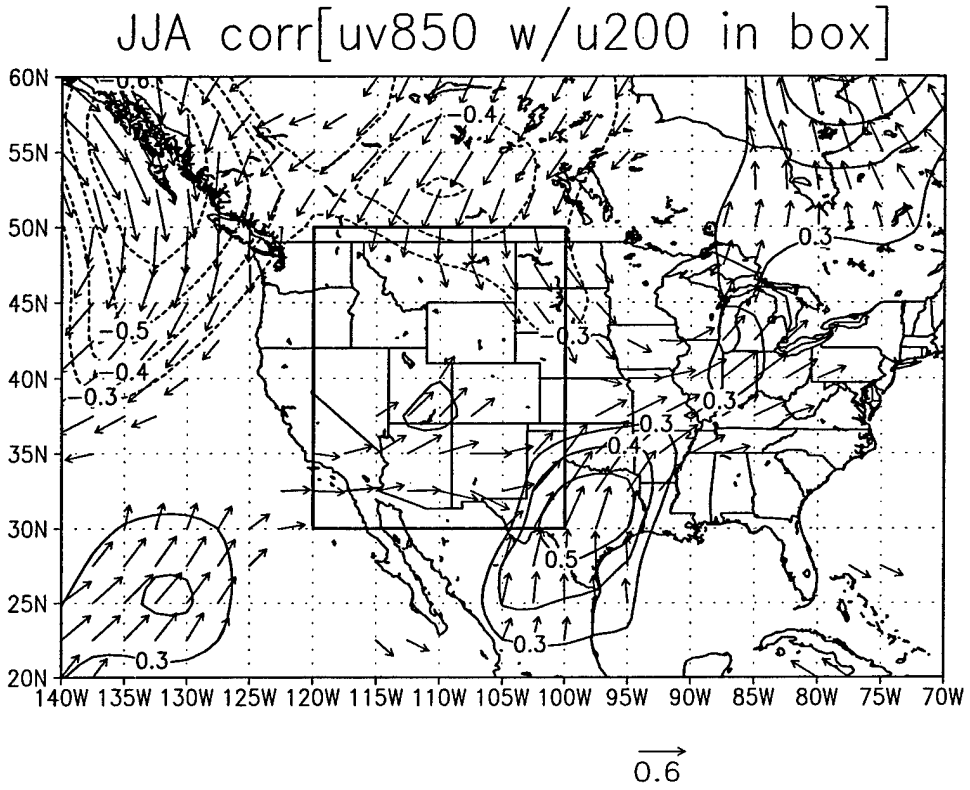


FIG. 4.4. The temporal correlation vectors of the area averaged, 200-mb, zonal wind in the outlined box (30°N-50°N, 120°W-100°W) with 850-mb wind at all locations for summer (JJA), 1951-2000. The magnitudes of the correlation vectors are indicated below the panel. The meridional components of the correlation coefficients are contoured, and only vector and meridional coefficients meeting the 99% statistical significance criteria (0.3) are shown.

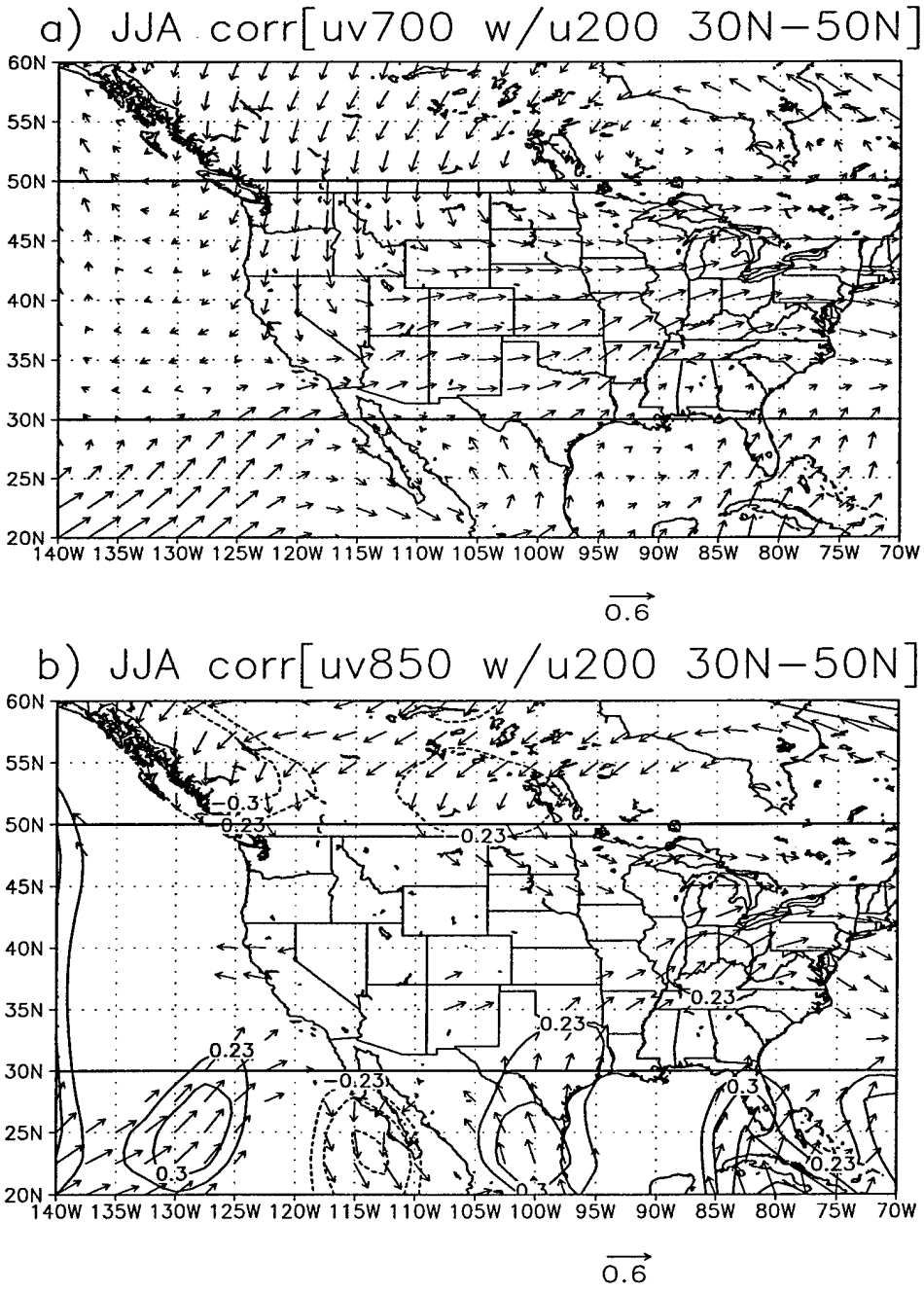


FIG. 4.5. Time correlation over North America (1951-2000) during summer (JJA). (a) Time correlation vectors of the area averaged, 200-mb, zonal wind around the globe from 30°N-50°N (outlined) with 700-mb wind at all locations. (b) Similar to (a), but for 200-mb, zonal wind correlated with vertically integrated moisture flux. The magnitudes of the correlation vectors are indicated at the bottom of each panel. In (b), the meridional components of the correlation coefficients are contoured, and only vector and meridional coefficients meeting the 95% statistical significance criteria (0.23) are shown.

mer. The seasonal and longer term changes of the ambient flow occurring on large scales may relate to fluctuations in the Great Plains LLJ, whose response occurs in summer on the smaller scales of cloud generation and precipitation. Helfand and Schubert (1995) showed the important role of the LLJ for vapor transport. Using a simulated moisture budget and the Goddard Earth Observing System (GEOS-1) atmospheric general circulation model, they found that the Great Plains LLJ transports about 30% of all the moisture entering the continental U.S.

Fig. 4.5b depicts correlations of the 850-mb wind at all locations with 200-mb winds in the outlined latitude belt around the globe. Only vectors and contours of the meridional component which are statistically significant at the 95% level (0.23) are depicted. Positive correlation coefficients extend from the western Gulf of Mexico into Texas and the Midwest. The signal is similar to, but weaker than, correlations where only the 200-mb zonal flow over the Rocky Mountain region is considered (Fig. 4.4). Fig. 4.6 displays time correlations similar to Fig. 4.5b, but of vertically integrated moisture flux correlated with area averaged, 200-mb zonal flow. The data are from a higher resolution, 29-year subset of the 50-year NCEP/NCAR Reanalysis. The subinterval is from 1968-1996 and contains 28 levels in the vertical, with seven levels below 850 mb (for details, see Mo et al., 1997). Only two levels are available below 850 mb for calculating the vertically integrated moisture flux in Fig 4.3b. The moisture flux data from which the correlations were computed are also based on daily, rather than monthly averaged values, thereby reflecting the effect of transients. Correlation coefficients that equal 0.31 are significant at the 95% level for this subset. Fig. 4.6 shows a cyclonic tendency in the correlation vectors over the central Rocky Mountains. Southerly and southwesterly correlation coefficients characterize most of the Great Plains, suggesting such flow may be favored in the presence of strong, 200-

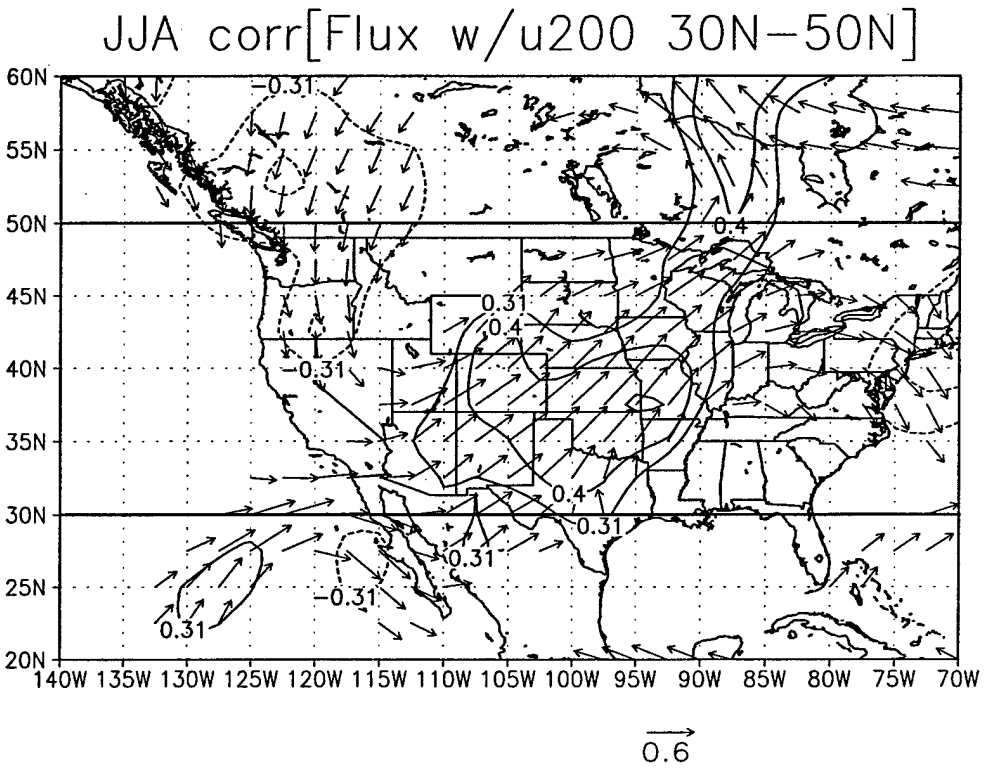


FIG. 4.6. The temporal correlation vectors of the area averaged, 200-mb, zonal wind around the globe from 30°N-50°N (outlined) with vertically integrated moisture flux at all locations during summer (JJA). The fluxes are derived from a 29-year, higher resolution subset of the NCEP/NCAR Reanalysis archive, from 1968-1996. The data set includes 28 vertical levels, with 7 below 850 mb; and averages were derived from daily, rather than monthly, variables. The meridional components of the correlation coefficients are contoured, and only vector and meridional coefficients meeting the 95% statistical significance criteria (0.31) are shown.

mb westerly flow around the latitude circle. The correlations of ambient, 200-mb flow with vertically integrated moisture flux (Figs. 4.3b and 4.6) suggest that an increase in moisture transport into the MRB via the LLJ occurs during periods of enhanced, upper troposphere westerlies over the Rocky Mountains.

The correlation coefficients displayed in the region of the mean LLJ in Figs. 4.3b and 4.6 suggest increased moisture flux into the MRB, and therefore heavier precipitation, may occur when upper tropospheric westerlies increase. This connection is illustrated with the time correlation of the local, summer precipitation with the ambient, 200-mb zonal flow between 30°N-50°N, in Fig. 4.7. Correlation coefficients greater than or equal to 0.3 appear over portions of the Great basin and the MRB. The same correlation for the 200-mb zonal flow averaged over the Rocky Mountain region in Fig. 1.3 shows an even stronger signal over the MRB, with the maximum coefficient (0.5) centered over Iowa. The pattern is similar to the correlation of 850-mb meridional flow over the Great Plains with precipitation (Fig. 1.4). In addition, correlations with precipitation in Fig. 4.7 and Fig. 1.3 appear to have a dipole pattern, with positive values over the Great Plains and negative values over the Southwest. Increased LLJ activity, coupled with precipitation over the Great Plains, is sometimes associated with a suppressed North American Monsoon in the southwestern U.S. Several investigators have noted this out-of-phase relationship (e.g., Higgins et al., 1997a and b; and Mo. et al., 1997). The correlations presented in this section suggest that increased cross-mountain flow may accelerate the hydrologic cycle in the MRB. This section has described monthly averaged fields to diagnose the interannual signal. While this shows large scale influences on the LLJ, it does not allow an assessment of shorter time scales, including diurnal influences.

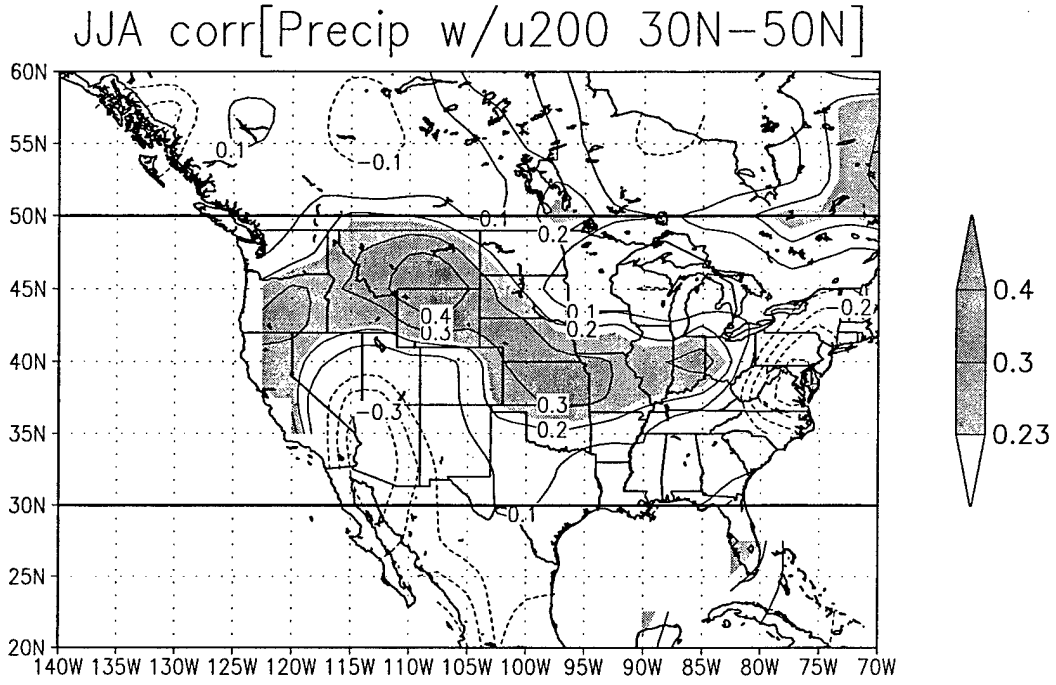


FIG. 4.7. The temporal correlation of the area averaged, 200-mb, zonal wind around the globe from 30°N-50°N (outlined) with gauge precipitation over land (PREC/L of Chen et al., 2002) for summer (JJA), 1951-2000. The contour interval is 0.1 and the zero line is omitted. Coefficients meeting the 95% statistical significance criteria (0.23) are shaded.

## 4.3 Model Experiments

### 4.3.1 Model and Data

Ensemble simulations are presented during two extreme periods within the GCIP domain. The goal is to examine the roles of dynamics and land-surface heating processes in the analyses and 13-day forecasts.

The model is a multilevel, spectral, primitive equation version of the model described by Paegle (1989). The UGM has been used primarily to address predictability questions (e.g., Vukicevic and Paegle, 1989; Paegle et al., 1997; Wang et al., 1999; and Miguez-Macho and Paegle, 2000). It is hydrostatic and filters acoustic waves and predicts vorticity, divergence, thermal and moisture fields on pressure-based sigma coordinates. The approach is similar to that used by operational centers, with the exception of numerical approximations of horizontal derivatives that are based on Fourier series in longitude and finite elements in latitude. A low-order turbulent kinetic energy equation is used to calculate vertical mixing coefficients. Radiative processes include cloud-radiative interactions, as described in Nicolini et al. (1993). The "emissivity" method is used for infrared radiative transfer (water vapor, carbon dioxide, clouds and the earth's surface are the only emitters and absorbers). The present experiments retain nodal spacing 2.22° in latitude and 42 waves in longitude on 20 vertical levels, situated at sigma .99, .98, .96, .94, .91, .88, .84, .78, .72, .66, .59, .53, .47, .41, .34, .28, .22, .16, .09 and .03. Physical parametrizations of precipitation (convective and stratiform) are similar to those used by the 1987 version of the NCAR Community Climate Model (Bath et al., 1987). Model clouds are diagnosed in terms of relative humidity. The model does not have a complete land parametrization. Initial surface temperature is specified over the globe from reanalysis data (ECMWF or NCEP); and subsequent surface temperature is computed from a heat balance equation

including long and shortwave radiation, turbulent and latent heat transfer in the atmosphere and conduction in the soil. Surface latent heat flux is specified from the NCEP/NCAR Reanalysis. A 15-minute time step is used in the present integrations.

Ensembles of forecasts during the summers of 1993 and 1988 are presented in section 4.3.2. Initial conditions are from the daily, 00 UTC values of horizontal wind, specific humidity, temperature, surface pressure and geopotential height from the NCEP/NCAR Reanalysis. Initial fields are interpolated linearly from pressure levels to model sigma levels. In addition, similar initial fields from the ECMWF Reanalysis are used, with the exception of elevation and surface pressure, which in all cases are specified from the NCEP model in order to minimize surface imbalances in the adjustment of sea-level pressure to the model surface. The ECMWF Reanalysis is a state-of-the-art assimilation system similar to the NCEP/NCAR Reanalysis, using observations from all available data sources. It is a spectral version (T106 resolution, with 31 vertical hybrid levels, or 17 pressure levels) of the ECMWF operational data assimilation system and model (Gibson et al.,1997).

Surface evaporation from the NCEP/NCAR Reanalysis is specified over the globe. Evaporation, a "Type C," model-derived product, is taken from daily-averaged values for the ensemble cases in 1988 and 1993. The 1988 initial days are 26 May, 28 May, 30 May, 1 June and 3 June. The 1993 initial days are 27 June, 29 June, 1 July, 3 July and 5 July. For a set of experiments, surface evaporation is switched between 1988 and 1993, and the monthly averaged evaporation from the alternating year is used. There is no diurnal cycle in the surface evaporation, which is prescribed at every time step. The model includes a diurnal cycle in solar radiation based on the season, day of the year and hour; and the radiation scheme includes water vapor absorption, cloud scattering and absorption and clear-

air scattering.

Model precipitation forecasts are compared with daily averaged observations from the Unified precipitation data set of the Climate Prediction Center (CPC) (Higgins et al., 1996). The data are available on a 0.25° X 0.25° grid from 140°W-60°W and 20°N-60°N. Data are derived from three sources using a Cressman scheme: (1) National Climatic Data Center co-op stations, (2) the CPC data set, and (3) the daily accumulations from hourly precipitation data set.

Averages of the vertically integrated, meridional moisture transport in the UGM are compared to those of the ECMWF Reanalysis for the 13-day ensembles in 1988 and 1993. ECMWF fluxes are computed on pressure coordinates, while UGM fluxes are computed on sigma coordinates.

### 4.3.2 Ensemble Simulations

A total of 10 forecasts are made during the 1993 U.S. summer floods, and another 10 during the U.S. drought of 1988. July 1993 was characterized by Mo et al. (1995) and Bell and Janowiak (1995) as a persistent, highly amplified wave period. Mo et al. (1995) showed strong, negative 500-mb height anomalies were maintained over the west-central U.S. (90°W-120°W) and positive 500-mb height anomalies were maintained over the eastern Pacific and eastern U.S. The flood region of the Midwest was located east of a large-scale trough axis, in an area of anomalously strong southwesterly flow (Bell and Janowiak, 1995). By contrast, June 1988 was during the height of a severe drought in which an anomalous ridge was anchored over the north, central U.S. (Mo et al., 1991; Namias, 1991) with a northward displacement of the jet stream.

The initial times for each 13-day forecast during the 1993 flood are 00 UTC 27 June, 29 June, 1 July, 3 July and 5 July 1993. Each forecast is initialized with NCEP data and

again with ECMWF data, for a total of 10 ensemble members ("June-July 1993" ensemble). During the 1988 drought, the forecast days are 00 UTC 26 May, 28 May, 30 May, 1 June and 3 June 1988. As in 1993, each time is initialized with NCEP data and again with ECMWF data to produce 10-member ensembles of 13-day forecasts ("May-June 1988" ensemble).

June-July 1993 precipitation accumulation is displayed in Fig. 4.8. Fig. 4.8a shows the average, observed accumulation for the 13-day periods during June-July 1993. More than 20 cm of precipitation falls over northeastern Kansas, northern Missouri and southern Iowa. A local peak of 27 cm occurs near the Kansas-Nebraska-Missouri-Iowa borders. Other maxima include 8 cm in western Montana and North Dakota, 10 cm over Wisconsin and 10 cm in Mississippi and southeastern Louisiana. The UGM ensemble for the same period is shown in Fig. 4.8b. The model has two precipitation maxima of 8 cm near the region of observed maximum precipitation. One is in western Kansas and another is located in west-central Illinois. The model precipitation pattern represents some of the major features across the north-central U.S., but lacks precipitation over west Texas, Oklahoma, and across the Gulf coast and into the southeastern U.S. The forecast values are substantially less than observations. The areal extent of both observed and model precipitation partially resembles the intraseasonal signal. This is shown by comparing them to the correlation coefficients of area averaged, upper tropospheric zonal flow with precipitation, depicted in Fig. 4.7 and Fig. 1.3.

Pan et al. (2000) demonstrated with a mesoscale model that a major contributor to the summer 1993 floods was a continuous generation of mesoscale convective complex (MCC)-like systems. The UGM simulations presented here are on a 2.2° latitude by 2.8° longitude horizontal grid and are too coarse to adequately resolve mesoscale features. Pan

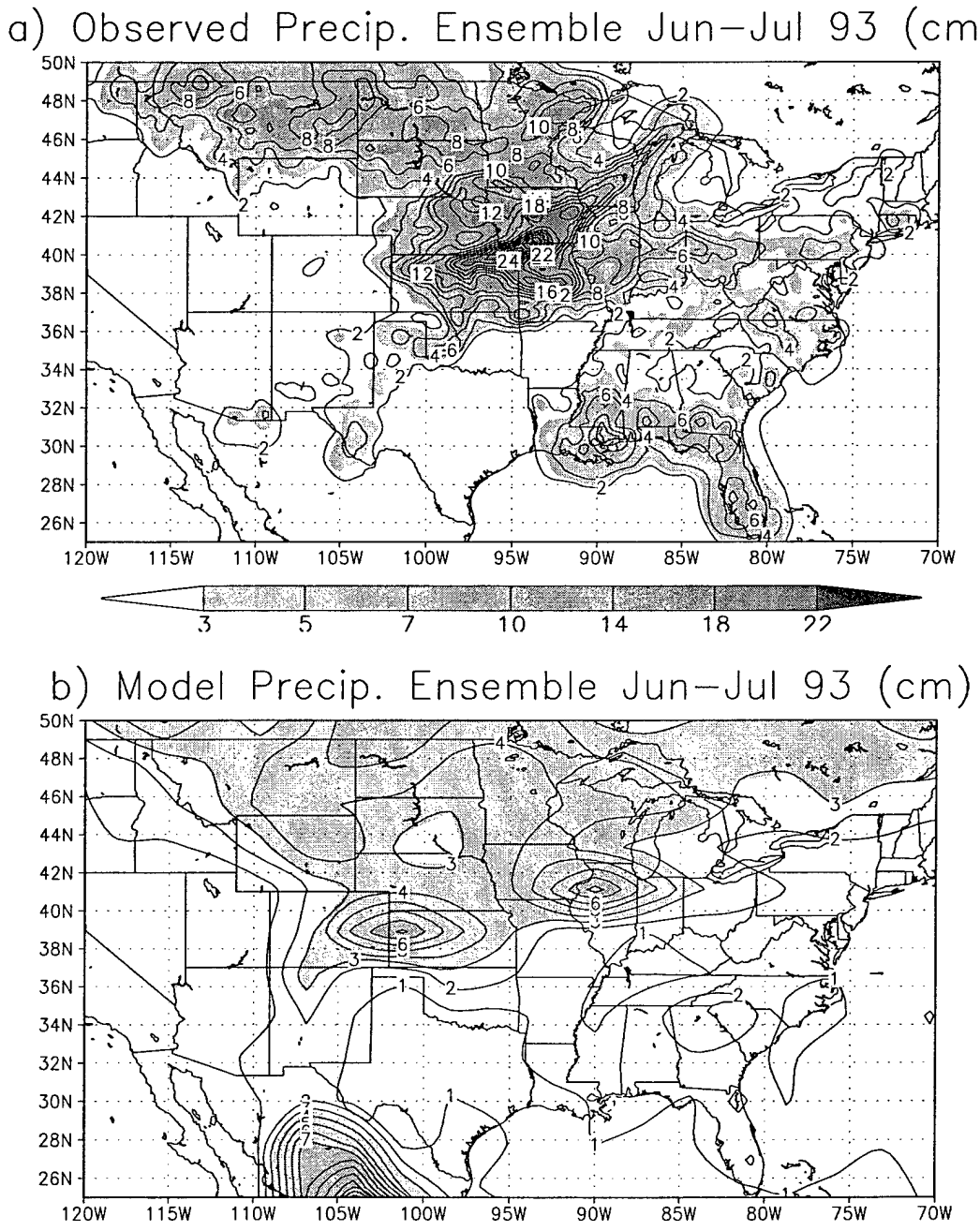


FIG. 4.8. Precipitation accumulation for the June-July 1993 composites. (a) Average accumulation for the 13-day periods. The start days are 27 June, 29 June, 1 July, 3 July and 5 July 1993. Data are from the CPC Unified daily precipitation data set (Higgins et al., 1996). (b) The UGM ensemble average accumulation for the 13-day periods in (a). Accumulations in (b) are an average of 10 UGM ensemble members, 5 initialized with the ECMWF and 5 initialized with the NCEP Reanalyses at 00 UTC on each of the 5 dates listed in (a). The contour interval is 2 cm in (a) and 1 cm in (b). Shading is for accumulations greater than or equal to 3 cm.

et al. (2000) also concluded that the anomalous, large scale environment during summer 1993 created conditions favorable for MCCs. Such interactions occurred in their 30-day simulations (and verified against observations) in regions away from the simulated boundary-forcing locations, where MCCs were favored substantially by the large scale anomalies. The large scale circulation resolved by the UGM may have contributed to the precipitation produced in the GCIP region (Fig. 4.8b). Wang et al. (1999) found similar results to the present ensemble flood cases using much higher local resolution (50 km) in a global, variable resolution model for 2-week simulations beginning 27 June 1993.

Fig. 4.9 displays the 13-day, ensemble precipitation accumulation for May-June 1988. In contrast to 1993, the midwestern U.S. is relatively dry, with only 2 to 4 cm of precipitation over Iowa, Missouri and Illinois (Fig. 4.9a). Accumulations exceed 6 cm over the Texas panhandle, and over central Texas and south Florida. The model simulation (Fig. 4.9b) is also dry over the Mississippi basin and midwestern U.S. Deficits in precipitation occur along the Gulf Coast and Florida, as in the 1993 ensemble. Figs. 4.8 and 4.9 suggest the forecasts for the ensembles of 1993 and 1988 distinguish some of the observed precipitation differences between these years, although the magnitude of the differences is underestimated.

To evaluate the role of surface latent heat flux on the 13-day forecast ensembles, the same 10 cases in each summer are presented with different surface evaporation. The June-July 1993 members are initialized with daily, 1993 variables, as before. However the monthly averaged, reanalyzed, surface evaporation from June 1988 is used for each case instead of daily, 1993 values. For the May-June 1988 cases, all initial variables are daily, 1988 variables, with surface evaporation from the monthly averaged reanalysis value of July 1993. Fig. 4.10 shows the monthly averaged, surface latent heat flux from the NCEP/

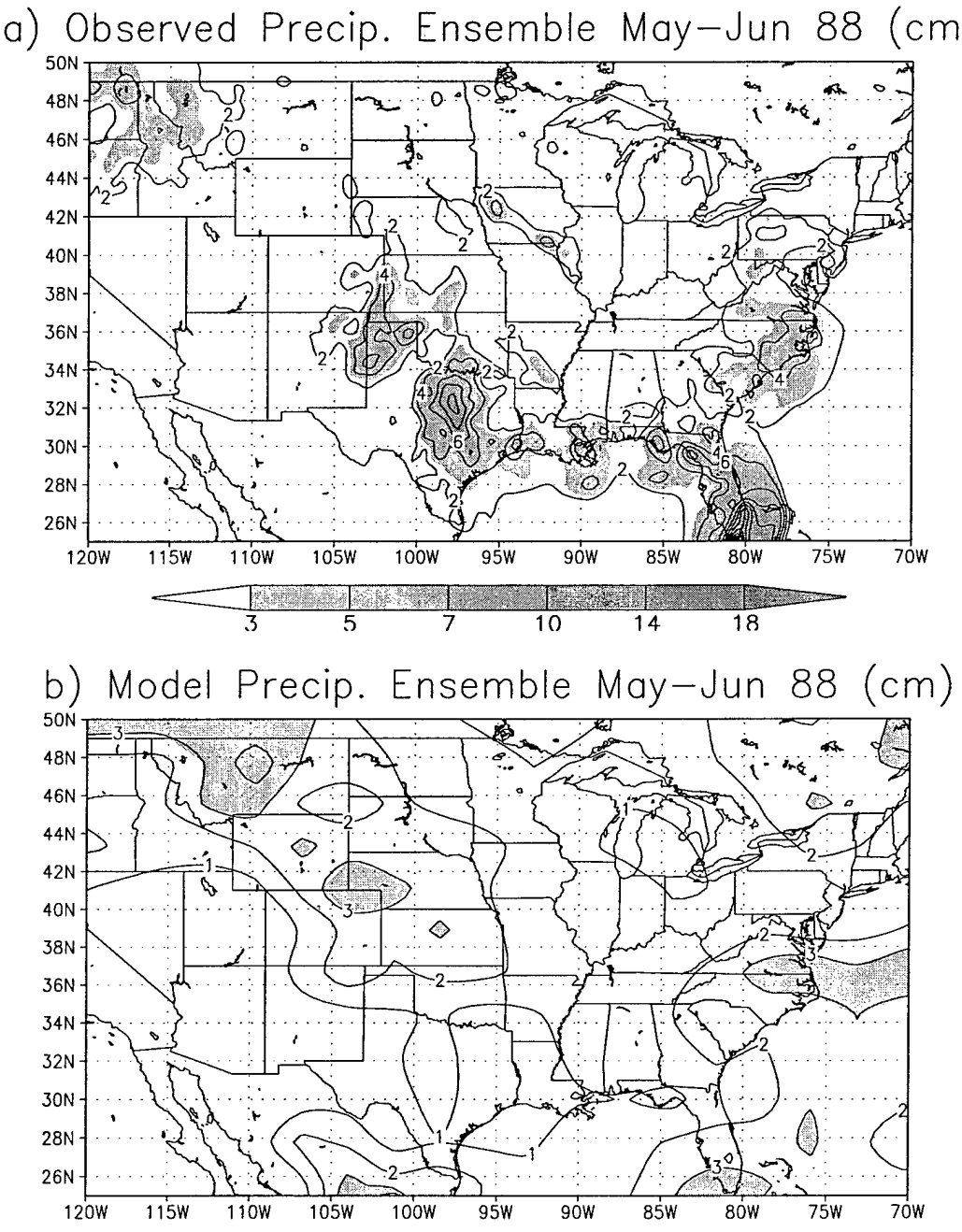


FIG. 4.9. Precipitation accumulation for the May-June 1988 composites. (a) Average precipitation accumulation for the 13-day periods. The initial times are 26 May, 28 May, 30 May, 1 June and 3 June 1988. Data are from the CPC Unified daily precipitation data set (Higgins et al., 1996). (b) The UGM, ensemble average precipitation accumulation for the 13-day periods in (a). Accumulations in (b) are an average of 10 UGM ensemble members, 5 initialized with the ECMWF and 5 initialized with the NCEP/NCAR Reanalyses at 00 UTC on each of the 5 dates listed in (a). The contour interval is 2 cm in (a) and 1 cm in (b). Shading is for accumulations greater than or equal to 3 cm.

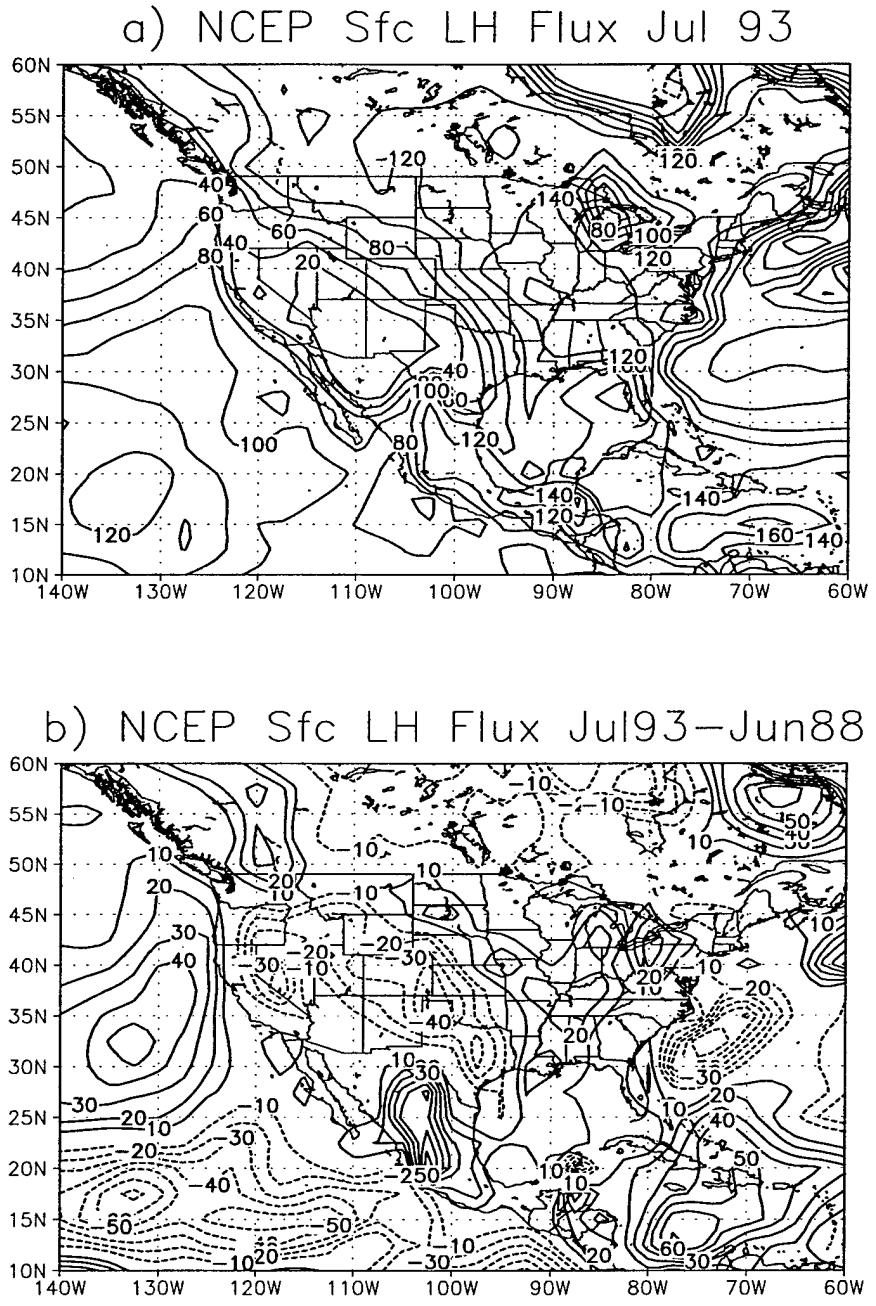


FIG. 4.10. Monthly averaged, surface, latent heat flux (W/(m*m)) from the NCEP/ NCAR Reanalysis for (a) July 1993, and (b) July 1993 minus June 1988. Contour interval is 20 W/(m*m) in (a) and 10 W/(m*m) in (b). Negative contours are dashed, positive contours are solid, and the zero line is omitted. The fields have been interpolated to a 2.5° latitude/longitude grid.

NCAR Reanalysis for July 1993 (Fig. 4.10a) and the difference field between July 1993 and June 1988 (Fig. 4.10b). Precipitation accumulation resulting from monthly averaged evaporation from the alternating years is illustrated in Fig. 4.11. Simulated June-July 1993 precipitation (Fig. 4.11a) is substantially reduced over the Midwest and north-central U.S. compared to the observations and to forecasts in Fig. 4.8. Kansas and Missouri are excessively dry. A peak of 4 cm is located over Iowa and Illinois and a maximum of 5 cm is evident over North Dakota. The May-June 1988 simulations with July 1993 evaporation do not deviate significantly from the May-June 1988 with May-June 1988 evaporation cases (compare Fig. 4.11b with Fig. 4.9b), and accumulation over most of the Great Plains and Midwest is only about 2 cm.

The moisture transport in the UGM simulations and the ECMWF Reanalysis is examined next. The ECMWF Reanalysis may provide better resolution of moisture transport, since it includes an additional grid level below 700 mb (775 mb) not contained in the NCEP/NCAR Reanalysis. The UGM and ECMWF Reanalysis values at 00 and 12 UTC each day are summed for each 13-day case and the ensemble average is then computed. The June-July 1993 ensemble average, vertically integrated, meridional moisture flux is depicted in Fig. 4.12. The ECMWF Reanalysis shows a pronounced northward flux of moisture over north-central Texas and the western Gulf of Mexico (Fig. 4.12a). The moisture flux is associated with the Great Plains LLJ (e.g., Mo et al., 1995; Paegle et al., 1996). The heaviest rain occurs just north of this jet core (see Fig. 4.8a). UGM, vertically integrated, meridional moisture flux is in fair agreement with the ECMWF Reanalysis (Fig. 4.12b). The highest values of northward flux over the Great Plains are displaced westward over the Texas panhandle, just south of the modelled Kansas precipitation maximum.

Fig. 4.12 suggests a significant, remote source of moisture for the June-July 1993

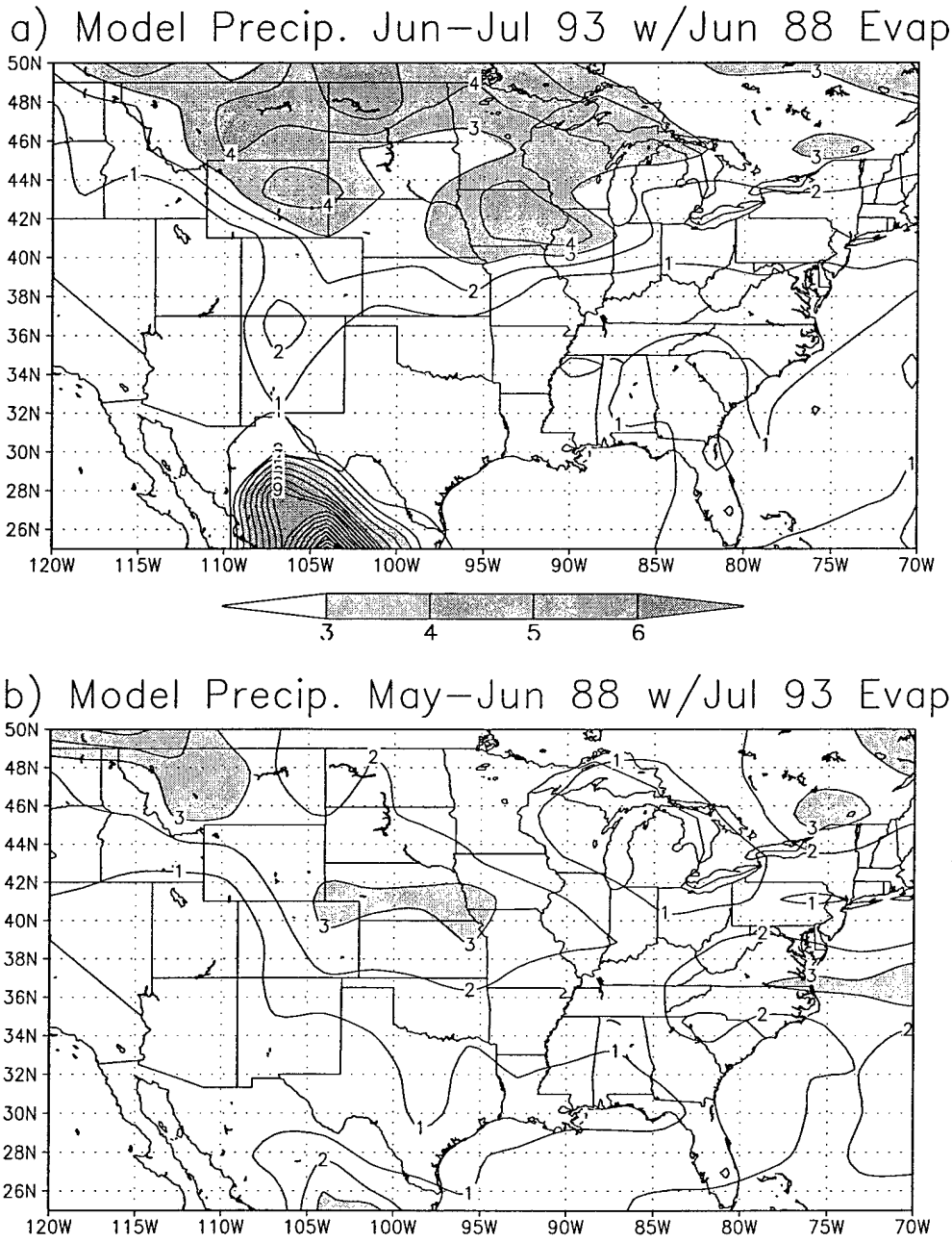


FIG. 4.11. Precipitation accumulation for the ensembles with switched evaporation. (a) The average accumulation of the UGM, 10-member ensemble in June and July 1993, where each simulation was initialized with the monthly averaged surface evaporation of June 1988. All other initial fields are from daily, 00 UTC values in 1993. (b) The average accumulation of the UGM, 10-member ensemble in May and June 1988, where each simulation was initialized with the monthly averaged surface evaporation of July 1993. All other initial fields are from daily, 00 UTC values in 1988. The contour interval is 1 cm and shading is for accumulations greater than or equal to 3 cm.

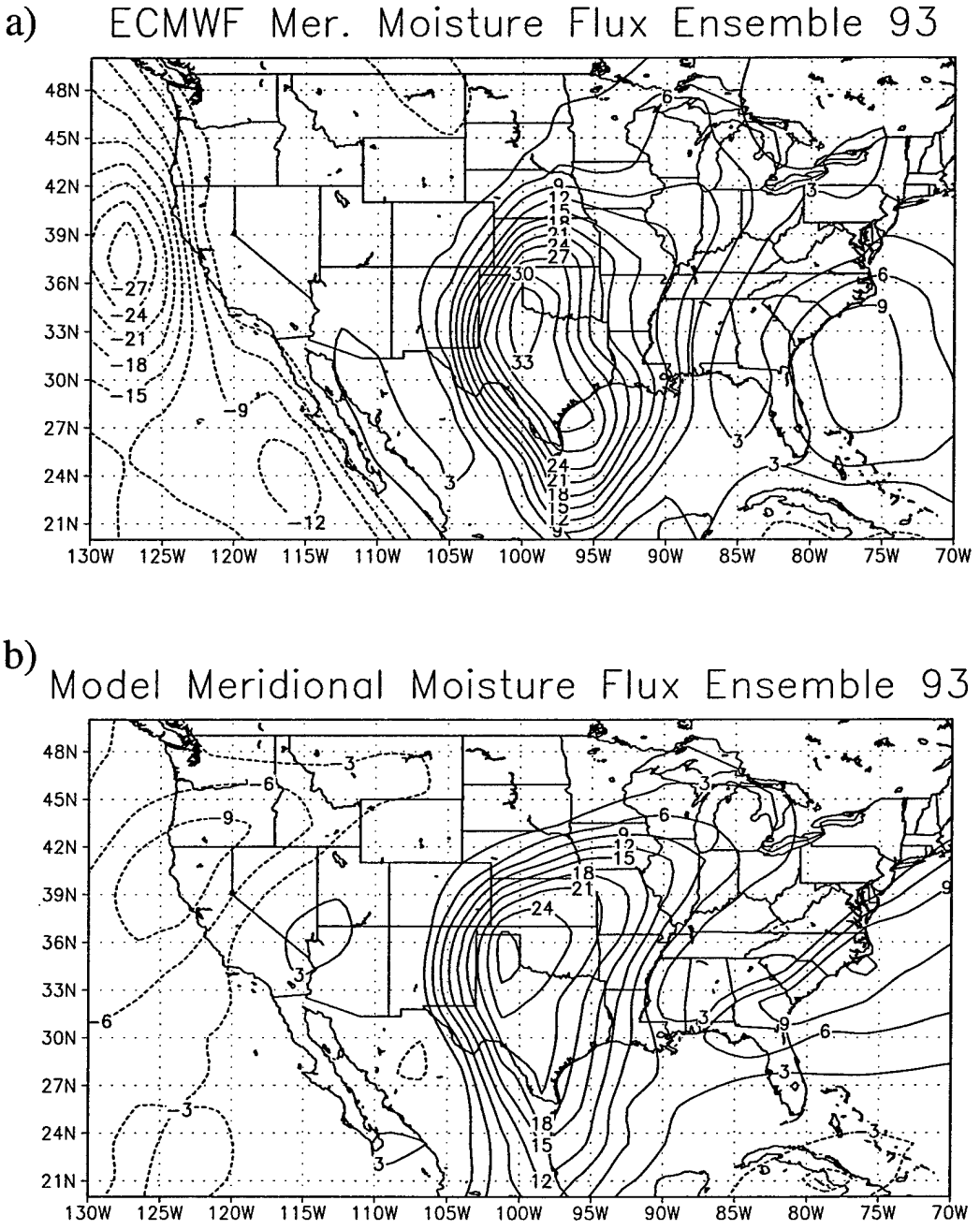


FIG. 4.12. Vertically integrated, meridional moisture flux for the June-July 1993 composites. (a) The average for the 13-day periods as depicted by the ECMWF Reanalysis. (b) The UGM, ensemble average for the cases in (a). Contours in (b) are an average of the 10 UGM ensemble members described in the text. Fluxes in (a) and (b) have been averaged over 00 UTC and 12 UTC each day for each ensemble. Values in (a) are on pressure coordinates, while UGM values in (b) are on sigma coordinates. The contour interval is 50 kg*(m/s) and the zero line is omitted.

ensemble, associated with the the Great Plains LLJ. Dirmeyer and Brubaker (1999) used a quasi-isentropic back trajectory analysis to show that the moisture source of peak flooding over the upper Mississippi and Missouri basins in July 1993 originated over the western Gulf of Mexico and the Caribbean Sea. They showed in contrast, moisture sources from the April to June 1988 drought period were mostly terrestrial in nature and moisture recycling from the surface was more prevalent.

The meridional moisture flux for the May-June 1988 ensemble is depicted in Fig. 4.13. The maximum, reanalyzed, southerly moisture flux over the Great Plains is about 60% smaller than that for June-July 1993 (compare Fig. 4.13a with Fig. 4.12a). The UGM shows similar results (Fig. 4.13b), but moisture does not penetrate significantly northward into Nebraska or the Dakotas as shown in the ECMWF Reanalysis.

The meridional moisture flux within present model integrations does not depend sensitively upon surface evaporation. This is illustrated in Fig. 4.14. For the June-July 1993 ensemble with June 1988 surface evaporation (Fig. 4.14a), the average moisture flux over the Great Plains and Midwest is slightly weaker, but the pattern resembles the June-July 1993 ensemble with June-July 1993 surface evaporation (compare Fig. 4.14a with Fig. 4.12b). For the May-June 1988 ensemble with July 1993 surface evaporation (Fig. 4.14b), the southerly moisture flux increases about 25-30% over Texas and western Oklahoma. The magnitude is similar to the May-June 1988 ensemble with May-June 1988 surface evaporation (Fig. 4.13b).

The time evolution of area averaged, accumulated precipitation for a box encompassing much of the GCIP region (105°W-88°W, 34°N-50°N) is displayed in Fig. 4.15. The model under predicts precipitation by about 30%-50% after the first week in the June-July 1993 ensemble (Fig. 4.15a, solid circles). Accumulations increase steadily in time, similar

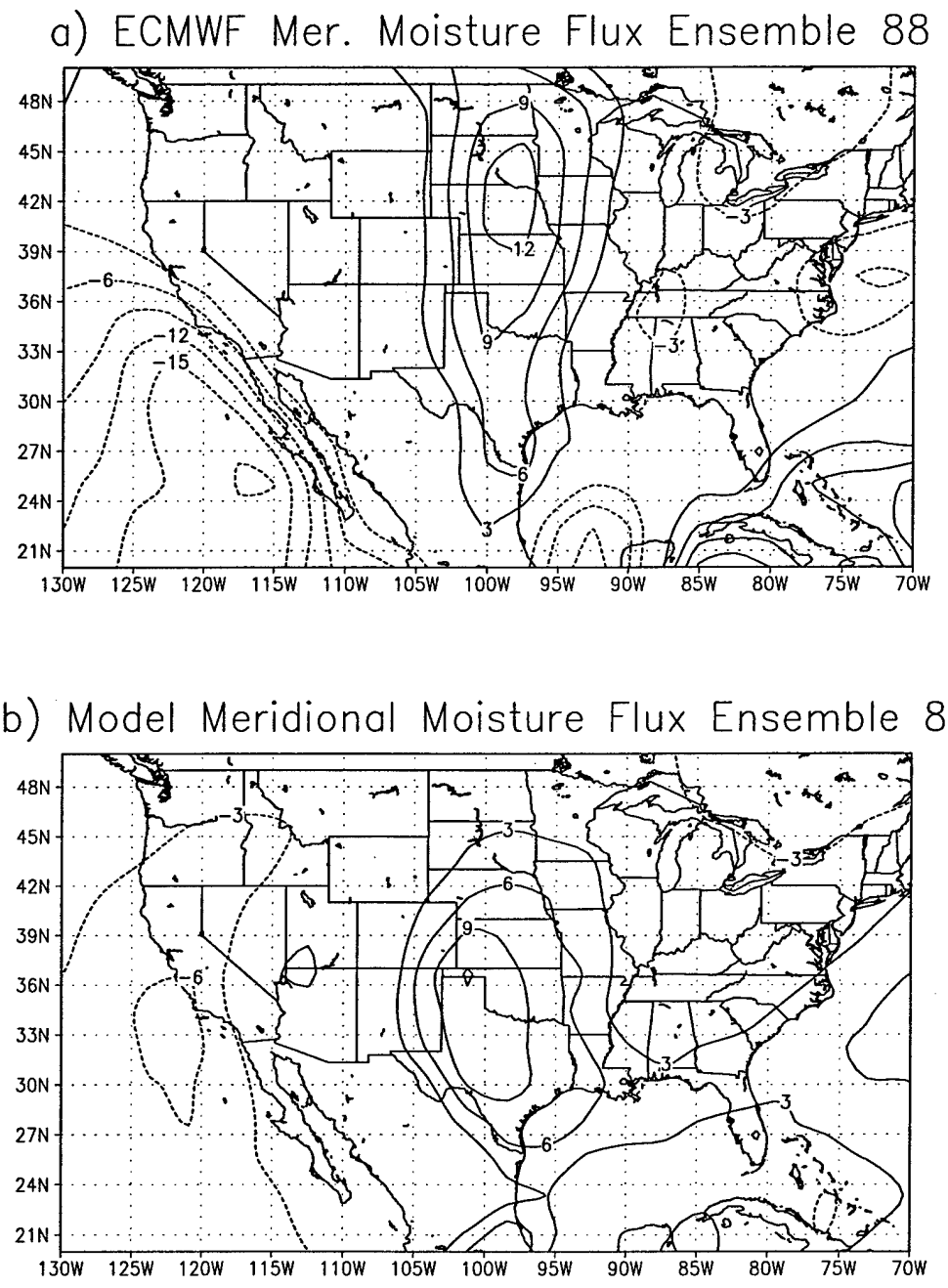


FIG. 4.13. Vertically integrated, meridional moisture flux for the May-June 1988 composites. (a) The average for the 13-day periods as depicted by the ECMWF Reanalysis. (b) The UGM, ensemble average for the cases in (a). Contours in (b) are an average of the 10 UGM ensemble members described in the text. Fluxes in (a) and (b) have been averaged over 00 UTC and 12 UTC each day for each ensemble. Values in (a) are on pressure coordinates, while UGM values in (b) are on sigma coordinates. The contour interval is 50 kg*(m/s) and the zero line is omitted.

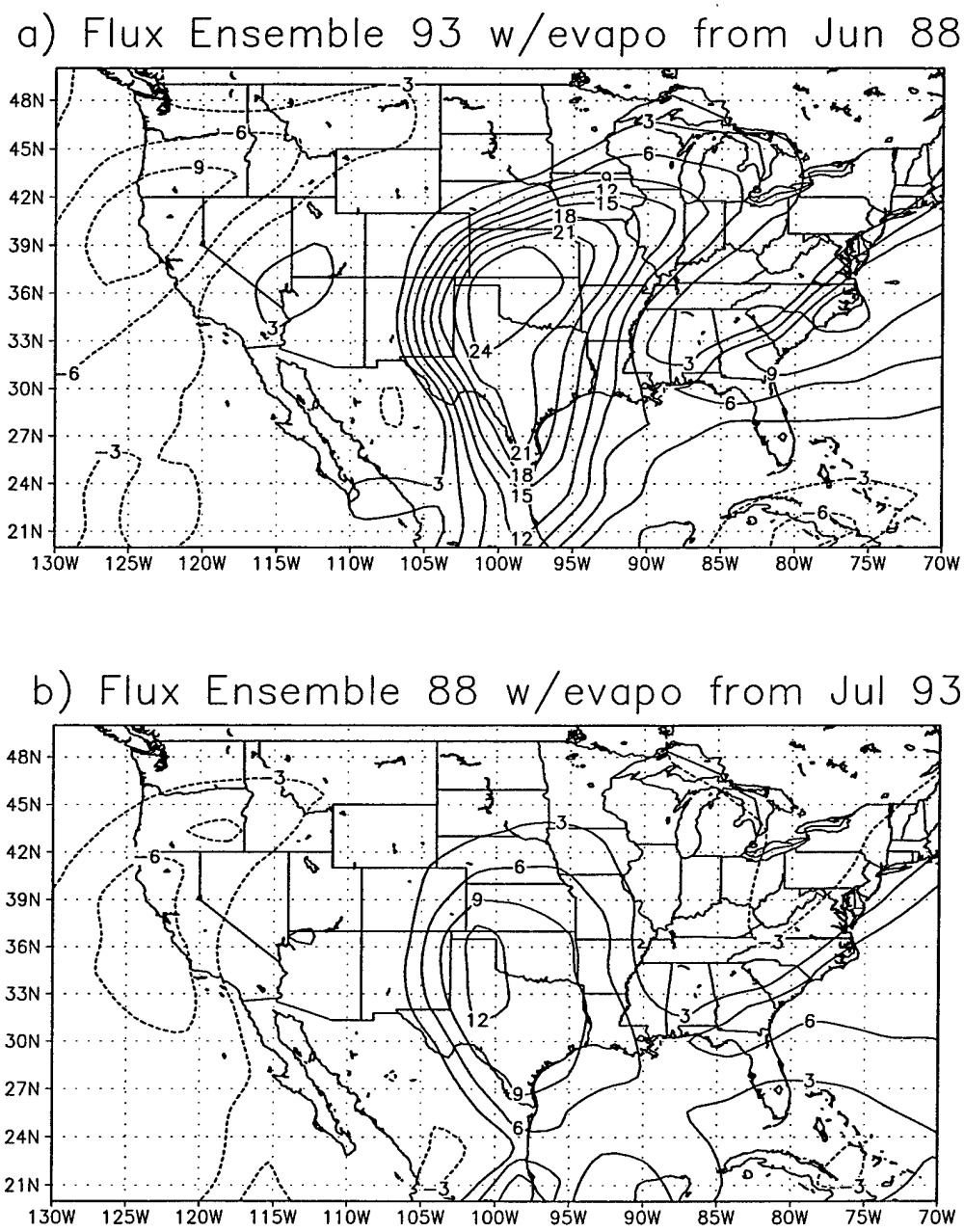


FIG. 4.14. Vertically integrated, meridional moisture for the ensembles with switched evaporation. (a) Average of the UGM, 10-member ensemble in June and July 1993, where each simulation was initialized with the monthly averaged surface evaporation of June 1988. All other initial fields are daily, 00 UTC values in 1993. (b) Similar to (a) but for the UGM, 10-member ensemble in May and June 1988, where each simulation was initialized with the monthly averaged surface evaporation of July 1993. All other initial fields are daily, 00 UTC values in 1988. Fluxes in (a) and (b) have been averaged over 00 UTC and 12 UTC each day for each ensemble on sigma coordinates. The contour interval is 50 kg*(m/s) and the zero line is omitted.

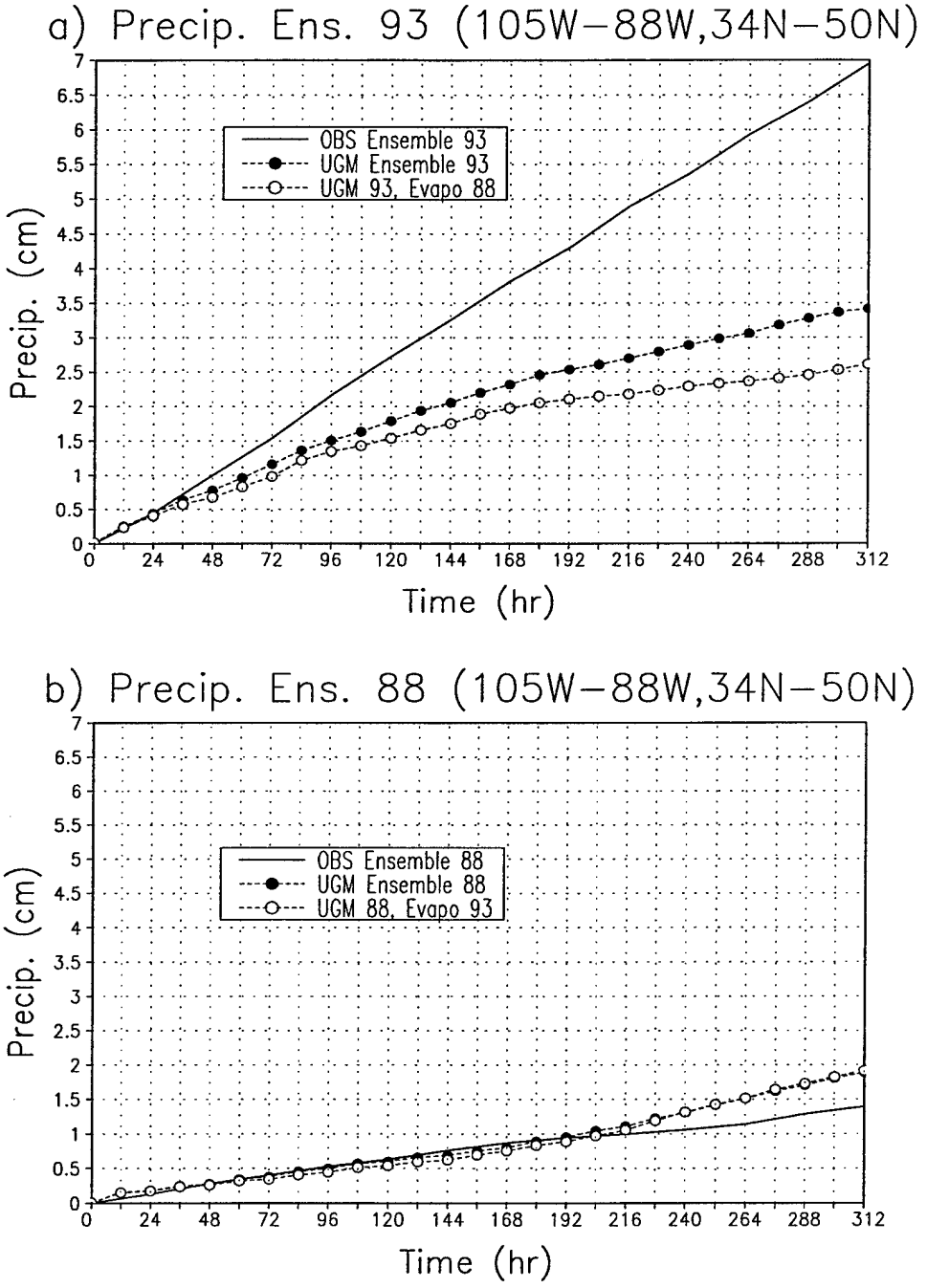


FIG. 4.15. Area averaged, precipitation accumulation from 105°W-88°W, 34°N-50°N, for (a) June-July 1993 ensemble averages, and (b) May-June 1988 ensemble averages. Solid contours show observation ensembles from the CPC Unified precipitation data set (Higgins et al., 1996), solid circles show the UGM ensemble solution, and open circles show the UGM ensemble solution with monthly averaged surface evaporation from June 1988 and July 1993 in (a) and (b), respectively.

to observations. For June-July 1993 with June 1988 surface evaporation, accumulations are lower (Fig. 4.15a, open circles). The curve tends to closely follow the June-July 1993 ensemble with June-July 1993 surface evaporation to about hour 168 (day 7), and then it levels off to between 2-2.5 cm. For May-June 1988, the accumulations in both sets of model ensembles are very similar and in close agreement with observations until about hour 216 (Fig. 4.15b).

Surface evaporation appears to have little impact on model precipitation averaged over the bulk of the MRB during the first week of the June-July 1993 ensemble forecast. This suggests an important role for the large scale circulation during this period. Surface processes and land-surface interactions appear to play a significant role in predictability beyond the first week in 1993, as supported by many previous studies using regional and global models over the GCIP domain.

The present results, and examination of vertical motion simulations (not shown), suggest that the dynamical effects of the large-scale circulation contribute to the predictability in the 1988 ensemble more than in the 1993 ensemble. Several investigators have noted the importance of large scale forcing on the 1988 U.S. drought. Namias (1991), for example, noted the spring-to-summer persistence of anomalous, upper-level anticyclones over the North Pacific, the central U.S. and the North Atlantic. Trenberth and Branstator (1992) demonstrated the role of anomalous equatorial SSTs on the drought of 1988, and concluded local soil moisture feedbacks were secondary to the large scale forcing.

Comparison of the 1993 and 1998 UGM simulations (Fig. 4.15) suggests that the large scale circulation influences whether evaporation impacts precipitation. Evaporation tends to influence precipitation only if the large scale conditions are favorable for precipitation (e.g., Barnston and Schikedanz, 1984), as during the summer of 1993. Pan et al. (2000) for

instance, demonstrate the important contribution of MCC-like systems to precipitation totals during the summer of 1993. Namias (1991) finds that the large scale circulation was not conducive to precipitation during the spring and early summer of 1988.

Student's t-statistics for precipitation (not shown) were computed for the June-July 1993 and May-June 1988 UGM ensembles to study the significance of the forecasts during the chosen summers. The results show that a 5% confidence level for 10° of freedom is maintained over the MRB after 1 week. During the second week, the response weakens as predictability weakens.

Currently selected cases represent extremes in the zonal flow over the Rocky Mountains. The area averaged, 200-mb zonal wind, averaged over all ensembles, calculated over the Rockies in the region described in section 4.2 (120°W-100°W, and 30°N-50°N), is 22.4 m/s for the June-July 1993 cases. In contrast, the magnitude for the May-June 1988 cases is 12.1 m/s. As previously noted, the strength of the cross-Rockies zonal flow appears to influence the circulation east of the Rockies, including the strength of the LLJ. The next section describes the mechanical effect of orography with emphasis on longer time scales than those that characterize the sets of ensembles presented here. This is helpful for dynamical interpretation of prior results.

## 4.4 Ambient Flow Oscillations: Subcritical and Supercritical Flows

A possible interpretation of ambient flow oscillations is found using the steady solution of the barotropic vorticity equation, summarized in section 2.6.1 and in the Appendix. The strength of the response maximizes near resonance (equation 2.4). The steady state response forms anticyclones over mountains and cyclones over valleys for supercritical conditions (equation 2.2), and the opposite distribution, with cyclones over the mountains for subcritical conditions (equation 2.3). Strong westerlies favor supercritical flows, while

weak westerlies favor subcritical conditions, as over South America (see section 2.6.1). Paegle et al. (1979) showed topographically induced ultralong waves in the Northern Hemisphere have a nearly equivalent barotropic structure in the troposphere.

Over North America, supercritical conditions are satisfied more easily in winter when stronger zonal winds prevail across the Rocky Mountains compared to summer, when the winds weaken. A consistent interpretation of reanalyzed fields (section 4.2) is that increased zonal flow during summer accelerates the orographic vortex as the resonant point in the response is approached.

One interpretation of the correlations of cross-orography zonal flows with lee-side responses of LLJs, moisture flux, and precipitation is that increasing cross-mountain flow accelerates the summer cyclone situated over the Rockies through mechanical processes relating to subcritical ambient flows approaching resonance. This interpretation is reasonable only to the extent that the dynamical processes in question actually tend to develop a cyclone over the central Rockies in the summer season. The next section demonstrates that the lower-tropospheric cyclone commonly observed above the central Rockies in summer may be at least partly explained by a subcritical, stationary, orographic Rossby wave response, and that the observed and modelled intraseasonal oscillations may therefore be partly explained by the simple dynamical processes described here and in section 2.6.1.

## 4.5 Seasonal Cycle Over North America

To more clearly support or refute the possibility that the observed summer cyclone reflects the orographic mechanism, it is necessary to demonstrate that the effects are simulated in a model that retains a full and realistic spectrum of orography. The model should also use realistic ambient flow, taken from observed conditions for each season and allow

reasonable vertical shear and more general processes than does a purely barotropic model. To show that the simple barotropic results are relevant to actual prediction, they should be reflected in a global, primitive equation model such as the Utah Global Model (UGM). Evidence is presented which suggests that mechanical effects influence the seasonal reversal around the Rocky Mountains, and hence the LLJ east of the mountains, using simulations initialized with monthly averaged variables and comparisons to reanalyses. Much of the Rocky Mountain region lies above 850 mb. The focus is therefore upon 700 mb (sigma level 0.72 in UGM integrations), where artificial interpolation below the surface of the earth is not required over most of the area.

The integrations are performed omitting radiative and latent heating. They consist of month long simulations of monthly averaged conditions taken from January and July from the NCEP/NCAR Reanalysis, averaged from 1951-2000. Orography is represented in a spherical harmonic, wave number 42 triangular truncation. The zonally averaged portion of the simulated circulation is maintained at the reanalysis value for each month by rapid relaxation of the rotational portion of the zonally averaged flow toward the climatology for each month. To isolate the mechanical, orographic effect of the Rockies, differences are taken between runs with orography over the entire globe and runs without orography over the North American region. In the latter case, initial surface pressure over North America is set to a constant (1013 mb) over the region from 20°N-60°N, and 130°W-70°W.

Fig. 4.16 shows differences in the average wind vectors (mountain minus no-mountain) for simulations with and without orography. The average is for the last 30 days of a 40-day forecast. During January (Fig. 4.16a), the mechanical effect of orography produces a lower tropospheric anticyclone over the western U.S. and northerly flow east of the

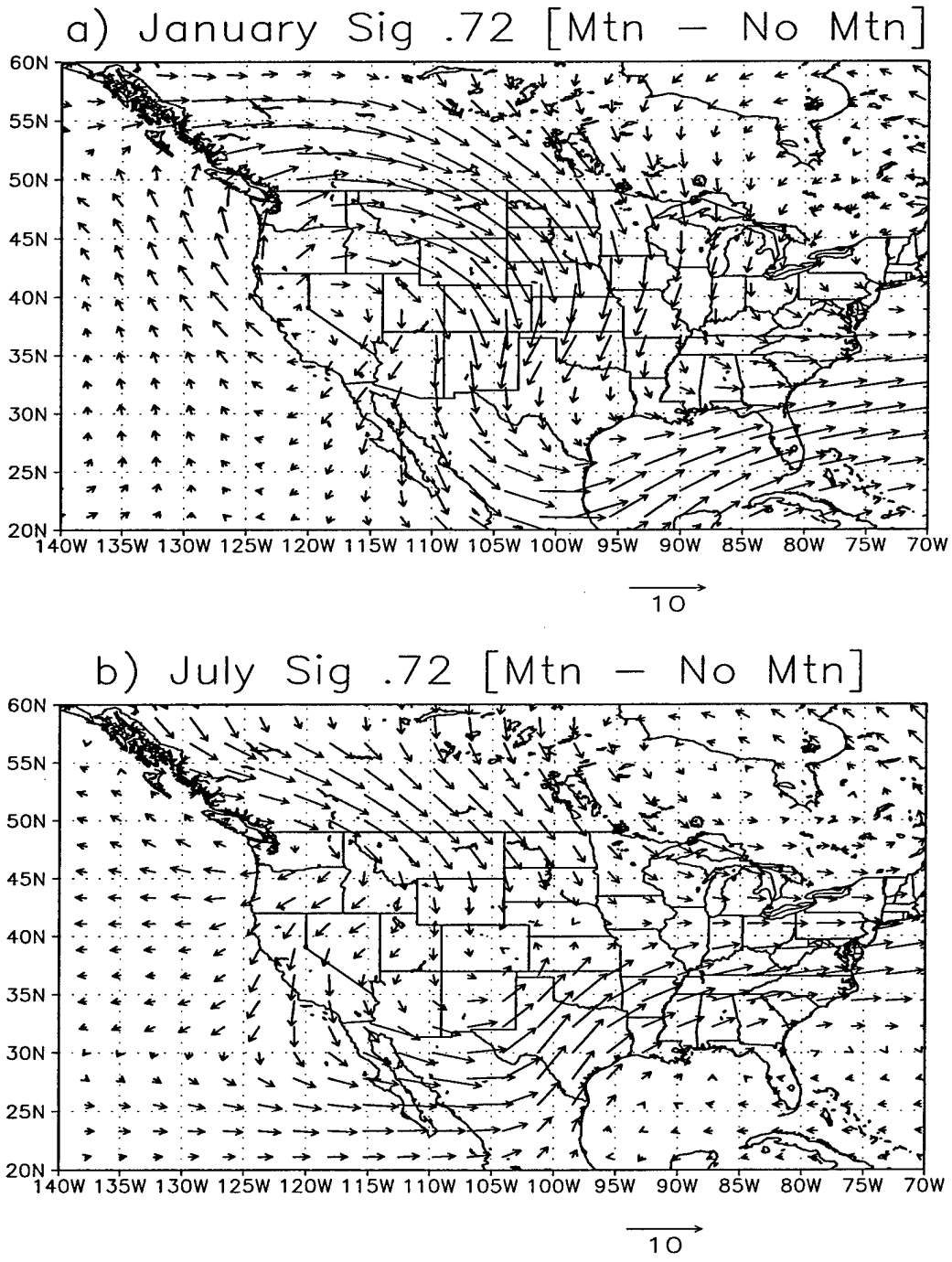


FIG. 4.16. Orographic effect for a 20-level, adiabatic version of the UGM, truncated at wave number 42, for month long integrations of the January (a) and July (b) climatological averages. The panels represent the average difference in wind vectors (m/s) between simulations with and without orography (mountain minus no-mountain) over North America for the last 30 days of 40-day simulations at sigma level 0.72.

mountains extending into Mexico. The orographic effect for July produces cyclonic curvature within the lower troposphere above the central Rocky Mountains (Fig. 4.16b) and southwesterly flow east of the mountains over the southern Great Plains.

The mechanical effect of the UGM (Fig. 4.16) is now compared to reanalyzed, climatological features of the low-level circulation flanking the orography over western North America during summer and winter, described in Chapter 2. The data are based on a 50-year record (1951-2000) of monthly averaged circulations from the NCEP/NCAR Reanalysis.

Fig. 2.7 shows the seasonal composites of the eddy height and wind fields for June to August (JJA) (Fig. 2.7a), and December to February (DJF) (Fig. 2.7b), for the years 1951-2000. The eddy fields are constructed by subtracting the zonal mean from the climatological average. The winter composite at 700 mb shows an anticyclone over the western U.S., centered near southeastern Washington (Fig. 2.7b). A trough becomes prominent in summer, centered just off the west coast of California (Fig. 2.7a). The spring and autumn fields (not shown) have intermediate patterns to summer and winter. The spring configuration is more similar to summer, while the fall is more similar to winter. Paegle et al. (1987) showed the upper troposphere exhibits ridge-trough reversals beginning in northern spring. The 850-mb eddy wind field for JJA (see Fig. 4.1a) displays the Great Plains LLJ over the western Gulf of Mexico and Texas.

The annual march of relative vorticity, area averaged from 30°N-50°N and 130°W-110°W has been described in Chapter 2 (Fig. 2.8). The area average has been taken in the vicinity of the circulation reversals shown in Fig. 2.7. The full and eddy fields (Fig. 2.8a and 2.8b, respectively) clearly indicate a winter anticyclone and spring cyclone near the

west coast of North America, with the strongest values of cyclonic (positive) vorticity occurring in May (full field) and June (eddy field).

The mean, cyclonic circulation during summer may be partly explained by seasonally reversing heating/cooling influences on elevated plateaus. Comparison of the orographic effect of the UGM in Fig. 4.16 with reanalyzed eddy fields in Fig. 2.7 suggests that the mechanical effect of orography also plays a prominent role in the seasonal reversals over the Rocky Mountains and indirectly supports the relevance of this mechanism to observed intraseasonal oscillations described in section 4.2 and modelled events in section 4.3.

The flood and drought ensembles presented in section 4.3 may be examples in which the orographic mechanism influences predictability over the MRB through ambient flow interaction with the Rocky Mountains. In this section, the potential for longer-term (e.g., intraseasonal) predictability and further understanding of the seasonal reversals based on this mechanism have been discussed. Previous studies have also described anomalously strong (weak) ambient flows in the upper troposphere and their persistence over the Rocky Mountains during the summer of 1993 (1988) (e.g., Mo et al., 1995 and Mo et al., 1991, respectively). It is hypothesized that the classic theory of ambient zonal flows over topography may provide an alternative mechanism for enhanced predictability of such features. The theory may apply to the subtropical Andes region, discussed in Chapter 2, as well as the Rocky Mountain region discussed in this chapter.

Predictability over North America in winter is discussed in the next chapter. Episodic enhancement of medium range predictability during winter is examined for anomalous initial states over the western U.S.

# CHAPTER 5

# WINTER CASES OVER NORTH AMERICA

## 5.1 Introduction

Precipitation prediction has remained a difficult challenge on both climate and shorter scales (e.g., 12-36 hours). Fritsch et al. (1998) discussed the very slow rate of improvement in quantitative precipitation forecasting (QPF) during the past decade. The complexity of orography, such as that over western North America, adds to this forecast challenge, and has been the subject of various field campaigns during recent winters. Orographic precipitation processes in Oregon's Cascade Mountains were a component of the Improvement of Microphysical Parametrization through Observational verification field experiment (IMPROVE) (Stoelinga et al., 2003). The Intermountain Precipitation Experiment (IPEX) focused on the Great Basin during February 2000 (Schultz et al., 2002). Gartner et al. (1996) partly motivated IPEX in documenting that Eta model QPF skill over the Intermountain West and eastern Rocky Mountains ranked the lowest in the U.S.

Smith et al. (1997) identified research needs and opportunities in mountain meteorology and summarized some of the difficulties in QPF and verification over complex terrain. They pointed out that while topography may locally enhance precipitation predictability by organizing precipitation, small shifts in ambient flows, which may be undetected in models, will cause a shift in which slopes favor heavy

precipitation. White et al. (1999) highlighted the difficulty of forecast verification over the western U.S., where gridded observations may contain lower resolution than forecast models. Medium range precipitation predictability over western North America has not received as much attention as predictability at shorter and longer (e.g., El Niño Southern Oscillation (ENSO)) time scales.

This chapter explores medium range predictability in winter cases of anomalous, upper troposphere zonal flows over the western U.S. Results from 15-day simulations using a variety of global model configurations are presented to diagnose the predictability of precipitation and large scale features.

The importance of second-week predictability of extreme events for both societal and economic benefit has been recognized by scientists involved in THORPEX, an international research program (Shapiro et al., 2003 and references therein). Goals of THORPEX include improving "high-impact" weather forecasts in the 1-14 day range. Shapiro et al. (2003) and others (e.g., Simmons and Hollingsworth, 2002) have noted that the limit of predictability is generally 7 days for synoptic scale weather systems and the associated high-impact weather occurring on smaller scales. The limits were attributed to initial state and data assimilation uncertainties, model uncertainties, and so-called "intrinsic uncertainties" that are unresolved in models.

Chapters 2 and 4 have explored the seasonal cycle and deviations from climatology around the Andes, Rockies and Tibetan plateau, focusing on the summer season. In the former two regions, low-level jet (LLJ) and precipitation responses occur east of the mountain ranges. These may be related to variations of ambient zonal flows interacting with orography during summer. The LLJ is a component of the mean, lower troposphere,

eddy cyclonic circulation which persists around the Andes and Rockies during summer. A preliminary conclusion is that if anomalously strong and broad, upper-level zonal flow exists over the orography, then the associated large inertia will promote predictability in all components, including the LLJ (e.g., the Great Plains LLJ) and precipitation, for a relatively long period.

The conclusion is based on 13-day, global, ensemble forecasts during the summer, 1993, Mississippi River basin (MRB) floods and the extreme summer droughts over the region in the spring and early summer of 1988 (Chapter 4). Some basin scale representation of observed precipitation features is evident into the second week of the forecasts. This implies longer predictability of extreme summer events than some other prior studies. It is now hypothesized that similar predictability enhancement occurs in winter cases of highly anomalous zonal flows over western North America.

Diagnostics from the NCEP/NCAR Reanalysis (Kalnay et al., 1996; Kistler et al., 2001) are presented in Section 5.2. Temporal correlations based upon a 50-year record suggest that winter precipitation is more intense over the western U.S. when the area averaged, upper troposphere, zonal flow is stronger than normal over that region. Subsequent sections explore the predictive signal during extremes in zonal flows over the western U.S.

Section 5.3 describes the models and experimental set up. Global model forecasts are selected based upon weak and strong, upper troposphere, anomalous zonal flows impinging upon the Rocky Mountains. Years of anomalously strong zonal winds are wetter over the region, while years with anomalously weak zonal winds are relatively drier. Simulations with 4 model configurations are examined: (1) the uniform resolution

Utah Global Model (UGM) (Paegle, 1989), with wave number 42 truncation on 20 levels; (2) the NCEP Medium Range Forecast system (MRF) Reforecasts, available from the Climate Diagnostics Center (Hamill et al., 2004), with wave number 62 truncation on 28 levels; (3) a rotated, variable resolution version of the UGM, which allows two-way interaction between an inner, 1° resolution region centered around the Rockies and an outer, 2° resolution global domain; and (4) a rotated, variable resolution "stretched" grid version of the UGM, which has a maxiumum of 0.5° resolution over the western U.S. Global simulations of the uniform resolution UGM, introduced in section 5.4, are able to delineate between the wet and dry regimes.

Model precipitation forecasts are compared in section 5.5. Ratios of accumulated precipitation comparing strong zonal flow (wet) and weak zonal flow (dry) events are used to assess how well the models distinguish extreme precipitation events over the western U.S. Model forecasts are able to delineate qualitatively between the wet and dry conditions 5 and 10 days into the forecast.

Section 5.6 evaluates model skill for larger scales with anomaly correlations of 500-mb geopotential heights. The composites for each model exhibit greater skill than typically found in the second week of the forecasts. Section 5.7 provides further interpretation.

## 5.2 Deviations from Winter Climatology

The Rocky Mountain region has a pronounced reversal in the low-level atmospheric circulation between summer and winter (e.g., Fig. 1.1a,b, and Fig. 2.7). The transition from a winter anticyclone to a summer cyclone is often described in terms of thermal influences, such as "thermal low" in summer; or "cold-core anticyclone" and associated

stagnant conditions in winter. Peyrefitte (1986) analyzed Great Basin surface anticyclones from 1962-1977. He found an anticyclone 64% of the time when snow cover over the plateau was 80% or more. He could not identify an instance during the 15 years when the plateau anticyclone persisted for more than 3 days with no snow cover. Gutzler and Preston (1997) examined winter snow cover as it related to summer convection over the Southwest and suggested a thermal explanation for the seasonal oscillations. They described surface heating in relation to dry and wet soils that occur in dry and snowy winters, respectively. This research suggests an alternate explanation for the winter anticyclone and the winter-summer seasonal reversal in the circulation, emphasizing dynamical processes associated with changing zonal flows over the Rocky Mountains (Chapters 2 and 4).

Fig. 5.1 shows the time correlation (1951-2000) during winter (DJF) between the area averaged, 200-mb zonal flow in the outlined box (30°-50°N, 130°-100°W) with 700-mb wind at all locations on the map. The eastward (northward) component of the vectors indicates the magnitude of the correlation coefficient between the area averaged, upper tropospheric wind in the box against the local zonal (meridional) flow component at 700 mb. Correlation coefficents of 0.3 are statistically significant with a 99% confidence level. The counterclockwise (cyclonic) orientation of the correlation vectors over western North America suggests that increased upper troposphere zonal flow over the mountains (given by the area average in the box) is associated with a weakened 700-mb eddy anticyclone (Fig. 2.7b) over the region.

Chapter 1 introduces a time correlation (1951-2000) between area averaged, 200-mb zonal flow in the same box with precipitation during winter (Fig. 1.5). The highest

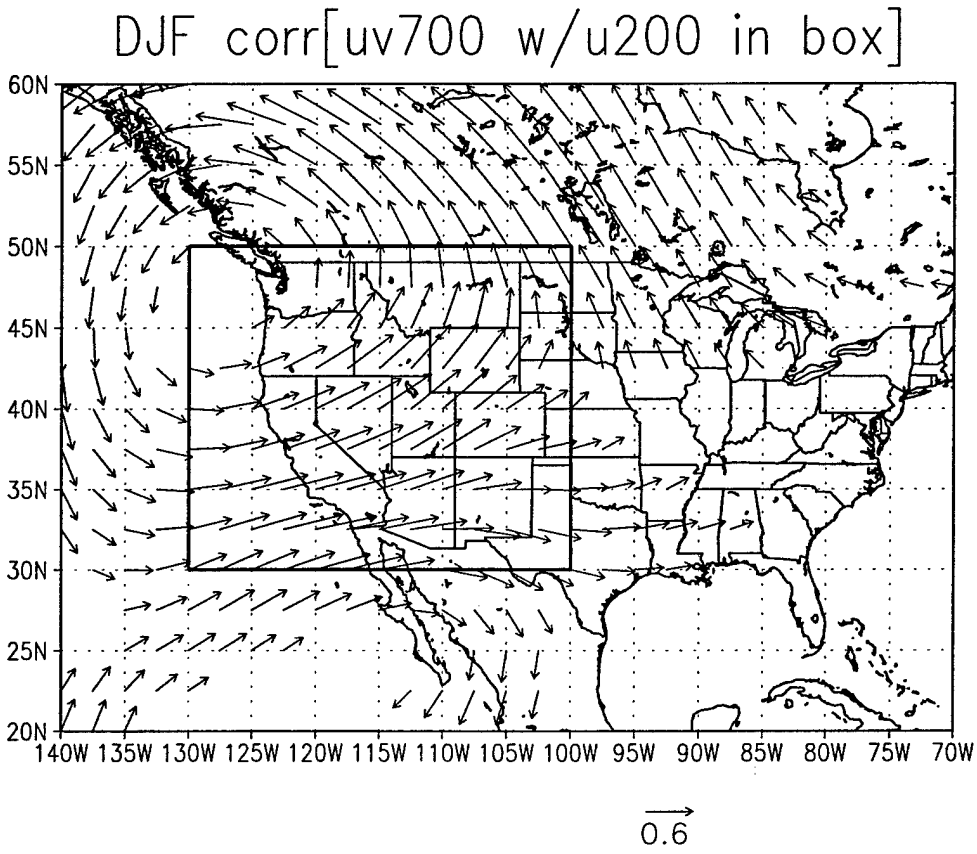


FIG. 5.1. Time correlation over North America (1951-2000) during winter (DJF). Correlation vectors of the area averaged, 200-mb zonal wind in the outlined box (30°N-50°N, 130°W-100°W) with 700-mb wind at all locations. The magnitude of correlation vectors is indicated at the bottom of the panel, and only coefficients meeting the 99% statistical significance criteria (0.3) are plotted.

correlation coefficients are centered over the western U.S., suggesting a precipitation response that affects winter hydrology and snow pack generation over high terrain. The region of highest correlation (0.6) extends from northern California and southern Oregon to the Intermountain West (Fig. 1.5).

Enhanced upper troposphere westerlies should tend to weaken the climatological anti-cyclone over the western U.S. (section 2.6), and may lead to more transient storm tracks. Anomalously strong, zonally averaged winds may be promoted over the northeast Pacific Ocean and into western North America, for example, during warm, ENSO events. The correlations presented above are not particularly sensitive to whether the longitudinal extent of the box is over land or just off the west coast of North America. For example, results are similar if the westward extent of the box for the area average is confined more to the continent at 120°W-100°W.

## 5.3 Model Methodology

### 5.3.1 Experimental Set up

Global simulations are used to examine how ambient zonal flow anomalies may influence predictability during winter over western North America. January months characterized by anomalous, upper troposphere zonal flow impinging upon the Rocky Mountains were selected. A time series of January, area averaged, 200-mb, westerly flow is depicted in Fig. 5.2 (1949-2000) from the NCEP/NCAR Reanalysis. The area average is taken over the region portrayed by the box in Fig. 5.1. The average, 200-mb zonal flow in the box during January for all years is 25.2 m/s (dashed line). Januaries with zonal flow exceeding the average by at least 1.2 standard deviations are referred to as "u200hi," and those for which the average zonal flow is at least 1.2 standard deviations below the aver-

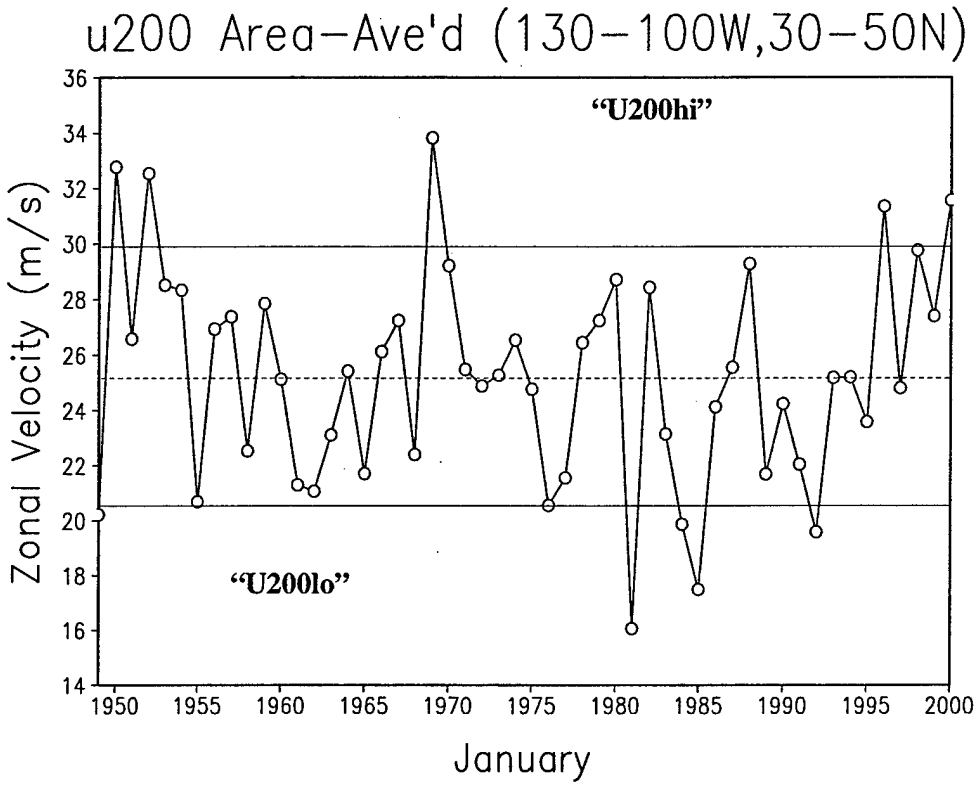


FIG. 5.2. Climatology of the area averaged, 200-mb zonal flow over western North America during January (30°N-50°N, 130°W-100°W), 1949-2000. The dashed horizontal line indicates the 52-year mean (25.2 m/s). Solid lines are drawn to indicate plus and minus 1.2 times the standard deviation from the mean.

age are referred to as "u200lo" cases. The strong flow years ("u200hi) have an area average 200-mb zonal flow of approximately 32 m/s, while the years of weaker zonal flow ("u200lo") average about 19 m/s. U200hi years are 1950, 1952, 1969, 1996 and 2000; and u200lo years are 1949, 1976, 1981, 1984, 1985 and 1992.

### 5.3.2 Uniform Resolution UGM and MRF Reforecasts

The uniform resolution UGM is initialized on 10 January at 00 UTC during each u200hi and u200lo year, and forecasts are made to 15 days (360 hours). The UGM is a multilevel, primitive equation version of the model described by Paegle (1989). Initial conditions are hourly NCEP/NCAR Reanalysis fields, except for latent heat flux, which is specified over the globe from the monthly-averaged Reanalysis climatology for January (1951-1999). Additional detail on the uniform resolution UGM configuration is provided in section 4.3.1.

The Climate Diagnostics Center has provided forecasts from the MRF Reforecast project (Hamill, 2003; Hamill et al., 2004). Ensemble average and individual ensemble member forecasts are available with wave number 62 truncation, 28 levels in the vertical, and they have been initialized with NCEP/NCAR Reanalyses. Bred modes of 15 members comprise the ensemble average forecasts (Toth and Kalnay, 1997), and they are based upon NCEP's operational MRF model during January to June 1998 (Caplan et al., 1997; Wu et al., 1998). The data are available through the worldwide web at cdc.noaa.gov/~jsw/refcst/, from 1979-2003. U200hi and u200lo (see section 5.3.1), 12-hour accumulated precipitation and 500-mb geopotential heights (every 24 hours) for the ensemble average forecasts initialized 10 January, 00 UTC were obtained. The u200hi years within this time frame are 1996 and 2000 (Fig. 5.2). The u200hi MRF composite forecasts presented in

sections 5.5 and 5.6 therefore represent an ensemble of 30 members (15 per year). The u200lo years available are 1981, 1984, 1985 and 1992, representing 60 ensemble members. The MRF sampling of strong and weak wind events is somewhat small and unbalanced, and is limited by the January cases that fall within the years of the MRF Reforecast project (1979-2003). The MRF sample is increased (section 5.6) by considering strong and weak zonal flow cases occurring in December, January and February. MRF u200hi and u200lo ensembles are analogous to the definition of "ensemble" used for simulations of the summer 1988 droughts and 1993 floods (Chapter 4). In Chapter 4, a single version of the uniform resolution UGM was initialized with different global reanalyses (NCEP/ NCAR and ECMWF) over 1 week during the respective drought and flood years.

### 5.3.3 Rotated, Variable Resolution UGM

Topographic representation should be improved to increase accuracy of precipitation forecasts. This may be accomplished with the UGM by applying rotated, variable resolution, as outlined in Fig. 5.3 (details are also provided in section 3.2.2). Fig. 5.3a shows the uniform resolution grid in the usual spherical coordinate. It depicts the same grid that is used for the uniform resolution UGM cases, with 129 points in longitude and 82 points in latitude. Contours of topography represent the Rocky Mountains as a broad massif, with peaks under 2500 m.

The rotated approach takes advantage of the convergence of the meridians and therefore closer spacing between grid points near the polar regions. Higher local resolution benefits from reduced horizontal diffusion, which is proportional to the latitudinal grid spacing. Lower diffusion favors a more realistic evolution of circulation and precipitation features.

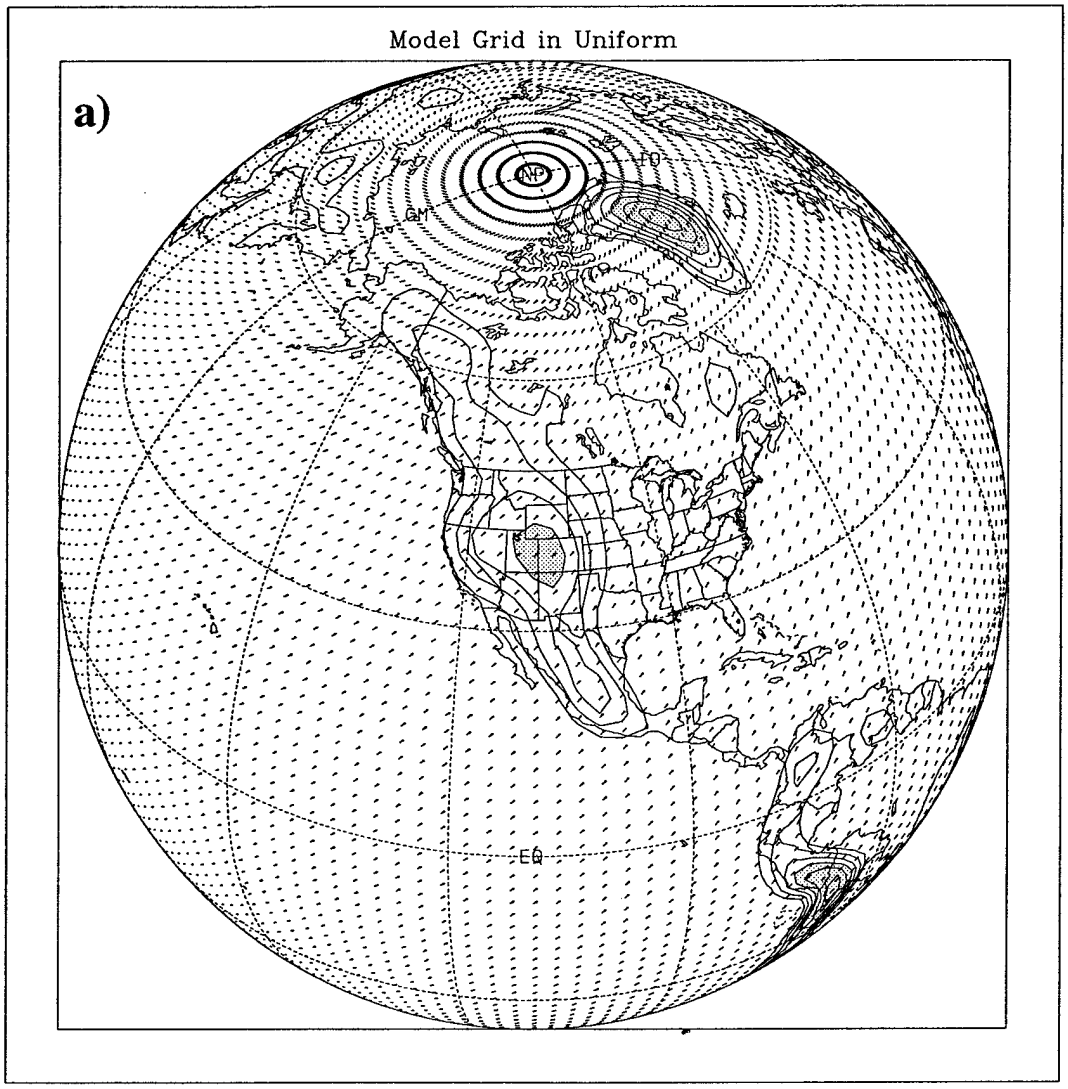


FIG. 5.3. Utah Global Model grid. (a) Contours of topography with uniform model resolution, 129 points in longitude, 82 points in latitude. (b) Two-way nested grid. The mathematical pole has been rotated to 40°N, 110°W. Latitudinal resolution is equally spaced, 1° north of 44°N to the rotated pole, and equally spaced, 2°, south of 44°N for a total of 115 points in latitude. (c) Stretched model grid. The mathematical pole is rotated to 40°N, 110°W. Latitudinal resolution is 0.52° at the rotated north pole, and spacing increases gradually by 1% with each grid point from north to south. Latitudinal spacing is 2.3° at the rotated south pole. The total number of latitudinal points is 152. The number of points in longitude remains unchanged in (b) and (c) (129 points or 2.8° spacing). Orography contours are every 500 m, and topography higher than 2000 m is shaded.

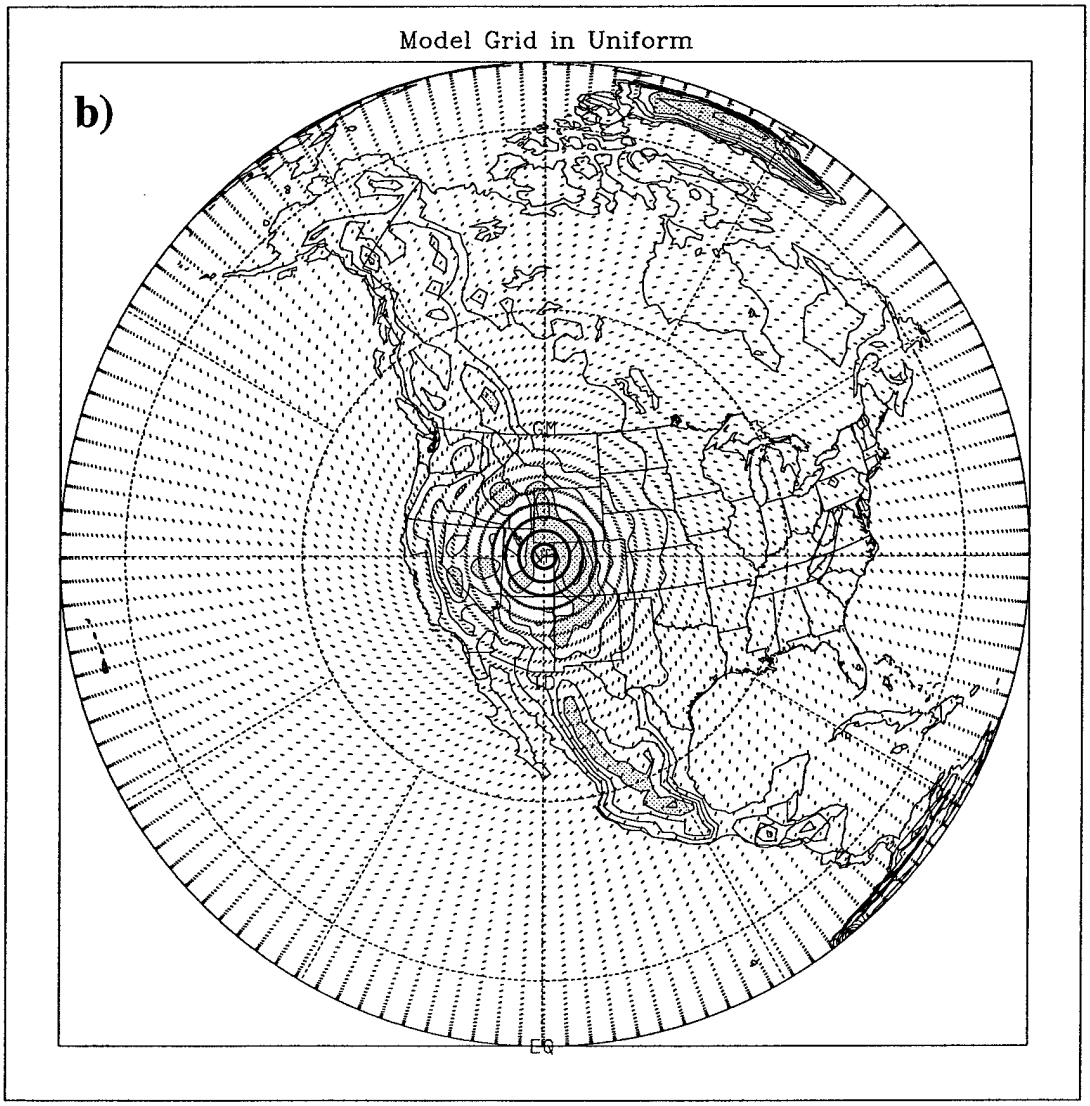


Fig. 5.3, continued.

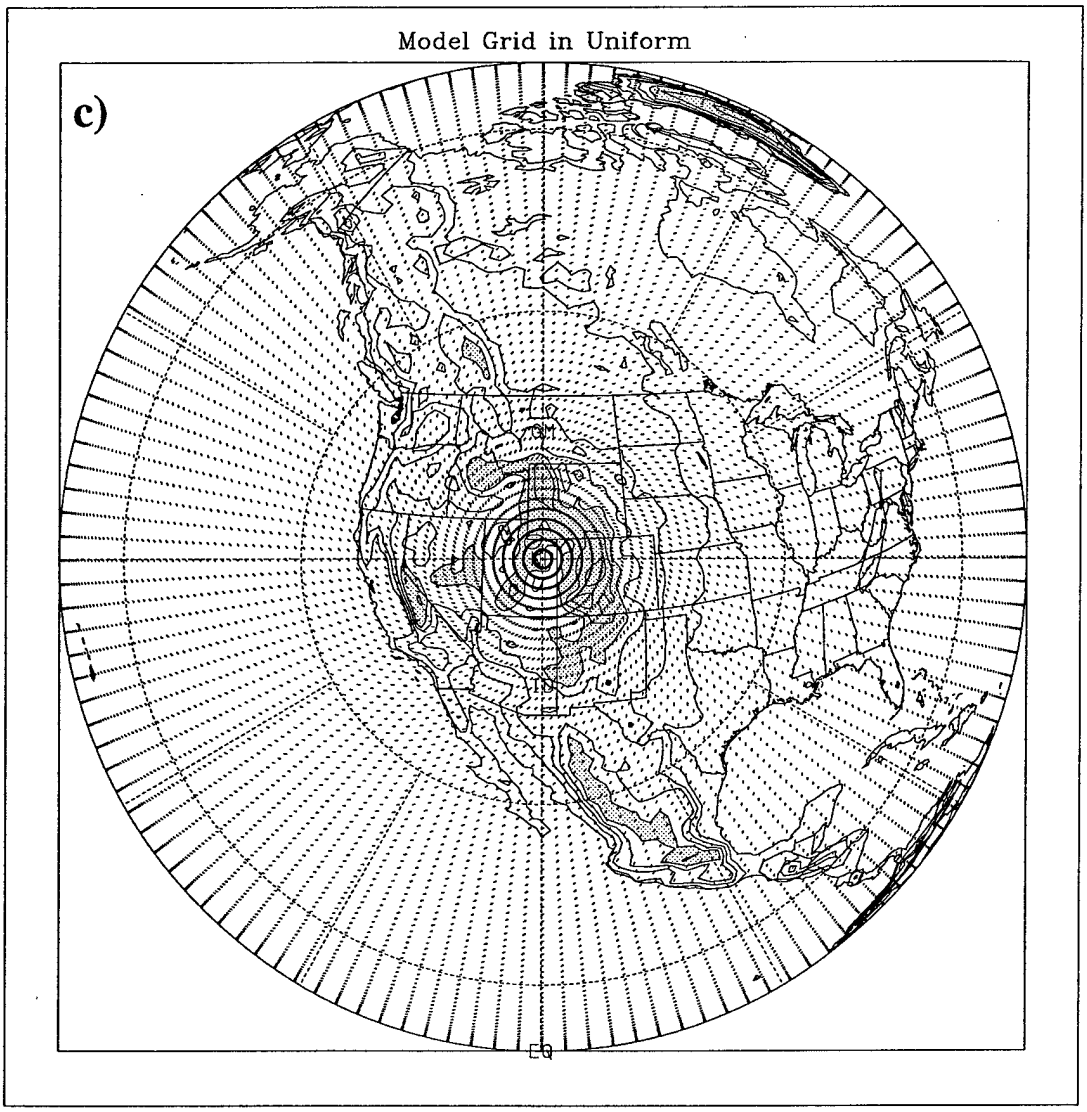


Fig. 5.3, continued.

The mathematical pole is rotated to 40°N, 110°W over northeastern Utah (Fig. 5.3b). The total number of latitude grid points is increased to 115, with longitudinal points remaining unchanged. The vertical grid contains 23 levels. Higher resolution near the mathematical north pole is obtained by increasing the concentration of latitudinal grid points north of 44°N while decreasing the resolution to the south (Fig. 5.3b). The first set of variable resolution experiments applies equally spaced, 2° latitude increments from the south pole, northward to 44°N, as in Fig. 5.3b. Resolution is increased to uniformly spaced, 1° latitude increments from 44°N to the north pole. Representation of the Rocky Mountains is improved, with peaks above 3000 m over Colorado. The Wasatch Mountains and Wind River range are delineated, as well as the Sierra Nevada range (Fig. 5.3b). This set of experiments will be referred to as "two-way nested" runs.

A second rotated, variable resolution configuration employs a stretched grid approach (Fig. 5.3c), and will be referred to as the "stretched" model. Resolution in latitude is 0.5° at the rotated north pole, located over Utah, as before (40°N, 110°W). Latitudinal grid spacing increases gradually by 1% with each grid point from north to south. The configuration also has 129 points in longitude, but latitudinal points have been increased to 152. The grid spacing gradually increases southward, so that the spacing at the rotated south pole is 2.3°. Topographical representation (Fig. 5.3c) is improved (compare to Fig. 5.3a and b). As examples, the Uinta Mountains east of the Great Salt Lake appear, as well as some of the other principal ridge heights of the Rockies. The Sierra Nevada Range becomes more clearly resolved over California.

The time step for the variable resolution simulations is 400 seconds, and integrations are run to 15 days. The model is initialized with NCEP/NCAR Reanalyses, as in the

uniform resolution UGM experiments and the MRF Reforecasts. Graphical representation of model output requires interpolation to a uniform resolution grid. For each of the variable resolution approaches outlined above, global output is interpolated to a uniform, 1° grid.

## 5.4 Uniform Resolution UGM Precipitation and Wind Verification

Results of the simplest forecasts are presented using the relatively low resolution version of the UGM. More advanced, variable resolution simulations with the UGM and ensemble forecasts from the MRF are summarized in section 5.5. The more advanced experiments enhance certain components of the predictions, but the fundamental predictability hypothesis also finds support in simpler, uniform resolution experiments, presented next.

Composites of precipitation accumulation are shown in Fig. 5.4. Fig. 5.4a depicts observed, 15-day precipitation totals averaged for years with significantly stronger than normal 200-mb zonal flow across the central Rocky Mountains (u200hi), and Fig. 5.4b presents averaged uniform resolution UGM forecasts for these cases. Observations are from the Climate Prediction Center's (CPC's) Unified data set of daily averaged precipitation over the continental U.S. (Higgins et al., 1996), and consist of station observations interpolated to a 0.25° x 0.25° grid using a Cressman scheme. Measurable precipitation covers a large portion of the western U.S., including Washington, Oregon and California, with peaks greater than 30 cm over the Sierra Nevada Range (Fig. 5.4a). Precipitation is also oriented north-to-south across Idaho. Observations of the 5 case, u200hi composite support the interannual signal of precipitation related to upper troposphere zonal flow over the region during winter (Fig. 1.5).

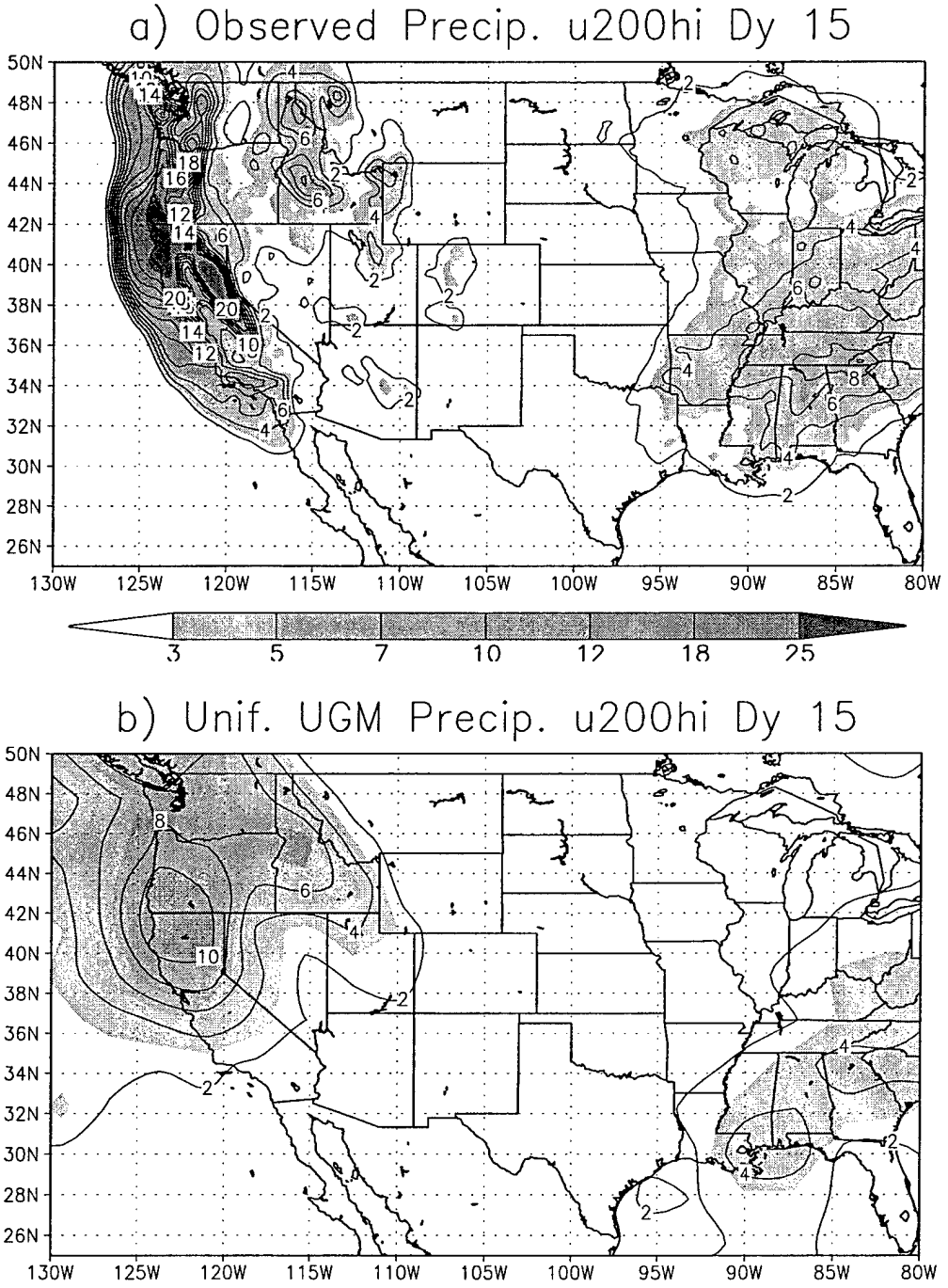


FIG. 5.4. Average precipitation accumulation for the 5, u200hi composites (cm). (a) Observed, 15-day accumulation (10-24 January 1950, 1952, 1969, 1996 and 2000). (b) 15-day accumulation of the uniform resolution UGM. The contour interval is 2 cm in (a) and (b) (contouring in (a) is up to 20 cm). Shading is for accumulation greater than or equal to 3 cm. The maximum observed accumulation in (a) is 33 cm.

Fig. 5.5 shows 15-day observed and predicted precipitation accumulation from the uniform resolution UGM for the composites with anomalously weak, upper troposphere zonal flow across the Rocky Mountains (u200lo). Accumulations during the u200lo years (Fig. 5.5a) are much smaller along the western coastal states (12 cm maximum over Washington), and the Intermountain West is dry compared to the u200hi composite (Fig. 5.4a). Average, u200lo predicted precipitation accumulation is depicted in Fig. 5.5b. The forecast is much drier, with a peak over the U.S. less than half the maximum of the u200hi prediction. Model results are smoothed relative to observations, owing to the coarser model grid (2.8° longitude x 2.2° latitude) compared to the CPC Unified grid (Fig. 5.4 and Fig. 5.5). The areal extent of accumulated precipitation is fairly representative in both sets of experiments, but peak magnitudes are underrepresented.

Time evolution of area averaged, accumulated precipitation for a box encompassing most of the western U.S. (124°-110°W, 34°-49°N) is displayed in Fig. 5.6. Observations (CPC Unified) show more than five times more precipitation for u200hi than for u200lo composites. The u200hi model ensemble curve closely matches observations for about 96 hours (4 days), then slightly under predicts accumulations to 216 hours (9 days). By around 240 hours (10 days), model accumulations level off compared with observations, predicting about 83% of the observed accumulations by the 15-day point. Area averaged, u200lo observed precipitation accumulation is under 1.5 cm after 15 days. The UGM over predicts the 15-day u200lo accumulation by about 40%. Model forecasts produce more than twice the precipitation in the u200hi simulations as in the u200lo ones at both 240 and 360 hours (10 and 15 days), suggesting they are able to distinguish between the relatively wet and dry extremes. The observed climatology is also included in Fig. 5.6.

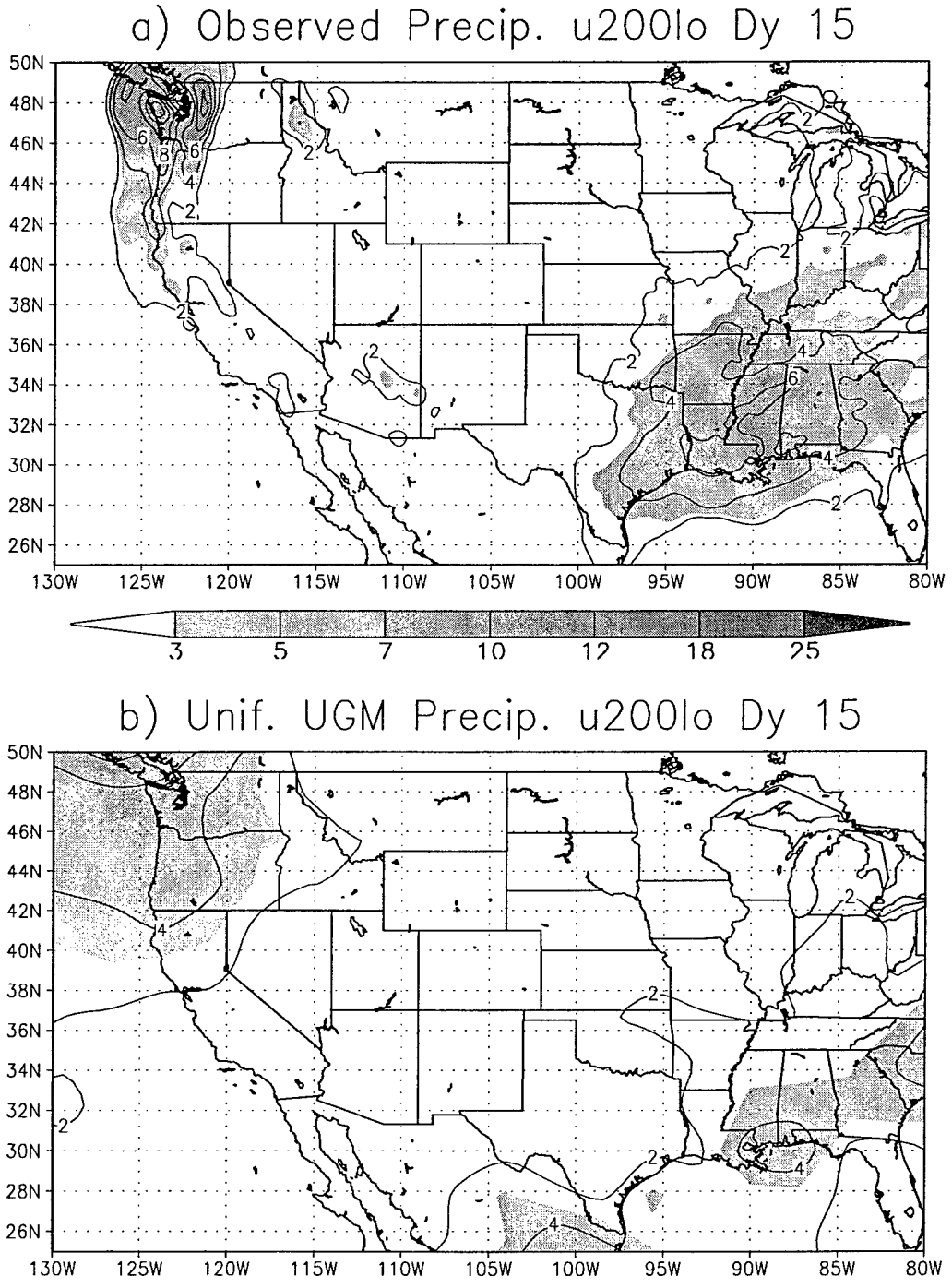


FIG. 5.5. Average precipitation accumulation for the 6, u200lo composites (cm). (a) Observed, 15-day accumulation (10-24 January 1949, 1976, 1981, 1984, 1985 and 1992). (b) 15-day accumulation of the uniform resolution UGM. The contour interval is 1 cm in (a) and (b). Shading is for accumulation greater than or equal to 3 cm.

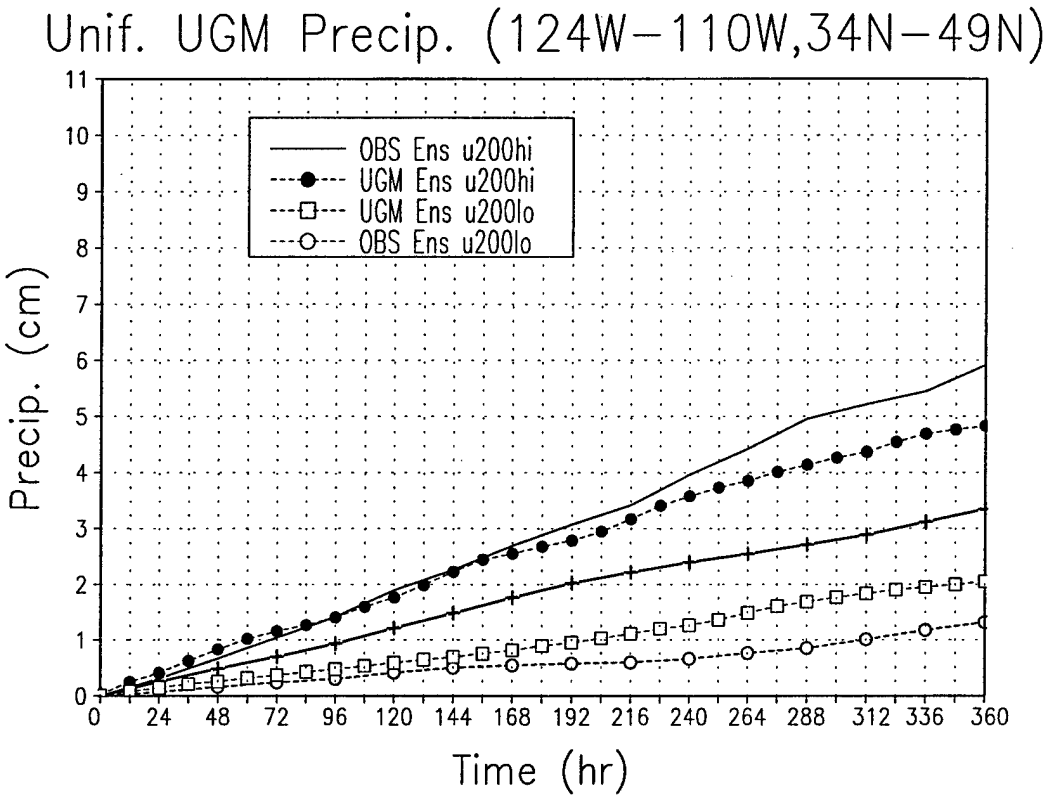


FIG. 5.6. Composite u200hi and u200lo, area averaged precipitation accumulation (cm) (124°W-110°W, 34°N-49°N) from observations and the uniform resolution UGM. Time 0 is on 10 January. Observations are from the CPC Unified data set (Higgins et al., 1996). The line labelled with (+) marks indicates the 30-year CPC climatology of 10-24 January precipitation accumulation over the same region from 1970-2000 (excluding 1973).

The model, area averaged precipitation for the winter, u200hi composite (Fig. 5.6) does not significantly diverge from observations until about 240 hours (10 days) into the forecast.

Fig. 5.7 shows the daily evolution of the area averaged, upper troposphere zonal wind for the uniform resolution UGM ensembles over the Rocky Mountain region (130°W-100°W, 30°N-50°N). The 200-mb zonal flow in the Reanalysis ranges between about 32 and 40 m/s for the u200hi cases. It is weaker in the u200lo cases, between approximately 16 and 21 m/s. The UGM ensemble forecasts are fairly representative of the reanalyzed, upper troposphere zonal flows during the 15 days. For the u200hi ensemble, the UGM zonal flow at sigma level 0.22 closely resembles that of 200 mb in the Reanalysis between days 9 and 11. The u200hi, area averaged, precipitation accumulation is also representative at 10 days, under predicting observations by about 0.4 cm (Fig. 5.6). The next section addresses the precipitation forecasts of other model configurations over the western U.S. and examines the extent to which they delineate between wet and dry events.

## 5.5 Comparison of Precipitation Forecasts

Precipitation accumulation and wind verification for the uniform resolution UGM (section 5.4) suggest predictability into the second week. This section assesses the extent to which other model configurations are able to delineate between u200hi and u200lo precipitation (section 5.5.1). Maps of 10-day accumulations are also presented (section 5.5.2).

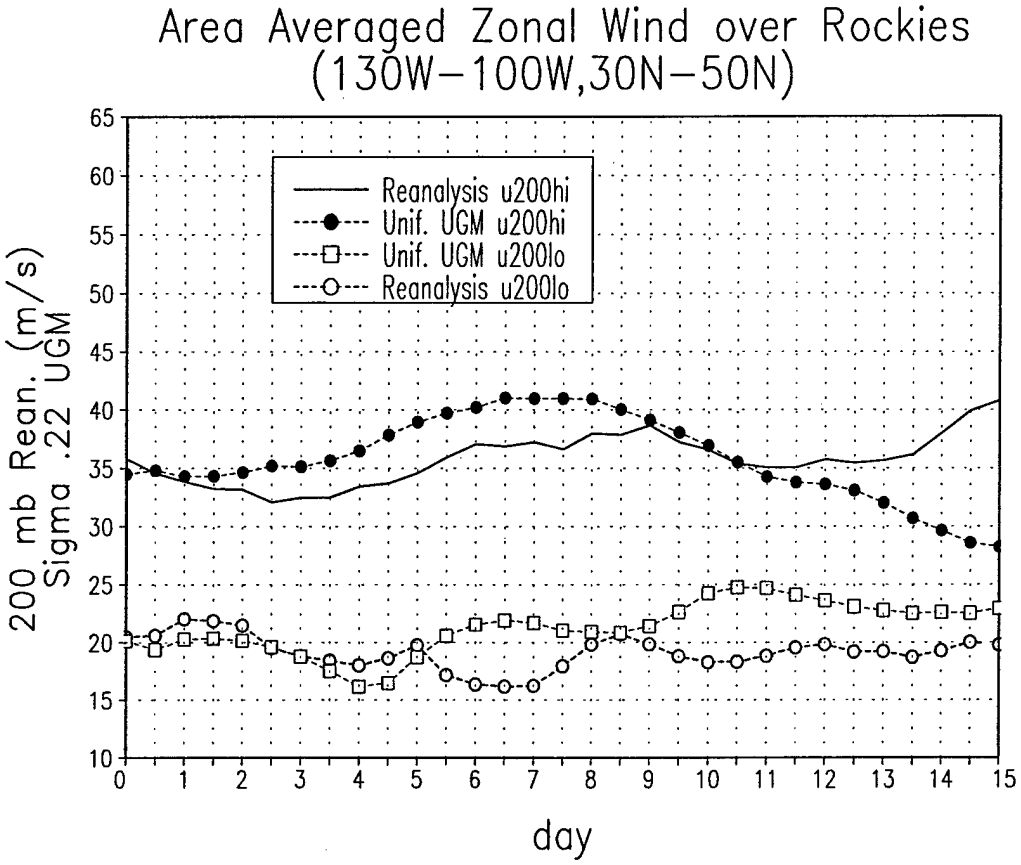


FIG. 5.7. Composite u200hi and u200lo, area averaged, upper troposphere zonal wind (m/s) (130°W-100°W, 30°N-50°N) from the NCEP/NCAR Reanalysis and the uniform resolution UGM. The 200-mb zonal flow is plotted for the NCEP/NCAR Reanalysis, and the sigma level 0.22 zonal flow is plotted for the uniform resolution UGM.

### 5.5.1 Area Averaged Accumulations

A ratio of accumulated precipitation between u200hi and u200lo composites is presented for the western U.S. and several subregions. Fig. 5.8 shows the regions over which the area averaged precipitation is calculated. Area I is a broad region of the West (Fig. 5.8a). It corresponds to the area average for which precipitation is calculated for the uniform resolution UGM in Fig. 5.6. Additional regions are depicted in Fig. 5.8b (II: northern states; III: California, Nevada; IV: Colorado basin). Along with I-IV, precipitation ratios for the combined area average of locations III and IV are also presented. Ratios of accumulated precipitation are presented in Tables 5.1-5.5.

Table 5.1 shows the ratio of u200hi to u200lo precipitation accumulation at days 5, 10 and 15 over region I of Fig. 5.8 (western U.S.). The first two models listed have uniform resolution ("Uniform UGM" and "MRF Reforecast"), and the others are the variable resolution UGM configurations ("UGM two-way grid" and "UGM Stretched grid"). Observed, CPC Unified precipitation ratios are in parentheses. Observed ratios of the MRF Reforecasts are different from the other three models because the former are a subset of the years comprising the 52-year time series (Fig. 5.2). They are limited by the u200hi and u200lo cases falling between 1979-2003 (2 u200hi and 4 u200lo cases). Over region I (Table 5.1), all models produce ratios greater than 2 at day 5, suggesting they differentiate between the observed wet and dry extremes. The MRF Reforecast is the lowest (2.6 compared to 4.9 observed). By day 15, the models' ability to distinguish between wet and dry events is clearly degraded. Only the uniform resolution UGM has a ratio above 2. Similar conclusions hold for the sub-basins and are summarized in the tables above.

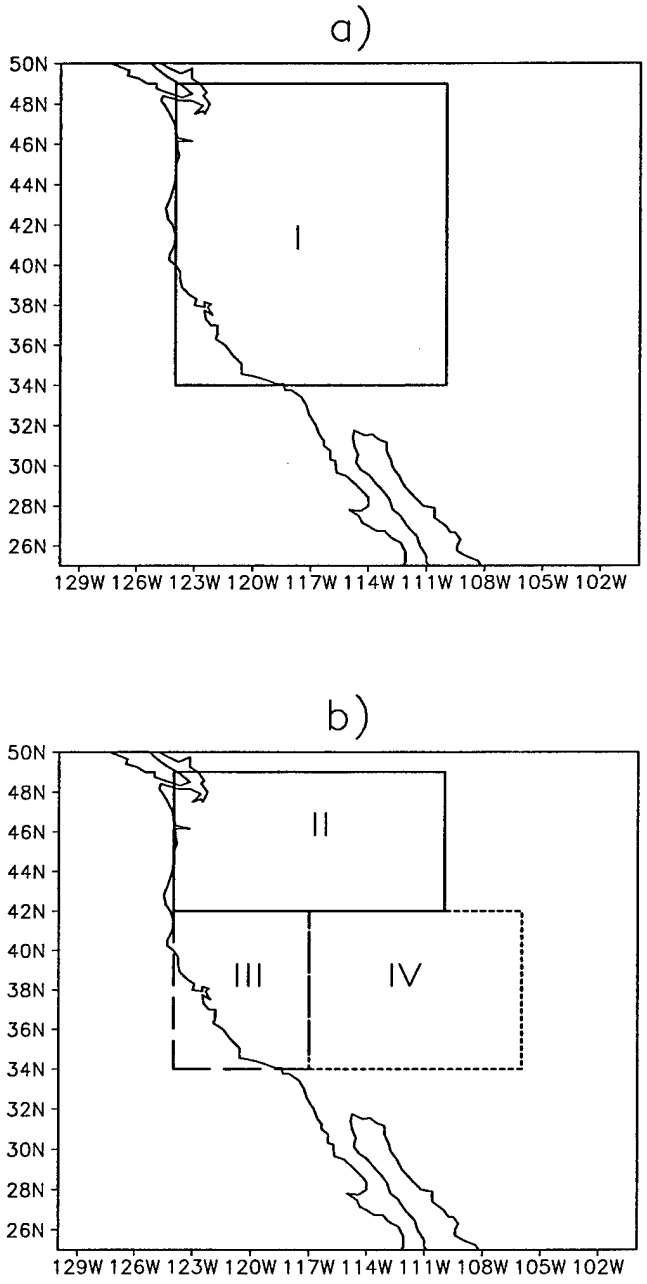


FIG. 5.8. Regions over which the area average precipitation accumulation is calculated for model forecast comparisons. (a) Region I (western U.S.); (b) region II (northern states); region III (California, Nevada) and region IV (Colorado River basin).

Table 5.1. Ratio of area averaged u200hi to u200lo precipitation over region I denoted in Fig. 5.8.

| Model Configuration | Day 5 | Day 10 | Day 15 |
|---|---|---|---|
| Uniform UGM | 3.0 (4.1) | 2.8 (5.4) | 2.4 (4.2) |
| MRF Reforecast | 2.6 (4.9) | 2.0 (7.9) | 1.6 (4.2) |
| UGM two-way grid | 3.2 (4.1) | 2.3 (5.4) | 1.3 (4.2) |
| UGM Stretched grid | 3.2 (4.1) | 1.9 (5.4) | 1.3 (4.2) |

*Parentheses denote ratio of observations.

Table 5.2. Ratio of area averaged u200hi to u200lo precipitation over region II denoted in Fig. 5.8.

| Model Configuration | Day 5 | Day 10 | Day 15 |
|---|---|---|---|
| Uniform UGM | 2.1 (3.2) | 2.3 (3.8) | 2.1 (3.1) |
| MRF Reforecast | 2.1 (5.4) | 1.9 (7.0) | 1.5 (3.3) |
| UGM two-way grid | 1.8 (3.2) | 1.6 (3.8) | 1.2 (3.1) |
| UGM Stretched grid | 1.9 (3.2) | 1.3 (3.8) | 1.4 (3.1) |

*Parentheses denote ratio of observations.

Table 5.3. Ratio of area averaged u200hi to u200lo precipitation over regions III and IV denoted in Fig. 5.8.

| Model Configuration | Day 5 | Day 10 | Day 15 |
|---|---|---|---|
| Uniform UGM | 3.8 (4.3) | 3.1(6.4) | 2.4 (4.8) |
| MRF Reforecast | 3.7 (2.6) | 2.2 (7.1) | 1.6 (5.0) |
| UGM two-way grid | 7.2 (4.3) | 3.3 (6.4) | 1.4 (4.8) |
| UGM Stretched grid | 7.1 (4.3) | 3.1 (6.4) | 1.2 (4.8) |

*Parentheses denote ratio of observations.

Table 5.4. Ratio of area averaged u200hi to u200lo precipitation over region III denoted in Fig. 5.8.

| Model Configuration | Day 5 | Day 10 | Day 15 |
|---|---|---|---|
| Uniform UGM | 6.9 (20.2) | 4.4 (14.4) | 3.2 (7.9) |
| MRF Reforecast | 6.9 (14.5) | 2.5 (13.8) | 1.8 (6.7) |
| UGM two-way grid | 12.8 (20.2) | 3.7 (14.4) | 1.4 (7.9) |
| UGM Stretched grid | 13.8 (20.2) | 3.6 (14.4) | 1.3 (7.9) |

*Parentheses denote ratio of observations.

Table 5.5. Ratio of area averaged u200hi to u200lo precipitation over region IV denoted in Fig. 5.8.

| Model Configuration | Day 5 | Day 10 | Day 15 |
|---|---|---|---|
| Uniform UGM | 1.9 (0.9) | 1.9 (2.0) | 1.5 (1.9) |
| MRF Reforecast | 1.7 (0.6) | 1.8 (2.3) | 1.3 (2.4) |
| UGM two-way grid | 3.8 (0.9) | 2.6 (2.0) | 1.6 (1.9) |
| UGM Stretched grid | 3.4 (0.9) | 2.3 (2.0) | 1.0 (1.9) |

*Parentheses denote ratio of observations.

Overall, the data suggest that most of the model configurations, particularly those of the UGM, delineate qualitatively between u200hi and u200lo precipitation at days 5 and 10. The uniform resolution UGM consistently has ratios at or above 2 when observed ratios are above 2, even on day 15. However, the poor performance of the other model forecasts suggests that 15-day results are not generally useful, and that the relatively good skill of the uniform resolution UGM at 15 days may be an artifact of the small sample.

### 5.5.2 Precipitation Maps

Composites of accumulated, 10-day precipitation are presented for each u200hi and u200lo model configuration. Observations are from the CPC Unified data set (Higgins et al., 1996) as in sections 5.4 and 5.5.1.

Fig. 5.9 displays u200hi precipitation accumulations corresponding to the composites available during the years of the MRF Reforecast project (1979-2003). Observations (Fig. 5.9a) show a maximum near 22 cm along the Oregon-California border, and another near 14 cm is over the Sierra Nevada range. The MRF Reforecast has a grid spacing 10 times as large as the observations. It depicts the general signature of the observations, with precipitation covering a broad area (Fig. 5.9b). The MRF misses details over the coastal states, and does not clearly distinguish between areas of precipitation to the east. Similar to the MRF, the UGM (also the average of 1996 and 2000 u200hi cases) has a maximum accumulation over California and Oregon (Fig. 5.9c).

U200lo composites corresponding to MRF Reforecast years are depicted in Fig. 5.10. The maximum observed accumulation over the West (Fig. 5.10a) is about 20% of the u200hi composite (Fig. 5.9a). The MRF produces more area averaged, u200lo precipitation than do both the uniform and variable resolution UGMs during the second

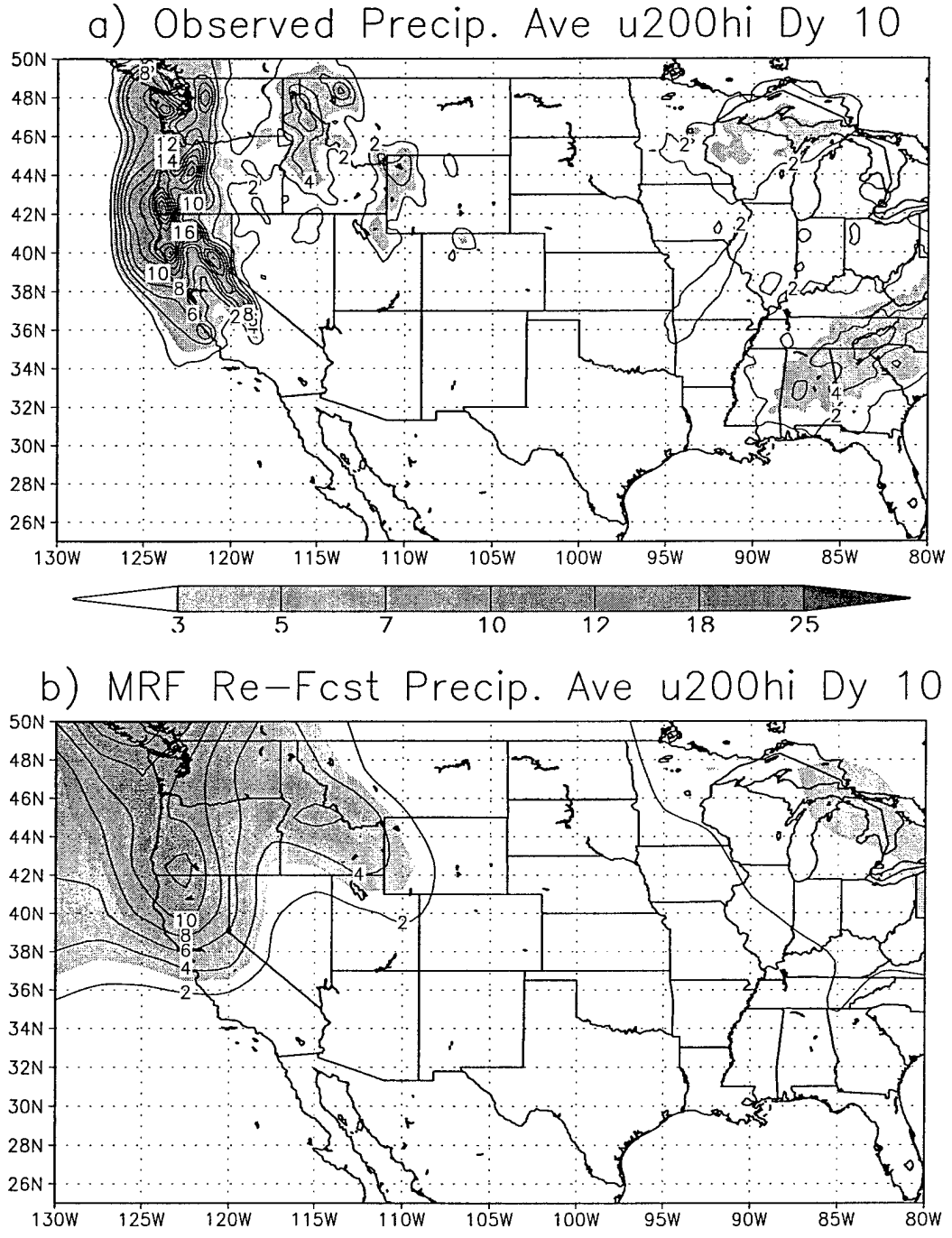


FIG. 5.9. Composite of average day 10 precipitation accumulation (cm) of u200hi years (1996 and 2000). (a) Observed u200hi precipitation (Higgins et al., 1996). (b) MRF u200hi precipitation. (c) Uniform resolution UGM, u200hi precipitation. The contour interval is 2 cm (contouring in (a) is up to 20 cm), and shading is for accumulation greater than or equal to 3 cm. The maximum observed accumulation in (a) is 24 cm.

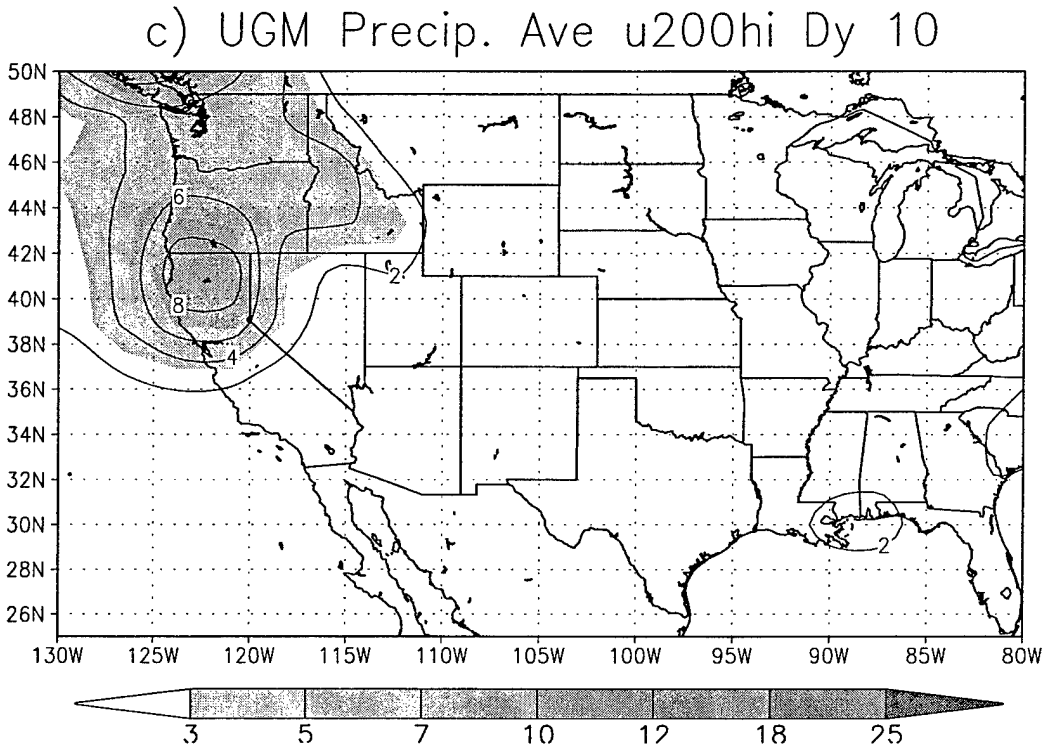


Fig. 5.9, continued.

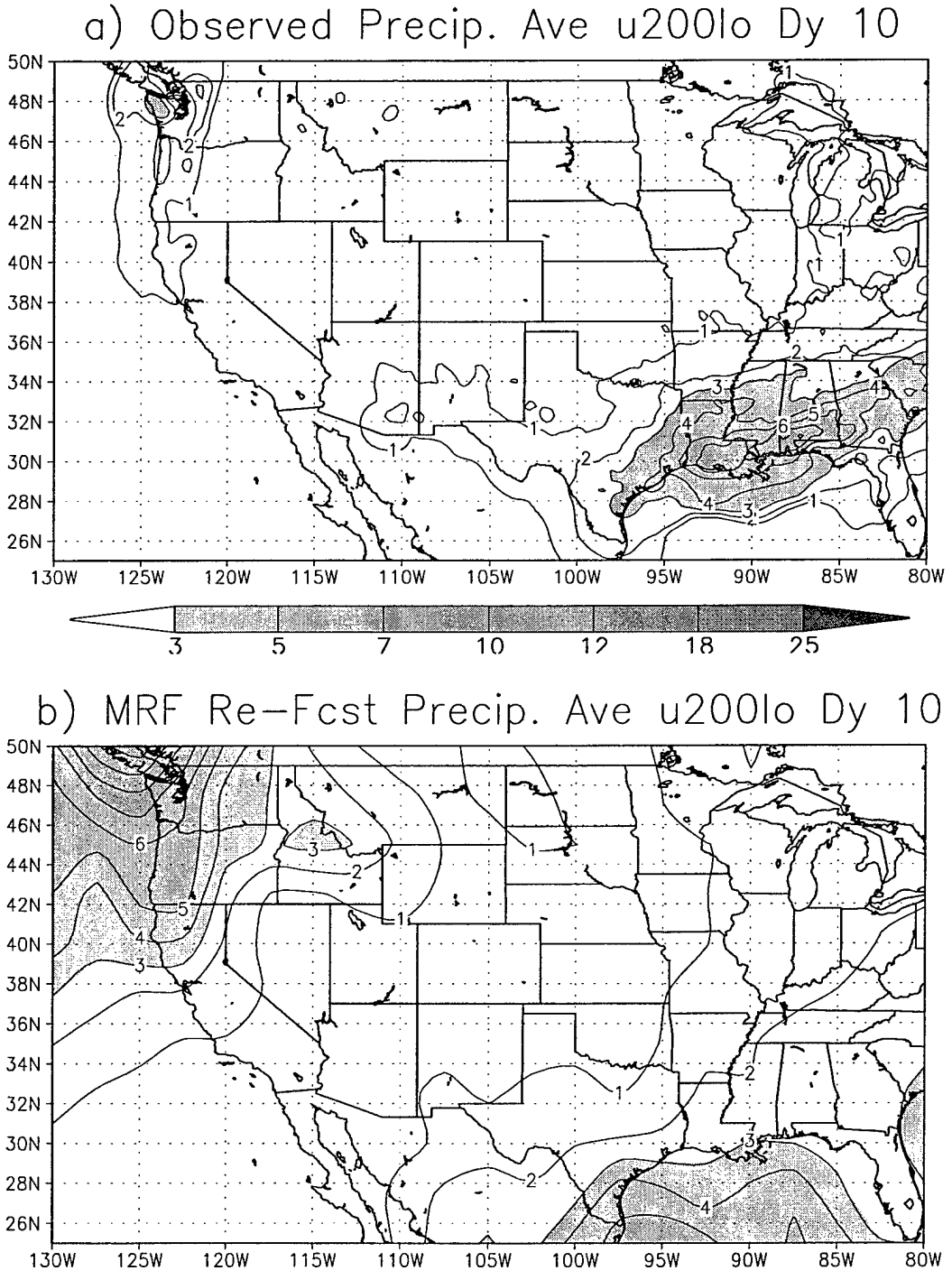


FIG. 5.10. Composite of average day 10 precipitation accumulation (cm) of u200lo years (1981, 1984, 1985, 1992). (a) Observed u200lo precipitation (Higgins et al., 1996). (b) MRF u200lo precipitation. (c) Uniform resolution UGM, u200lo precipitation. The contour interval is 1 cm, and shading is for accumulation greater than or equal to 3 cm.

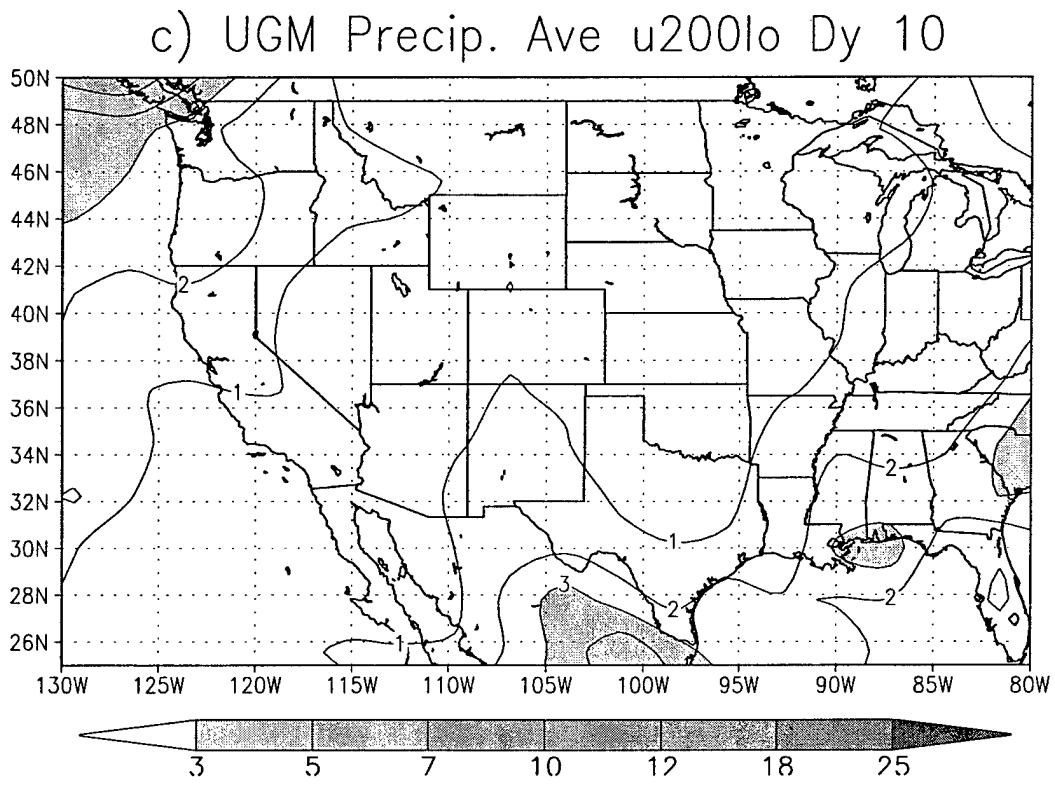


Fig. 5.10, continued.

week (compare Fig. 5.10b and Fig. 5.10c). The uniform resolution UGM produces a broad area of 1-2 cm accumulation (Fig. 5.10c).

Fig. 5.9 and Fig. 5.10 show composites of the u200hi and u200lo cases between 1979-2003. Fig. 5.11 and Fig. 5.12 show similar maps of u200hi and u200lo observations and UGM configurations covering the 52 years (1949-2000). While areal coverage of uniform resolution UGM precipitation is broader than observed (Fig. 5.11a,b and Fig. 5.12a,b), variable resolution forecasts produce more realistic spatial structure (Fig. 5.11c,d and Fig. 5.12c,d). Areal coverage and magnitude, however, are generally lower in the variable resolution forecasts.

All model forecasts over predict u200lo precipitation accumulation at day 10. As an example, the stretched model predicts almost twice the amount of observed precipitation near the western border of Idaho (compare Fig. 5.12a and Fig. 5.12d). Area averaged amounts tend to be on the order of half the amounts in the u200hi composites (section 5.5.1), similar to that shown for the uniform resolution UGM (Fig. 5.6).

## 5.6 Forecast Validation of Height Field

Precipitation validation emphasizes forecast skill on relatively smaller spatial scales. It is instructive to consider geopotential height prediction which emphasizes larger scales and is generally evaluated in terms of anomaly correlations. Anomaly correlations were computed over the Northern Hemisphere (NH) (20°N-90°N), and locally, over western North America, including the central Rocky Mountains (30°N-60°N, 130°W-100°W), each without bias correction. Anomaly correlations for forecast variable Z are calculated as:

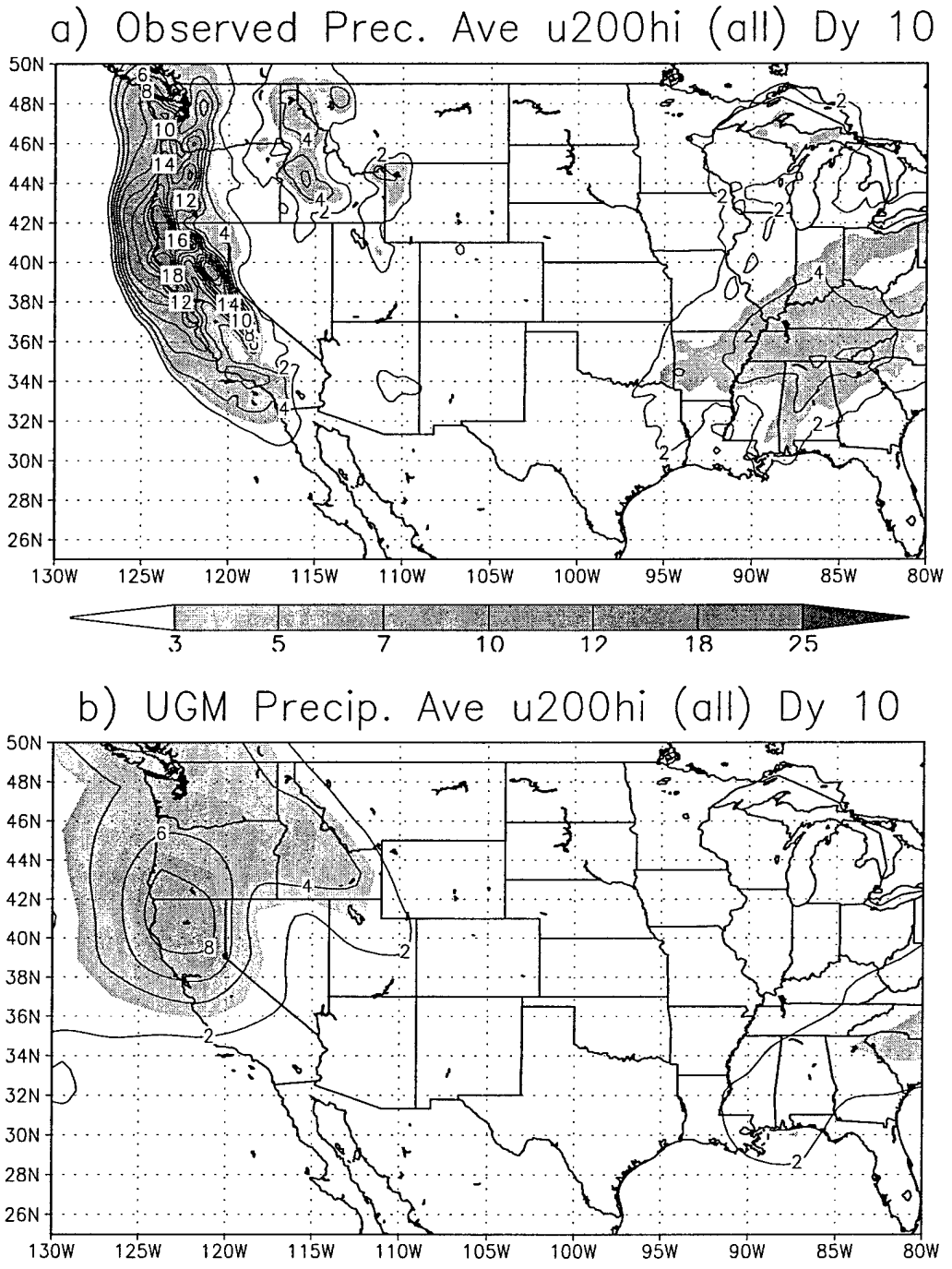


FIG. 5.11. Composite of average day 10 precipitation accumulation (cm) of all u200hi years (1950, 1952, 1969, 1996 and 2000). (a) Observed u200hi precipitation (Higgins et al., 1996). (b) Uniform resolution UGM, u200hi precipitation. (c) Two-way nested UGM, u200hi precipitation. (d) Stretched UGM, u200hi precipitation. The contour interval is 2 cm (contouring in (a) is up to 20 cm), and shading is for accumulation greater than or equal to 3 cm. The maximum observed accumulation in (a) is 24 cm.

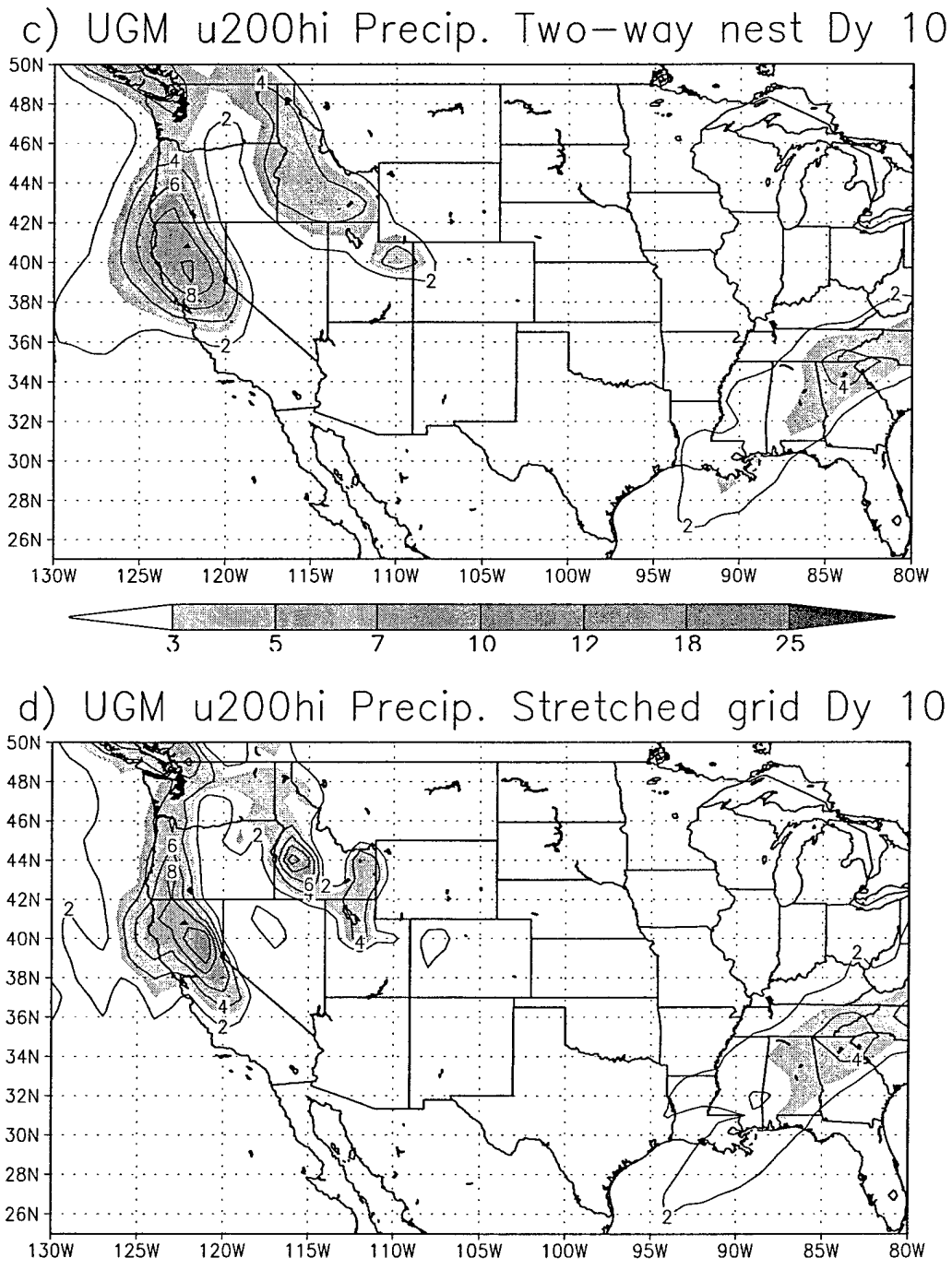


Fig. 5.11, continued.

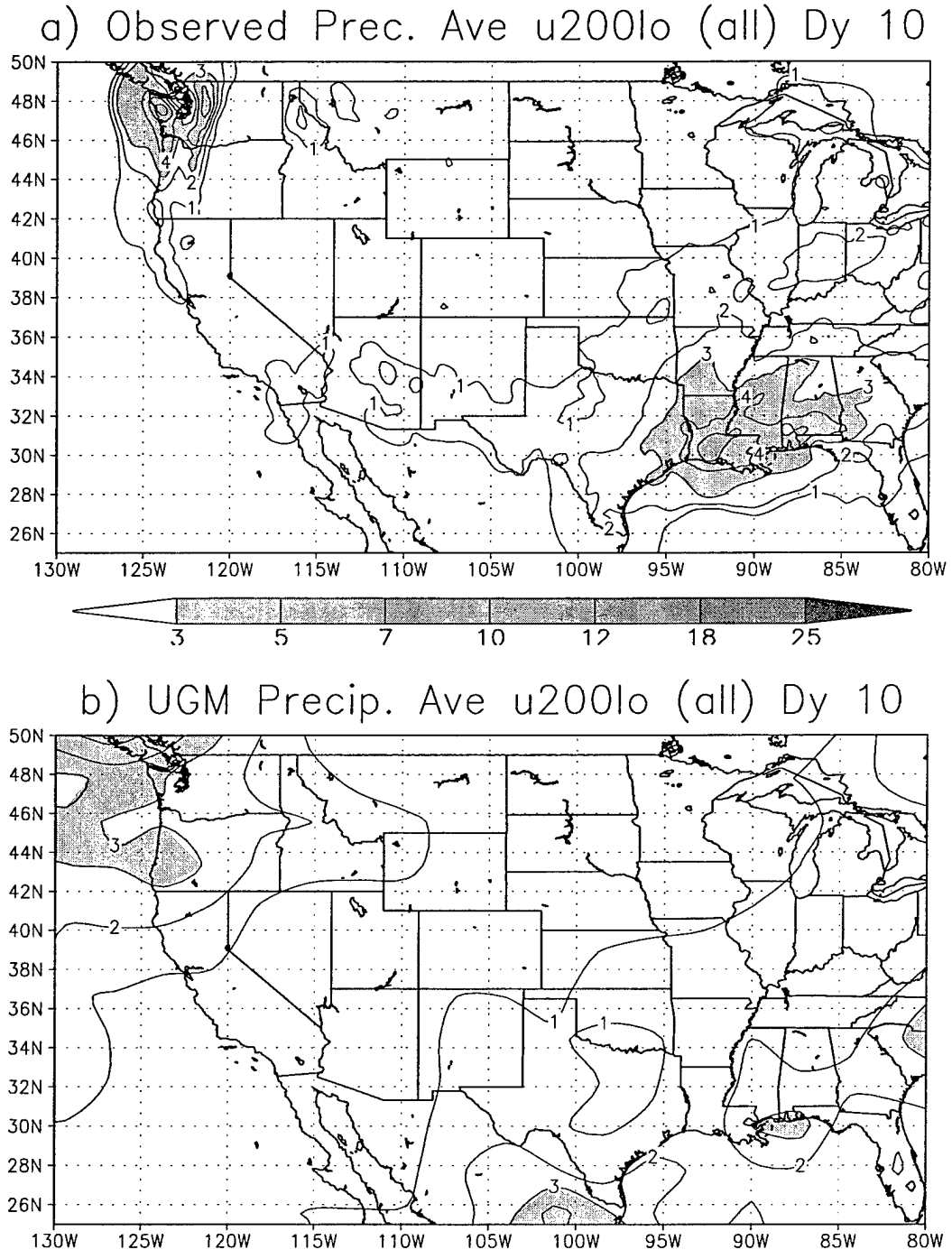


FIG. 5.12. Composite of average day 10 precipitation accumulation (cm) of all u200lo years (1949, 1976, 1981, 1984, 1985 and 1992). (a) Observed u200lo precipitation (Higgins et al., 1996). (b) Uniform resolution UGM, u200lo precipitation. (c) Two-way nested UGM, u200lo precipitation. (d) Stretched UGM, u200lo precipitation. The contour interval is 1 cm, and shading is for accumulation greater than or equal to 3 cm.

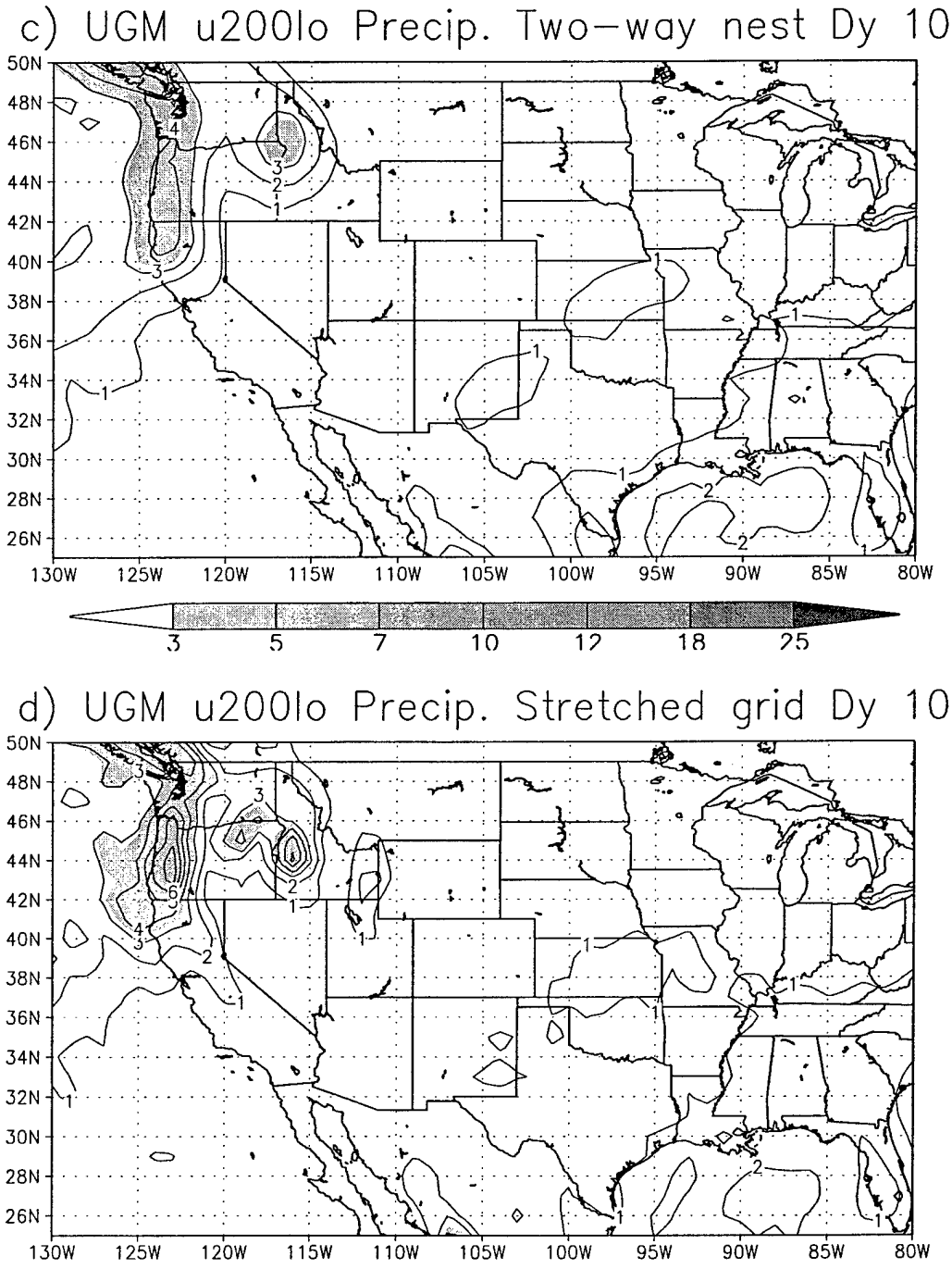


Fig. 5.12, continued.

$$\text{anom. corr.} = \frac{\overline{(Z - Z_{cl})(Z_{ob} - Z_{cl})}}{\left[\overline{(Z - Z_{cl})^2}\,\overline{(Z_{ob} - Z_{cl})^2}\right]^{1/2}} \tag{5.1}$$

where Zcl represents the climatological value of Z, and Zob is the observed value. The bars represents area averages of the variables. Climatology is defined by the 50-year, January average (1951-2000) from the NCEP/NCAR Reanalysis. "Observations" are also defined using the Reanalysis.

Fig. 5.13 displays 500-mb anomaly correlations for the uniform resolution UGM. The sigma level output has been interpolated to pressure coordinates, and Reanalyses have been bilinearly interpolated to a 2.8° longitude x 2.2° latitude grid to match the model resolution. This accounts for correlation coefficients below 1.0 at the initial hour. Fig. 5.13a shows composites of the 11 cases (u200hi and u200lo) described in section 5.3.1. The UGM maintains useful predictive skill (generally considered at or above 0.6) over the NH for almost 144 hours (6 days) into the forecast. Over the Rocky Mountain region, the composite anomaly correlation for all cases maintains a higher value, longer into the forecast. The curve is similar to the zonally averaged curve for all cases during the first 108 hours (4.5 days). Subsequently, the local curve climbs to just under 0.7 at the 168 hour (7 day) point and remains above 0.6 until 180 hours (7.5 days). The 11-case composite indicates useful predictability at and beyond 6 days for the zonal average and Rockies region, respectively. When the individual u200hi and u200lo composites were considered separately, uniform resolution UGM u200hi composites performed better, both over the NH and western North America.

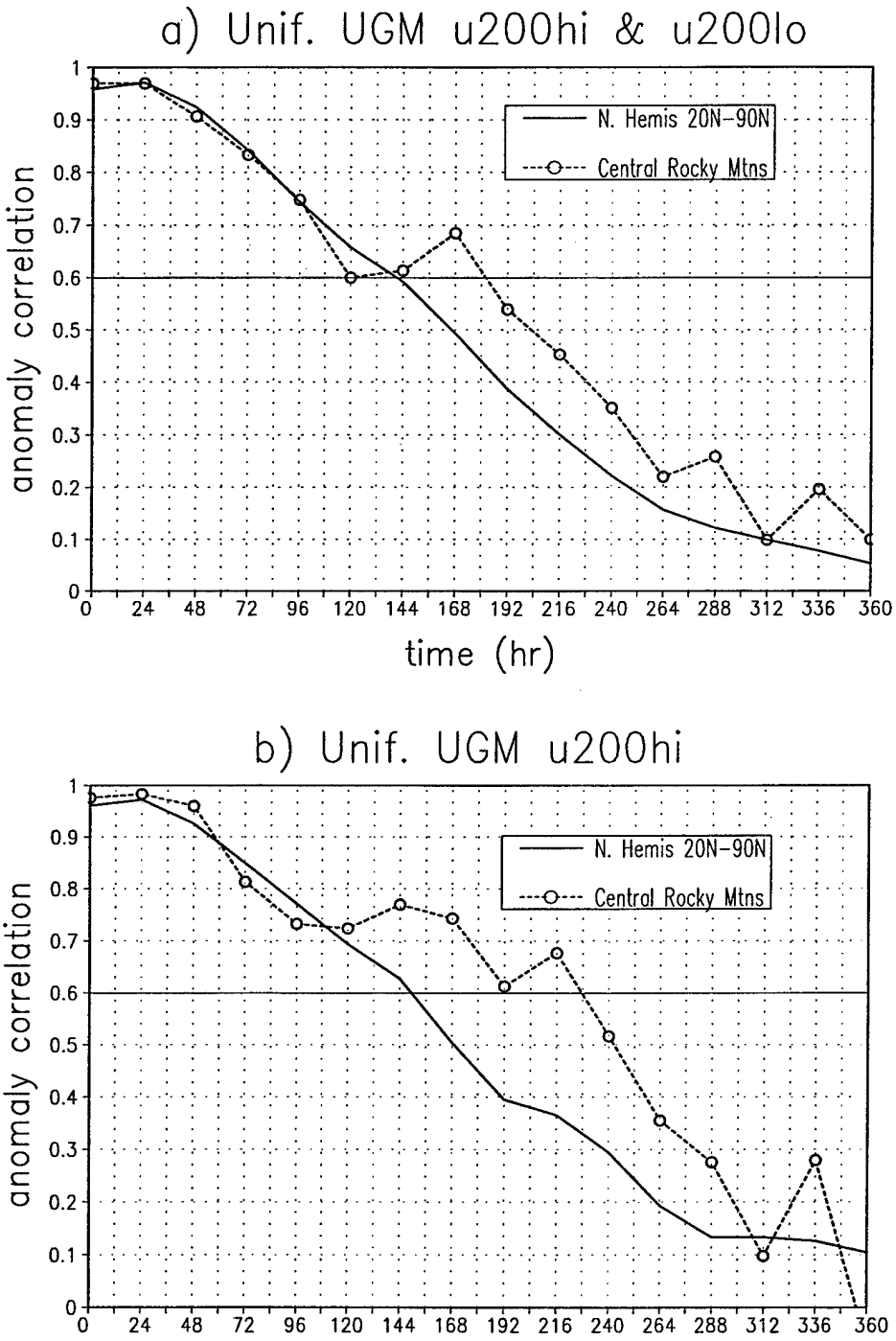


FIG. 5.13. Time evolution of 500-mb, geopotential height anomaly correlations of the uniform resolution UGM. Anomaly correlations are computed over the Northern Hemisphere from 20°N-90°N, and over western North America from 30°N-60°N, 130°W-100°W. (a) The u200hi and u200lo composite anomaly correlations (11 cases). (b) The u200hi composite anomaly correlations (5 cases).

The u200hi (wet) cases tend to be of greater societal importance for these time scales. The u200hi composite anomaly correlation is illustrated in Fig. 5.13b. Useful forecast skill for the NH zonal average is maintained to just beyond 144 hours (6 days), approximately 7 hours longer than for the 11-case average (compare Fig. 5.13a and Fig. 5.13b), and about 12 hours longer compared to the u200lo composite (not shown). The anomaly correlation over the Rockies region is significantly larger beyond 108 hours (4.5 days), and does not fall below 0.6 until 228 hours (9.5 days) into the forecast. Local predictive skill for 500-mb heights is maintained for about 3.5 additional days compared to the entire NH.

Anomaly correlations are also computed for the Rocky Mountain region for u200hi years corresponding to the MRF Reforecast project (1979-2003) (Fig. 5.14). To extend the winter sample, corresponding u200hi years for December and February, chosen with the same criteria for January described in section 5.3.1, are averaged with those for January (1996 and 2000). December u200hi years are 1981, 1983 and 1996; and February u200hi years are 1979, 1986, 1994, 1998 and 1999. This forms a composite of 10 independent, u200hi weather events. As with the UGM, "observations" and climatology for the correlations are from the NCEP/NCAR Reanalysis. For the MRF (Fig. 5.14), the monthly averaged, climatological 500-mb geopotential height (1951-2000) corresponding to the month of the forecast is used. For example, anomaly correlations for December forecasts use December climatology. The composite MRF correlation for the Rockies region remains above 0.6 for about 228 hours (9.5 days). Fig. 5.14 also depicts the anomaly correlation for climatology, based upon forecasts initialized on 10 December,

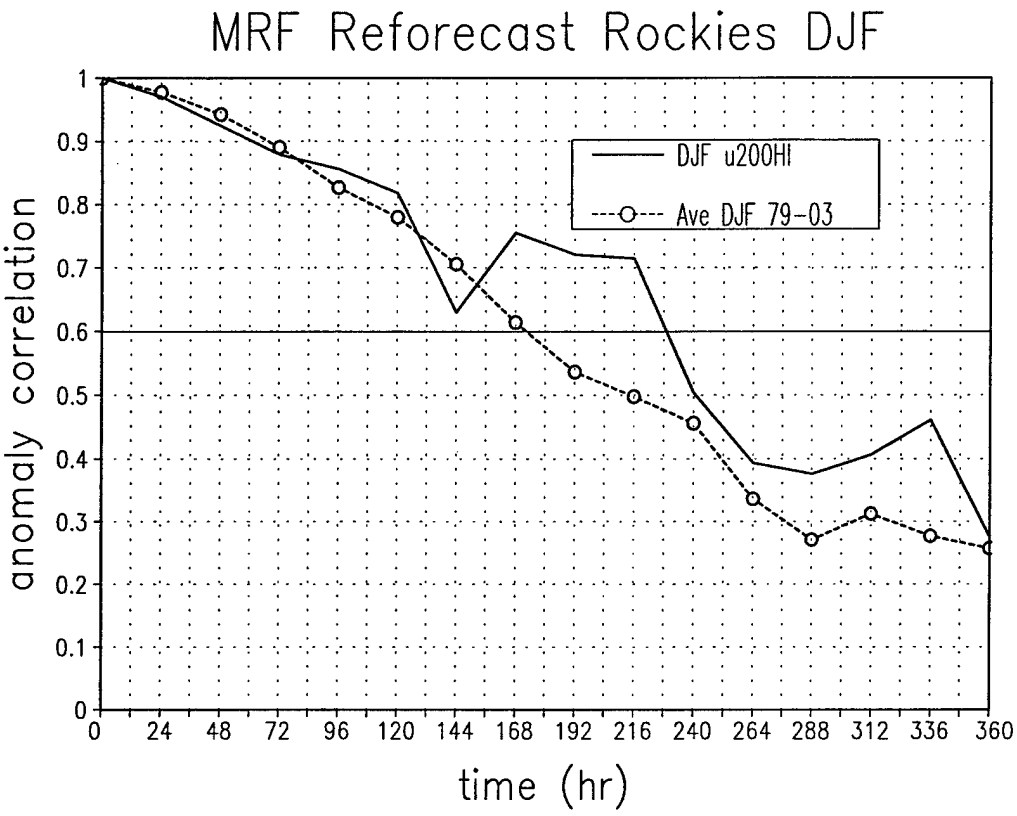


FIG. 5.14. Time evolution of the composite 500-mb, geopotential height anomaly correlations from the MRF Reforecast project for winter (DJF), u200hi cases. Anomaly correlations are computed over western North America from 30°N-60°N, 130°W-100°W. The u200hi composite (line) is for forecasts made on 10 December 1981, 1983 and 1996; 10 January 1996 and 2000; and 10 February 1979, 1986, 1994, 1998 and 1999 (10 cases). The anomaly correlation for climatology (circles) is the average for all MRF forecasts on 10 December, January and February, from 1979-2003 (75 forecasts).

January and February, from 1979-2003 (the average of 75 forecasts). Climatology shows useful forecast skill over western North America to approximately 168 hours (7 days).

The rotated, variable resolution output is interpolated to a 1° grid, as mentioned in section 5.3.3. NCEP/NCAR Reanalysis "observations" and climatology are also interpolated to the same grid spacing to compute the anomaly correlations. Anomaly correlations of the composite u200hi and u200lo, variable resolution forecasts are shown in Fig. 5.15. Fig. 5.15a depicts curves for the two-way nested model, which has a 1° resolution polar cap north of the 44°N latitude circle. Fig. 5.15b shows the composite for the stretched model. Correlations of the uniform resolution UGM are included in both panels for comparison. Variable and uniform resolution curves closely match each other through the first 96 hours (4 days) of prediction (Fig. 5.15a and Fig. 5.15b). Some loss of skill in the variable resolution forecasts is noticeable beyond 4 days. The stretched model curve is briefly superior to the uniform resolution UGM around the Rocky Mountain region near 168 hours (1 week) (Fig. 5.15b).

## 5.7 Discussion

The larger scale characteristics of cold season events have been found to contribute to overall greater forecast skill of extreme winter precipitation events (Olson et al., 1995). Gartner et al. (1996) suggested that understanding the role of topography in organizing precipitation is more difficult. They noted that for the continental U.S., the highest equitable threat scores of the meso-Eta were around the West coast, which is just downstream of the data sparse Pacific. The orographic organization of precipitation around the West Coast may partially account for the improved predictability. However, the same explanation did not apply to portions of the central and eastern Rocky

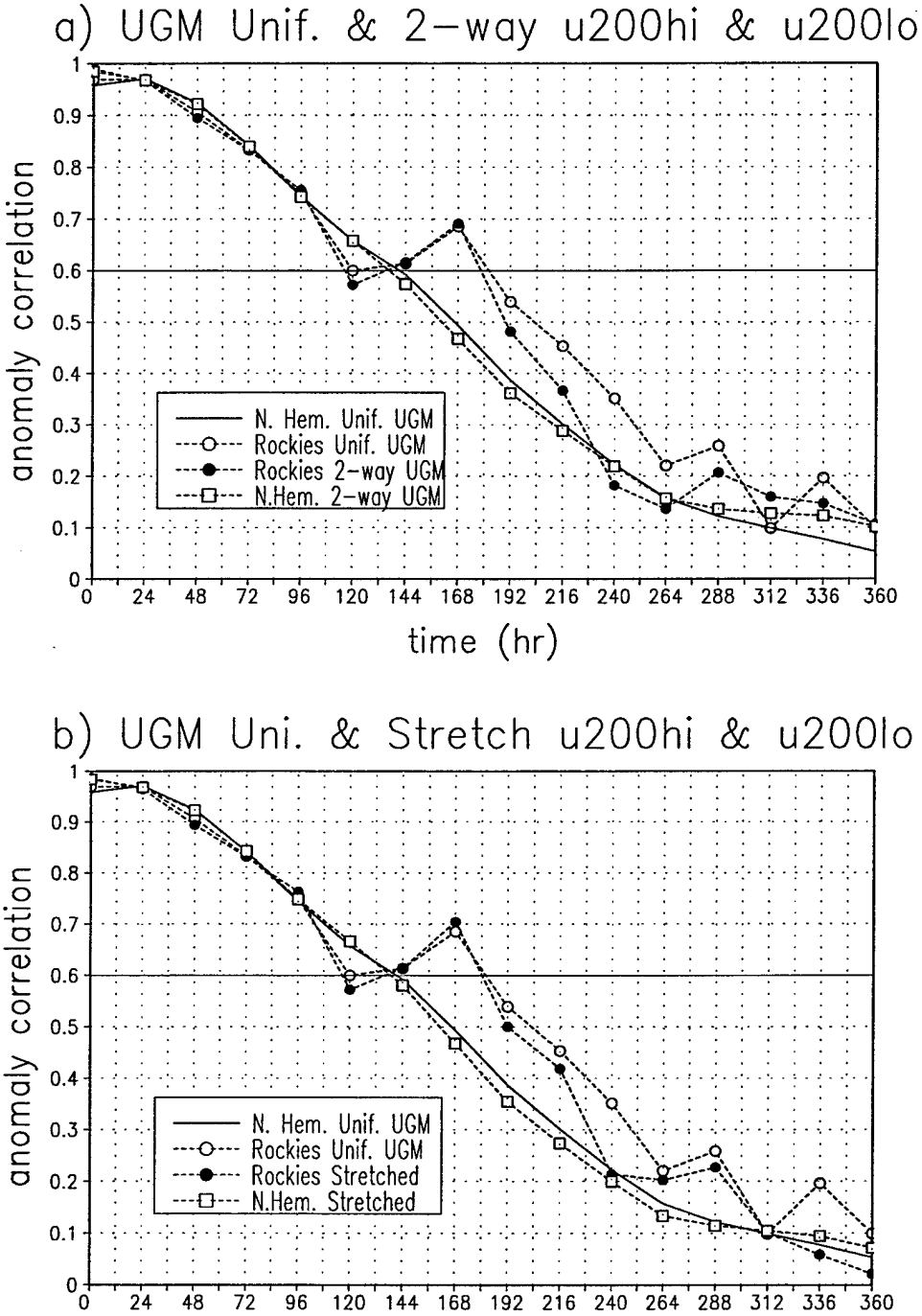


FIG. 5.15. Time evolution of 500-mb, geopotential height anomaly correlations of the rotated, variable resolution and uniform resolution UGMs. Anomaly correlations are computed over the Northern Hemisphere from 20°N-90°N, and over western North America from 30°N-60°N, 130°W-100°W. (a) The two-way nested UGM. (b) The stretched UGM. Anomaly correlations for the uniform resolution UGM (also plotted in Fig. 14a) are included in each panel for comparison.

Mountains, where the skill scores of the Eta model were relatively low (Gartner et al., 1996).

Medium range January forecasts have been presented during extremes of upper troposphere zonal flow over the Rocky Mountain region. Ratios of area averaged u200hi (wet) to u200lo (dry) precipitation accumulation over the western U.S. and various sub-basins illustrate some of the challenges on these time scales (Tables 5.1-5.5). Over the Colorado River basin, for example (region IV of Fig. 5.8), ratios are too high at day 5, suggesting higher potential for false alarm forecasts of wet events (Table 5.5). Over California and western Nevada, the variable resolution forecasts delineate best between wet and dry events at day 5 (Table 5.4).

The composite, uniform resolution UGM maintains a 500-mb geopotential height anomaly correlation at or above 0.6 over the NH for 6 days in these extreme events (Fig. 5.13a), approximately 1.5 days longer than usually found with the same model during winter (Miguez-Macho and Paegle, 2000; and Roman et al., 2004). Useful anomaly correlation of the MRF geopotential height field over the NH for the composite u200hi (1996 and 2000) and u200lo (1981, 1984, 1985 and 1992) cases in January also extends to 9.5 days (not shown).

In u200hi cases, the large inertia associated with a persistent and strong background zonal flow, both upstream and over the central Rockies, may contribute to a relatively longer forecast signal (see Fig. 5.13b and Fig. 5.14). In the uniform resolution UGM, local predictability of 500-mb heights is maintained approximately 3.5 additional days compared with the NH (Fig. 5.13b). Previous studies (e.g., Mo et al., 1995) have suggested that anomalous zonal flows interacting with orography may have contributed to

extreme summer flooding of the Mississippi River basin (MRB) during summer 1993 and that the flow anomalies may have contributed to extended predictability over the MRB (Chapter 4). Both the u200hi and u200lo winter composites show relatively high predictability of 500-mb geopotential heights. For example, a composite (8 cases) of u200lo, MRF winter forecasts (DJF), does not fall below 0.6 for the NH until 9 days (not shown). Large scales of the anomalies may therefore enhance predictability, even if the regional inertia is small. Lorenz (1969) demonstrates that larger scales possess longer predictability. It is speculated that both u200hi and u200lo cases are characterized by large scale anomaly fields that could promote predictability. This hypothesis is supported by the capacity of the simplest experiments using the uniform resolution UGM (section 5.4). Those experiments provide competitive 10-day skill over large regions of western North America

NH anomaly correlations in both sets of variable resolution experiments are slightly higher than the uniform resolution UGM during the first 72 hours (3 days) (Fig. 5.15). Some degradation of the forecasts was anticipated owing to larger formal truncation error in the variable resolution models compared to the fourth order truncation error of uniform resolution. Evidence of this is found over the Rockies region, where the variable resolution curves have fallen below the uniform resolution UGM curves at 120 hours (5 days). NH curves also remain slightly behind the uniform resolution composites from hour 120 (day 5) through most of the second week.

The overall similarity of the variable resolution correlations to those of the uniform resolution UGM is favorable given the lower formal accuracy in the variable resolution models and the possible numerical irregularities in the two-way nested model (e.g., the

abrupt transition from the 1° polar cap to the 2° outer grid). Examination of the 500-mb error fields (not shown) suggests that there are no irregularities around the regions of the rotated pole or the regions of abrupt change in resolution, and the higher local resolution produces more realistic precipitation patterns even though the higher resolution does not provide systematically better 500-mb anomaly correlation.

# CHAPTER 6

# DISCUSSION AND CONCLUSIONS

The primary goal of this dissertation has been to explore mechanical influences of orography and large scale ambient flows on surrounding low-level circulations. The perspective is based upon a classical dynamical theory which states that sufficiently strong westerly winds tend to produce anticyclonic responses over orography, while relatively weaker winds tend to produce cyclones over orography. The theory enhances understanding of climatological, annual and interannual variations observed around the largest mountain ranges (Chapters 2, 4 and 5). This study also examines associated predictability enhancement on medium range to intraseasonal time scales.

In addition, the relative importance of initial state detail over South America and detail external to the region were investigated with a set of experiments using a variable resolution version of the Utah Global Model (UGM) designed to assess impact of initial state changes upon regional predictability (Chapter 3). Results suggest that forecasts of lower troposphere winds are strongly influenced by local detail of the initial state specification. The subsections below provide a more detailed discussion and conclusions for each of the chapter topics.

## 6.1 Modulation Around the Andes

Analyses of eddy fields within monthly averaged gridded data and model simulations with the UGM (Chapter 2) emphasized an orographically bound cyclonic vortex of the

lower troposphere in the vicinity of the highest Andes in both summer and winter. Climatological averages suggest roles for both mechanical and heating effects for the east Andes circulation. The heating is most important in summer, but the similarity of the lower tropospheric winter and summer flows suggests a prominent role for mechanical influences in both seasons. Initial comparison of this feature with circulations found in the vicinity of the Tibetan plateau and the Rocky Mountains suggests more similarity with seasonal and vertical structures found over South Asia than over midlatitude portions of western North America. This is also supported by simple barotropic theory (a detailed analysis is provided in the Appendix).

Zhou and Lau (1998) note that the circulation in the vicinity of the higher Andes has many characteristics in common with the Asian monsoon. By contrast, seasonal and vertical variations found over the central Rockies are quite distinct from those that characterize the central Andes region. In particular, the lower tropospheric circulation over the central Rockies reverses from cyclonic to anticyclonic between summer and winter, while the lower tropospheric motion about both the Andes and the Tibetan plateau is cyclonic in both seasons.

Relatively wet episodes tend to occur over portions of the La Plata River basin during El Niño (e.g., Genta et al., 1998; Grimm et al., 1998). Results in Chapter 2 suggest a mechanistic contribution to this linkage, in which the stronger cross-Andes flow during El Niño accelerates both the orographically bound cyclone and its associated east Andes LLJ. The latter then transports more water vapor from the western Amazon basin to the La Plata basin, where it subsequently converges, rises, condenses and precipitates.

Chapter 2 advances a classical theory (e.g., Charney and Devore, 1979; and Nogués-Paegle, 1979) regarding the stationary Rossby wave response to orography within a west-

erly current to explain some of the observations of orographically forced low-level circulations. In this perspective, the subtropical Andes, as well as the subtropical Tibetan plateau, typically experience ambient zonal flows that, in the presence of the relatively large value of the subtropical Beta parameter, produce a "subcritical" response, assuming the form of an orographically bound cyclone. As the ambient westerlies increase, a resonant point of the solution is approached, and this enhances the orographically bound cyclonic response. The cyclonic circulation in the winter and summer average is also evident over South America for month long, primitive equation integrations of the UGM, with realistic shear and wave number 42 resolution of orography.

By contrast, the broadest orography of North America exists in midlatitudes, where the Beta parameter is weaker, and zonal flow during winter is relatively strong. Therefore, the summer-to-winter transition from subcritical to supercritical conditions may contribute to phase reversals from cyclonic to anticyclonic conditions.

This explanation is likely to have most relevance for quasi-stationary features on time scales of the order of a month or more. Higher frequency components of the flow possess additional modifications due to the interaction of transient Rossby waves with the Andes mountains, producing substantial first order modifications of the quasi-stationary flow emphasized in the present study. Campetella and Vera (2002) present further model analyses of such interactions in a baroclinically unstable environment. Salio et al. (2002) describe observed interactions of synoptic scale transients with the Chaco low that is part of the local cyclone. The modifications provided by higher frequency dynamical forcing, as well as by monsoonal heating, are certainly first order elements in the complete picture. Friction also modifies the quantitative character of theory (Dickinson, 1978).

One intent of this research is to add mechanical effects as simulated by simple barotropic models to the rich spectrum of influences that modulate South and North American weather regimes. The mountain minus no-mountain analysis over South America with the UGM is based upon relatively coarse orographic representation, truncated at approximately wave number 62 in the Reanalyses. Present inferences regarding the orographic modulation are therefore constrained to the relatively larger spatial scales represented by this truncation. The role of the mechanical effect relative to other processes remains to be clearly delineated using more complete observations and carefully constructed model experiments designed to refine understanding and predictability of related phenomena.

## 6.2 Sensitivity to Initial Data Changes

Chapter 3 assesses the impact of initial state changes upon regional predictability over South America. It is unclear whether data sparse regions of the oceans or continents represent the most strongly limiting components of the southern observing system. The relative importance of summer initial state detail over South America and detail external to South America are studied with a set of experiments using a rotated, variable resolution version of the UGM. GDAS analyses represent surrogates for analyses which include higher resolution observations. Results are compared to similar experiments which target NH midlatitudes during winter.

In the latter experiments, initial, regional data changes over the northeast Pacific represent a small contribution to the total, global forecast differences after 4 days. Results support the conclusion of Miguez-Macho and Paegle (2001, MMP01) that initial state modifications made over that region during winter are not as important as initial state differences external to the northeast Pacific through 96 hours into the forecast. This result is

also found using the new rotated, variable resolution approach and higher resolution GDAS analyses.

Over South America, targeting experiments are initialized on 17 and 30 January 2003, and results of the former are detailed in Chapter 3. Forecasts of lower troposphere winds and moisture are strongly influenced by detail of the initial state specification over South America through about the first 4-5 days of prediction. Therefore, initial information over South America may be at least as important as initial state specification outside the region in some summer events. This was never the case after 36 hours for MMP01, whose investigation included 34 different NH, midlatitude, winter cases. Preliminary results suggest an important role for detailed observational data coverage for both the description and prediction of regional and continental-scale hydrologic processes over South America.

Tests for numerical irregularities in the rotated, variable resolution approach support the feasibility of the two-way nest method for present time scales.

### 6.3 Modulation of the Great Plains Low-Level Jet

Chapter 4 proposes that intraseasonal, seasonal and interannual variations of the Great Plains LLJ may be partly explained by variations of ambient zonal flow over the Rockies. Following the theory described in Chapter 2, it is suggested that the Rockies induce an orographically bound, lower tropospheric cyclone in summer. One explanation for this is that the ambient flow is then subcritical with regard to quasi-stationary Rossby waves. As the ambient flow increases/decreases, the response of the orographically bound cyclone increases/decreases as the solution approaches/departs near-resonance, similar to the South American case described in Chapter 2. Chapter 4 shows obervational evidence in support of the proposed mechanism, and presents medium range forecasts of extreme

droughts and floods that appear to retain some skill into the second week of prediction.

Chapter 4 is related to past studies by Mo et al. (1995) and Wang et al. (1999) that examine extended range influences on the atmospheric portion of the hydrologic cycle over the Global Energy and Water Cycle Experiment (GEWEX) Continental-Scale International Project (GCIP) domain. Mo et al. (1995) examine the onset and maintenance of the 1993 summer floods using Eliassen-Palm fluxes. They suggest that an anomalously strong, westerly flow over the Rocky Mountains was maintained by low-pass filtered eddies over the north Pacific, and that orographic effects accelerated a cyclonic pattern in the vicinity of the Rocky Mountains. These features supported a strong, southerly LLJ east of the mountains and accelerated the influx of water vapor from the Gulf of Mexico toward the upper and central Mississippi River basins.

Chapter 4 includes diagnostics of monthly averaged, NCEP/NCAR Reanalyses to demonstrate that the Great Plains LLJ during summer, related water vapor transports, and MRB rains tend to increase during extended periods of anomalously strong zonal flow over the western U.S. Time correlations suggest that an orographically enhanced, cyclonic acceleration occurs over the western U.S. when the summer, upper troposphere zonal flow is relatively strong above the Rockies, as summarized in Figs. 1.3 and 1.4. Similar correlations are found in the Northern Hemisphere between the midlatitude zonal index averaged over the full latitude circle and orographically bound cyclones in summer.

This research hypothesizes that over western North America, orography provides a scale transfer mechanism, focussing global scale features into regional responses (Chapter 4). The LLJ east of the Rocky Mountains is one component of a larger scale, orographically bound, summer cyclone whose strength increases with increasing cross-barrier flow. This interpretation provides an alternative, mechanical explanation to thermodynamic pro-

cesses related to surface heating influences that have often been used to explain the anomalous response of the 1993 floods (e.g., Giorgi et al., 1996; Paegle et al., 1996 and references therein; Beljaars et al., 1996; Dirmeyer and Brubaker, 1999; and Viterbo and Betts, 1999).

Thermal effects of sensible and latent heating have been frequently cited as potential sources of enhanced predictability of the coupled ocean-land-atmosphere system. In particular, a large number of investigations have been made of the influence of soil moisture anomalies upon model forecasts; others have considered ice and snow states and the influence of surface albedo. Unlike soil moisture, ice state, and albedo, orography is relatively fixed over periods of short to medium range climate change. The orographically induced response is nevertheless not fixed, but depends upon the ambient atmospheric state and its anomalies.

In cases where anomalies of the atmospheric state possess relatively large scales, the orographic influence may promote a relatively predictable lee-side LLJ response, and may help to explain and possibly predict extreme events such as those observed over the GCIP domain in 1988 and 1993. In these cases there appears to be some basin-scale skill in anomalous precipitation prediction for 1-2 weeks.

## 6.4 Winter Predictability Over Western North America

Chapter 5 examines episodic enhancement of medium range predictability in anomalous initial states over the western U.S. in winter. It compares uniform resolution and variable resolution predictions by the UGM with ensemble approaches using the Medium Range Forecast (MRF) model of the National Centers for Environmental

Prediction (NCEP), and finds that all approaches retain useful skill to about 10 days in selected extreme precipitation events.

A premise of the hypothesis for enhanced predictability is the interaction of Rocky Mountain orography with the ambient, upper troposphere, zonal flow (Chapters 2 and 4). Large scale predictability is explored with anomaly correlations of 500-mb geopotential height (Chapter 5). Over the NH and the Rocky Mountain region, forecasts during anomalously strong (wet) and weak (dry) zonal flow events exhibit higher skill than is typical of the UGM and MRF. The variable resolution UGM models also perform at least as well as, or better than the uniform resolution UGM during the first 4 days of prediction. Useful predictability (anomaly correlation greater than 0.6) for some cases extends to 9.5 days in the uniform resolution composites (Fig. 5.13b, Fig. 5.14). Improved performance may be related to the large inertia of the flow in wet events, and to increased predictability of initial, large scale anomalies in both wet and dry events (Lorenz, 1969).

While anomaly correlations emphasize large scales, precipitation prediction reflects smaller scales. Four different model configurations delineate qualitatively between wet and dry events at both 5 and 10 days. They also exhibit regional strengths and weaknesses, as summarized in section 5b, but 15-day predictions are generally not useful for these cases.

The uniform resolution model forecasts maintain representative precipitation to about 10 days over the western U.S. (e.g., Fig. 5.6). Horizontal maps of 10-day accumulation suggest more detail in the variable resolution UGM forecasts, particularly in the "stretched" model. The stretched model composite of u200hi events differentiates

between 3 of the observed regions of precipitation (Fig. 5.11). Thus, value is added in the rotated, variable resolution approach in precipitation detail, even though added value is not evident in the anomaly correlations.

Chapter 5 diagnosed the predictability for a small sample of extreme cases. A question for further examination is whether the extended predictability applies only to the extreme, chosen events; or whether systematic forecasts of opportunity may be possible without prior information about monthly averaged anomalies. Future work will include the search for prior signals of extended predictability.

Many issues and questions remain. A few of these are outlined below:

(1) Why is the observed response west of the highest topography? As described in section 2.6, the Reanalysis depicts eddy circulation centers displaced west of the highest orography, rather than over the orography, as predicted by theory (see Fig. 2.1 and Fig. 2.7). The effective mountain profile may account for not only the surface topography, but also the blocking effect of the stagnated airmass commonly found upwind of large orographic barriers. This would increase the effective barrier width and tend to shift its effective center westward. Additionally, the inclusion of Ekman pumping in the barotropic model may account for the shift in the response to the west of the mountains, as shown by Dickinson (1978) and Holton (1992, and references therein).

The possible role for upstream stagnation and Ekman pumping have not been examined here and require further study. The effects of these components, however, would be present in the primitive equation model simulations presented to examine the mechanical effects of orography in Chapters 2 and 4 over South and North America, respectively. This research has focused largely upon practical elements of the single layer barotropic theory, including how ambient flows over orography may contribute to improved medium range

predictability.

(2) Can enhanced predictability be determined beforehand and with minimal false alarm? The current research is based upon the hypothesis that global scale elements of the atmosphere possess relatively long predictability (Chapters 2, 4 and 5). This result is well founded in early predictability studies (e.g., Lorenz, 1969). Predictability to 10 days may be enhanced by orography over regions with spatial dimensions similar to those of river basins or sub-basins (Chapter 5) (e.g., Colorado and Columbia River basins). Future research will examine whether the atmosphere exhibits signals which indicate beforehand that a period of extended predictability will follow.

(3) What will be the effect of real SALLJEX observations (rather than GDAS surrogates used in Chapter 3) upon forecasts? Experiments tesing the impact of initial data changes over South America revealed that local specification during summer over the region is important to local forecast evolution in some cases through 4-5 days, particularly in the lower troposphere. Repeating the targeting experiments using SALLJEX observations will promote further understanding of these influences.

# APPENDIX

# MECHANICAL EFFECTS OF OROGRAPHY

The derivation of the barotropic model starts with the complete vorticity equation in P-coordinates:

$$\frac{\partial \zeta}{\partial t} + V_h \bullet \nabla\zeta + \omega\frac{\partial \zeta}{\partial p} + k \bullet \nabla\omega \times \frac{\partial V_h}{\partial p} + \beta v = -(f+\zeta)\nabla \bullet V_h. \qquad \text{(A.1)}$$

Here, $\zeta$ is vorticity, $\omega$ is vertical motion, $V_h$ is the horizontal velocity vector, p is pressure, $f$ is the Coriolis parameter ($2\Omega\sin\phi$), $\beta$ is the meridional gradient of the Coriolis parameter, assumed constant for a "beta-plane" approximation, and $v$ is the meridional wind component. Following standard quasi-geostrophic simplifications, the third and fourth terms of the left-hand side, and part of the right-hand side of (A.1) are neglected. Steady state solutions are sought, so the first term is also neglected. Therefore, (A.1) becomes (A.2):

$$V_h \bullet \nabla\zeta + \beta v = -f\nabla \bullet V_h . \qquad \text{(A.2)}$$

The next step is to decompose the flow as:

$$V_h = \bar{u}\hat{i} + v'\hat{j}, \qquad \text{(A.3)}$$

where $\bar{u}$ is the background zonal flow assumed to be uniform and $v'$ is a perturbation flow. Introduction of the eddy perturbation streamfunction $\psi'$ leads to:

$$\zeta = \nabla^2\psi' \qquad \text{(A.4)}$$

$$v = \frac{\partial \psi'}{\partial x} \quad . \tag{A.5}$$

Introduction of (A.4) and (A.5) into a linearized version of (A.2) gives:

$$\bar{u}\frac{\partial \nabla^2 \psi'}{\partial x} + \beta \frac{\partial \psi'}{\partial x} = -f \nabla \bullet V_h . \tag{A.6}$$

Using the continuity equation:

$$\frac{\partial \omega}{\partial p} = -\nabla \bullet V_h \tag{A.7}$$

in (A.6) yields:

$$\bar{u}\frac{\partial \nabla^2 \psi'}{\partial x} + \beta \frac{\partial \psi'}{\partial x} = f \frac{\partial \omega}{\partial p} . \tag{A.8}$$

Next assume a one-layer atmosphere of pressure thickness $\Delta P$. At the top of the atmosphere:

$$\omega_{top} = 0 . \tag{A.9}$$

At the bottom, take:

$$\omega_{sfc} = -\rho g W_{sfc} , \tag{A.10}$$

$$W_{sfc} = \bar{u}\frac{\partial Z_t}{\partial x}, \tag{A.11}$$

where $\rho$ is the density; $g$ is the acceleration of gravity; $W_{sfc}$ is the vertical velocity at the surface, given by the surface wedging effect of orography; and $Z_t$ is the surface elevation. Equation (A.11) represents a linearized lower boundary condition. Now, $\frac{\partial \omega}{\partial p}$ is replaced by the finite difference quotient approximation:

$$\frac{\partial \omega}{\partial p} = \frac{(\omega_{sfc} - \omega_{top})}{\Delta P} = -\frac{\left(\rho g \bar{u}\frac{\partial Z_t}{\partial x}\right)}{\Delta P} \tag{A.12}$$

using (A.9), (A.10) and (A.11). Substitution of (A.12) into (A.8) gives:

$$\bar{u}\frac{\partial \nabla^2 \psi'}{\partial x} + \beta\frac{\partial \psi'}{\partial x} = -\frac{\left(f\rho g \bar{u}\frac{\partial Z_t}{\partial x}\right)}{\Delta P}, \tag{A.13}$$

or

$$\bar{u}\frac{\partial \nabla^2 \psi'}{\partial x} + \beta\frac{\partial \psi'}{\partial x} = -\gamma\frac{\partial Z_t}{\partial x}, \tag{A.14}$$

where

$$\gamma = \frac{(f\rho g \bar{u})}{\Delta P}. \tag{A.15}$$

$\gamma$ is a positive/negative constant in the Northern/Southern Hemisphere. Assuming an orographic corrugation of the form:

$$Z_t = A_{kl}[\cos(kx)\cos(ly)], \tag{A.16}$$

where $A_{kl}$ is the amplitude of wavenumber $k$ in x and $l$ in y, and substituting (A.16) into (A.14) yields the solution:

$$\psi'(x, y) = B_{kl}[\cos(kx)\cos(ly)], \tag{A.17}$$

where

$$B_{kl} = \gamma \frac{A_{kl}}{[\bar{u}(k^2 + l^2) - \beta]}. \tag{A.18}$$

Inspection of (A.16), (A.17) and (A.18) shows that a positive/negative streamfunction perturbation occurs in the Northern/Southern Hemisphere (i.e., an anticyclone) when the cross-mountain flow is sufficiently strong, so that:

$$\bar{u} > \frac{\beta}{(k^2 + l^2)}, \tag{A.19}$$

and a cyclone is favored over the mountain when

$$\bar{u} < \frac{\beta}{(k^2 + l^2)}. \tag{A.20}$$

Condition (A.19) is more easily satisfied for stronger westerlies, smaller $\beta$ (higher latitudes) and narrower mountains. Condition (A.20) is more easily satisfied for weaker westerlies, larger $\beta$ (lower latitudes) and broad mountains.

## REFERENCES


Anthes, R. A., 1983: Regional models of the atmosphere in middle latitudes. *Mon. Wea. Rev.*, **111**, 1306-1335.

Barnston, A. G., and P. T. Schickedanz, 1984: The effect of irrigation on warm season precipitation in the southern Great Plains. *J. Climate Appl. Meteor.*, **23**, 865-888.

Bath, L. M., M. A. Dias, D. L. Williamson, G. S. Williamson, and R. J. Wolski, 1987: User's Guide to NCAR CCM1, Technical Report NCAR/TN-286+IA, National Center for Atmospheric Research, 173 pp.

Beljaars, A. C. M., P. Viterbo, M. J. Miller, and A. K. Betts, 1996: The anomalous rainfall over the United States during July 1993: sensitivity to land surface parametrization and soil moisture anomalies. *Mon. Wea. Rev.*, **124**, 362-383.

Bell, G. D., and J. E. Janowiak, 1995: Atmospheric circulation associated with the Midwest floods of 1993. *Bull. Amer. Meteor. Soc.*, **76**, 681-695.

Blackadar, A. K., 1957: Boundary layer wind maxima and their significance for growth of nocturnal inversions. *Bull. Amer. Meteor. Soc.*, **38**, 282-290.

Bonner, W. D., and J. Paegle, 1970: Diurnal variations in boundary layer winds over the south central United States in summer. *Mon. Wea. Rev.*, **96**, 833-850.

Broccoli, A. J., and S. Manabe, 1992: The effects of orography on midlatitude Northern Hemisphere dry climates. *J. Climate*, **5**, 1181-1201.

Campetella, C., and C. Vera, 2002: The influence of the Andes mountains on the South American low-level flow. *Geophys. Res. Lett.*, **29**, No. 17, 1826, doi: 10.1029/2002 GLO15541.

Caplan, P., J. Derber, W. Gemmill, S.-Y. Hong, H.-L. Pan, and D. Parrish, 1997: Changes to the 1995 NCEP operational Medium-Range Forecast Model analysis-forecast system. *Wea. Forecasting*, **12**, 581-594.

Charney, J. G., and A. Eliassen, 1949: A numerical method for predicting the perturbations of the middle latitude westerlies. *Tellus*, **1**, 38-54.

_____, and J. Devore, 1979: Multiple flow equilibria in the atmosphere and blocking. *J. Atmos. Sci.*, **36**, 1205-1216.

Chen, M., P. Xie, J. E. Janowiak, and P. A. Arkin, 2002: Global land precipitation: a 50-yr monthly analysis based on gauge observations. *J. Hydrometeor.*, **3**, 249-266.

Coté, J., S. Gravel, A. Methot, A. Patoine, M. Roch, and A. Staniforth, 1998a: The Operational CMC-MRB Global Environmental Multiscale (GEM) Model. Part I: design considerations and formulation. *Mon. Wea. Rev.*, **126**, 1373-1395.

_____, J.-G. Desmarais, S. Gravel, A. Methot, A. Patoine, M. Roch, and A. Staniforth, 1998b: The Operational CMC-MRB Global Environmental Multiscale (GEM) Model. Part II: results. *Mon. Wea. Rev.*, **126**, 1397-1418.

Dickinson, R. E., 1978: On planetary waves. Preprints, National Center for Atmospheric Research colloquium, *The General Circulation: Theory, modeling and observations*, 59-79.

Dirmeyer, P. A., and K. L. Brubaker, 1999: Contrasting evaporative moisture sources during the drought of 1988 and the flood of 1993. *J. Geophys. Res.*, **104**, 19383-19397.

Douglas, M., M. Nicolini, and C. Saulo, 1998: Observational evidences of a low level jet east of the Andes during January-March 1998. *Meteorologica*, **23**, 63-72.

_____, M. Nicolini, and C. Saulo, 1999: The low-level jet at Santa Cruz, Bolivia, during January-March 1998, pilot balloon observations and model comparison. Preprint Volume, Tenth Conference of the AMS on Global Change Studies, Dallas, Texas, January 1999.

Errico, R., and D. Baumhefner, 1987: Predictability experiments using a high-resolution limited-area model. *Mon. Wea. Rev.*, **115**, 488-504.

Fritsch, J. M., R. A. Houze, Jr., R. Adler, H. Bluestein, L. Bosart, J. Brown, F. Carr, C. Davis, R. H. Johnson, N. Junker, Y.-H. Kuo, S. Rutledge, J. Smith, Z. Toth, J. W. Wilson, E. Zipser, and D. Zrnic, 1998: Quantitative precipitation forecasting: report of the eighth prospectus development team, U.S. Weather Research Program. *Bull. Amer. Meteor. Soc.*, **79**, 285-299.

Gandu, A. W., and J. E. Geisler, 1991: A primitive equations model study of the effect of topography on the summer circulation over tropical South America. *J. Atmos. Sci.*, **48**, 1822-1836.

Garstang, M., S. Ulanski, S. Greco, J. Scala, R. Swap, D. Fitzjarrald, D. Martin, E. Browell, M. Shipman, V. Connors, R. Harriss, and R. Talbot, 1990: The Amazon Boundary-Layer Experiment: a meteorological perspective. *Bull. Amer. Meteor. Soc.*, **71**, 19-32.

Gartner, W. E., M. E. Baldwin, and N. W. Junker, 1996: Regional analysis of quantitative precipitation forecasts from NCEP's "early" Eta and meso-Eta models. Preprint volume, 16 Conference of the American Meteorological Society on Weather and Forecasting, Norfolk, VA, 187-189.

Genta, J. L., G. Pérez-Iribarren, and C. R. Mechoso, 1998: A recent increasing trend in the streamflow of rivers in southeastern South America. *J. Climate*, **11**, 2858-2862.

Gibson, J. K., P. Källberg, S. Uppala, A. Nomura, A. Hernandez, and E. Serrano, 1997: ERA description, ECMWF Reanalysis Project Report Series, 1. European Center for Medium-Range Weather Forecasts, Geneva.

Giorgi, F., L. O. Mearns, C. Shields, and L. Mayer, 1996: A regional model study of the importance of local versus remote controls on the 1988 drought and the 1988 flood over the central United States. *J. Climate,* **9**, 1150-1162.

Grimm, A. M., S. T. Ferraz, and J. Gomes, 1998: Precipitation anomalies in southern Brazil associated with El Niño and La Niña events. *J. Climate*, **11**, 2863-2880.

Gutzler, D. S., and J. W. Preston, 1997: Evidence for a relationship between spring snow cover in North America and summer rainfall in New Mexico. *Geophys. Res. Lett.*, **24**, 2207-2210.

Hamill, T. M., 2003: Evaluating forecasters' rules of thumb: a study of d(prog)/dt. *Wea. Forecasting*, **18**, 933-937.

____, J. S. Whitaker, and X. Wei, 2004: Ensemble re-forecasting: improving medium-range forecast skill using retrospective forecasts. *Mon. Wea. Rev.*, in press.

Helfand, H. M., and S. D. Schubert, 1995: Climatology of the simulated Great Plains low-level jet and its contribution to the continental moisture budget of the United States. *J. Climate*, **8**, 784-806.

Higgins, R. W., J. E. Janowiak, and Y.-P Yao, 1996: A gridded hourly precipitation data base for the United States (1963-1993). NCEP/Climate Prediction Center, Atlas 1. NCEP/Climate Prediction Center, Camp Springs, MD.

____, Y. Yao, J. E. Janowiak, and K. C. Mo, 1997a: Influence of the Great Plains low-level jet on summertime precipitation and moisture transport over the central United States. *J. Climate*, **10**, 481-507.

____, ____, and J. Wang, 1997b: Influence of the North American monsoon system on the United States summer precipitation regimes. *J. Climate*, **10**, 2600-2622.

Holton, J. R., 1967: The diurnal boundary layer wind oscillation above sloping terrain. *Tellus*, **19**, 199-205.

_____, 1992: *An Introduction to Dynamic Meteorology.* Academic Press, New York, 511 pp.

Kalnay, E., M. Kanamitsu, R. Kistler, W. Collins, D. Deavan, L. Gandin, M. Iredell, S. Saha, G. White, J. Woollen, Y. Zhu, M. Chelliah, W. Ebisuzaki, W. Higgins, J. Janowiak, K.C. Mo, C. Ropelewski, J. Wang, A. Leetma, R. Reynolds, R. Jenne, and D. Joseph, 1996: The NCEP/NCAR 40-year reanalysis project. *Bull. Amer. Meteor. Soc.*, **77**, 437-471.

Kistler, R., E. Kalnay, W. Collins, S. Saha, G. White, J. Woollen, M. Chelliah, W. Ebisuzaki, M. Kanamitsu, V. Kousky, H. Dool, R. Jenne, and M. Fiorino, 2001: The NCEP-NCAR 50-year reanalysis: monthly means cd-rom and documentation. *Bull. Amer. Meteor. Soc.*, **82**, 247-268.

Kleeman, R., 1989: A modeling study of the effect of the Andes on the summertime circulation over tropical South America. *J. Atmos Sci.*, **46**, 3344-3362.

Langland, R. H., Z. Toth, R. Gelaro, I. Szunyogh, M. A. Shapiro, S. J. Majumdar, R. E. Morss, G. D. Rohaly, C. Velden, N. Bond, and C. H. Bishop, 1999: The North Pacific Experiment (NORPEX-98): targeted observations for improved North American weather forecasts. *Bull. Amer. Meteor. Soc.*, **80**, 1363-1384.

Lorenz, E. N., 1969: The predictability of a flow which possesses many scales of motion. *Tellus*, **21**, 289-307.

Mechoso, C. R., and G. Pérez-Iribarren, 1992: Streamflow in southeastern South America and the southern oscillation. *J. Climate*, **5**, 1535-1539.

Miguez-Macho, and J. Paegle, 2000: Sensitivity of a global forecast model to initializations with reanalysis datasets. *Mon. Wea. Rev.*, **128**, 3879-3889.

_____, and J. Paegle, 2001: Sensitivity of North American numerical weather prediction to initial state uncertainty in selected upstream subdomains. *Mon. Wea. Rev.*, **129**, 2005-2022.

Mo, K. C., J. R. Zimmerman, E. Kalnay, and M. Kanamitsu, 1991: A GCM study of the 1988 United States drought. *Mon. Wea. Rev.*, **119**, 1512-1532.

_____, J. N. Paegle, and J. Paegle, 1995: Physical mechanisms of the 1993 summer floods. *J. Atmos. Sci.*, **52**, 879-895.

_____, J. N. Paegle, and R. W. Higgins, 1997: Atmospheric processes associated with summer floods and droughts in the central United States. *J. Climate*, **10**, 3028-3046.

Namias, J., 1983: Some causes of United States drought. *J. Climate Appl. Meteor.*, **22**, 30-39.

_____, 1991: Spring and summer 1988 drought over the contiguous United States--causes and prediction. *J. Clim*ate, **4**, 54-65.

Nicolini, M., K. M. Waldron, and J. Paegle, 1993: Diurnal variations of low-level jets, vertical motion and precipitation: a model case study. *Mon. Wea. Rev.*, **121**, 2588-2610.

_____, Y. G. Skabar, A. G. Ulke, and A. C. Saulo, 2002: RAMS model performance in simulating precipitation during strong poleward low level jet events over northeastern Argentina. *Meteorologica*, **27**, 89-98.

Nigam, S., I. M. Held, and S. W. Lyons, 1988: Linear simulation of the stationary eddies in a GCM. Part II: the "mountain" model. *J. Atmos Sci.*, **45**, 1433-1452.

Nogués-Paegle, J., 1979: The effect of topography on a Rossby wave. *J. Atmos. Sci.*, **36**, 2267-2271.

_____, and K.C. Mo, 1997: Alternating wet and dry conditions over South America during summer. *Mon. Wea. Rev.*, **125**, 279-291.

_____, K. C. Mo, and J. Paegle, 1998: Predictability of the NCEP-NCAR Reanalysis model during austral summer. *Mon. Wea. Rev.*, **126**, 3135-3152.

Olson, D. A., N. W. Junker, and B. Korty, 1995: Evaluation of 33 years of quantitative precipitation forecasting at NMC. *Wea. Forecasting*, **10**, 498-511.

Paegle, J., J. N. Paegle, F. P. Lewis, and A. J. McGlasson, 1979: Description and interpretation of planetary flow structure of the Winter 1976 DST Data. *Mon. Wea. Rev.*, **107**, 1506-1514.

____, C. D. Zhang, and D. P. Baumhefner, 1987: Atmospheric response to tropical thermal forcing in real data integrations. *Mon. Wea. Rev.*, **115**, 2975-2995.

____, 1989: A variable resolution global model based upon Fourier and finite element representation. *Mon. Wea. Rev.*, **117**, 583-606.

____, K.C. Mo, and J. N. Paegle, 1996: Dependence of simulated precipitation on surface evaporation during the 1993 United States summer floods. *Mon. Wea. Rev.*, **124**, 345-361.

____, Q. Yang, and M. Wang, 1997: Predictability in limited area and global models. *Meteor. Atmos. Phys.*, **63**, 53-69.

_____, 1998: A comparative review of South American low-level jets. *Meteorologica*, **23**, 73-81.

_____, 2000: The dependence of seasonal oscillation of Western Cordillera flows upon the mountains and the ambient flow. *Proceedings of the twenty-fifth annual climate diagnostics and prediction workshop,* Palisades, New York, U.S. Dept. of Commerce, 246-249.

Pan, Z., R. W. Arritt, and M. Segal, 2000: Effects of quasi-stationary large-scale anomalies on some mesoscale features associated with the 1993 flood: a regional model simulation. *J. Geophys. Res.*, **105**, 29551-29564.

Peyrefitte, A. G., 1986: The plateau anticyclone of the western United States. Doctoral dissertation, Department of Meteorology, University of Utah, 123 pp.

Ralph, M., and Coauthors, 1999: The California Land-Falling Jets Experiment (CALJET) objectives and design of a coastal atmosphere ocean observing system deployed during a strong El Niño. Preprints, *Third Symp. on Integrated Observing Systems*, Dallas, TX, Amer. Meteor. Soc., 78-81.

Rao, G. V., and S. Ergodan, 1989: The atmospheric heat source over the Bolivian Plateau for a mean January. *Bound.-Layer Meteor.*, **46**, 13-33.

Ringler, T. D., and K. H. Cook, 1999: Understanding the seasonality of orographically forced stationary waves: interaction between mechanical and thermal forcing. *J. Atmos Sci.*, **56**, 1154-1174.

Roman, J. C., G. Miguez-Macho, L. A. Byerle, and J. Paegle, 2004: Intercomparison of global research and operational forecasts. *Wea. Forecasting*, **19**, 534-551.

Ropelewski, C. H., and S. Halpert, 1987: Global and regional scale precipitation patterns associated with the El Niño/Southern Oscillation. *Mon. Wea. Rev.*, **115**, 1606-1626.

Salio, P., M. Nicolini, and A. C. Saulo, 2002: Chaco low-level jet events characterization during the austral summer season by the ERA Reanalysis. Extended Abstracts, VAMOS/CLIVAR/WCRP Conference on the South American low-level jet, February 2002, Santa Cruz, Bolivia.

Saulo, A. C., M. Seluchi, C. Campetella, and L. Ferreira, 2001: Error evaluation of NCEP and LAHM Regional Model daily forecasts over southern South America. *Wea. Forecasting*, **16**, 697-712.

Schultz, D. M., W. J. Steenburgh, R. J. Trapp, J. Horel, D. E. Kingsmill, L. B. Dunn, W. D. Rust, L. Cheng, A. Bansemer, J. Cox, J. Daugherty, D. P. Jorgensen, J. Meitin, L. Showell, B. F. Smull, K. Tarp, and M. Trainor, 2002: Understanding Utah

winter storms: the Intermountain Precipitation Experiment. *Bull. Amer. Meteor. Soc.*, **83**, 189-21.

Shapiro, M. A., A. J. Thorpe, B. Atlas, D. Carlson, W. Dabberdt, A. Frolov, R. Gelaro, N. Gustafsson, P. Houtekamer, S. Jones, R. Langland, A. Lorenc, M. Morgan, R. Morss, T. Nakasawa, T. E. Nordeng, H. Olafsson, T. Palmer, H.-L. Pan, F. Rabier, R. Rotunno, P. Sardeshmukh, B. Smith, L. Smith, C. Snyder, Z. Toth, C. Velden, V. Wulfmeyer, and T. Xu, 2003: THORPEX international science plan, Version 2, August 2003, http://www.mmm.ucar.edu/uswrp/programs/thorpex.html.

Simmons, A. J., and A. Hollingsworth, 2002: Some aspects of the improvement in skill of numerical weather prediction. *Quart. J. Roy. Meteor. Soc.*, **128**, 647-677.

Smith, R., J. Paegle, T. Clark, W. Cotton, D. Durran, G. Forbes, J. Marwitz, C. Mass, J. McGinley, H.-L. Pan, and M. Ralph, 1997: Local and remote effects of mountains on weather: research needs and opportunities. *Bull. Amer. Meteor. Soc.*, **78**, 877-892.

Stoelinga, M. T., P. V. Hobbs, C. F. Mass, J. D. Locatelli, B. A. Colle, R. A. Houze, Jr., A. L. Rangno, N. A. Bond, B. F. Smull, R. M. Rasmussen, G. Thompson, and B. R. Colman, 2003: Improvement of microphysical parametrization through observational verification experiment. *Bull. Amer. Meteor. Soc.*, **84**, 1807-1826.

Stone, E. J., 2004: Seasonal cycles of atmospheric circulations in the vicinity of the western United States. Masters thesis, Department of Meteorology, University of Utah, 76 pp.

Toth, Z., and E. Kalnay, 1997: Ensemble forecasting at NCEP and the breeding method. *Mon. Wea. Rev.*, **125**, 3297-3319.

Trenberth, K. E., G. W. Branstator, and P. A. Arkin, 1988: Origins of the 1988 North American drought. *Science*, **242**, 1640-1645.

____, ____, 1992: Issues in establishing causes of the 1988 drought over North America. *J. Clim*ate, **5**, 159-172.

Uccellini, L. W., and D. R. Johnson, 1979: The coupling of upper and lower tropospheric jet streaks and implications for the development of severe convective storms. *Mon. Wea. Rev.*, **107**, 682-703.

____, 1980: On the role of upper tropospheric jet streaks and leeside cyclogenesis in the development of low-level jets in the Great Plains. *Mon. Wea. Rev.*, **108**, 1689-1696.

Virji, H., 1981: A preliminary study of summertime tropospheric circulation patterns over South America estimated from cloud winds. *Mon. Wea. Rev.*, **109**, 167-178.

Viterbo, P., and A. K. Betts, 1999: Impact of the ECMWF reanalysis soil water on forecasts of the July 1993 Mississippi flood. *J. Geophys. Res.*, **104**, 19361-19366.

Vukicevic, T., and J. Paegle, 1989: The influence of one-way interacting lateral boundary conditions on predictability of flow in bounded numerical models. *Mon. Wea. Rev.*, **117**, 340-350.

Wang, M., J. Paegle, and S. P. DeSordi, 1999: Global variable resolution simulations of Mississippi River basin rains of summer 1993. *J. Geophys. Res.*, **104**, 19399-19414.

Wexler, H., 1961: A boundary layer interpretation of the low-level jet. *Tellus*, **13**, 368-378.

White, B. G., J. Paegle, W. J. Steenburgh, J. D. Horel, R. T. Swanson, L. K. Cook, D. J. Onton, and J. G. Miles, 1999: Short-term forecast validation of six models. *Wea. Forecasting*, **14**, 84-108.

Wu, W.-S., M. Iredell, S. Saha, and P. Caplan, 1997: Changes to the 1997 NCEP operational MRF model analysis/forecast system. National Centers for Environmental Prediction Technical Procedures Bulletin 443. National Weather Service, Office of Meteorology, Programs and Plans Division, Silver Spring, MD, 20910.

Zhou, J., and K.-M. Lau, 1998: Does a monsoon climate exist over South America? *J. Climate*, **11**, 1020-1040.